Experimental, numerical and analytical study for the Improvement of Biomass Fluidized Bed Gasifiers

Thesis submitted to Cardiff University of the Requirements for the degree of Doctor of Philosophy in Mechanical Engineering – Renewable Energy

By

Ahmed Salih Shaker Al-Akaishi

B.Sc. Mechanical Eng. & M.Sc. Mechanical Eng.

Cardiff School of Engineering
Cardiff – United Kingdom
September 2018

DECLARATION

This work has not been submitted in substance for any other degree or award at this or any other university or place of learning, nor is being submitted concurrently in candidature for any degree or other award.

Signed …… (candidate) Date ……

STATEMENT 1

This thesis is being submitted in partial fulfillment of the requirements for the degree of PhD.

Signed …… (candidate) Date ……

STATEMENT 2

This thesis is the result of my own independent work/investigation, except where otherwise stated, and the thesis has not been edited by a third party beyond what is permitted by Cardiff University's Policy on the Use of Third Party Editors by Research Degree Students. Other sources are acknowledged by explicit references. The views expressed are my own.

Signed …… (candidate) Date ……

STATEMENT 3

I hereby give consent for my thesis, if accepted, to be available online in the University's Open Access repository and for inter-library loan, and for the title and summary to be made available to outside organisations.

Signed …… (candidate) Date ……

STATEMENT 4: PREVIOUSLY APPROVED BAR ON ACCESS

I hereby give consent for my thesis, if accepted, to be available online in the University's Open Access repository and for inter-library loans **after expiry of a bar on access previously approved by the Academic Standards & Quality Committee.**

Signed …… (candidate) Date ……

Abstract

The gasification of biomass is considered one of the most important sources of renewable energy due to the sustainability of agriculture waste around the world. There are many types of gasification systems depending on the mechanism of gasification. BFBG is one of the powerful gasifiers due to the mixing mechanism between the solid materials (biomass and the inert material) and the gas phase (air). Gasification process in the BFBG involves three main interactive factors: hydrodynamics, heat transfer and chemical reaction.

The present work focuses on improving the hydrodynamic performance and the product gas quality of a new BFBG developed at Cardiff University. Hydrodynamics has been analysed experimentally and numerically using four different distributors designed to improve the fluidized bed fluidic patterns. The tests have been performed experimentally using a representative perspex prototype, while an isothermal 3D unsteady-state CFD simulation by using OpenFOAM software based on multiphase resolution was employed in order to select the optimal design that can improve the system performance. The post improving of the BFBG product gas with catalyst has been analysed numerically by using ASPEN PLUS software.

The hydrodynamic behaviour of the BFBG with four different air distributors was studied experimentally in terms of pressure drop and bubble formation. Two design factors were observed as the major contributors towards the impact on the BFBG performance, i.e. the orifice size and the distribution of orifices. Small orifices with triangular arrangement have demonstrated superior performance than large orifice size with square arrangement. Similar findings were obtained from the CFD simulation of the BFBG with the four distributors with an accepted comparison with the experimental results and literature.

Regarding the post -gasification improvement, ASPEN PLUS analysis showed the using of BFBG product gas with suitable amount of N_2 and Ar can increase the H_2 and CO selectivity, H_2/CO ratio and decrease the heat duty. The analysis results were compared with literature.

Acknowledgements

Thanks to the Ministry of Higher Education, Iraq Government (Al-Kufa University) for providing me with a scholarship which has made my PhD possible. Thanks for the staff of the Iraqi cultural attaché in London for their help and support.

I would like to express my sincerest gratitude to Dr. Agustin Valera-Medina and Dr. Richard Marsh for their supervisory support and giving me the opportunity to study a PhD at Cardiff University. They have been supportive of my work and ideas that I have had about my research. They have been very patient with my demanding nature, and I really appreciate having been able to knock on their doors whenever I have needed help and finance.

Without the help of the Engineering Workshop I would not have been able to design and produce my rig. In particular, Malcolm Seabourne has always been there to translate my ideas into a workable solution. His technical support has been invaluable to meeting my practical needs.

I would also like to thank all the staff in the research office. Special thanks to Aderyn Reid, Jeanette Whyte and Chris Lee for their extraordinary help.

I would like to say thank you to my mother for encouraging me to finish my PhD, you are waiting for this day a long time ago. Special thanks to my lovely wife Ban for being patient with me during the whole period of study and always pushing me forward to achieve my best. I could have not done this without you. Lastly, I would like to give a special thanks to my children, Zaid, Shahad and Ali for their love and support over the last 4 years. I hope I can compensate your patient.

Contents

List of Figures

List of Tables

List of Equations

	Nomenclature	
Symbol	**Description**	**Unit**
Ar	Archimedes number	-
BFB	Bubbling Fluidised bed	Abbreviation
BFBG	Bubbling Fluidised Bed Gasifier	Abbreviation
CFB	Circulating Fluidised Bed	Abbreviation
CFBG	Circulating Fluidised Bed Gasifier	Abbreviation
CFD	Computational Fluid Dynamics	Abbreviation
C_{ps}	Specific heat of the solid particles	kJ/kg.K
CRM	Combined Reforming of Methane	Abbreviation
D	BFBG diameter	m
DESA	Department of Economic and Social Affair (UN)	Abbreviation
d_p	Particle diameter	m
DPM	Discrete Phase Model	Abbreviation
DRM	Dry reforming of methane	Abbreviation
E_a	Activation energy for the reaction	J/mole
EIA	Energy Information Administration (US)	Abbreviation
ER	Equivalence ratio	-
F	Rate of momentum exchange per volume between the fluid and particle phases (MP-PIC model).	N/m^2
FBG	Fluidised Bed Gasifier	Abbreviation

FFB	Fast fluidised bed	Abbreviation
g	Gravitational acceleration	m/s^2
h	Heat transfer coefficient	$W/m^2.K$
H, H_s	Bed height, static bed height	m
HSM	Hard Sphere Model	Abbreviation
IEA	International Energy Agency	Abbreviation
IPCC	Intergovernmental Panel on Climate Change	Abbreviation
k	Reaction rate constant	
MPPIC	Multiphase Particle in Cell	Abbreviation
MRM	Mixed Reforming of Methane	Abbreviation
N	Number of orifices per unit area of the distributor	-
P	The pitch between two holes in the distributor	m
p	Fluid pressure	pa
R	The universal gas constant	J/K.mole
RPLUG	Plug flow tubular reactor (PFR)	Abbreviation
SF	Sweep factor	Abbreviation
SLPM	Standard Litter Per Minute.	Abbreviation
SRM	Steam reforming of methane	Abbreviation
SSM	Soft Sphere Model	Abbreviation
TFM	Two-Fluid Model	Abbreviation
U, u_s	Superficial gas velocity	m/s
U_{mf}, u_{mf}	Minimum fluidisation velocity	m/s

UNEP	United Nations Environmental Programme	Abbreviation
U_t	Terminal velocity	m/s
WMO	World Meteorological Organization	Abbreviation
X_A	Chemical conversion rate in the BFB reactor	%
Greek symbols		
β	Interphase drag coefficient (Two Fluid Model)	-
ϕ	probability distribution function (MP-PIC model).	-
$\bar{\bar{I}}$	Unit tenser (Two Fluid Model)	-
λ_s	The bulk viscosity of the solid	pa.s
ρ_g	Gas density	kg/m^3
ρ_p	Solid particle density	kg/m^3
ρ_{sus}	suspension density	kg/m^3
$\bar{\bar{\tau}}$	Stress-strain tensor (Two Fluid Model)	N/m^2
ΔH_o	Heat (enthalpy) of reaction	kJ/mole
Δp	Pressure drop	pa
μ_g	Gas dynamic viscosity	pa.s
υ	Kinematic viscosity	m^2/s
ϵ	Void fraction (voidage)	-

Chapter 1: Introduction

1.1. Introduction

Over the past decades, the global consumption of energy has recorded high levels (Amasyali and El-Gohary, 2018). The rapid increase in technology and the modern lifestyle are the main reasons which stand behind this boom in energy consumption. In the same context, the global energy demand will rise by more than 25 % by 2040 due to the global growth in economy and population (IEA, 2018). Almost 80% of the worldwide supplied energy comes from fossil fuel sources (natural gas, oil, and coal) and the rest comes from other sources such as nuclear, hydro, and other renewable energy sources. This reliance is expected to be maintained until 2040 (EIA, 2016a).

Two important facts must be considered about fossil fuels. Firstly, fossil fuels are responsible for global warming. The burning of fossil fuels produced about 36.2 billion tonnes of carbon dioxide (CO_2) in 2017 which is the main component of greenhouse gases, while the CO_2 emissions were expected to increase in 2018 to reach 37.1 billion tonnes. i.e. 2.7 % more than in 2017 which is the highest recorded CO_2 level (Le Quéré et al., 2018).

The second fact is about the endurance of fossil fuels. The three forms of fossil fuels (oil, coal, and natural gas) are estimated to run out by 2088. According to this estimation, oil reserves will be exhausted by 2052, gas will run out by 2060, and coal will vanish by 2088 as presented in figure 1.1 (Ecotricity, 2018).

The relationship between the three components of the energy trilemma (shown in figure 1.2) can affect the future of energy. This relationship defers from country to country depending on the importance of each factor and their energy policy. However, most countries try to reconcile between these components.

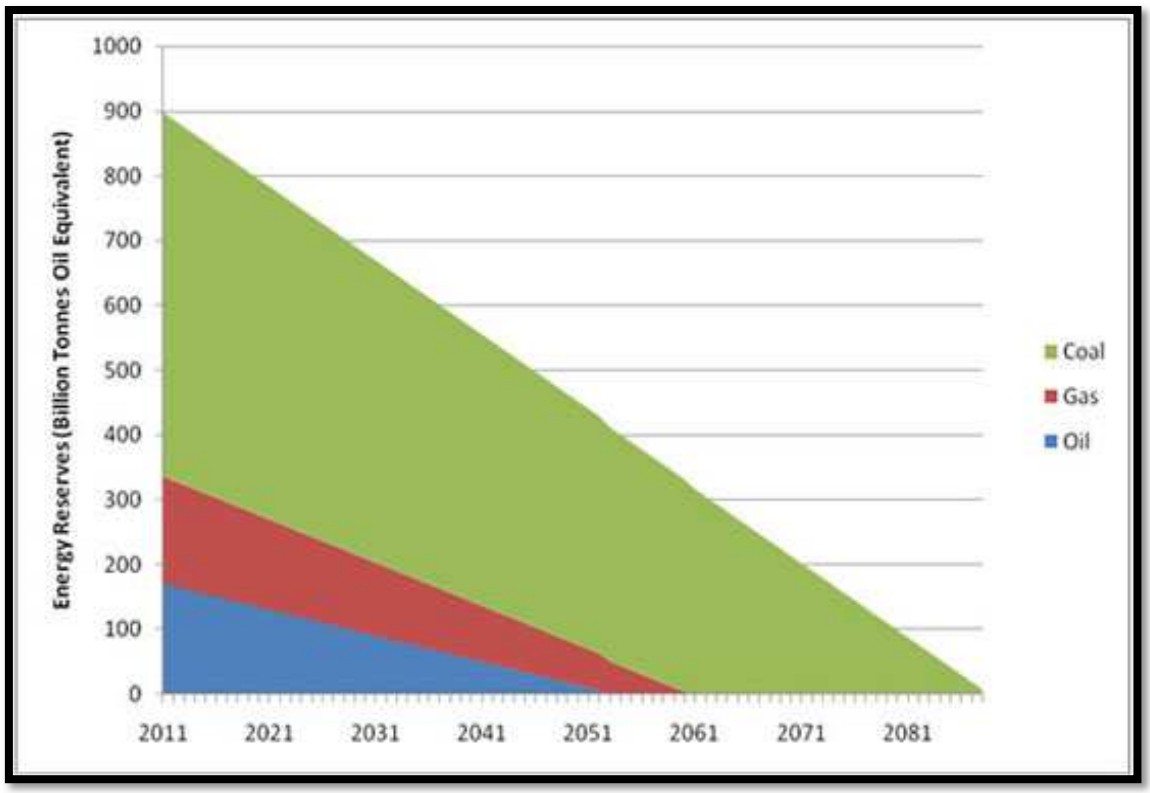

Figure 1.1. The predicted end of fossil fuels (Ecotricity, 2018).

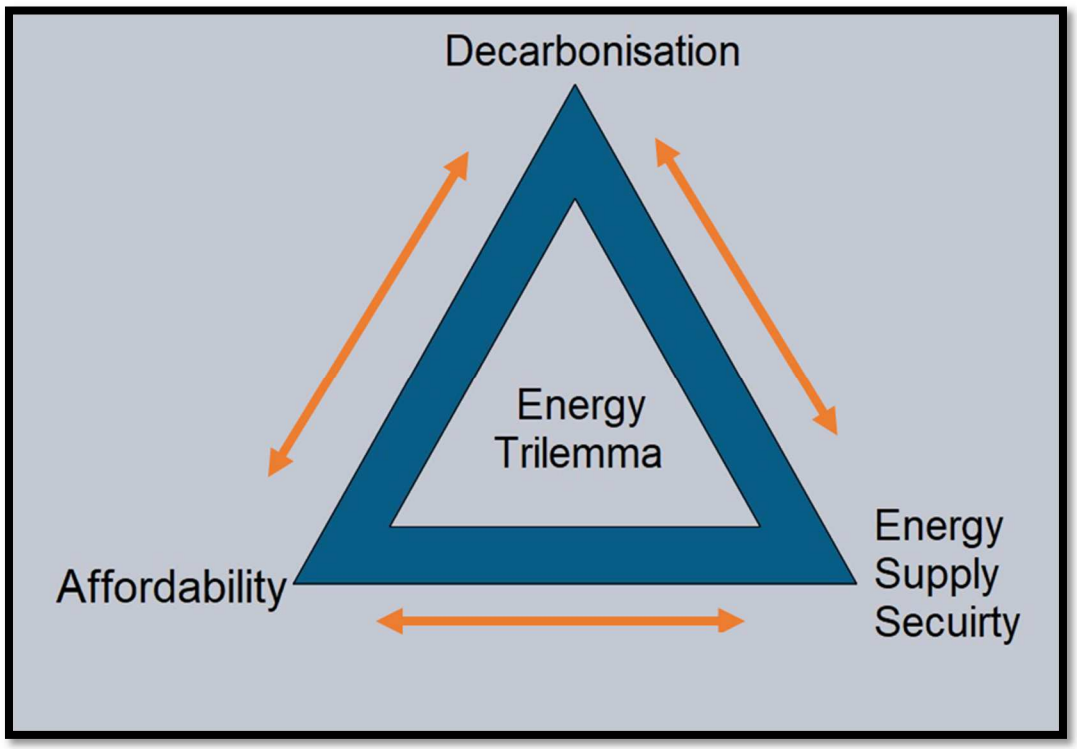

Figure 1.2. The energy trilemma components (Dawson, 2016).

Hence, there is a persistent need to improve clean and sustainable sources of energy. Renewable energies grab the attention of both researchers and investors due to the promising future of energy after fossil fuels run out. Wind, solar, hydro and biomass are the most common forms of renewable energy. Production cost and intermittency are the major challenges that the development of sustainable energy face. Biomass gasification is one of the emerging sources of renewable energy that depends mainly on agriculture waste (Belgiorno et al., 2003). This source can provide environmentally friendly fuels such as hydrogen (H_2) while getting rid of waste at the same time. As the other sustainable sources of energy, gasification processes need to be modified in both the gasification mechanism, i.e. the hydrodynamic behaviour and the quality of the product (synthetic gases) which is the aim of this dissertation.

1.2. Energy challenges

While fossil fuels will run out in the near future, the rapid growth of world population causes an increased demand for energy. The United Nations Population Division estimates a global population of approximately 9.6 billion people in 2050 and more than 11 billion by 2100 (world population now is 7.3 billion people). Global Gross Domestic Product (GDP) will be more than doubled in 2050 (DESA, 2015). This growth will create more need for affordable, reliable energy – energy demand for homes, transportation, business, and industry.

1.3. Energy and Climate Change

Although the rapid increase in energy demand is a great challenge, there is another important challenge which has a major impact on the life on our planet. The type and quality of energy sources (fuels) that have a direct influence on the environment. Most energy sources (especially fossil fuels) have a detrimental effect on the environment due to the emissions of greenhouse gases (CO_2 and CH_4).

Climate change is a real threat facing our entire species and the life on earth. There are many possible causes of climate change that can be divided into two groups (Robock, 1978):

1- Internal forcing mechanisms such as rising sea level and

2- External forcing mechanisms such as Orbital Variations, Solar Output, Volcanism, Plate Tectonics and Human Influences.

Human activities contribute to climate change through several forms, such as deforestation and energy sources (fossil fuels). Globally, the burning of fossil fuels (solid, liquid and gas) in 2013 released about 9776 million metric tons of carbon to the atmosphere, representing an all-time high and a 1.1% increase over 2012 emissions, as presented in figure 1.3 (Boden et al., 2016). In total, more than 35 billion tonnes of carbon dioxide was released to the atmosphere in 2013.

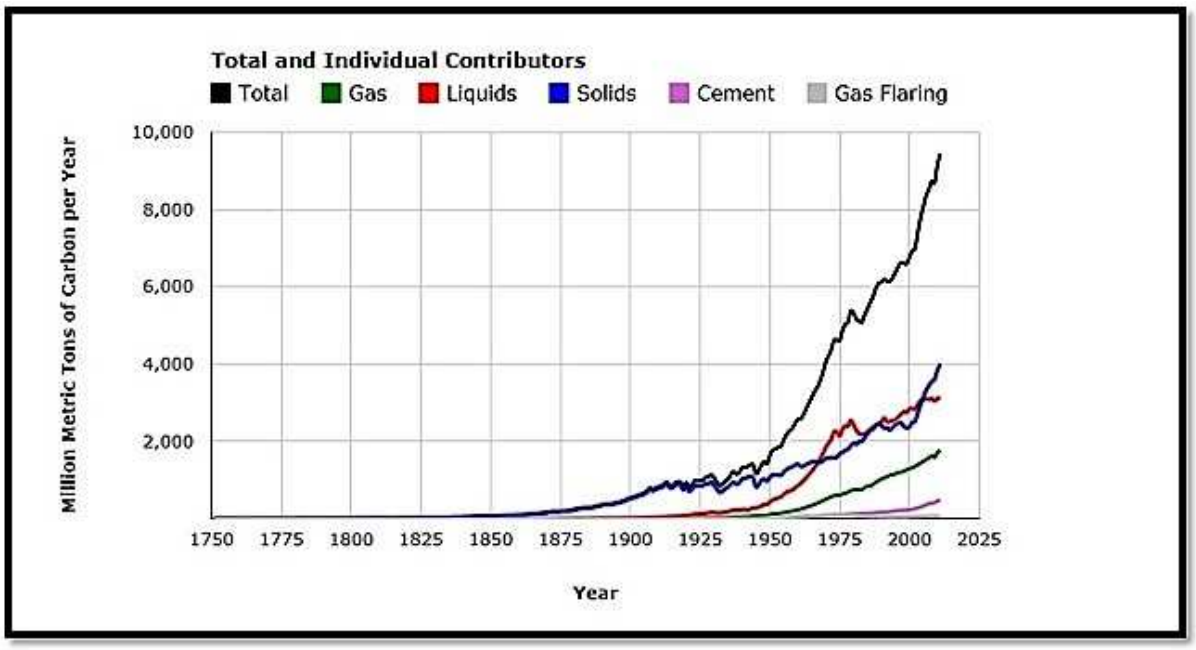

Figure 1.3. Annual Global Fossil-Fuel Carbon Emissions (Boden et al., 2016).

This rise in CO_2 concentration relates to the global increase in surface temperature due to the greenhouse effect of carbon dioxide. This unprecedented rise in surface temperatures has a significant impact on the earth via melting of ice caps and glaciers, rising sea levels, and impacting ecosystems. This tragic scenario for the earth can be stopped by cutting down carbon dioxide emissions, especially, the CO_2 emissions due to the burning of fossil fuels for energy purposes(Boden et al., 2016).

Thus, the question in this context is how to harmonize between the extendable demand on energy while saving the planet from the tragic scenario caused by global warming? The answer to this controversial question can be summed up in three words: Biomass Renewable Energy.

1.4. Legislations and Policies

Many governments in developed and developing countries throughout the world have taken a number of steps to limit the emissions of greenhouse gases through legally binding targets, both now and in the future. In 1988 the Intergovernmental Panel on Climate Change (IPCC) was established by the United Nations Environmental Programme (UNEP) and the World Meteorological Organization (WMO) “to provide policymakers with regular assessments of the scientific basis of climate change, its impacts and future risks, and options for adaptation and mitigation” (IPCC, 2013). This step followed by many steps to control climate change by many agreements such as the Paris Agreement(Agreement, 2015).

The EU efforts to tackle climate change concentrate on three targets (EC, 2015):

1- Reduce the emissions of greenhouse gases.
2- Increase the sharing of energy provided by renewable sources.
3- Increase energy efficiency.

The European Union sets many directives in this context to achieve the following targets by 2020 (TheCCC, 2017).

A- A cut off the greenhouse emissions by 20% compared to 1990 levels.

B- 20% of the total provided energy comes from renewable sources.

C- 20% increase in energy efficiency than 2007 levels.

In the 2030 framework for the climate and energy, the EU countries have agreed to achieve new targets (ECE, 2016).

- A reduction in greenhouse gases emissions by 40% on 1990 levels.

- 27% or more of the total provided energy comes from renewable sources.

- 27% or more is the savings in energy compared with the business-as-usual scenario.

Apart from the EU countries, the other world countries (developed and developing) made their own targets.

1.5. Renewable Energy

In contrast to conventional energy sources such as fossil fuels, which are more geographically concentrated, all the countries in the world have at least one abundant renewable resource and many countries have a portfolio of resources such as solar energy, wind power, geothermal energy, and biomass. Renewable energy sources contributed by about 11% of the world marketed energy consumption with an estimation to be 15% by 2040. In the electricity sector, the sharing of renewable energy was about 22% in 2013 with a projection of 25% by 2040 (EIA, 2013).

Year by year, the global investment in the renewable energy sector is increasing. In 2015, a record $367 billion was invested in renewable energy around the world. Figure 1.4 shows the world annual investments in the clean renewable energy sector in the last five years (Clean Energy Canada, 2016).

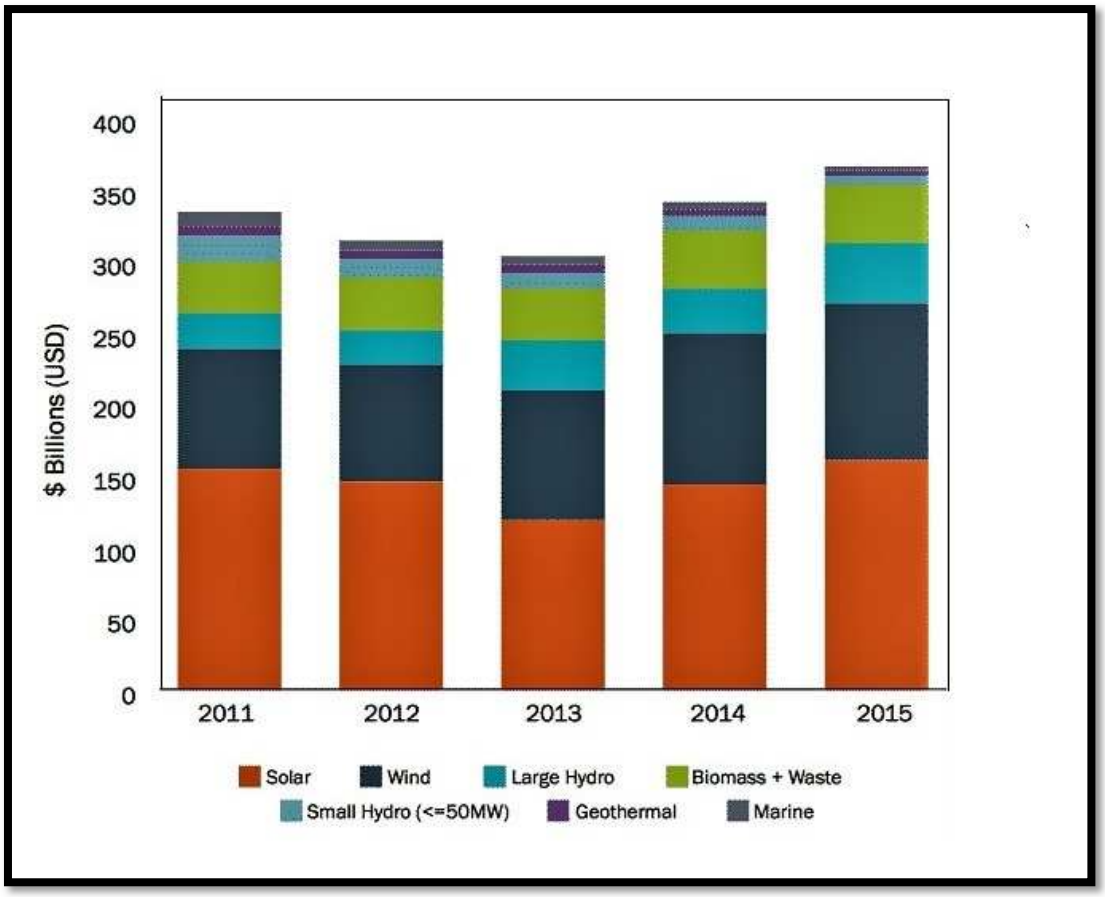

Figure 1.4. Total annual investment in the renewable energy sector (Globally) (Clean Energy Canada, 2016).

1.6. Biomass energy

One of the sustainable resources of energy is a renewable organic waste. This organic waste can include scrap lumber, forest debris, agricultural harvest waste, and other industrial byproducts that serve no other purpose. In the United States, about 50% of the produced renewable energy came from biomass in 2011. Biomass and waste can be turned into biofuels through a natural process such as anaerobic digestion by bacteria to produce biogas or synthetic thermochemical processes such as gasification (CHO, 2011).

1.7. Gasification

The process of converting solid organic-based carbonaceous materials into gaseous products such as carbon monoxide, hydrogen, and carbon dioxide is called gasification. Without

combustion, the materials react at high temperatures (>700 ^{o}C) with a controlled amount of Oxygen and/or steam (Yokoyama and Matsumura, 2008). This reaction produces a gas mixture called syngas (stands for synthesis gas or synthetic gas) or producer gas. This is a form of fuel. Gasification can be considered as a renewable source of energy if the gasified compounds were obtained from biomass or waste (sustainable feedstocks).

1.8. Gasifier Types

There are several types of gasifiers currently available for commercial purposes. These depend on (Couto et al., 2013):

- Feedstock feeding method and direction into the gasifier.

- Whether using air, oxygen and/or steam as an oxidant.

- Operating temperature ranges.

- Working pressure inside the gasifier, and

- Heating method of the feedstock (directly or indirectly).

Thus, the main gasifier types are:

1.8.1. Counter-Current (Updraft) Fixed Bed Gasifier

This is the oldest and simplest type of gasifier, in this gasifier, the feedstocks (biomass) is fed in at the top and the air (or oxygen) comes from the bottom and produced syngas leaves from the top of the gasifier, hence the biomass and gases move in opposite directions. The advantages of this type of gasifier are the simplicity and low-cost process, the burn out of charcoal is high and low temperature of exit gas due to internal heat exchange and equipment efficiency is high. It can work with a wide range of feedstock from coal to biomass. The main drawback of this gasifier is the tar (A highly viscous liquid of hydrocarbons) content in the

produced gases (10 - 20% of tar by weight), requiring extensive clean-up before using these gases in later applications (Ciferno and Marano, 2002). Figure 1.5 shows an updraft gasifier scheme.

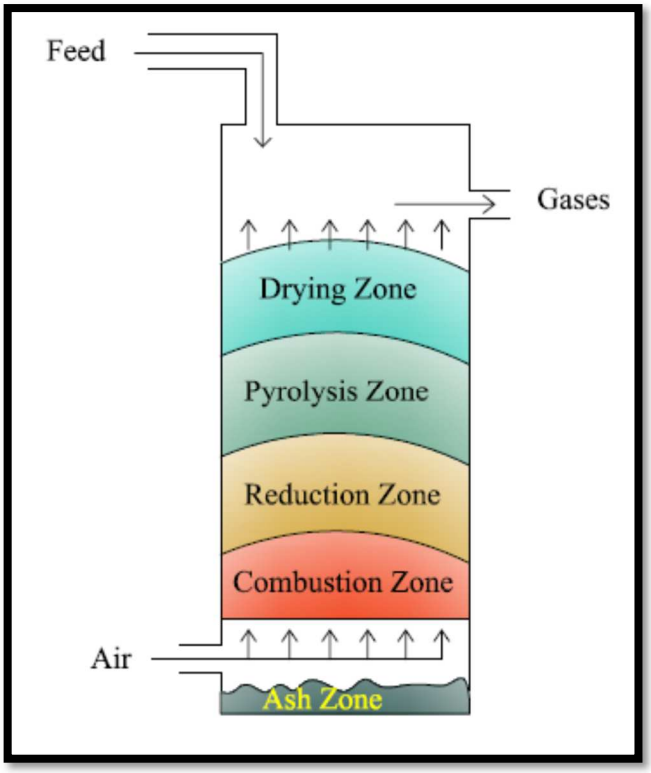

Figure 1.5. Updraft Gasifier (Belgiorno et al., 2003).

1.8.2. Co-Current (Downdraft) Fixed Bed Gasifier

Tar entrainment in the outgoing product gas is a real problem in updraft gasifiers. This can be solved by introducing the primary gasification air at or above the oxidation zone in the gasifier. The fuel and gas move in the same direction as the syngas is taken out from the bottom.

On their way down, the acid and tarry distillation products from the fuel are turned into synthetic gases such as hydrogen, carbon dioxide, carbon monoxide and methane when they pass through a glowing bed of charcoal. The amount of the broken-down tar depending on the hot zone temperature and the tarry vapours residence time.

The possibility of producing tar free gases for engine operation is the main advantage of downdraft gasifiers, i.e. up to 99.9% of the produced tar was consumed, leading to minimal or no tar cleanup. As the minerals stay down with the char/ash, the need for a cyclone is reduced. This makes the process low cost, simple, and has been proven (Ciferno and Marano, 2002).

The main drawback of the downdraft gasifier is that it cannot work with a different range of feedstocks. Flow problems and excessive pressure drop occur with the low-density feedstock. Low moisture content (<20%) feed requires using feed dryer. The downdraft gasifiers demand using a secondary heat recovery system due to the high temperature of the produced gases. The percent of unconverted carbon in this type of gasifier is between 4% and 7% (Ciferno and Marano, 2002). Figure 1.6 shows a scheme for the co-current gasifier.

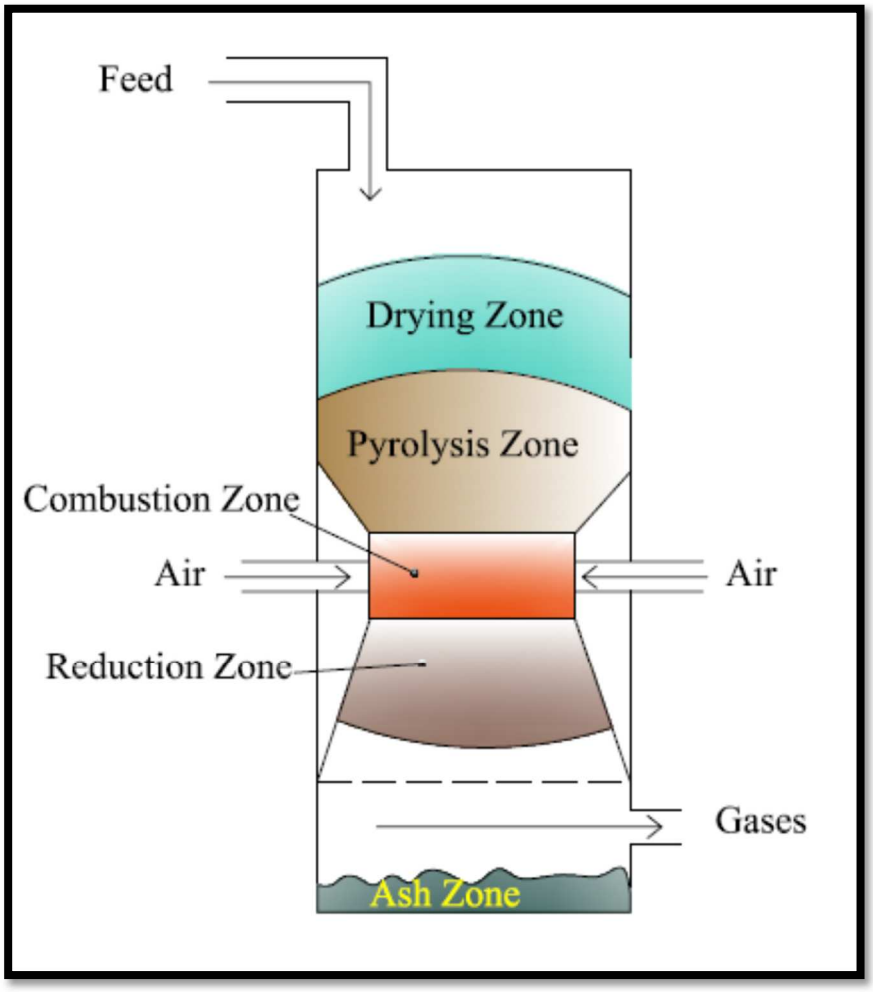

Figure 1.6. Downdraft Gasifier(Belgiorno et al., 2003).

1.8.3. Cross-Draft Fixed Bed Gasifier

The cross-draft gasifier is the lightest and simplest type of gasifiers. It is adapted for the use of charcoal feed. The cross-draft gasifiers operate in a high temperature (> 1500 ^{o}C) in the oxidation zone which causes material problems. The main advantage of cross draft gasifiers lies on the very small scale at which they can be operated. Under certain conditions, the setup of below 10 kW (shaft power) system can be economically feasible due to the very simple gas-cleaning train (only a hot filter and a cyclone) which can be used with small engines(Saravanakumar et al., 2010).

Main disadvantage lies in the minimal tar-converting capabilities this requires high quality (low volatile content) charcoal (Wood et al., 1986). Figure 1.7 shows the cross-draft gasifier scheme.

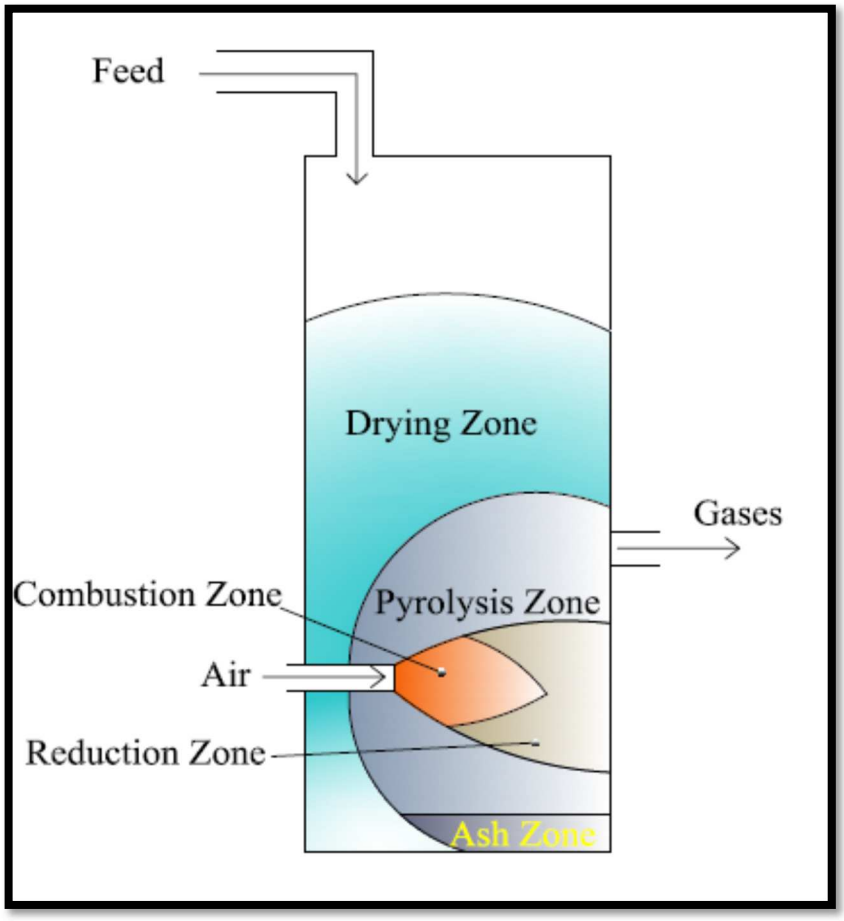

Figure 1.7. Cross-draft Gasifier (Brar et al., 2012).

1.8.4. Fluidised Bed Gasifier (FBG)

In fluidised bed gasifiers, air at a sufficient velocity (fluidisation velocity) is blown through a bed of inert solid particles (sand or alumina) to keep these in a state of suspension. After the bed is externally heated to a suitable high temperature, the feedstock is introduced. When the fuel particles are introduced to the gasifier, it would quickly be mixed with the bed material at the bottom of the reactor and heated up to the bed temperature instantaneously. Figure 1.8 shows a schematic sketch of the FBG.

The fuel is rapidly pyrolysed as a result of this treatment, leading to a component mix with a relatively large amount of gaseous materials. In the gas phase, further gasification and tar-conversion reactions occur in conjunctions. The ash particles are carried over the top of the reactor and removed by using cyclone and candle filters. Feedstocks processing is the major advantage of the fluidised bed. A fluidised bed gasifier is mostly used for high ash coal and biomass due to the relatively simple handling of ash below the softening temperature in this type of gasifier (Wood et al., 1986).

There are two main types of fluidised bed gasifier, the bubbling fluidised bed gasifier (BFBG) and the circulating fluidised bed gasifier (CFBG). In the bubbling fluidised bed gasifier, the gas velocities are relatively small which are typically less than 1 m/s. The low gas velocities of the BFBG make most of the conversion of the feedstock occurs at the bottom of the gasifier in the dense bed region. However, some of the small particles of the feedstock have continuous pyrolysis in the freeboard section of the gasifier. Figure 1.9 shows a schematic drawing of the BFBG (Olofsson et al., 2005).

In contrast, the CFBG operates with high gas velocities which are between 3 to 10 m/s. The high gas velocities drive solid particles to spread along the gasifier riser and then to the cyclone which splits the solid particles from the gas. The particles drop down the cyclone and finally, they return back to the gasifier bottom to complete the cycle. This process results in a long

contact time between gas and particles and better hydrodynamic interactive. Figure 1.10 represents a CFBG scheme (Olofsson et al., 2005).

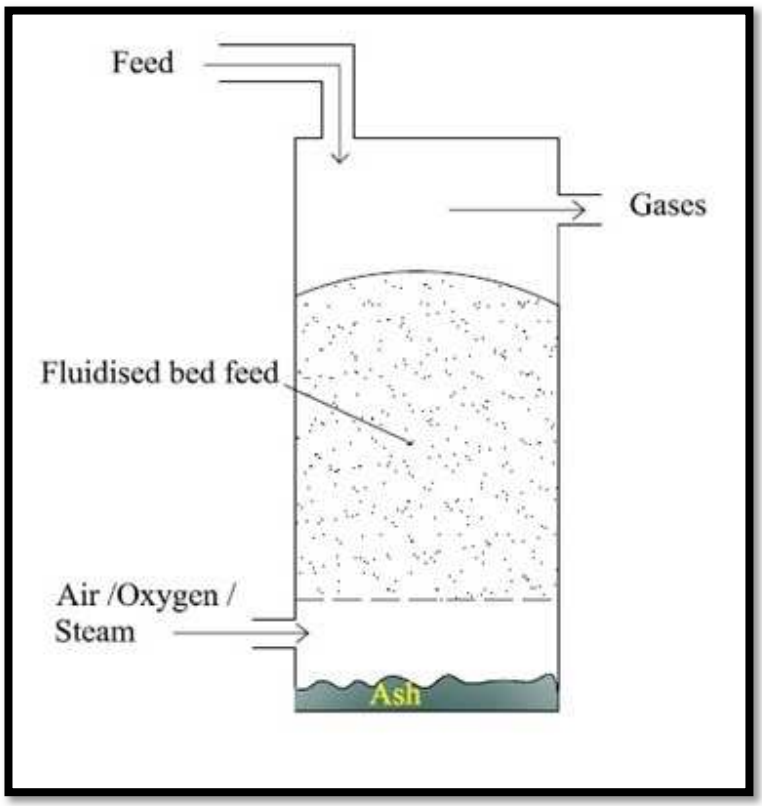

Figure 1.8. Fluidised bed Gasifier (Belgiorno et al., 2003).

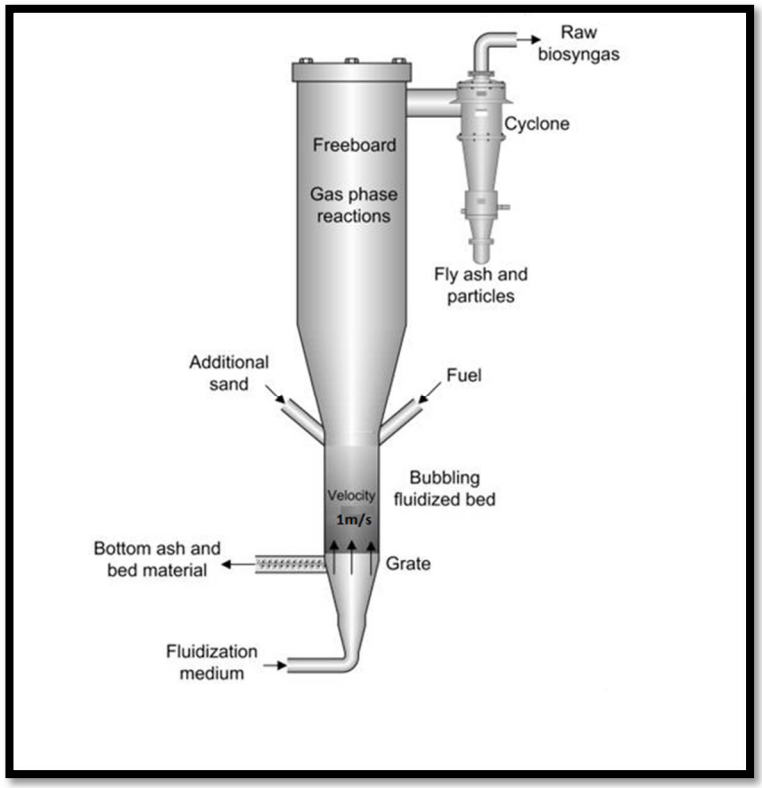

Figure 1.9. BFBG scheme (Olofsson et al., 2005).

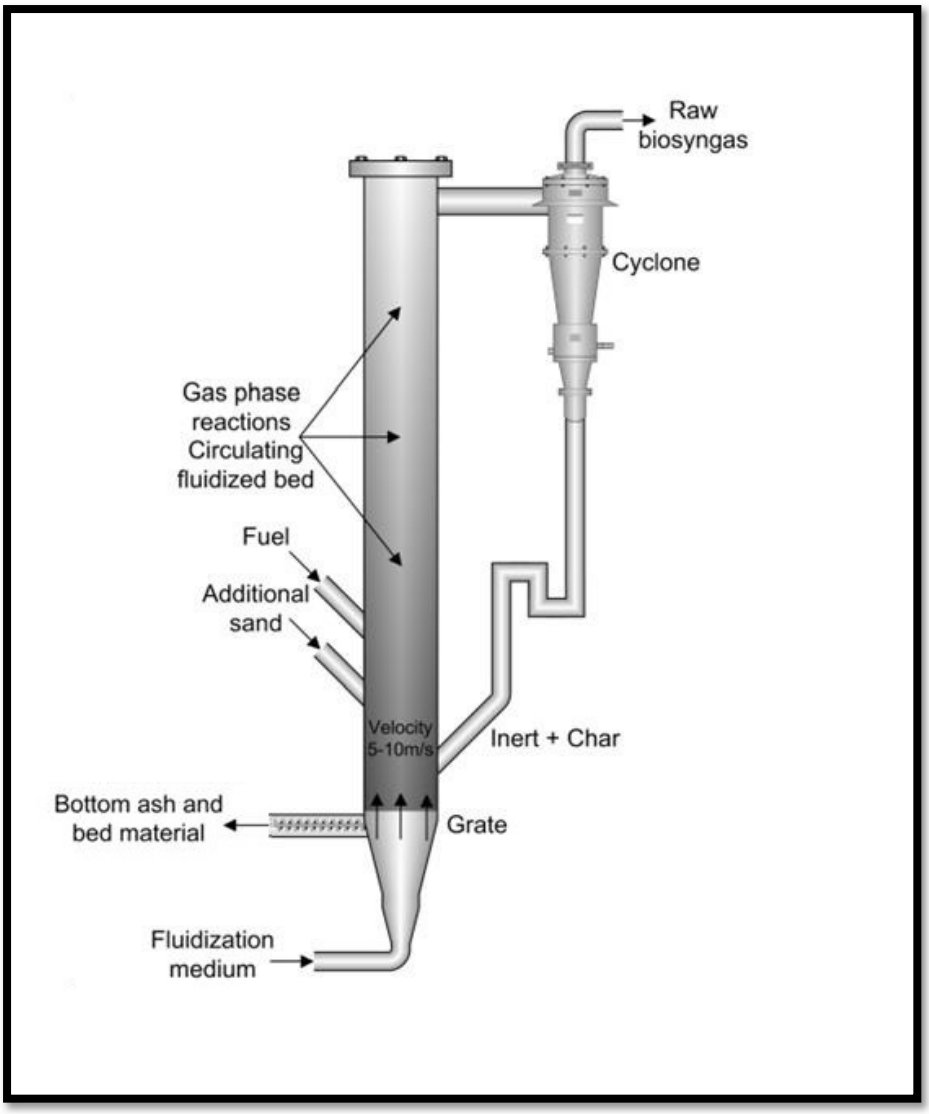

Figure 1.10. CFBG scheme (Olofsson et al., 2005).

1.9. Thesis Motivation

Throughout history, energy is connected with civilization. How much energy consumed is a factor of how advanced a civilization is (Smil, 2004). On the other hand, the excessive use of energy in the last centuries has led to different problems such as depletion of energy sources (fossil fuels) and climate change. The depending on renewable sources of energy can tackle these problems. Biomass gasification is a highly potential renewable energy source as biomass/agriculture waste are available permanently.

The work in this thesis focuses on two stages, the first stage is connected to the design of the BFBG which affects the main principles of the fluidised bed regime. The design of the gas distributor has a great influence on the gasification process in general. For example, the transition from packed bed to fluidised bed depends mainly on the gas distributor.

When the bed fluidises, the solid particles will have a good opportunity to contact the gas directly which means greater heat transfer between them. This heat transfer mechanism is the important part of the gasification process. On the other hand, more heat transfer occurs between the gasifier wall and the solid particles and gas. The experimental study of gas and solid movement inside the fluidised bed is a topic which requires complex devices. However, the simulation techniques can provide a good prediction of this issue without disturbing the fluidised bed regime.

Improving the heat transfer mechanisms inside the BFBG leads for more opportunity for chemical reactions between the biomass and air (gasification). In figure 1.11 the relationship between the main three elements in the bubbling fluidised bed gasification process is illustrated.

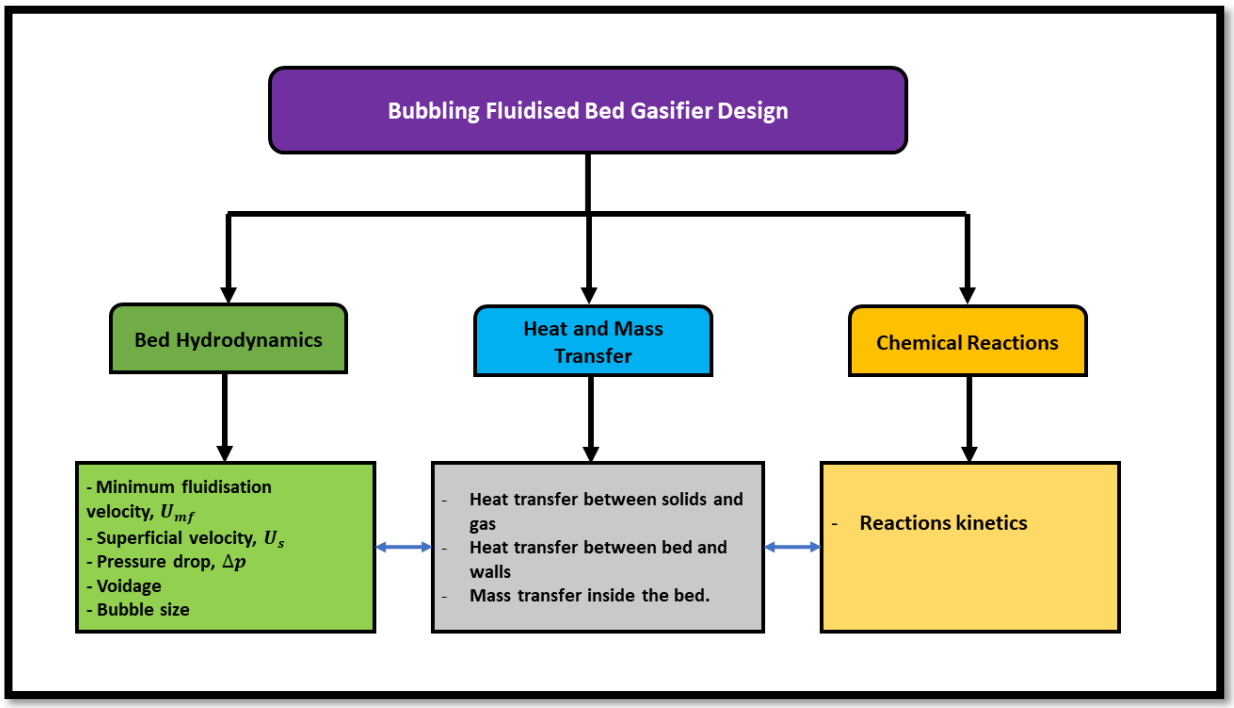

Figure 1.11. The main three elements of the bubbling fluidised bed gasification.

After the gasification stage and the gases are produced another modification stage will start. In this stage we trying to make the components of the product gas more industrially useful by enhancing the syngas components.

1.10. Aim and Objectives

The aim of this thesis is to study and improve the performance of the prototype BFBG in Cardiff school of engineering. These goals can be achieved through the following steps:

1- Conducting an experimental study in a prototype BFBG under isothermal conditions to test the effect of the air distributor design on the hydrodynamic behaviour of the BFBG. The experiments will be carried out for four different air distributors at different flow conditions.

2- Introducing a comprehensive unsteady state 3D CFD study of the effect of air distributor design on a BFBG to predicate all the hydrodynamic properties of the system especially the complex pints which cannot be reached experimentally without disturbing the fluidised bed regime. The simulation results then will be validated with experimental results and literature.

3- Assessing the post-gasification improvement for the BFBG's product gas by enhancing the syngas (H_2 and CO) and decreasing the greenhouse gas component (CO_2). This assessment will be carried out by using ASPUN PLUS simulation in order to use a novel auxiliary system (i.e. microwaves) with the support of catalytic materials.

1.11. Structure of The Thesis

The thesis involves seven chapters covering all aspects of the program goals.

1- Chapter One – Introduction.

2- Chapter Two – Literature Review.

A comprehensive review of many previous works that cover the study area. Literature about FBG, solid-gas flow models, catalytic methane reforming, and microwave heating have presented in this chapter.

3- Chapter Three – Methodology

This chapter presents the research methods of the thesis topics. Isothermal BFBG experimental procedure, isothermal BFBG simulation tools, and analysis for the post-gasification improvement is explained in this chapter.

4- Chapter Four – Experimental Study of BFBG Hydrodynamics

Review of the multi experiments which have been conducted in a prototype isothermal BFBG with four different perspex perforated disc distributors under different flow conditions.

5- Chapter Five –CFD Analysis of BFBG Hydrodynamics

In this chapter, a CFD simulation for the isothermal BFBG has been carried out. A modelling of isothermal BFBG with four different air distributors and two different superficial velocities per distributor case by using OpenFOAM software has been comprehensively covered. The results were validated with the experimental work and literature.

6- Chapter Six – Post Gasification Improvement

This chapter contains an assessment study of improving the product gas of the BFBG by increasing the syngas components. The study involves Aspen plus simulation of the catalytic plug flow reactor used in this process.

7- Chapter Seven – Conclusions and Future Work

A short brief about what have done in this program and presenting the main achievements in each part of the program area. The chapter also involves many important suggestions to improve the analytical and the experimental work in these fields. Moreover, many research ideas were intreduced which worthwhile to study and developed.

Finaly, this chapter discussed the issues that faced the experimental part of the post – gasification improvement. The unexpected fault in the gas analyser (gas chromatograph) was the main cause of postponing the work.

Chapter 2: Literature Review

2.1. Introduction

Biomass gasification, as a part of renewable energy sources, has gotten its fair share of research in both hydrodynamic and chemical behaviours. Doors are still open for more research on this subject to improve the quality of the produced gases.

2.2. Gasification Systems

Thermal gasification machines (gasifiers) can be classified mainly into three groups according to the gasification process (Phillips, 2006):

1- Moving (fixed) bed gasifiers such as counter-current gasifier.
2- Entrained flow gasifiers such as co-current gasifier. And,
3- Fluidised bed gasifiers such as BFBG and CFBG.

In figure 2.1 the temperature profiles of gasification materials along each gasifier are illustrated (Phillips, 2006).

2.3. Fluidised Bed Gasification

The process in which solids are forced to behave like a fluid by blowing gas or liquid upwards through the solid-filled reactor is called fluidisation. Fluidisation was firstly invented by the German Scientist Fritz Winkler in 1921 by injecting a gas through the bottom of a crucible containing coke particles. He found out that gas-particles mixture behaves like a boiling liquid

as a result of the floating of coke particles due to the effect of gas drag forces. Winkler experiment was recorded as the first fluidised bed gasification attempt (Basu, 2006).

2.4. Fluidised Beds and New Concepts

There are many types of gasifiers (E4Tech, 2009) starting from simply packed bed gasifiers to the more complex fluidised bed gasifiers (bubbling and circulating fluidised bed). In fluidised bed gasification, the biomass particles have a better chance to mix with fluid inside the gasifier which makes some of these particles suspended in the fluid (gas) stream (Chen, 2003). The hydrodynamic and heat transfer mechanisms of surface – bed, fluid-particles, and particles – particles interaction still having more interest due to the complexity of this interaction.

Heat transfer between bed and surface (walls) depends mainly on three factors: superficial gas velocity, suspension density, and particle size. For the BFB the superficial gas velocity has the major impact on the heat transfer coefficient between the bed and surface. The heat transfer coefficient is proportional to superficial gas velocity until the velocity reaches its optimum value at which bed height (H) reaches its maximum value (Fan and Zhu, 1998, Masoumifard et al., 2010, Tsukada and Horio, 1992).

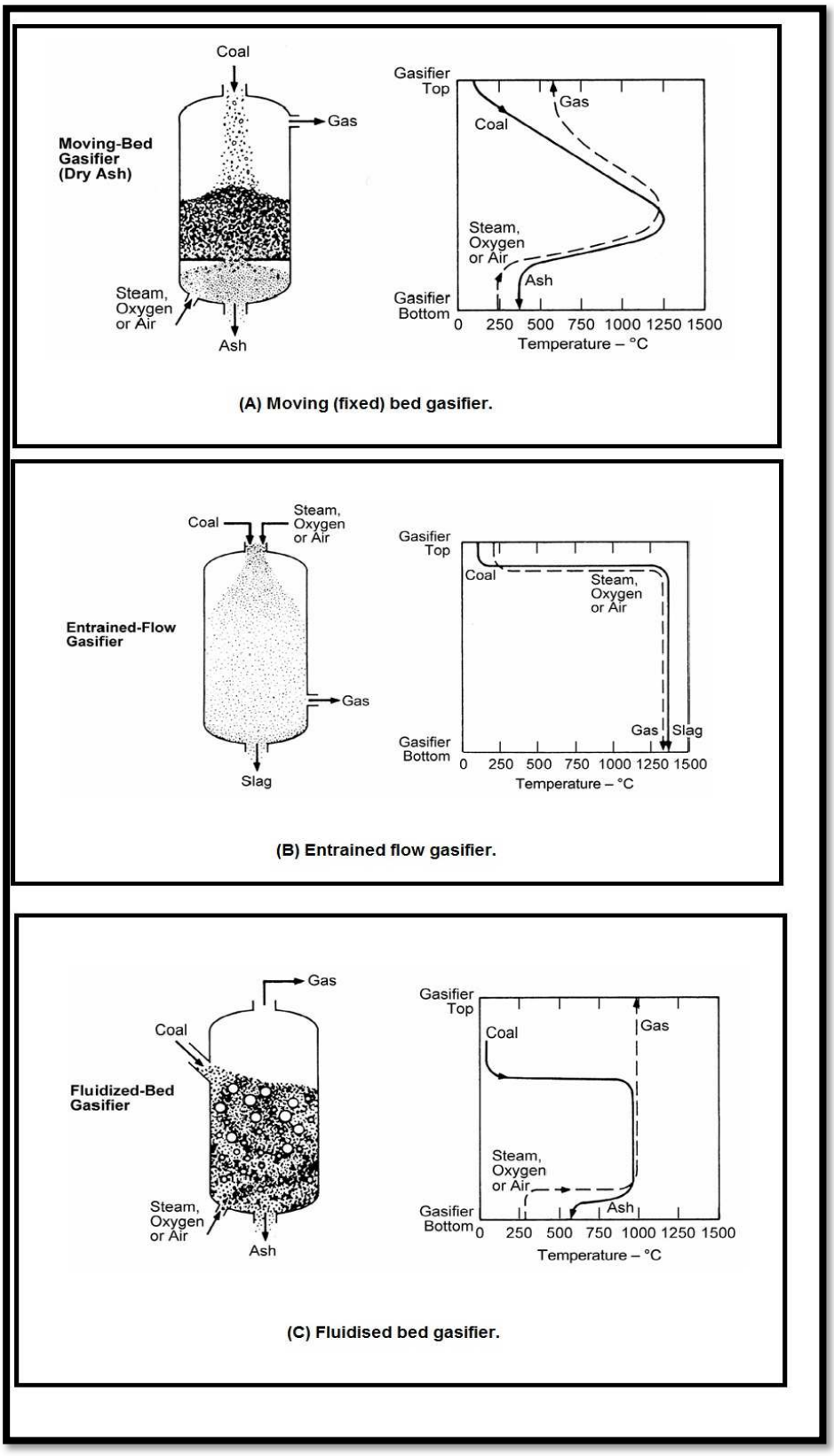

Figure 2.1. The variation of temperature along the three gasifier types (Phillips, 2006).

However, in CFB the dominant operating factor in heat transfer is the suspension density (Basu and Nag, 1996, Fox et al., 1999, Pagliuso et al., 2000). The CFB is a fast-fluidised bed (FFB) compared with the BFB. This makes the CFB, a fluidised clusters bed (Basu et al., 1990). The cluster (or the agglomerate in some literature (Cabezas-Gomez et al., 2008)) is a group of particles move as a single body with a little internal relative movement (Helland et al., 2002). Figure 2.2 shows a normal and an improved image of a cluster in a CFB (Zou et al., 1994).

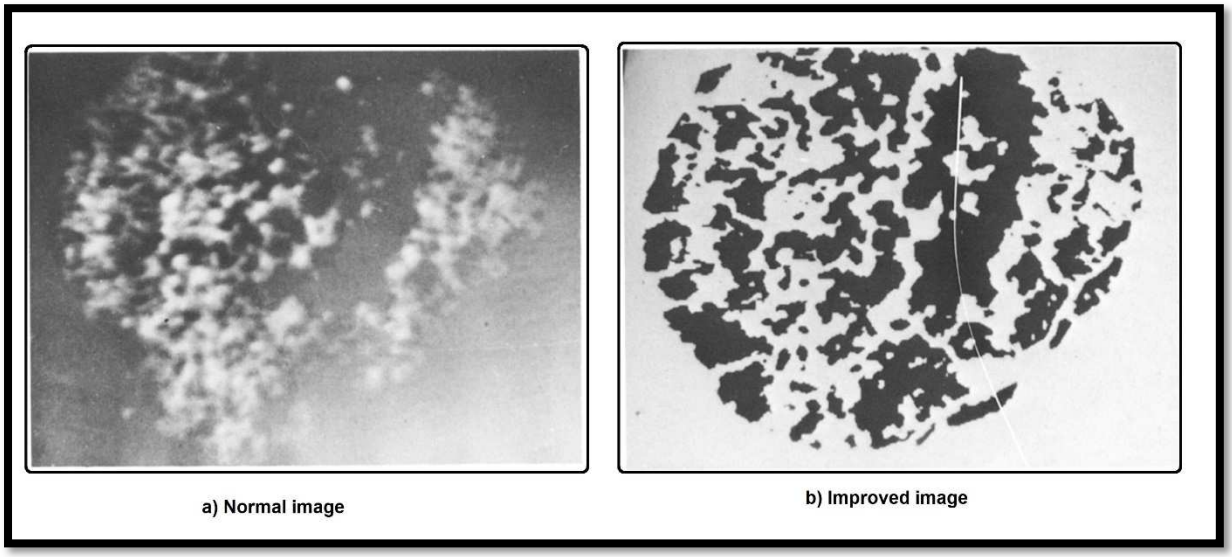

Figure 2.2. Cluster image in a CFB (Zou et al., 1994).

These clusters are moving up and down in the CFB reactor making a dilute zone between the clusters as illustrated in figure 2.3. Accordingly, the suspension density of solid gas mixture in the FFB can be calculated by the following equation (Basu and Nag, 1987):

$$\rho_{\text{sus}} = y.\rho_p + (1 - y).\rho_g \quad \text{..... 2-1}$$

Where ρ_{sus} is the suspension density in the FFB, ρ_p is solid particle density, ρ_g is the gas density and y is the volumtric concentration of dispersed solid particles in the dilute zone inside the FFB.

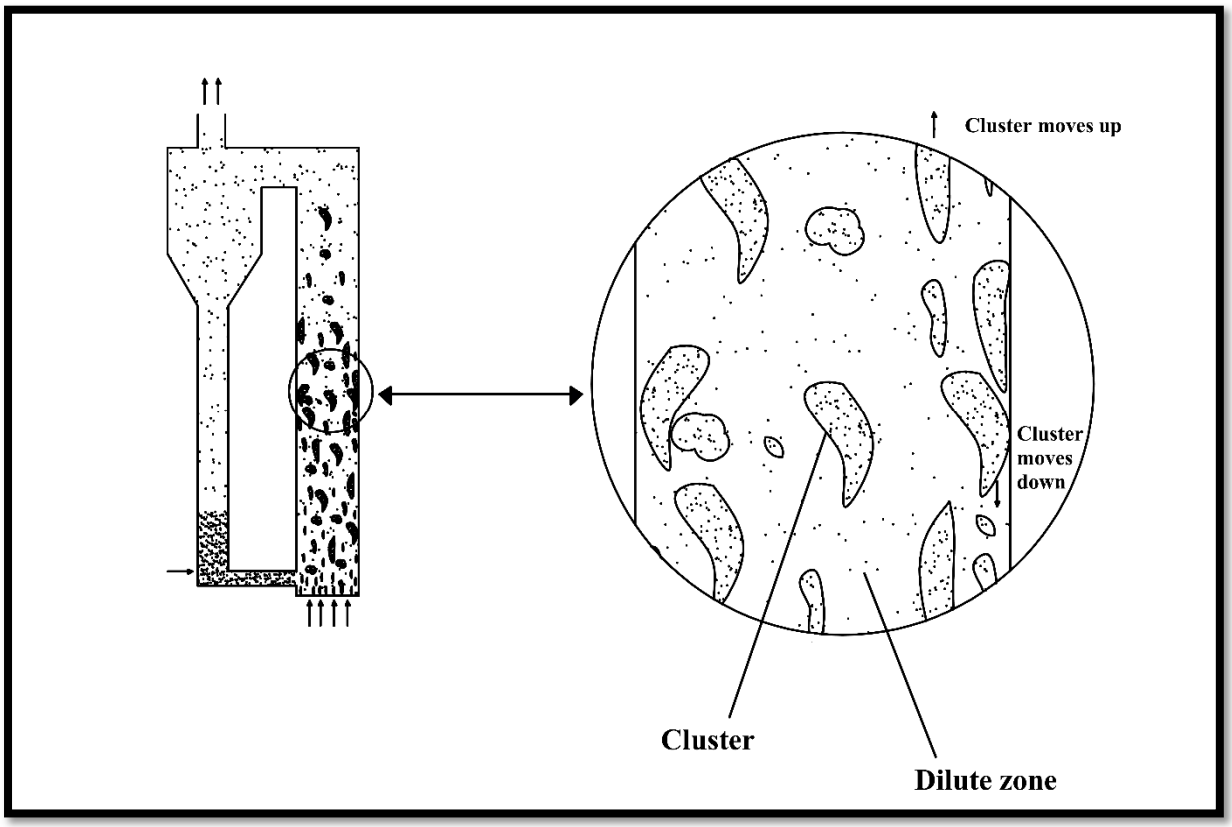

Figure 2.3. Clusters forming and movements in CFB (FFB) (Basu, 2015).

The relationship between suspension density and the heat transfer coefficient in a FFB has presented in Wen and Miller correlation (Wen and Miller, 1961):

$$h = \frac{c_{ps} \cdot \mu_g}{d_p} \cdot \left(\frac{\rho_{sus}}{\rho_p}\right)^{0.3} \left(\frac{U_t^2}{g.d_p}\right)^{0.21} \quad \text{..... 2-2}$$

Where:

h – Heat transfer coefficient in the FFB, (W/m^2.K).

c_{ps} – Specific heat of the solid particles, (kJ/kg.K).

μ_g – Gas dynamic viscosity, (pa.s).

d_p – Particle diameter, (m).

U_t – Particle terminal velocity, (m/s).

g – Gavitational acceleration, (m/s^2).

Thus, the heat transfer coefficient in the CFB proportional directly to the suspension density. This is also supported by the experimental work of (Fraley et al., 1983, Mickley and Trilling, 1949, Kobro and Brereton, 1986, Kiang et al., 1976, Basu and Nag, 1987, Basu and Large, 1988, Fox et al., 1999). Figure 2.4 shows the relationship between the heat transfer coefficient and suspension density in CFB (FFB) for some experimental works (Basu and Nag, 1987).

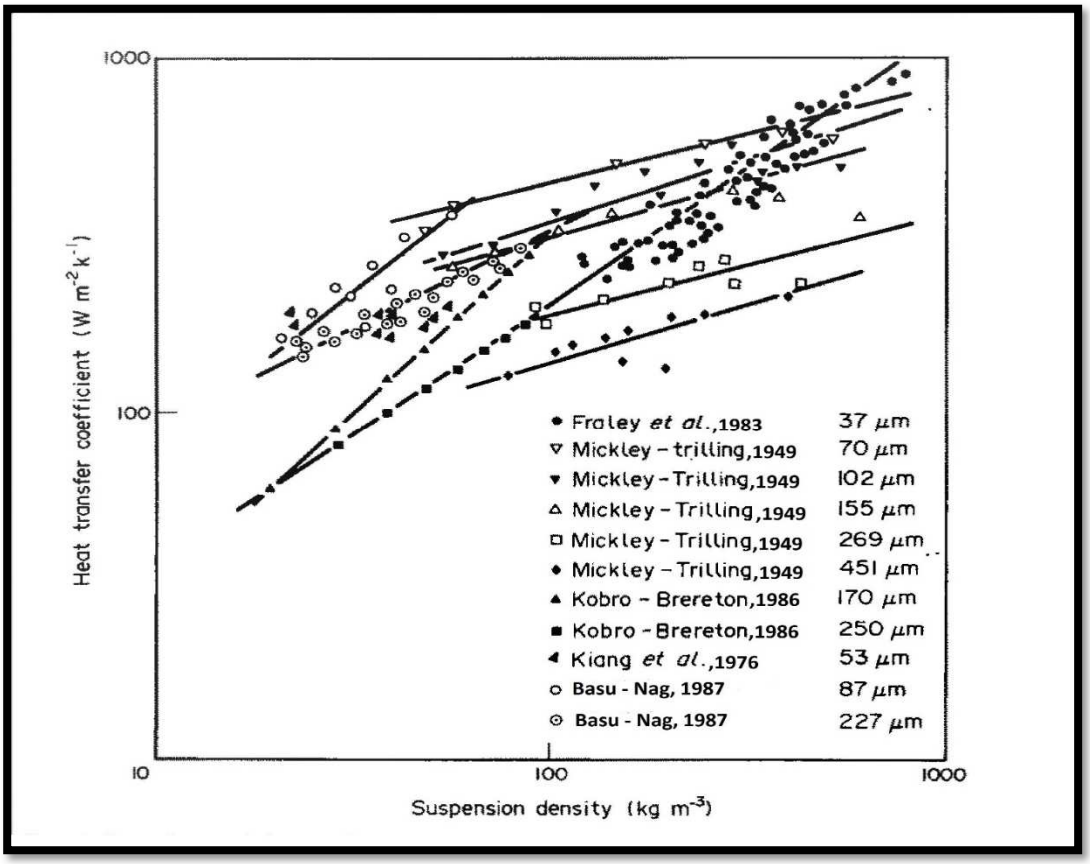

Figure 2.4. Experimental data for the relationship between heat transfer coefficient and suspension density in FFB (Basu and Nag, 1987).

2.5. Solid - Particles Grouping (Geldart Groups)

Geldart classified granulate powders used for fluidisation purposes into four groups. These groups were characterised by solids– fluid density difference and mean particle size. However, fluidised bed designs mostly rely on the particle's Geldart grouping (Geldart, 1973):

Group A: Particles in this group have sizes ranging between 20 and 100 µm and particle density of less than 1400 kg/m^3. This group of solid particles has the following fluidisation

properties: Easy and smooth fluidisation, low fluidisation velocities and a considerable expansion in the particles bed after the fluidisation starts and prior to the initiation of a bubbling phase. Most of the solid powders in the catalytic fluidised bed reactors are classified in this group.

Group B: In this group, Particles have sizes ranging between 40 and 500 µm and a particle density between 1400 kg/m^3 and 4000 kg/m^3. Sand is one of the typical powders in this group. Bubbles start to form in the bed directly at incipient fluidisation and it has a small bed expansion and it collapses rapidly when stop supplying the gas.

Group C: Particles in this group are very fine (20 – 40 µm) in size and extremely cohesive. Fluidisation of these particles is very difficult due to the cohesion forces between particle – particle and particle – wall.

Group D: Significantly, large particles sizes above 600 µm and typically, high particle density. High fluid energies are required for the fluidisation of these particles group. Mostly, they are used in drying processes such as corn grains, pea and coffee beans.

2.6. The Design of BFBG

The design of the BFBG is standing on three main factors (Patil and Shinde, 2017):

1- Hydrodynamics. This represents the relationship between solid particles and gas mixture inside the reactor forming the bubbling fluidised bed regime. The study of this case includes many aspects such as the influence of superficial velocity, pressure drop, bubble size, particle size and bed height on each other and on the other design factors.

2- Heat and mass transfer. The heat transfer between gas and particles, particles and particles, gas – particles and walls and the mass transfer due to solid particles reaction

with the gas are covered in this factor (Papadikis et al., 2009, Armstrong et al., 2010, Fattahi et al., 2016, Parmar and Hayhurst, 2002).

3- Chemical reactions. The reactions between solid particles (biomass) and gas in the BFBG is the third important factor in the BFBG design. The study of these reactions kinetics is the key to estimate the solid particles (biomass) heat of pyrolysis, the product gases quantities and the formation amount of ash and tar (Al-Farraji, 2017, Shao et al., 2018, Narváez et al., 1996).

However, these three factors affect each other, especially the bed hydrodynamics which has a major impact on heat and mass transfer and the chemical reactions (Andersson and Karlsson, 2014, Gidaspow, 1986, Radmanesh et al., 2006, Philippsen et al., 2015).

2.7. Hydrodynamics in BFBG

The bed hydrodynamics and its effects on heat transfer and reactions kinetics inside the BFBG, has widely been studied in different experimental, analytical and numerical works. Many research papers have been done to describe the relationship between the hydrodynamic parameters and the other design factors of the BFBG such as the heat and mass transfer and the chemical processes.

2.7.1. Solid Particle Size in BFBG

According to Geldart grouping of particle sizes (Geldart, 1973), the particle size in fluidised bed reactors has a significant impact on the other hydrodynamic parameters and the other design factors. The minimum fluidisation velocity, U_{mf} in the BFBG has a direct relationship with the particle size. When the particle size increases, the minimum fluidisation velocity increases too (Wu et al., 2008, Sun and Grace, 1990, Shen and Zhang, 1998, Sun and Grace, 1992).

Moreover, the bubble size is also affected by particle size (Wu et al., 2008). Bubbles in small particles BFB are small and still have a uniform shape throughout the bed with relatively low bubble velocity. However, the bubbles in medium and large particles BFB are large and changed through the bed height and have high bubble velocity.

The heat transfer and reaction rate are also affected by particle size. Many experimental and numerical studies found that the heat transfer coefficient decreases with the increase of particle size (Salwe et al., 2014, Ngoh and Lim, 2016). Regarding the chemical reaction (gasification), the fluidised bed gasifier with biomass of small particles size produces syngas with better quality and yield than the large particles size (Lv et al., 2004).

2.7.2. Gas Velocity (Superficial Velocity) in BFBG

The relationship between superficial gas velocity, u_s and the bed pressure drop, Δp is presented in figure 2.5. The bed pressure drop increases linearly with the increase of superficial velocity in the fixed bed zone (before fluidisation) , i.e. $u_s < u_{mf}$ However, the pressure drop tends to be relatively constant after the fluidisation grows, i.e. $u_s > u_{mf}$ (Kunii and Levenspiel, 1991).

On the other hand, Salwe studied experimentally the relationship between the bed heat transfer coefficient and the gas (air) velocity. They found that the heat transfer coefficient increases when the air velocity increases (Salwe et al., 2014). The reaction rate is also affected by the gas superficial velocity, the reaction rate increases linearly with gas velocity until the superficial velocity reaches eight times the minimum fluidisation velocity and then the reaction rate does not change (Zhang et al., 2015).

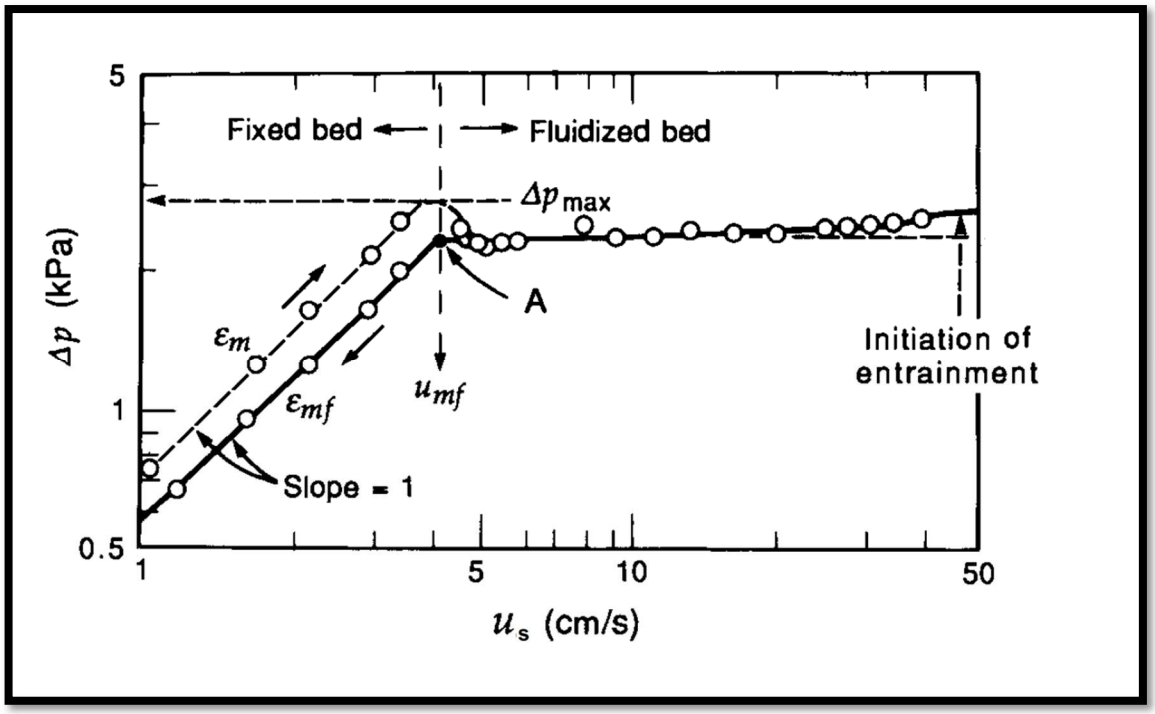

Figure 2.5. The relationship between superficial gas velocity and pressure drop in a BFB reactor(Kunii and Levenspiel, 1991).

2.7.3. Pressure Drop in the BFBG

The pressure drop inside the fluidised bed is another important hydrodynamic character. This pressure drop is mainly caused by bed solid particles (Wang et al., 2007). Hence, the pressure drop is high in the dense particle's zones and low in the dilute zones. However, pressure drop decreases with bed height as shown in figure 2.6 due to the decrease in particles column height (Halvorsen and Arvoh, 2009).

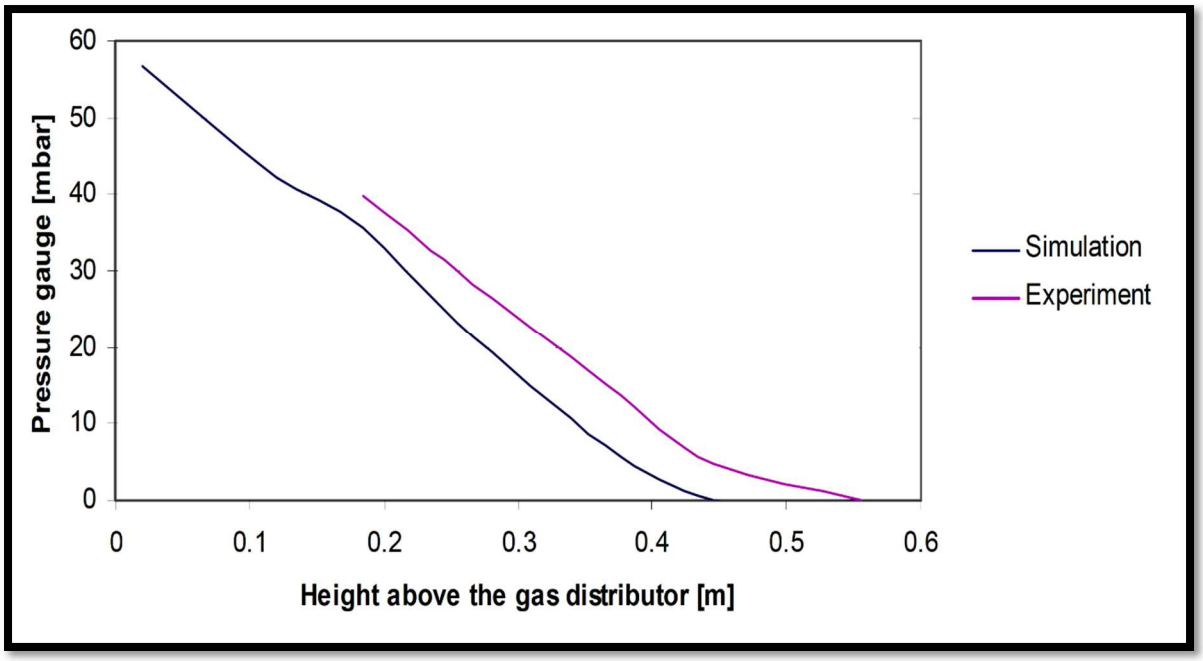

Figure 2.6. Pressure drop variation along fluidised bed height in BFB reactor (Halvorsen and Arvoh, 2009).

2.7.4. Bed Porosity (Voidage)

The porosity (voidage) in a fluidised bed is the gas voids between the solid particles and it is also called void fraction or gas holdup which represents the ratio of void volume to the total bed volume (Franka et al., 2008). This parameter is low at the packed bed and it starts to increase at incipient fluidisation when the bed stars expansion, the voidage at which point is called the minimum fluidisation voidage, ε_{mf}.

Many experimental, analytical and numerical research papers were published to study the behaviour of bed voidage and its effect on the other parameters (Khan et al., 2016, Jayarathna et al., 2014, Foscolo et al., 1983, Chen et al., 2005, Behjat et al., 2008). Figure 2.7 shows different time snapshots for the transient bed voidage in a bubbling fluidised bed reactor with 550 µm sand particles (Chen et al., 2005).

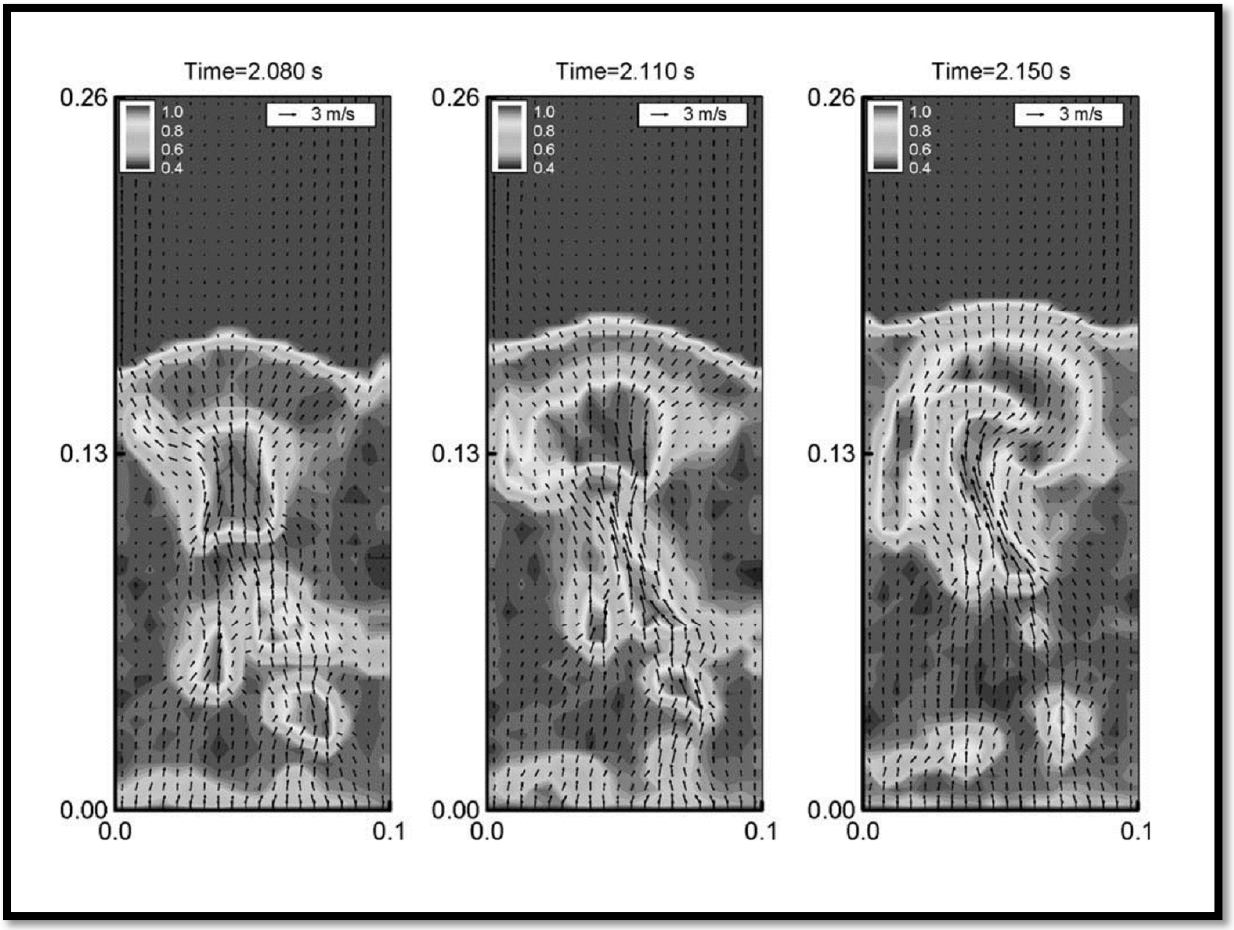

Figure 2.7. Bed voidage in a BFB reactor (Chen et al., 2005).

2.7.5. Gas Bubbles in BFBG

The generation of bubbles is one of the most important parameters in the bubbling fluidised bed gasifier which takes its name from. Bubbles have an essential role in particles movements which enhance the heat and mass transfer between solid particles and gas. Figure 2.8 shows the relationship between the number of formed bubbles per second and the local heat transfer coefficient where the angular positions represent the positions of the thermocouples (Kim et al., 2003).

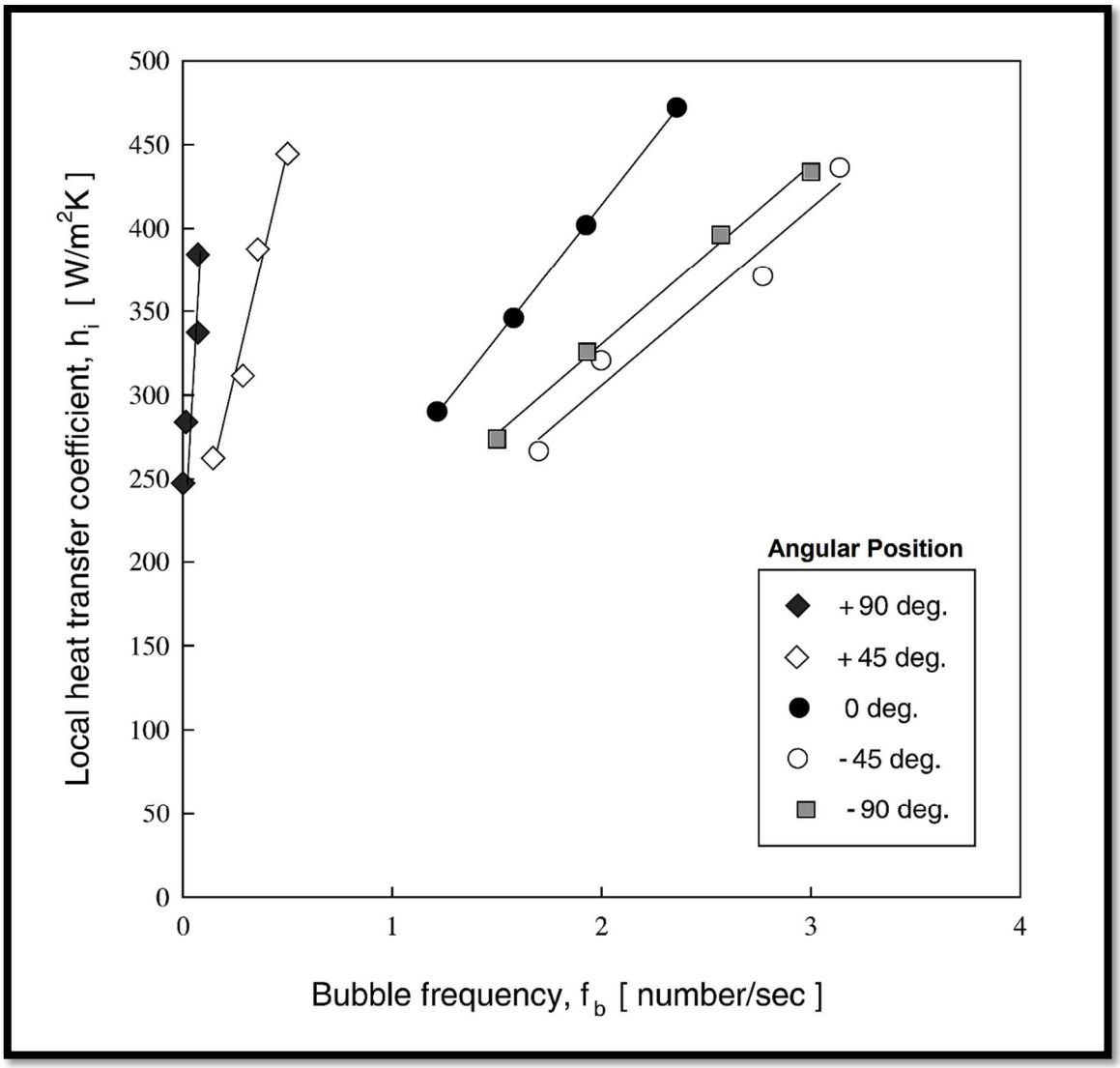

Figure 2.8. The variation of the local heat transfer coefficient with bubble frequency inside the BFB (Kim et al., 2003).

The reaction rate in the BFB reactors improves with the generation of bubbles and reduces in the dense bed. This is due to the expansion in the bed caused by bubbles movement which provides better contact between the gas and solid particles (Maurer et al., 2016). However, bubble size has a significant effect on the conservation and selectivity in the BFB gasification. For example, a BFB with bubbles size of 32 cm has a 32% chemical conversion. While the conversion reaches 84% when the bubbles size reduces to 8 cm as shown in figure 2.9 (Levenspiel, 2002).

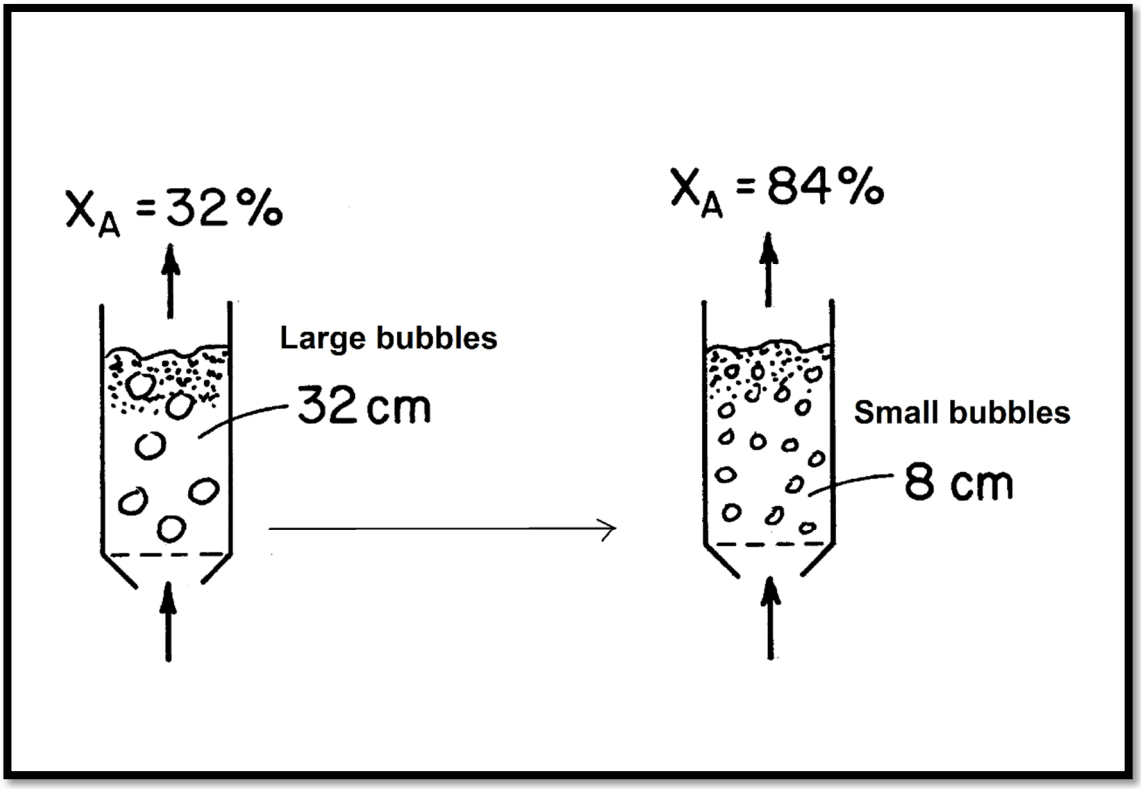

Figure 2.9. Effect of bubbles size on bed chemical conversion in the BFB reactor (Levenspiel, 2002).

Moreover, the syngas selectivity also increases when the bubbles size decreases (Kaart, 2002). Many methods were used to reduce the bubble size in the BFB reactors, such as applying mechanical vibration to the bed (Kwauk, 1992), applying magnetic fields to the bed (Rosensweig, 1995, Hristov, 2002, Hristov, 2010), injecting pulsed or fractal feeds (Coppens, 2001) and using electrical fields (van Willigen et al., 2003).

The mechanism of bubbles formation and movement in a bubbling fluidised bed reactor and their effect on the solid particles movement throughout the bed has been visualised analytically by (Kunii and Levenspiel, 1968) bubbling bed model.

Figure 2.10 shows the bubbles generation and movement and corresponding solid particles movement inside a bubbling fluidised bed reactor according to the bubbling bed model (Kunii and Levenspiel, 1968). When the bubble rises the size of the bubble increases due to the gas expanding inside the bubble as the bed weight force decreases.

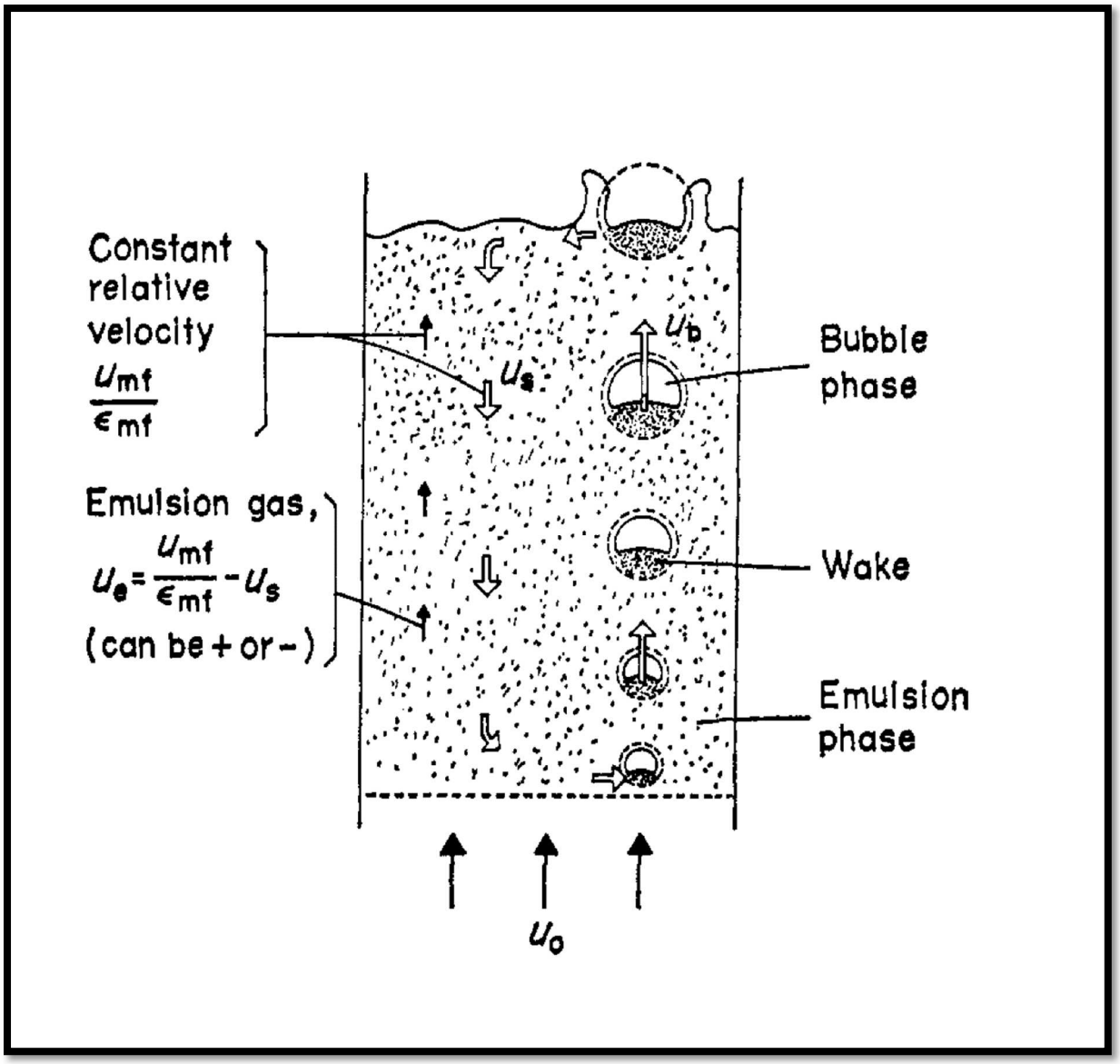

Figure 2.10. Gas-solid movement in the BFB according to the bubbling bed model (Kunii and Levenspiel, 1968).

However, particles size also has a significant impact on bubbles size and velocity. The bubbles in the fine solid particles are large and have a high velocity and surrounded by a thin cloud of circulating gas. This gas cloud separates the bubble from the other free gas in the bed and the raising of bubbles in the fine particles bed is like vortex rings (Levenspiel, 2002). While the bubbles in the coarse solid particles bed are smaller and have low velocity and the free gas can flow through the bubbles. Figure 2.11 shows bubbles specifications in fine and coarse solid particles beds (Levenspiel, 2004).

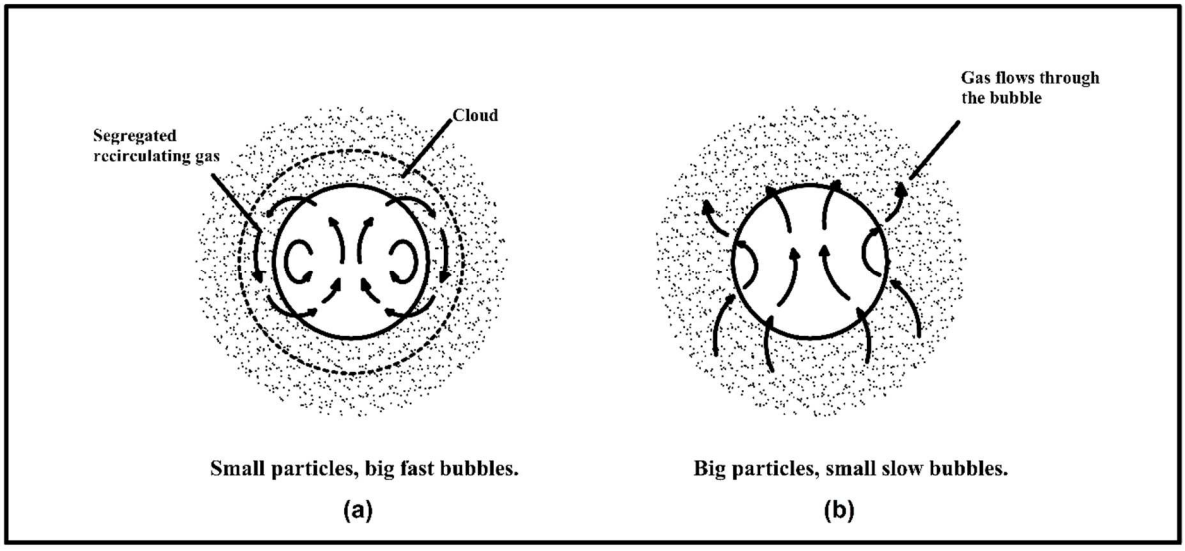

Figure 2.11. Bubbles specifications in (a) fine particles bed. (b) Coarse particles bed (Levenspiel, 2004).

2.7.6. CFD Simulation of the BFBG

The development in computer performance in both computational speed and data storage accompanied with the development of CFD in different engineering branch. The hydrodynamic behaviour of the BFBG has been studied by different CFD models. A 3D Eulerian two-phase model for the BFB system in cold conditions was studied somewhere else (Li and Ma, 2011). The study showed that the fluid velocity in the triangular arrangement distributor was more stable than the square distributor.

Another simulation for the BFBG with the multiphase Eulerian model in the commercial software ANSYS FLUENT for two different type of solid bed was studied somewhere else (Thapa and Halvorsen, 2013). There simulation results were deviated 18% from the experimental measurements at the minimum fluidisation conditions.

2.8. Improvement of Gasification Product Gases

The product gases from the gasification processes have different components. This mainly depends on the feedstock (biomass) type and the gasification conditions. Hence, there is a need to enhance these product gases (increase the most useful ones and decrease the less useful) to use it in the later applications.

In energy fields, methane gas (CH_4) is considered as the most common component in the natural gas and in the gasification product gases. However, methane gas is considered as one of the greenhouse gases which affect the environment. There are many methods introduced to crack methane into hydrogen (H_2), the most environmentally friendly power gas and the feedstock of the well-known power units (Fuel Cells).

Wet reforming (with steam), dry reforming (with carbon dioxide) and combined reforming (with both steam and carbon dioxide) of methane are the most effective cracking methods as stated by many researchers.

2.8.1. Steam Reforming of Methane (SRM)

Steam reforming (SRM) is a method of producing hydrogen (H_2) and other useful gases such as carbon monoxide (CO) from hydrocarbon fuels such as Methane. H_2 is produced by using steam (H_2O) as reacting material with the hydrocarbon. This process occurs in a device called reformer in a temperature ranging between (675 – 1000 K) in the presence of a metallic catalyst (Xu and Froment, 1989).

The main reaction for steam reforming is:

$$C_nH_m + nH_2O \leftrightarrow nCO + \left(n + {}^{m}/_{2}\right)H_2 \quad \text{2-3}$$

And for methane (SRM):

$CH_4 + H_2O \leftrightarrow CO + 3H_2$ …… 2-4

This reaction happens simultaneously with other reaction called water – gas shift (WGS):

$CO + H_2O \leftrightarrow H_2 + CO_2$ …… 2-5

The SRM reaction (equation 2-4) is a strongly endothermic reaction with a heat of reaction (ΔH=+ 206 KJ/mole) and the WQS reaction (equation 2-5) is an exothermic reaction with a heat of reaction (ΔH=-41.7 KJ/mole) (Pal and Prasad, 2014). In figure 2.12 the main parts of the ordinary heating steam – methane reformer is illustrated.

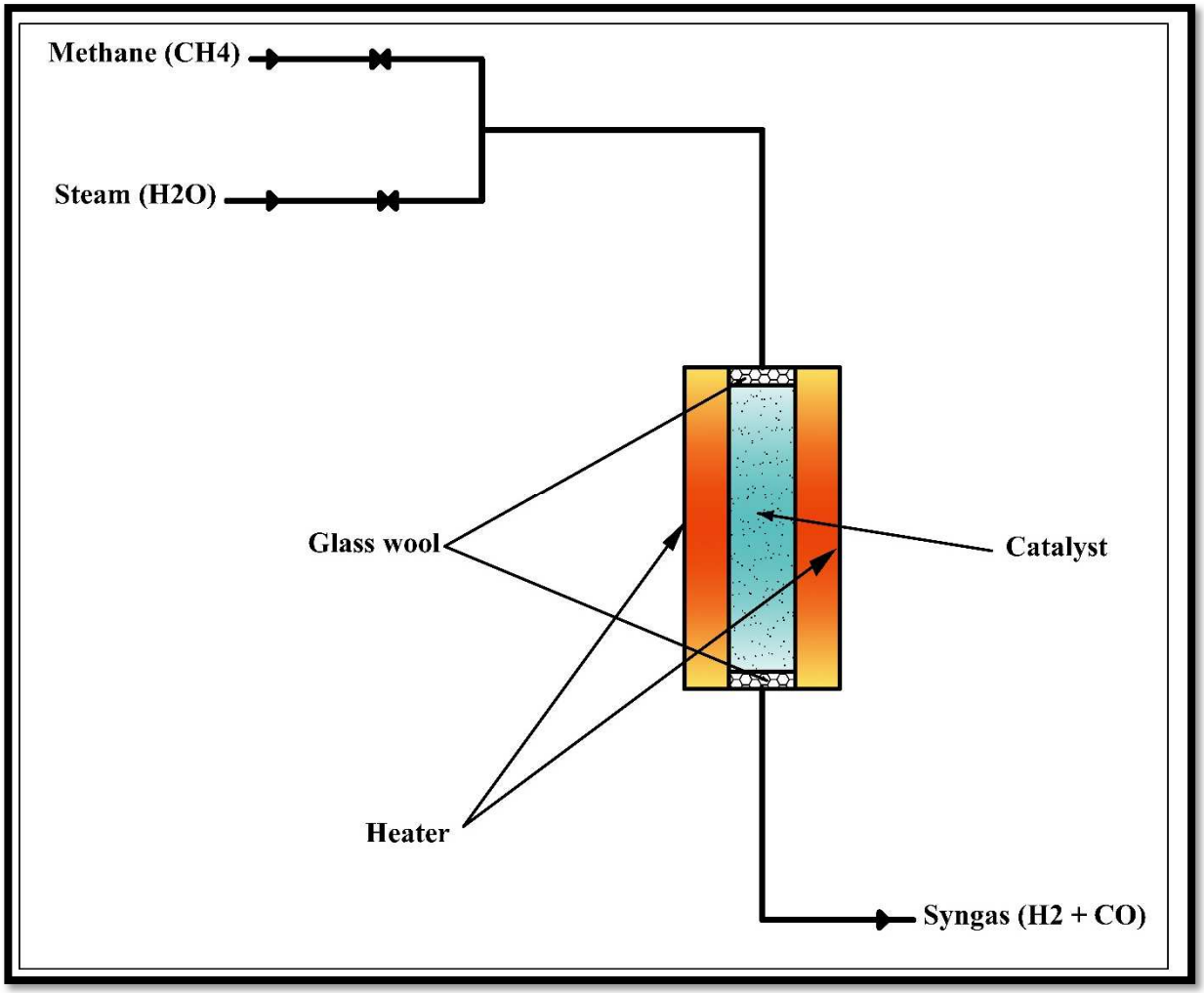

Figure 2.12. Steam – Methane Reformer scheme (Matthey, 2018).

2.8.2. Other Reforming Methods

There are many other reforming methods. Dry reforming of methane (DRM) uses CO_2 to crack the methane in presence of a catalytic material to synthesis gases (CO and H_2). Dry reforming has been considered as a very convenient way for the conversion of greenhouse gases into synthesis gas (Zhang et al., 2001, Zhang et al., 2008, Benguerba et al., 2015). This is due to the conversion of the most popular greenhouse gases, i.e. CO_2 and CH_4 to very useful gases H_2 and CO.

Moreover, DRM produces syngas with low H_2/CO which is suitable for many industrial applications such as the production of liquid hydrocarbons (Fischer–Tropsch synthesis), formaldehyde and polycarbonates (Bradford and Vannice, 1998).

Mixed reforming (MRM) is another ideal method used to control the H_2/CO ratio in the product gases without incorporation of additional process units (Park et al., 2014). In MRM, dry reforming is simultaneously carried out with steam reforming. Carbon dioxide and steam are injected together with the methane at the same time.

This process will reduce the deposition rate of carbon on the catalyst compared to the deposition rate of carbon in the dry reforming (Choudhary and Rajput, 1996)**.**

2.8.3. Catalysts of the Reforming System

The substance that causes or accelerates a chemical reaction without itself undergoing any permanent chemical change is called catalyst material. From an operational standpoint, there are three main factors according to which the catalysts are classified (Abatzoglou and Fauteux-Lefebvre, 2016):

1- The hydrogen and carbon monoxide yields.

2- The conservation rate of the reactant.

3- Catalyst activity duration.

The relationship between catalyst types and the production of H_2 and CO has a crucial interest for many researchers. (Wang et al., 2012) studied the effect of different bimetallic catalysts on hydrogen yield. Wang finds out that the supported Pt and Pt-Co bimetallic catalysts on single-walled carbon nanotubes (SWNTs) have better hydrogen yield and activity than Pt−alumina catalyst. Figure 2.13 shows Wang's results for hydrogen yield.

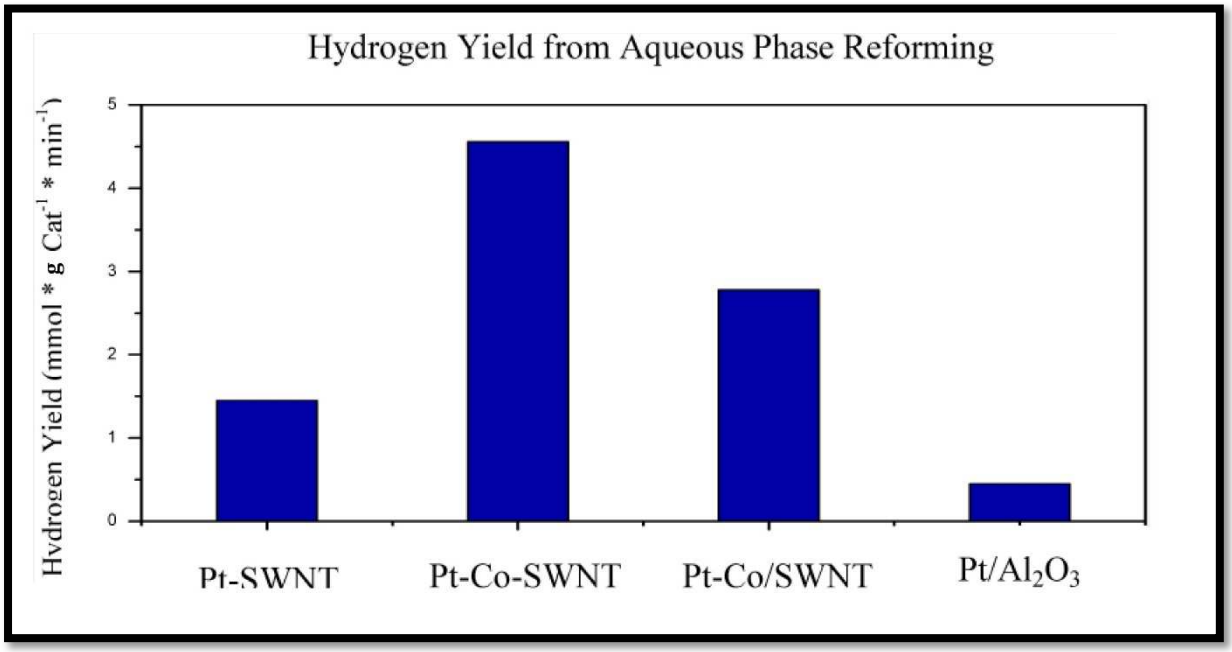

Figure 2.13. The hydrogen production activity for different catalysts (Wang et al., 2012).

Nickel bimetallic catalysts have a good impact on carbon monoxide yield and activation of molecules (Diskin et al., 1998, Ermakova et al., 2000, Benguerba et al., 2015). Regarding the hydrogen yield, the Ni catalysts show a remarkably high conversion rate to H_2 (Hao et al., 2009, Wang et al., 2016). Figure 2.14 illustrates the effect of nickel loadings in aerogel catalysts on the conversion rate of methane and carbon dioxide along with the selectivity rate of hydrogen and carbon monoxide in fluidised bed dry reforming at a reaction conditions of: Temperature = 800 ^{0}C, Pressure = 1 bar, gases flowrate = 300 ml/min at gases molar ratio (CH_4:CO_2:N_2) = (1:1:1) respectively, and the catalyst loading amount = 0.2 gram (Hao et al., 2009).

In figure 2.14 the selectivity rate of hydrogen and carbon monoxide were calculated by the equations (Hao et al., 2009):

$$H_2 \text{ - Selectivity} = \frac{\text{Produced } H_2 \text{ (moles)}}{2(CH_{4,in}(\text{moles}) - CH_{4,out}(\text{moles}))} \times 100\% \quad \text{.....2-6}$$

$$\text{CO- Selectivity} = \frac{\text{Produced CO (moles)}}{\left((CH_{4,in}(\text{moles}) + CO_{2,in}(\text{moles})) - (CH_{4,out}(\text{moles}) + CO_{2,out}(\text{moles}))\right)} \times 100\% \quad \text{..... 2-7}$$

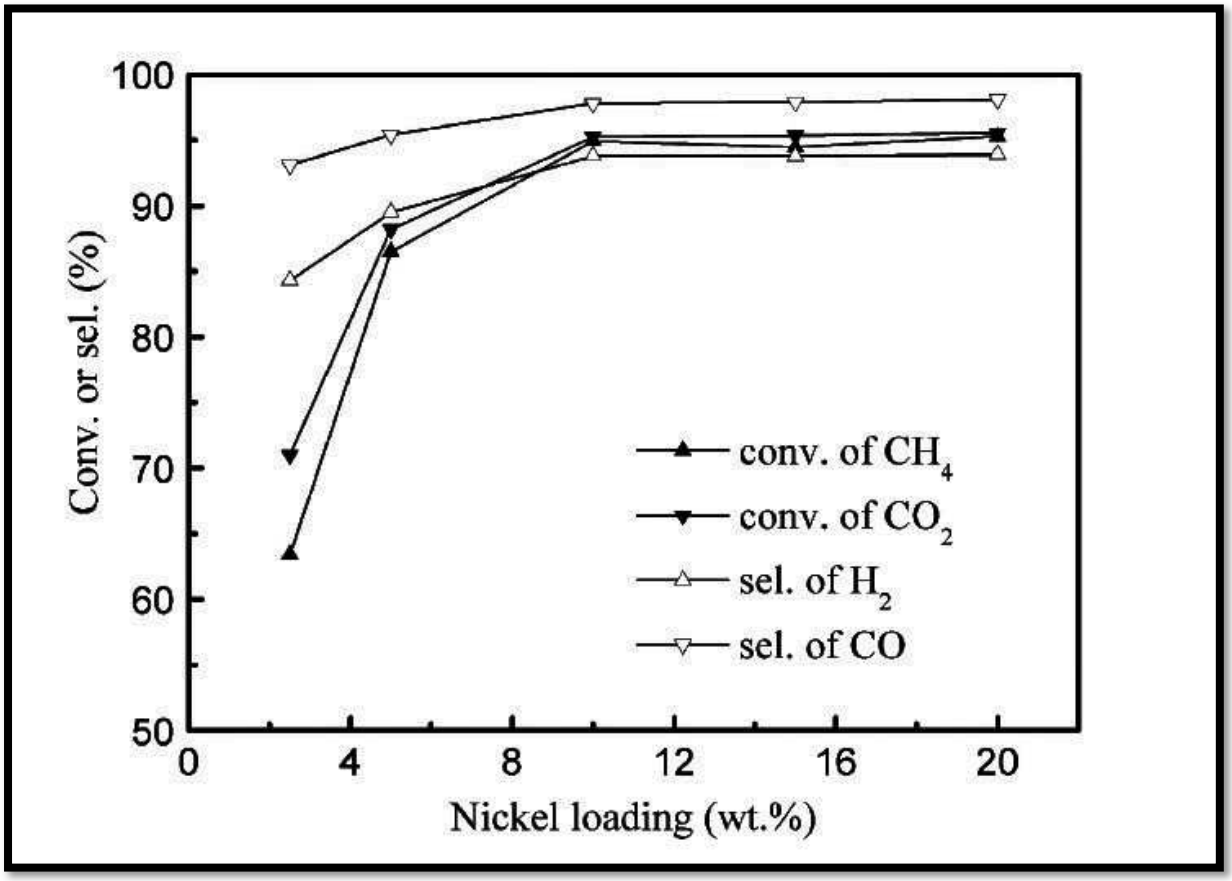

Figure 2.14. The influence of nickel loadings in the aerogel catalysts on the conversion of (CH_4 and CO_2) and the selectivity of (H_2 and CO) (Hao et al., 2009).

In the SRM, catalyst type has a significant effect on conversion and selectivity in different reforming temperatures. For low reaction temperatures (500 – 600) ^oC, the nickel-based catalyst ($Ni/Ce_{0.15}Zr_{0.85}O_2$) has the highest activity among the other nickel-based catalysts ($Ni/Ce_{0.25}Zr_{0.75}O_2$, $Ni/Ce_{0.5}Zr_{0.5}O_2$, Ni/ZrO_2 and $Ni/\gamma\text{-}Al_2O_3$) as shown in figure 2.15 (Kusakabe et al., 2004). However, the ($Ce_{1-x}Zr_xO_2$) catalyst with (Ce:Zr ratio) higher than 0.5 showed a

very high activity in carbon monoxide oxidation (Thammachart et al., 2001), methane partial oxidation and methane dry reforming with CO_2 (Mattos et al., 2003).

Most catalytic blends composed of two materials: the first one is the active catalyst which is usually metal such as (Ni, Pt, Ir, Rh and Ru) and it forms a little portion in the blend with a low surface area. The second component is the catalyst support, which is a high surface area material in which active catalyst is affixed (McNaught and Wilkinson, 1997). The catalyst

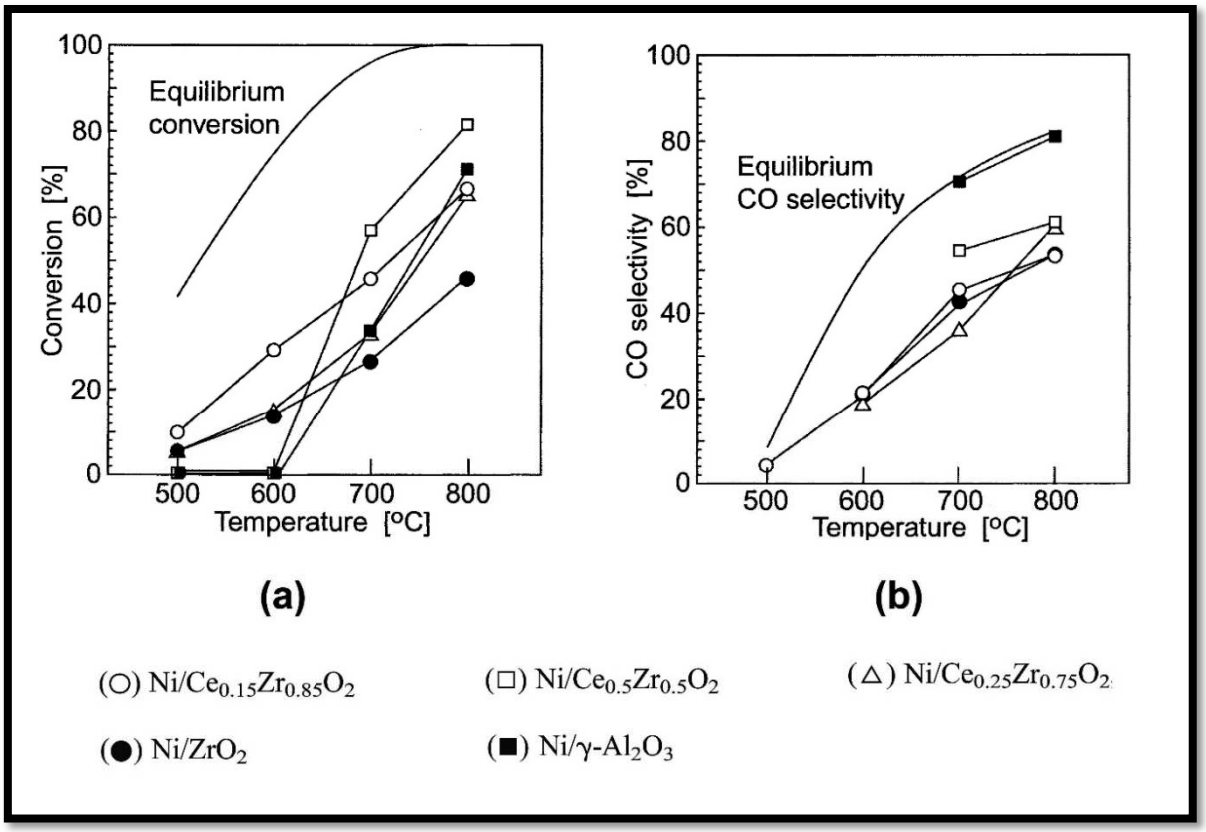

Figure 2.15. Effect of nickel-based catalysts in SRM on different reaction temperatures and (a) methane conversion. (b) CO selectivity (Kusakabe et al., 2004).

support can be an inert or reactive material which typically can include different kinds of alumina, silica and carbon (Ma and Zaera, 2014). Figure 2.16 shows the microscopic stages of a typical chemical reaction in the presence of a catalyst blend (Rothenberg, 2017). However, the effect of catalysts support materials have widely been studied through literature

(Gadalla and Bower, 1988, Ferreira-Aparicio et al., 1998, Aksoylu et al., 2001, Wang et al., 2009, Karim et al., 2017).

On the other hand, there is a physical factor which has a great impact on the catalyst reaction activity, this factor is the surface area of the catalyst. The increase in catalyst surface area provides more contacts between the reactants and the catalyst which as a result increasing the reaction rate. The fine catalyst particles the higher surface area the higher reaction rate and larger particle size the smaller surface area the lower reaction rate (Sivagami et al., 2016, Deutschmann et al., 2011).

Many researchers have studied the effect and behaviour of surface area for different catalysts and under different conditions (Burtin et al., 1987, Karpenko et al., 2007, Gregor et al., 2010, Leofanti et al., 1998, Machida et al., 1987, Aigner et al., 2017).

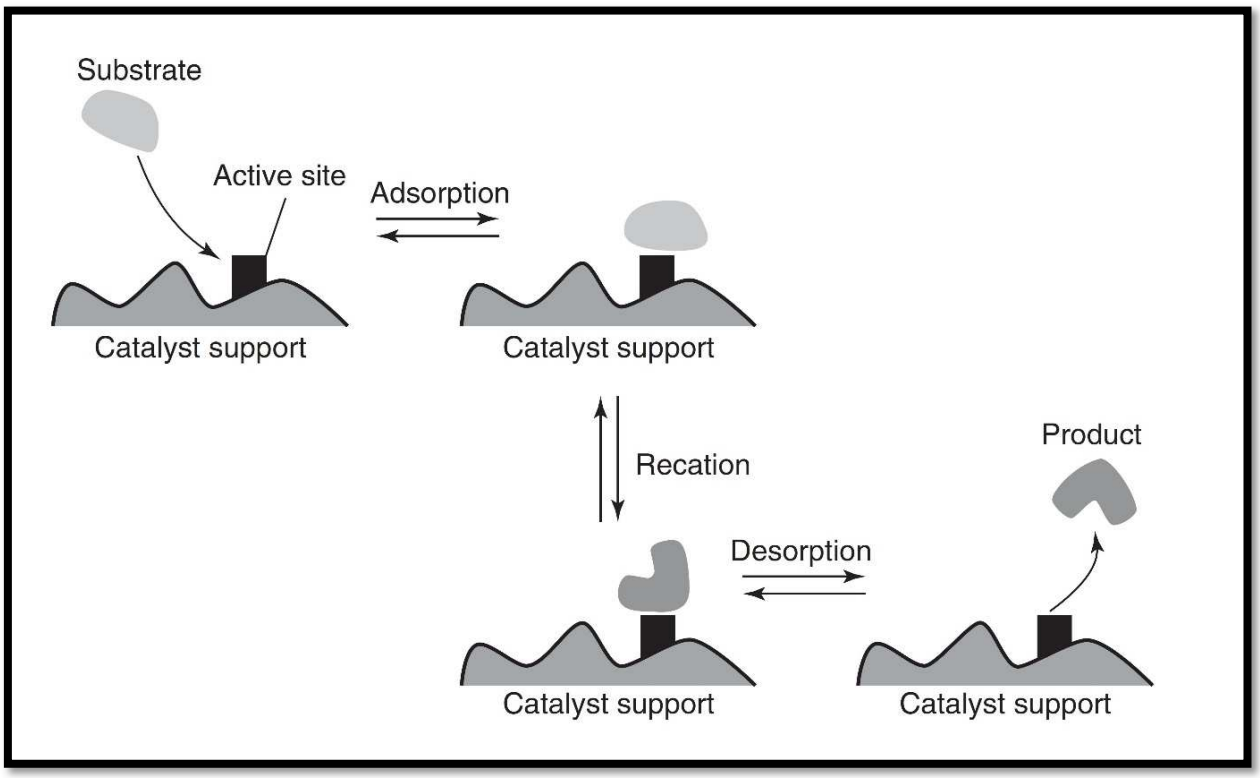

Figure 2.16. The mechanism of chemical reactions in the presence of a catalyst blend (Rothenberg, 2017).

However, the activity of different catalysts types will deteriorate after each reaction period. The deactivation of catalysts has three forms (Fogler, 2006):

1- Sintering (Aging)

This type of deactivation happens due to the prolonged exposure of the catalyst to high-temperature gases. This exposure leads to gradual loss of the catalyst active surface area by either narrowing or closing the pores inside the catalyst or by crystal agglomeration as the deposited metals grow on the catalyst support. Figure 2.17 shows two forms of sintering (ageing) catalysts deactivation.

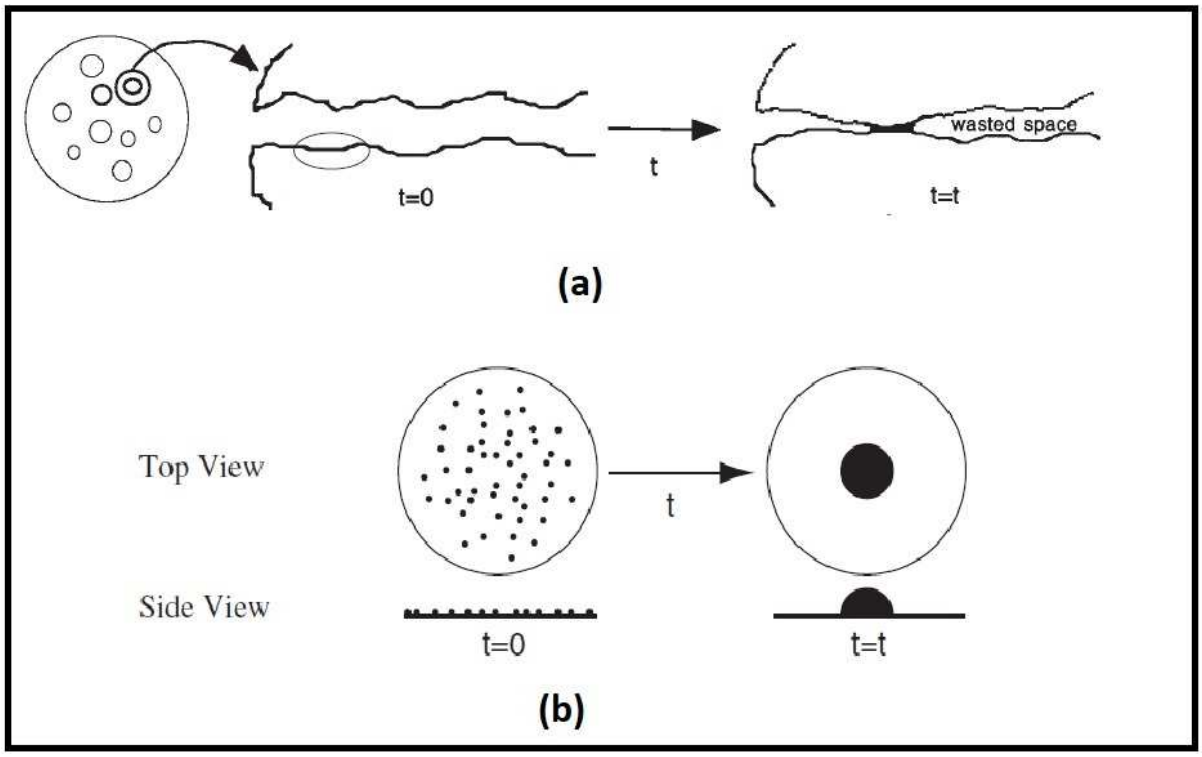

Figure 2.17. Catalyst deactivation by sintering: (a) Pore closure. (b) Agglomeration of deposited metal along the catalyst surface (Fogler, 2006).

2- Fouling (Coking)

This type of catalyst deactivation is very common with the reactions containing hydrocarbons. The main cause of this decay is the deposition of the carbonaceous

material (coke) on the catalyst surface and pores. Figure 2.18 illustrates the catalyst deactivation case related to coke deposition on the catalyst surface.

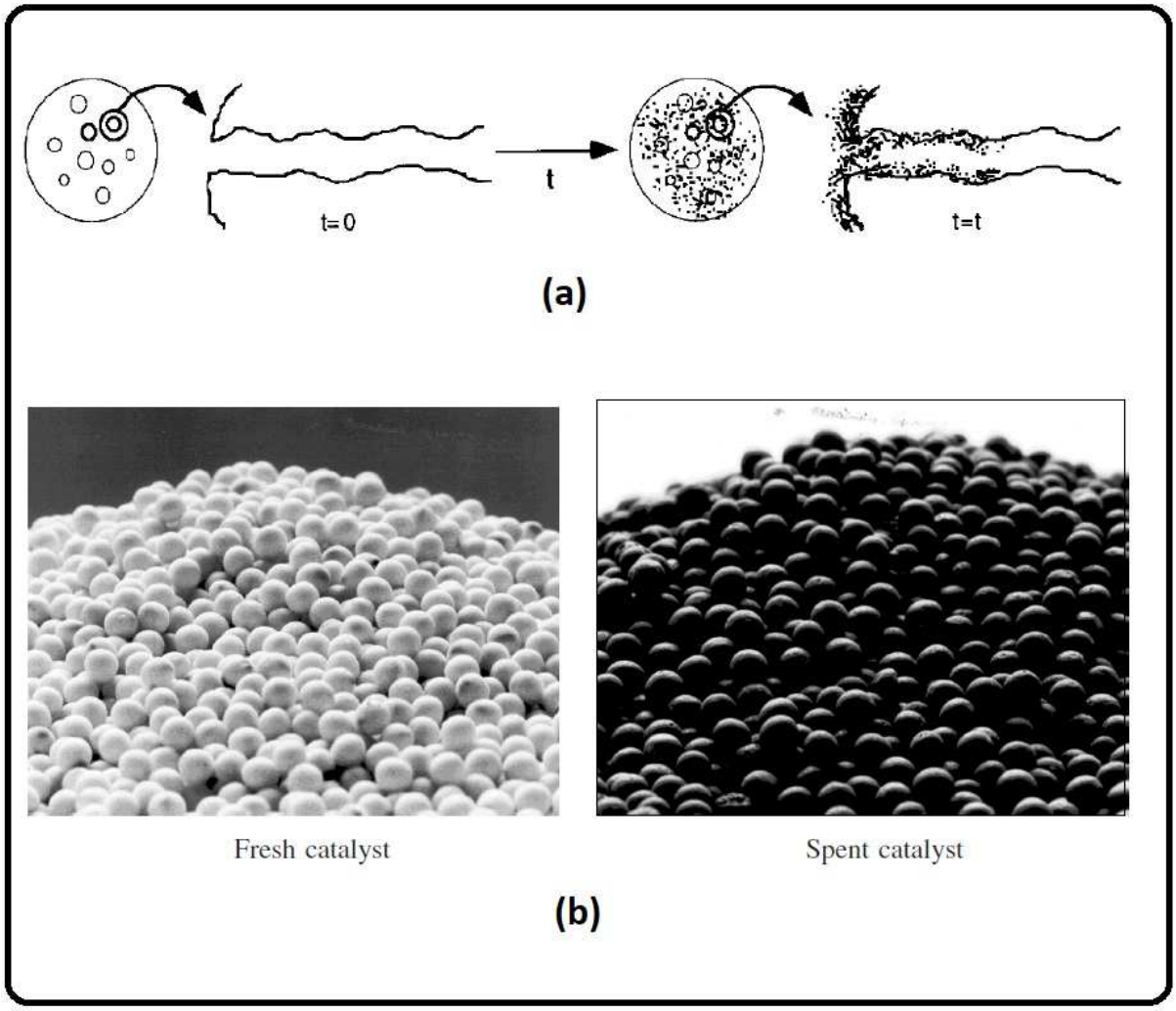

Figure 2.18. Fouling (coking) deactivation of catalysts: (a) Coke accumulation on surface and pore. (b) Before and after catalyst coking decay (Fogler, 2006).

3- Poisoning

Catalyst poisoning occurs when the catalyst is exposed to a certain chemical compound which can cause partial or total deactivation. However, the poisoning processes can be useful in some cases such as the improvement of selectivity by stimulating the reduction of alkynes (Lindlar and Dubuis, 1966). In contrast, the bad effect of poisoning has a good example of the deactivation of catalytic converters in cars due to the lead used in the leaded gasoline.

The mechanism of poisoning involves a chemical bond between the poisoning molecules (P) and the active surface of the catalyst. Hence, the number of the active catalytic sites will decrease, and the more active surface area is reduced and as a result, the reaction acceleration declines significantly (Hagen, 2015). Figure 2.19 shows the poisoning deactivation mechanism.

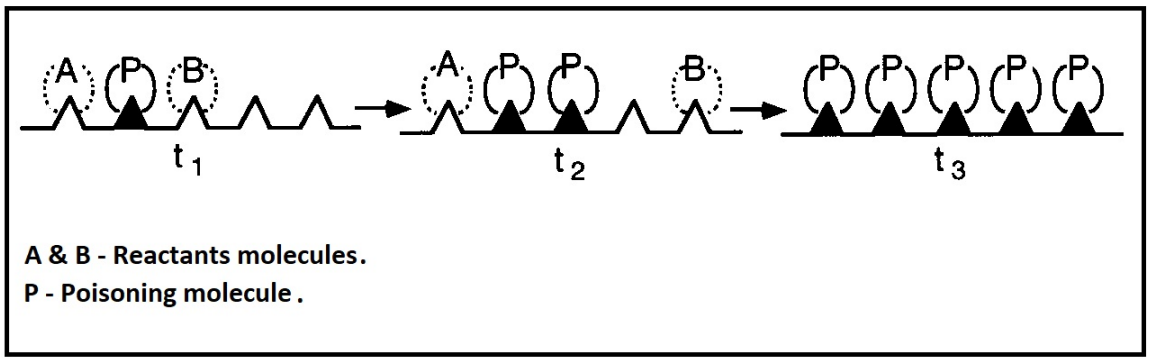

Figure 2.19. The poisoning decay mechanism (Fogler, 2006).

2.8.4. Microwave Heating System

In 1945, Percy Spencer accidentally invented the heating effect of microwaves while he was working on building magnetrons for radar settings. The heating effect melted the peanut butter candy bar in his pocket while he was standing in front of the activated magnetron of the radar set. Nowadays, microwaves heating has vast applications in different fields such as food processing, medical applications and engineering.

Microwaves are electromagnetic energy waves with a frequency range from 300 MHz to 300 GHz as shown in figure 2.20. This energy has a nonionized radiation that boosts ions migration and dipoles rotation resulting in molecular motion. However, this action does not affect the molecular structure of the material (Kingston and Jassie, 1988).

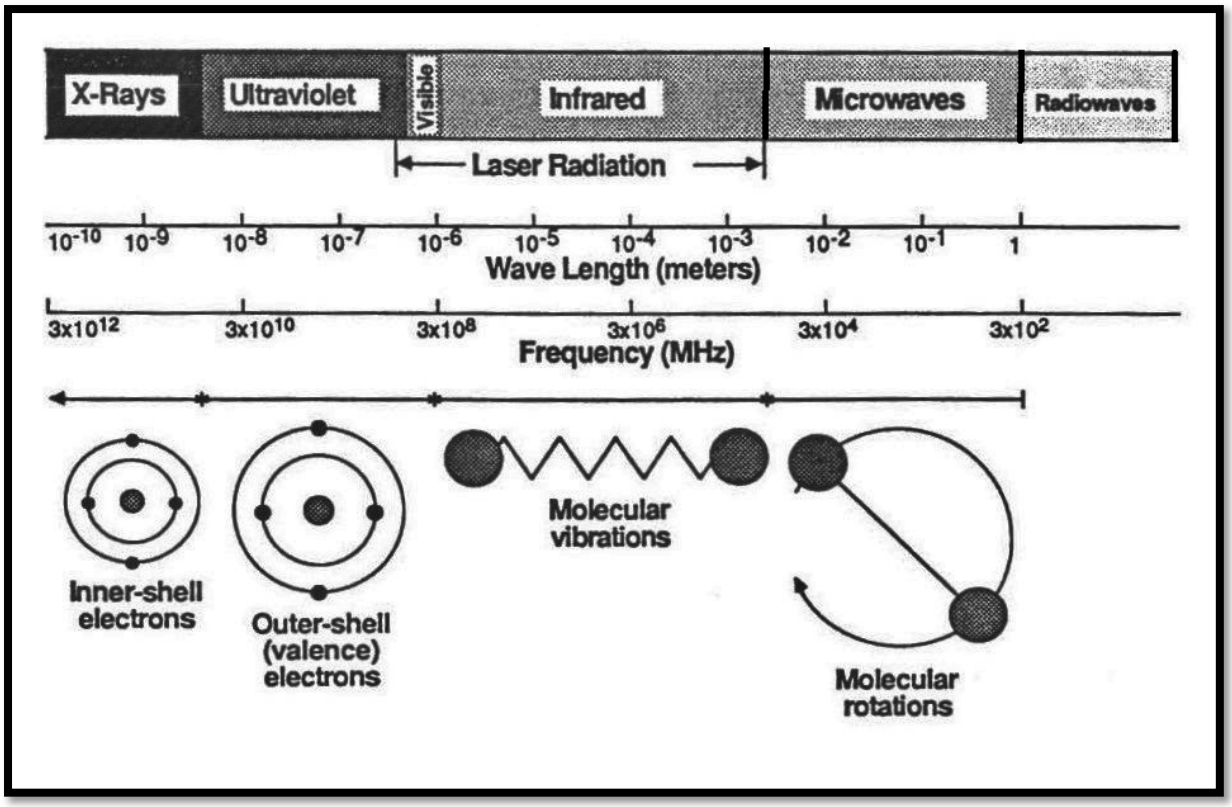

Figure 2.20. The spectrum of electromagnetic waves (Kingston and Jassie, 1988).

2.8.4.1. Conventional and Microwave Heating

These days, one barely can find a house without a microwave oven due to the simplicity and time saver in making and reheating food compared with conventional ways of cooking and heating. This fact can be clearly seen in industrial food applications, for example, green beans blanching in microwaves consumes half processing time than the conventional industrial method (Ruiz-Ojeda and Peñas, 2013).

This distinction between the two heating methods can be related to the difference in heating patterns of the two methods. The conventional heating, for instance, depends mainly on conduction and convection heat transfer modes. This transports the heat slowly through the substance especially when the substance and container have low or medium thermal conductivity. Figure 2.21.a illustrates the conventional heating patterns of liquid substances.

However, microwaves heating has a different mechanism, the heating effect starts from the substance itself at the points where microwaves pass through. Then, the heat will spread out from this heated points to other points (the points where microwaves did not pass through) in the substance, see figure 2 .21. b. In this case, the container will not be heated, and the heating process will consume less time and energy.

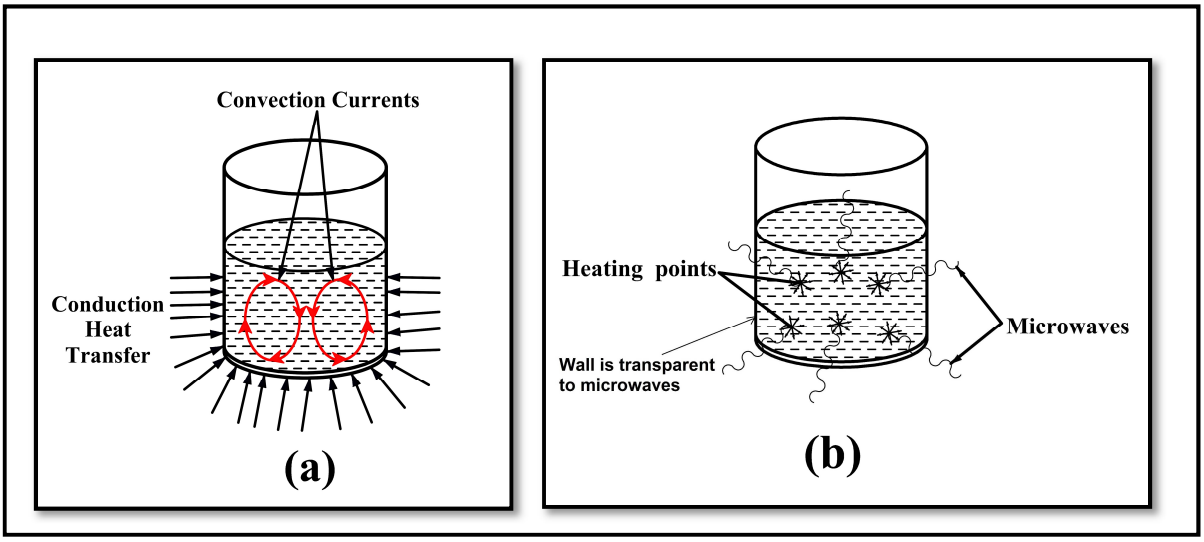

Figure 2.21. The heating mechanism in (a) Conventional mode and (b) Microwaves mode (Collins Jr, 2010).

Thermal comparison between microwave heating and oil – bath conventional heating is illustrated in figure 2.22 (Gude et al., 2013).

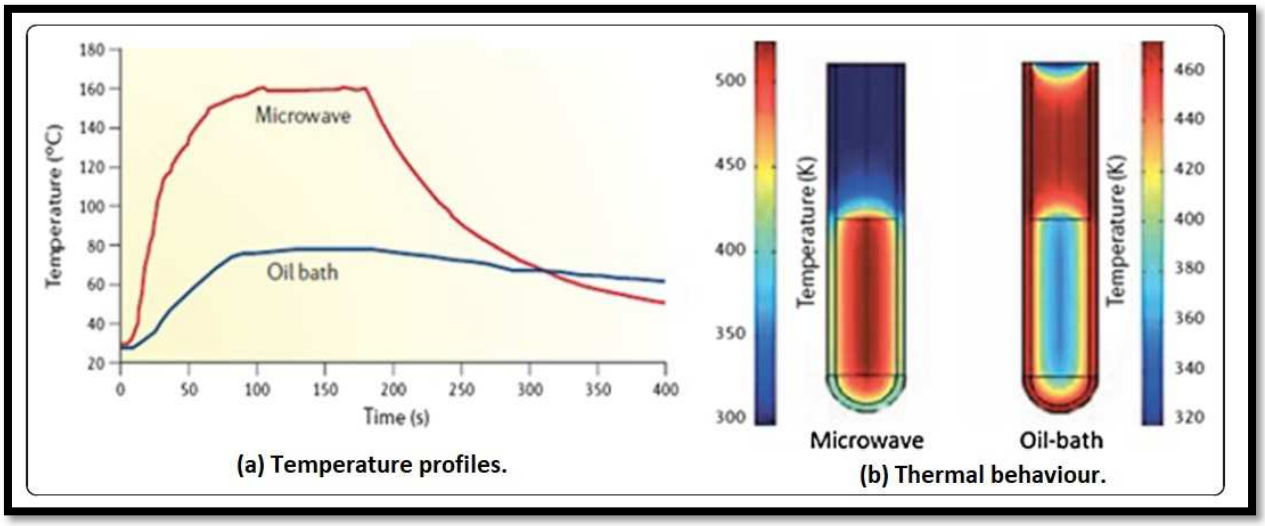

Figure 2.22. Comparison between microwave and conventional heating (Gude et al., 2013).

2.8.4.2. Microwave in Gasification and Methane Reforming

Specifications of microwave heating and its low consequences stimulates many researchers to use microwave heating in gasification processes and methane reforming instead of conventional heating methods. Gasification of four types of coal with O_2 and steam in microwave plasmas have shown an increase in H_2 production (Yoon and Lee, 2012).

In the same context, gasification of biomass waste in a microwave - driven plasma may produce syngas with heating values up to 84% more than the microwave energy used in the process (Sturm et al., 2016). Microwave heating has been proven as an effective method in biomass gasification in the presence of (Ni/Al_2O_3) as well as having good effects on the removal of tar compounds from the produced syngas (Xie et al., 2014).

Much more details about using microwave energy in gasification processes can be found in the literature (Kabalan et al., 2011, Beneroso et al., 2014, Ismail and Ani, 2014, Bermúdez et al., 2014, Ho et al., 2017, Liu et al., 2018, Sanlisoy and Carpinlioglu, 2018).

The presence of tar in the product gases of biomass gasification is a serious problem. Tar can cause a coke formation, fouls, downstream units and deactivate catalysts. Hence, tar cracking is an important process to decrease tar's hazards in the system. Using microwave plasma technology for tar decomposition has proven as an efficient method with more than 95% cracking efficiency (Wnukowski, 2014).

Regarding methane and CO_2 reforming in microwave environments, it seems that the process produces high H_2 yield especially for high reforming temperatures and long retention time (Lim and Chun, 2017). More promising results have been recorded in using the microwaves for steam reforming, higher methane conversion than the conventional way of methane steam reforming and the system can easily be scaled for the low volumes gas production compared with the conventional reforming systems (O'Connor and Crandell, 2012).

Combined reforming of methane has also its share in microwave technology, good results have been achieved with providing a proof for a stable run of the microwave system at the high gas flow rates (several thousands of NL/h) (Li et al., 2016, Czylkowski et al., 2016).

Thus, microwave reforming topic has a growing interest. Many research papers have been published recently (Gangurde et al., 2018, Zhang et al., 2018, Li et al., 2018, Hamzehlouia et al., 2018, Jamróz et al., 2018, Bawah et al., 2018, Sun et al., 2018).

2.9. The Simulation of Methane Reforming

The reforming process of methane has been covered by different modelling studies. A central finite difference approach was used in a heterogeneous dynamic model for steam reforming of methane (Pantoleontos et al., 2012). The results of this model have been validated with industrial experiments. Another CFD model for the SRM was carried out in the ANSYS FLUENT software for the tube reactor with a packed bed catalyst (Lao et al., 2016). Aspen Plus software was used in modeling the SRM and WGS for the natural gas with Langmuir-Hinshelwood-Hougen-Watson (LHHW) kinetic model in RPLUG reactor (Amrana et al., 2017). The simulation results showed a good agreement with literature.

2.10. Summary

The production of high-quality biofuels and syngas from renewable sources depends on many factors. These factors vary according to the biofuel production process and mechanism. In fluidised bed gasification, for example, the hydrodynamic activity of the gas-solid mixture has a noticeable effect on the gasification process. The relationship between gas and solid particles in the packed and fluidised bed reactors has been studied widely. Many experimental studies were carried out in the BFBG in order to examine the hydrodynamic behaviour of the fluidised bed in different conditions. Hydrodynamic properties such as superficial gas velocity, pressure drop, and bubble size were measured and tested in many references.

However, in the first part of this work the effect of the air distributor design on the BFBG performance in terms of hydrodynamic properties. The experimental study contains measuring the pressure drop and bubble formation in the prototype BFBG for each distributor design and for different superficial velocities.

The second part of this work introduces a 3D visualisation of the BFBG with the different distributors in order to present the hydrodynamic properties of the fluidised bed in each point in the system. The MP-PIC fluid-particle interaction model was used in the simulation of the BFBG. The MP-PIC model is a Discrete Phase Model (DPM) which depends on the Largrangian -Eulerian approach in solving the gas-particle and particle-particle interaction in the fluidised bed system. The MP-PIC model has explained briefly in chapter three in this thesis.

Moreover, the modification of the produced syngas quality is not limited to the gasification process period. There are many post-gasification processes that can improve the syngas quality and specification such as methane reforming and tar removal. Post-gasification processes have a good cover in literature, for instance, wet, dry, and mixed reforming of methane in the presence of different catalytic materials are vastly studied in both industrial and academic research to produce hydrogen-rich product gases. Before start building the methane reforming reactors, many researchers simulate the entire system to estimate the outcome of the process. In the third part of this thesis the performance of post-gasification reactor for the BFBG product gas was simulated by using the Aspen Plus® software.

Finally, after the accidental discovery of the heating effects of microwaves in 1949, the attention has turned to the use of microwave heating in gasification and post-gasification processes due to the proven “specifications” of this type of heating, with the potential of low energy consumption for even higher hydrogen yields. Thus, these techniques will be evaluated to improve a bespoke bubbling fluidised bed gasifier located at Cardiff University.

Chapter Three: Methodology

3.1. Introduction

The research in this thesis contains three parts as mentioned in chapter two: the first part involves an experimental study of the effect of the perforated distributor design on the BFBG. The study aims to examine the hydrodynamic behaviour of the BFBG for each distributor to select the one that provided the best hydrodynamic behaviour. The process includes measuring the pressure drop at a number of points along the gasifier inner surface and the size of bubbles generated in the fluidised bed for deferent air flow rates. In the second part, an unsteady state three dimensional CFD simulation for BFBG with four different air distributors under isothermal conditions was carried out in the modified open source software (OpenFOAM) (ESI-OpenCFD, 2018). The simulation results will be validated by the experimental data (first part).

The third part relates to the improvement in syngas produced from the bubble fluidised bed gasifier. A simulation with Aspen Plus® software(Plus, 2009) was carried out to assess the modification process in order to build an experimental rig for the modification process. The CO_2 and CH_4 concentrations in the BFBG produced gas will be reduced to enhance the CO and H_2 components in the syngas.

3.2. BFBG Experimental Study

The experimental study will be done at Cardiff School of Engineering. The rig components are listed in table 3-1 and the rig design in SolidWorks and the system photo are illustrated in figure 3.1.

Table 3-1. Isothermal BFBG rig parts.

Part No.	Part Name	Material	Dimensions (mm)	Quantity	Figure No.	Notes
1.	Gasifier tube	Perspex	83 (ID) x 800 height x 4 thick	1		
2.	Gasifier holder	Perspex	91 (ID) – 170 (OD) x 20 thick	1		With 8 (10mm) holes
3.	Perforated distributor	Perspex	170 (OD) x 10 thick	4		With 8 (10mm) holes for each and multi small holes (Fig.4.2)
4.	Air feeder	steel	83 (ID) x 200 height x 4 thick	1		
5.	System stand	steel	1500 L x 500 W x 2000 H	1		
6.	Bolts and Nuts	Steel	M10	12		
7.	Gate valve	Brass	12.7 ID	1		
8.	Digital gas flowmeter MF 5712	Plastic frame	97 L x 50 W x 134 H	1		Fig. 3.9
9.	Digitron PM-20 Model Digital Pressure Meter	Plastic frame	155 L x 67 W x 40 H	1		Fig. 3.10
10	High-speed camera	Photron fastcam		1		Fig. 3-11

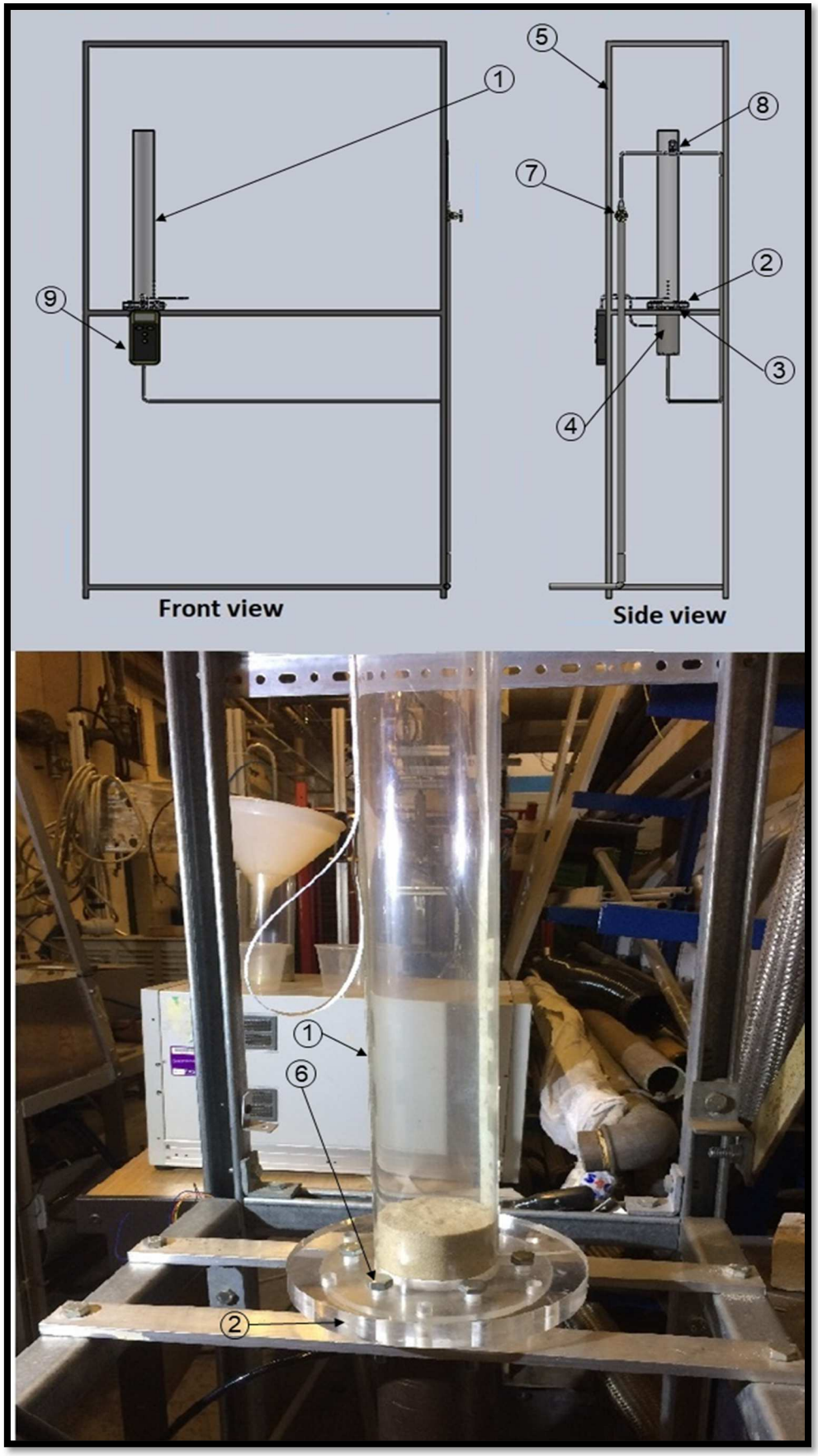

Figure 3.1. Isothermal BFBG rig schematic design and picture.

The experimental work contains two parts:

1- Measuring the pressure drop in five different positions along the inner wall of the isothermal BFB gasifier. However, the measurements in each position are carried out for different air flow rates (i.e. different superficial gas velocities) starting from the low magnitudes (before fluidisation) to the high magnitudes (fluidisation phase).

   A digital thermal gas flowmeter (MF5712), shown in figure 3.2, was used to regulate and measure the different air flow rates. The main specifications of the (MF5712) flowmeter are listed in table 3-2. A digital gas pressure meter (Digitron PM-20) shown in figure 3.3, was used to measure the pressure drop in each position. The main specifications of the (Digitron PM-20) pressure meter are listed in table 3-3.

Figure 3.2. Digital thermal gas flowmeter: MF5712 model with Siargo's proprietary MEMS calorimetric mass flow sensor.

Table 3-2. The main specifications of the digital thermal gas flow metre (MF5712) (Siargo Ltd., 2017).

	Features	Specifications	Unit
1	Flow range	1-200	SLPM
2	Turn-down ratio	30:1	%
3	Accuracy	±(2.0+0.5FS)	%
4	Repeatability	0.5	%
5	Response time	≤ 2	Sec
6	Display resolution	Instant flow: 0.1 Accumulated flow: 0.001	SLPM NCM
7	Max. pressure	≤ 0.8	MPa
8	Pressure loss	≤ 2000	Pa
9	Working temperature	-10 ~ 55	^{o}C
10	Calibration gas	N_2 at 20 °C,101.325 kPa	

Figure 3.3. Digital gas pressure meter model: Digitron PM-20.

Table 3-3. The main specifications of the digital gas pressure meter (Digitron PM-20) (Digitron, 2017).

	Features	Specifications
1	Pressure measurement	0-130 mbar
2	Resolution	0.01 resolution up to 19.99 mbar then auto ranges from 0.1 up to 130 mbar
3	Accuracy	±0.2% of reading ±0.2% of full scale ±1 digit
4	Calbration	PM 20 gauge comes complete with traceable calibration certificate
5	Operating Temperature	–10°C to 50°C/+14°F to 122°F (Ambient)

2- A study of the bubbles forming inside the fluidised bed in the internal face of isothermal BFB gasifier was performed by measuring the bubbles size and their velocities for different air flow rates. A Photron (FASTCAM-APX RS) High-Speed Video Camera, shown in figure 3.4, was used to capture the bubbles forming and measure the bubble speed before they blasted on the fluidised bed surface. The main specifications of the Photron (FASTCAM-APX RS) High-Speed Video Camera are listed in the table 3-4.

The experimental system set - up and the procedure of experiments are illustrated in chapter 4.

Figure 3.4. Photron (FASTCAM-APX RS) High-Speed Video Camera (Photron Limited, 2006).

Table 3-4. The main specifications of the Photron (FASTCAM-APX RS) High-Speed Video Camera (Photron Limited, 2006).

	Features	Specifications
1	Imaging sensor	C-MOS imaging sensor
2	Sensor resolution	1024 x 1024 pixels
3	Frame rate	Up to 3,000 FPS, full resolution
4	Recording grayscale	Monochrome: 10 bits Colour: 10 bits each on RGB (Bayer colour filter array)
5	Shutter	Electronic shutter
6	Recording media	IC memory
7	Random frame recording	The frame rate can be set to any external sync signal of 50 Hz to 250,000 Hz

3.3. BFBG CFD Simulation

In CFD, which is a branch of fluid mechanics, the problem that involves fluid flows is analysed by a suitable theoretical model and then solved numerically through a data structure in high-speed computers. Boundary conditions for the case study should be specified and represented in the CFD model.

3.3.1. Particles – Fluid Flow Models

The hydrodynamic behaviour of fluid (gas) - solid (particles) flows has received a growing interest over the decades. This is due to the wide range of usages in different engineering and industrial applications, such as fluidised bed dryers, fluid catalytic cracking, fluidised bed reactors, and various types of gasifiers. It is very difficult (if not impossible) to measure experimentally the gas-solid properties (velocities, pressure, and porosity (Voidage)) inside a fluidised bed control volume without disturbing the flow field as illustrated in chapter two. To overcome these practical measurement difficulties and limitations, many analytical models have been introduced to simulate the fluid-solid movements inside the fluidised bed system.

Thanks to the rapid advancement in computer hardware, numerical algorithms and physical understanding, analytical models with computational fluid dynamics (CFD) have become powerful tools to provide both qualitative and quantitative insight into the complex fluid (gas) – solid (particles) flows.

In recent studies, there are many models used to simulate the gas-solid flow mechanisms depending on different interpretations of the gas-solid interaction (Chen and Wang, 2017).

3.3.2. Two-Fluid Model (TFM)

TFM has been used to simulate the hydrodynamic interaction inside the fluidised bed for a long time (Ding and Gidaspow, 1990, Kuipers et al., 1992a, Yang et al., 2017, Ye et al., 2008). The models are based on an Eulerian - Eulerian continuum approach (Anderson and Jackson, 1967, Gidaspow, 1994). Basically, in the two-fluid models, both fluid and solid phases are continuous, fully interpenetrating and both momentum and heat transfer can be exchanged between the two phases (Kuipers et al., 1992b).

The phases are represented by separate sets of equations with suitable interaction terms referring to the coupling between phases. Moreover, the physical properties of the solid particles such as shape and size are included in the continuum terms through empirical relations for the interfacial friction. However, the discrete character of the solid phase (particles) is not recognised in the two fluid models. Normally, the solution of the TFM approach relies on grid-based methods such as finite difference method FDM and finite volume method FVM.

The Two-Fluid Model governing equations are (Chen and Wang, 2014):

Continuity Equation;

$$\frac{\partial}{\partial t}(\epsilon_f.\rho_f) + \nabla \cdot \left(\epsilon_f.\rho_f \cdot u_f\right) = 0 \quad \text{(Fluid Phase)} \quad \text{3-1}$$

$$\frac{\partial}{\partial t}(\epsilon_s.\rho_s) + \nabla \cdot (\epsilon_s.\rho_s \cdot u_s) = 0 \quad \text{(Solid Phase)} \quad \text{3-2}$$

Where f and s refer to fluid and solid phase respectively, and ϵ, ρ and u represent the void fraction (Voidage), density and velocity, respectively.

Momentum Conservation Equations;

For Fluid Phase;

$$\frac{\partial}{\partial t}(\epsilon_f \cdot \rho_f \cdot u_f) + \nabla \cdot (\epsilon_f \cdot \rho_f \cdot u_f \cdot u_f) + \epsilon_f \cdot \nabla p_f = \nabla . \bar{\bar{\tau}}_f + \epsilon_f \cdot \rho_f \cdot g + \beta \cdot (u_f - u_s) \quad \text{3-3}$$

For Solid Phase;

$$\frac{\partial}{\partial t}(\epsilon_s \cdot \rho_s \cdot u_s) + \nabla \cdot (\epsilon_s \cdot \rho_s \cdot u_s \cdot u_s) + \epsilon_s \cdot \nabla p_s = \nabla . \bar{\bar{\tau}}_s + \epsilon_s \cdot \rho_s \cdot g + \beta \cdot (u_s - u_f) \quad \text{3-4}$$

Where p and $\bar{\bar{\tau}}$ are pressure and stress-strain tensor for fluid or solid phase, respectively and g and β are gravitational acceleration and the interphase drag coefficient, respectively.

$$\bar{\bar{\tau}}_f = \epsilon_f \cdot \mu_f (\nabla u_f - \nabla u_f^T) - \frac{2}{3}\epsilon_f \cdot \mu_f (\nabla u_f) \cdot \bar{\bar{I}} \quad \text{3-5}$$

$$\bar{\bar{\tau}}_s = -p_s \cdot \bar{\bar{I}} + \mu_s (\nabla u_s - \nabla u_s^T) + (\lambda_s - \frac{2}{3}\mu_s) \cdot (\nabla u_s) \cdot \bar{\bar{I}} \quad \text{3-6}$$

Where: $\bar{\bar{I}}$ is the unit tenser and λ_s is the bulk viscosity of the solid.

The interphase drag coefficient, β and the other solid variables such as p_s , μ_s and λ_s can be calculated through empirical equations (Lun et al., 1984, Oger and Savage, 2013, Wen and Yu, 1966).

However, one of its drawbacks is that the use of the standard TFM to simulate the hydrodynamic behaviour of BFB with Geldart A particles over-predicts the results in a bed expansion (Ferschneider and Mege, 1996, Mckeen and Pugsley, 2003, Zimmermann and Taghipour, 2005).

3.3.3. Continuum (Eulerian) – Discrete (Lagrangian) Models

In the Continuum – Discrete Models, the continuity and momentum equations are applied for the fluid phase just like the two-fluid models (i.e. equations 3-1 and 3-3 with some differences in calculating the interphase drag force term). The drag force in the TFM depends only on the averaged parameters such as fluid and solid velocities and local solid fraction in addition to

the fixed properties of the fluid and the solid. Meanwhile, in the Continuum – Discrete Models, the drag force term in the momentum equation 3-3 is obtained by calculating and summing the drag force for each particle in a fluid cell over all particles in that fluid cell.

3.4. Discrete Particle Model (DPM)

The discrete particle model (DPM) can be considered as one of the best Computational Fluid Dynamics –Discrete Element Model (CFD-DEM) approaches (Zhu et al., 2008). In this model, the Newtonian equations of motion are solved for each individual particle, and an interaction model is applied to handle particle encounters. Meanwhile, the Navier - Stokes equations based on the concept of local average as used in CFD are used to solve the fluid flow continuum, taking momentum transfer between the fluid and the particles into account (Kawaguchi et al., 2000).

According to particles collision models, discrete particle models can be classified mainly into two approaches, the hard sphere approach (Campbell and Brennen, 1985, Hoomans et al., 1996) and the soft sphere approach (Tsuji et al., 1993).

3.4.1. Hard Sphere Model (HSM)

The particles in this model are assumed to be impenetrable and cannot overlap in space. Here, particle-particle collisions and particle-wall collisions happen immediately. Moreover, momentum binary collisions are used to determine particles trajectories. Figure 3.5 shows the collision between two hard sphere particles with (r_1, r_2) radii with some of the relevant physical variables. The after-collision velocities for the two collide particles can be derived from the following equations (Li et al., 2012):

$$m_1 \cdot \left(V_1 - V_1^{(0)}\right) = J \quad \text{..... 3-7}$$

$$m_2 \cdot \left(V_2 - V_2^{(0)}\right) = -J \quad \text{..... 3-8}$$

$$I_1 \cdot \left(\omega_1 - \omega_1^{(0)}\right) = r_1 \cdot n \times J \quad \text{..... 3-9}$$

$$I_2 \cdot \left(\omega_2 - \omega_2^{(0)}\right) = r_2 \cdot n \times J \quad \text{.....3-10}$$

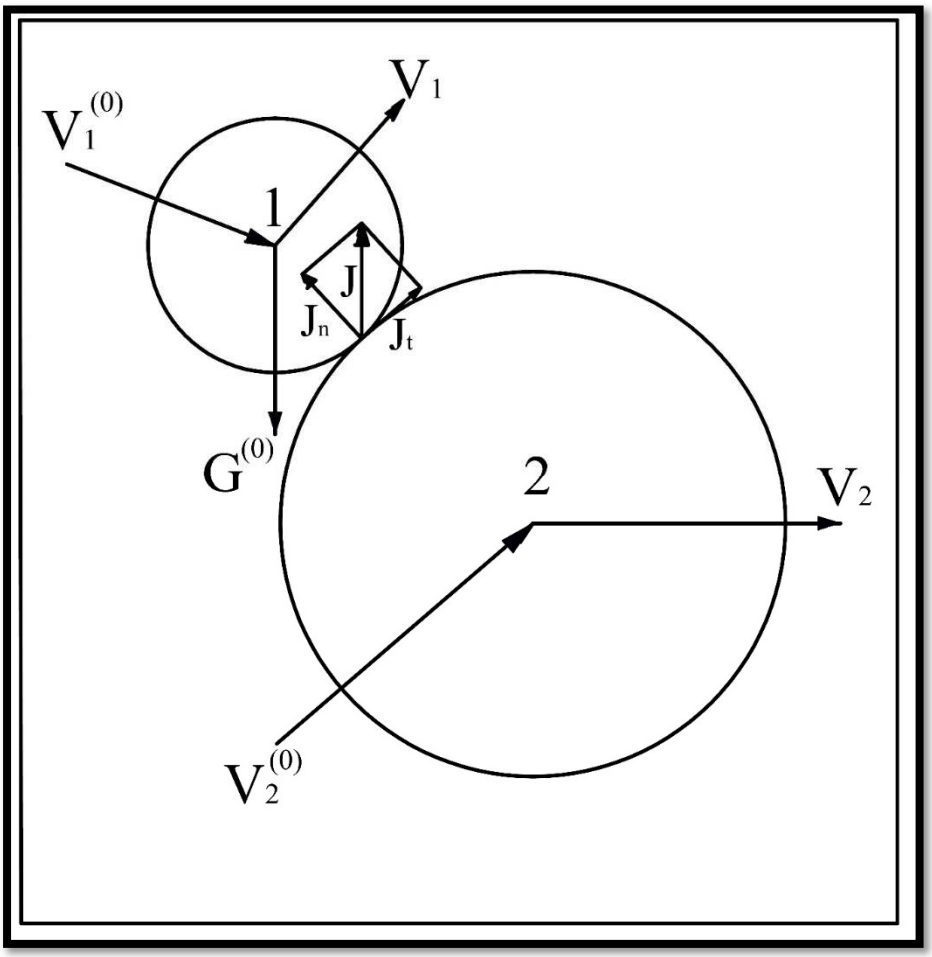

Figure 3.5. Two hard sphere particles in a collision (Li et al., 2012).

Where:

m_1, m_2 - Masses of the particles 1 and 2 respectively (kg).

$V_i^{(0)}, V_i$ - Velocity vector of the particle (i) before and after the collision (m/s).

J - Vector of collision impulse (kg.m/s).

I_1, I_2 – Moment of inertial of particle 1 and 2 respectively (kg.m^2).

$\omega_i^{(0)}, \omega_i$ - Angular velocity of the particle (i) before and after the collision (1/s).

r_1, r_2 – Particle 1 and 2 radii (m).

n – Unit normal vector of the contact point of particle collision.

3.4.2. Soft Sphere Model (SSM)

This model was originally developed by Cundall and Strack (Cundall and Strack, 1979). In this approach, particles deform due to the collision. Particles remain geometrically rigid, and "deformation" is considered in the force models. Typically, soft sphere approach simulations are more complicated and time-consuming than hard sphere approach.

The spring-dashpot model introduced by Cundall and Strack is mostly used to calculate the contact forces as shown in figure 3.6. The normal and tangential components of the contact force in the soft-sphere model can be calculated by the following equations (Xue et al., 2017):

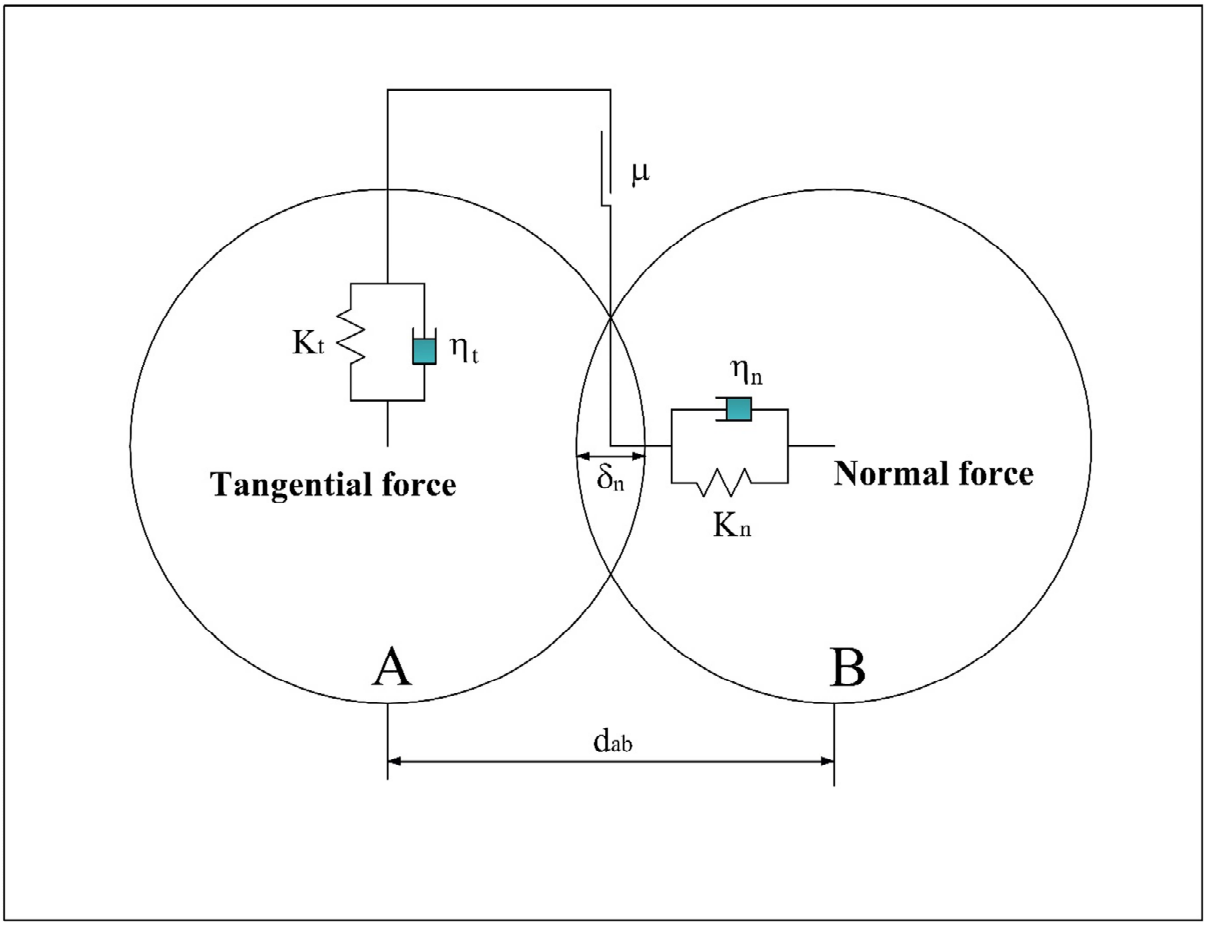

Figure 3.6. Soft sphere model description (Xue et al., 2017).

For the normal component of the contact force.

$$\vec{f}_{ab}^{n} = k_n \cdot \delta_n \cdot \vec{n}_{ab} - \eta_n \cdot \vec{u}_{ab}^{n} \quad \text{..... 3-11}$$

Where:

$\vec{f}_{ab}^{n}$ – The normal component of the contact force between particles A and B. (N)

k_n – The normal spring stiffness. (N/m)

δ_n – The normal overlap between particles A and B. (m)

$\vec{n}_{ab}$ – The normal unit vector.

η_n – The normal damping coefficient. (N.s/m)

$\vec{u}_{ab}^{n}$ – The normal relative velocity between particles A and B. (m/s)

$$\vec{u}_{ab}^{n} = \left((\vec{u}_a - \vec{u}_b) \cdot \vec{n}_{ab}\right)\vec{n}_{ab} \quad \text{3-12}$$

$\vec{u}_a$ – The velocity of particle A. (m/s)

$\vec{u}_b$ – The velocity of particle B. (m/s)

And for the tangential component of the contact force.

$$\vec{f}_{ab}^{t} = \begin{cases} -k_t \cdot \delta_t \cdot \vec{t}_{ab} - \eta_t \cdot \vec{u}_{slip} & \left|\vec{f}_{ab}^{t}\right| < \mu\left|\vec{f}_{ab}^{n}\right| \\ -\mu\left|\vec{f}_{ab}^{n}\right| \cdot \vec{t}_{ab} & \left|\vec{f}_{ab}^{t}\right| \geq \mu\left|\vec{f}_{ab}^{n}\right| \end{cases} \quad \text{3-13}$$

Where:

K_t – The tangential spring stiffness. (N/m)

δ_t – The tangential displacement. (m)

$\vec{t}_{ab}$ – The tangential unit vector.

η_t – The tangential damping coefficient. (N.s/m)

$\vec{u}_{ab}^{t}$ – The slipping velocity. (m/s)

μ – The friction coefficient.

$$\vec{u}_{ab}^{t} = (\vec{u}_a - \vec{u}_b) - \vec{u}_{ab}^{n} \quad \text{3-14}$$

$$\vec{t}_{ab} = \frac{\vec{u}_{ab}^{t}}{|\vec{u}_{ab}^{t}|} \quad \text{3-15}$$

The spring stiffness k and the damping coefficient η can be calculated by the following (Capecelatro and Desjardins, 2013):

$$k = \frac{m_{ab}}{\tau_{col}^2(\pi^2+(ln\, e)^2)} \quad \text{..... 3-16}$$

$$\eta = -2 \cdot ln\, e \, \frac{\sqrt{m_{ab} \cdot k}}{\pi^2+(ln\, e)^2} \quad \text{..... 3-17}$$

Here,

$$m_{ab} = \left(\frac{1}{m_a} + \frac{1}{m_b}\right)^{-1}$$

m_a, m_b – The mass of particle A and B respectively. (kg)

e – Coefficient of restitution $0 < e < 1$.

τ_{col} – The collision time (sec).

3.5. Multiphase Particle-In-Cell (MP-PIC) Method

The MP-PIC model is considered a Discrete Particle Model as it deals with the fluid phase as a continuum (Eulerian) and the solid phase is treated as Lagrangian computational particles. This model has emanated from the particle – in – cell (PIC) method originally introduced by Harlow for a single-phase flow (Harlow, 1957).

In the (PIC) method, the Lagrangian particles approach is used to transport mass, momentum, and energy through a fixed Eulerian grid in a way that preserves the identities of the different solid particle materials. Moreover, the interactions of the particles are determined on the Eulerian grid with an interpolation of particle properties in the grid. Then, the fluid field is updated on the grid (Pannala, 2010).

The MP-PIC method was proposed firstly by Andrews and O'Rourke to simulate one - dimensional dense flow of particles and gas with comparison with an analytical solution and experimental data (Andrews and O'rourke, 1996). This method can be considered as an extension of the stochastic particle method of the KIVA code, which is a computer programme

for the numerical calculation of transient, two- and three-dimensional chemically reactive fluid flows with sprays, due to the addition of the isotropic particle stress gradient to the equation of motion of the particles (Amsden et al., 1989).

The MP-PIC method can calculate the flow of particles with different volume fraction from the dilute to the close pack limits. In particles -fluid flows, it is difficult to determine the particle stress gradient for each particle in a dense flow. Thus, the particle stress gradient is calculated as a gradient on the grid with fully coupling to the other particles and fluid acceleration term and is then interpolated to the discrete particles. The MP- PIC method was extended to two-dimensional flows by (Snider et al., 1997) and then (Snider, 2001) extended the method for three-dimensions.

3.6. MP-PIC Model Methodology

The Multiphase Particle-In-Cell method can be described by the following governing equations, the interpolation operators and the particle stress model (Snider, 2001).

3.6.1. The Governing Equations

The governing equations in the MP-PIC model can be divided into two sets: the fluid phase equations and the particles phase equations.

3.6.1.1. Fluid phase (continuum phase)

The Continuity Equation for the incompressible fluid:

$$\frac{\partial \epsilon \rho_f}{\partial t} + \nabla \cdot \left(\epsilon \rho_f \cdot u_f\right) = 0 \quad \text{..... 3-18}$$

Where:

ϵ – Voidage (Porosity). (-)

ρ_f – Fluid density. (m^3/kg)

u_f – Fluid velocity. (m/s)

The Navier- Stokes' Momentum equation:

$$\frac{\partial \epsilon \rho_f \cdot u_f}{\partial t} + \nabla \cdot \left(\epsilon \rho_f \cdot u_f \cdot u_f\right) + \nabla p = -F + \epsilon_f \cdot \rho_f \cdot g \quad \text{..... 3-19}$$

Where:

p – Fluid pressure. (pa)

F - The rate of momentum exchange per volume between the fluid and particle phases. ($N.m/m^3$)

ϵ_f – Fluid volume fraction (void fraction).

g – The gravitational acceleration. (m/s^2).

3.6.1.2. Particulate Phase (Particle Phase)

In the particulate phase, the probability distribution function (ϕ) is used to describe the particles dynamics. Here, the probability distribution function (ϕ) is a function of $\left(x, u_p, \rho_p, V_p, t\right)$, where x is the particle position, u_p is particle velocity, ρ_p is the particle density, V_p is the particle volume, and t represents the time (Andrews and O'rourke, 1996).

The evolution of the probability distribution function (ϕ) with time can be calculated by solving the Liouville equation;

$$\frac{\partial \phi}{\partial t} + \nabla \cdot \left(\phi \cdot u_p\right) + \nabla_{u_p} \cdot (\phi . A) = 0 \quad \text{..... 3-20}$$

Where A is the particle acceleration $\left(du_p / dt\right)$ and can be determined by the following equation:

$$A = D_p \cdot \left(u_f - u_p\right) - \frac{1}{\rho_p} \cdot \nabla p + g - \frac{1}{\epsilon_p \cdot \rho_p} \cdot \nabla \tau \quad \text{..... 3-21}$$

Where D_p is a drag function, ϵ_p is the particle volume fraction, and τ is the interparticle stress gradient.

The integration of the probability function (ϕ) over the velocity and mass of the particle gives the probable number of particles per unit volume at any position, x and time, t in the domain. Thus, the particle local properties (Particle volume fraction (ϵ_p), Average particle density ($\overline{\epsilon_p \cdot \rho_p}$) and Mean particle velocity ($\overline{u_p}$) can be calculated by the following equations:

$$\epsilon_p = \iint \emptyset \cdot \frac{m_p}{\rho_p} \cdot dm_p \cdot du_p \quad \text{..... 3-22}$$

$$\overline{\epsilon_p \cdot \rho_p} = \iint \emptyset \cdot m_p \cdot dm_p . d\, u_p \quad \text{..... 3-23}$$

$$\overline{u_p} = \frac{1}{\overline{\epsilon_p \cdot \rho_p}} \iint \emptyset \cdot m_p \cdot u_p \cdot dm_p \cdot du_p \quad \text{..... 3-24}$$

Here (m_p) is the particle mass ($m_p = \rho_p \cdot V_p \; and \; dm_p = d\rho_p \cdot dV_p$).

In the flow region, the sum of the particle volume fraction and the fluid volume fraction (Voidage) must be unity at any position, x and time, t: $\epsilon_p + \epsilon_f = 1$.

Back to the momentum equation of the fluid phase, the rate of momentum exchange per volume between the fluid and particle phases, F is;

$$F = \iint \emptyset \cdot m_p \left[D_p \left(u_f - u_p\right) - \frac{1}{\rho_p} \cdot \nabla p \right] dm_p \cdot du_p \quad \text{..... 3-25}$$

3.6.2. Interpolation Operators

The particles properties in the MP-PIC scheme are interpolated to and from the Eulerian grid using different interpolation operators such as linear and trilinear interpolation operators. For a rectangular grid with cuboid cells, the vector particle properties such as momentum transfer

between particles are interpolated to the cell faces and the scalar properties such pressure drop are interpolated to the call centres. However, in the case of using the nonorthogonal grid in the MP-PIC scheme, the control volumes and particles are transformed to a square computational grid and then interpolation operators and gradients are calculated. After that, it is transformed back to the normal grid (Snider, 2001).

3.6.3. Particle Stress Model

The particle stress is modelled by applying a continuum calculation for the particle pressure and the subsequent normal stress force to discrete particles. Here, the interparticle stress gradient, τ is calculated from Harris and Crighton model (Harris and Crighton, 1994)**:**

$$\tau = \frac{P_s \cdot \epsilon_p^{\beta}}{max[\epsilon_{cp} - \epsilon_p, \theta(1-\epsilon_p)]} \quad \text{3-26}$$

where: P_s is a constant with pressure units, ϵ_{cp} is the particle volume fraction at close packing as shown in Fig. 3.7, β is a constant and has a value of $2 \leq \beta \leq 5$ as recommended by (Auzerais et al., 1988), and θ is a constant with a small value in the order of 10^{-7} (Snider, 2001).

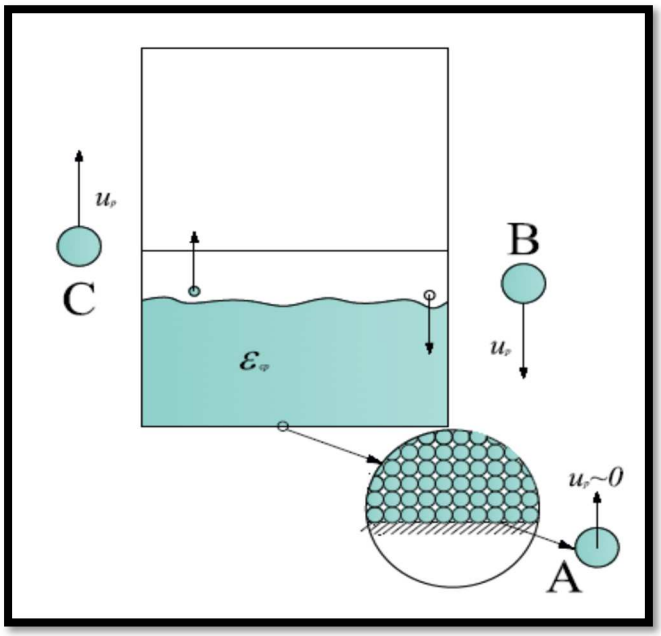

Figure 3.7. Particles in closed pack control volume (Snider, 2001).

Figure 3.7 shows three different particles (clouds) in a close pack. Particle A is near the wall. This particle is surrounded by a wall or other neighbour particles and it has zero mean velocity u_p=0 due to the limited particle movement due to the particle collision mean free path and stress transfer to the wall. However, the packed bed is slightly expanding due to the influence of the large particle normal stress on the particle's depth within the bed.

Particle B may move through a high voidage region with a large mean free path between particles. While this particle approaches the closed pack, its velocity starts decreasing due to the large particle normal stress from the closed pack bed region. This large particle normal stress will also prevent the particle, when it reaches the closed pack region, from penetrating the cell and move it from the volume centre.

As the particle C starts leaving the closed pack region, the particle normal stress decreases and the collision between the particle and the other neighbouring particles will diminish, i.e. the particle-mean-free paths will increase too (Snider, 2001).

3.7. Air Distributors in BFBG

When making improvements in the hydrodynamic mechanism between the solid phase (particles) and the fluid phase (air) in the fluidised bed gasifier, it is crucial to choose an air distributor which provides uniform air distribution throughout the fluidised bed control volume, optimum fluidised air velocity, suitable pressure drops, and the optimum bubble size, which finally modify the heat transfer and the gasification process in general (Shukrie et al., 2016).

There are many types of gas distributors used in BFB gasification systems, which ranged from the simple shapes to extremely complex ones. However, the selection of suitable gas distributors subject to several criteria such as manufacturing cost, hydrodynamic efficiency, etc. Generally, the perforated plate distributors are the most common to manufacture among other gas distributors (Shukrie et al., 2016).

3.7.1. Perforated Disc Distributor Design

The design of the perforated distributor is subjected to several criteria such as the gas pressure drop across the bed (Δp_b), hole (orifice) diameter (d_o), and holes arrangement in the distributor (Geldart and Baeyens, 1985). The distributor should provide enough pressure drop to initiate fluidisation uniformly. Hence, the pressure drop across a bubbling bed with (H) height, can be calculated via the equation (Basu, 2006):

$$\Delta p_b = \rho_p(1-\epsilon_g)\cdot H\cdot g = \rho_p(1-\epsilon_{gmf})\cdot H_{mf}\cdot g \quad \text{..... 3-27}$$

Where:

ϵ_{gmf} – The voidage (porosity) at minimum fluidisation conditions. (-)

H_{mf} – The bed height at minimum fluidisation conditions. (m)

Another important factor in distributor design is the fractional opening area of the orifices:

$$Fractional\ opening\ area\ of\ the\ orifices = N\frac{\pi}{4}d_o = \frac{U\cdot\rho_g}{U_o\cdot\rho_{go}} \quad \text{..... 3-28}$$

Where:

N – Number of holes (orifices) per unit area of the distributor. (m^2)

$N = \frac{1}{P^2}$ For square arrangement pitch.

$N = \frac{2}{\sqrt{3}\cdot P^2}$ For triangular arrangement pitch.

P- The pitch between two holes. (m)

U, U_o – Superficial gas velocity and orifice gas velocity respectively. (m/s)

Figure 3.8 demonstrates the different parameters in a perforated plate distributor having disc diameter (D) and orifice diameter (d_o).

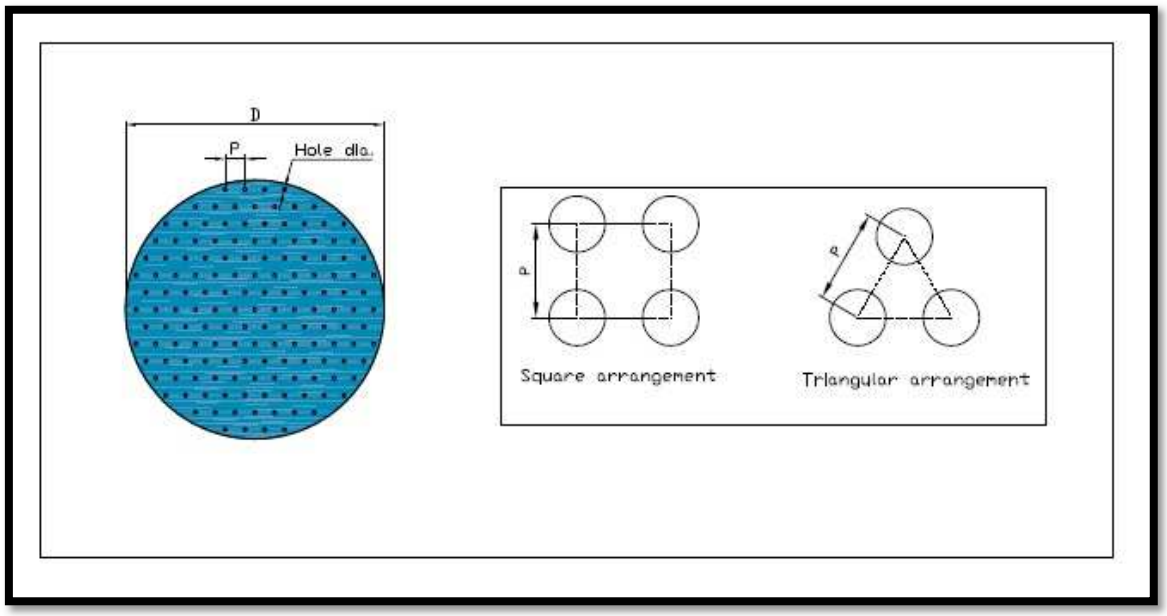

Figure 3.8. Perforated plate distributor.

3.7.2. Minimum Fluidization Velocity, U_{mf}

The minimum fluidisation velocity (U_{mf}) in a fluidised bed control volume can be calculated by using the Ergun's equation for the pressure drop along a packed bed in conjunctions with the fluid drag equations (Ergun, 1952).

$$\frac{\Delta p}{H} = 150 \cdot \frac{\mu \cdot U}{(\phi \cdot d_p)^2} \cdot \left(\frac{(1-\epsilon_g)^2}{\epsilon_g^3}\right) + 1.75 \cdot \frac{\rho_g \cdot U^2}{\phi . d_p} \cdot \frac{(1-\epsilon_g)}{\epsilon_g^3} \quad \text{..... 3-29}$$

And

$$\text{Fluid Drag} = \Delta p \cdot A = A \cdot H \cdot (1-\epsilon_g)(\rho_p - \rho_g) \cdot g \quad \text{..... 3-30}$$

Where:

H – Bed height (m).

μ - Fluid dynamic velocity ($^{\mathrm{N.s}}/_{\mathrm{m}^2}$).

ϕ - Particle sphericity. $\phi = 1$ for spherical particles.

Thus, for minimum fluidisation conditions (Kunii and Levenspiel, 1991):

$$U_{mf} = \frac{(d_p)^2 \cdot (\rho_p - \rho_g) \cdot g}{150 \cdot \mu} \left(\frac{\epsilon_{mf}^3 \cdot \phi^2}{1 - \epsilon_{mf}} \right) \quad \text{..... For small particles } \mathrm{Re_{p,mf}} < 20. \quad \text{..... 3-31}$$

And

$$U_{mf}^2 = \frac{d_p \cdot (\rho_p - \rho_g) \cdot g}{1.75 \cdot \mu} \cdot \epsilon_{mf}^3 \cdot \phi \quad \text{..... For large particles } \mathrm{Re_{p,mf}} < 1000. \quad \text{..... 3-32}$$

If ϵ_{mf} and / or ϕ are unknown, then U_{mf} can be calculated by the following equation:

$$U_{mf} = \frac{\mu}{d_p \cdot \rho_g} \cdot [(C_1^2 + C_2 \cdot Ar)^{0.5} - C_1] \quad \text{..... 3-33}$$

Where:

Ar - Archimedes number. $\left(\mathrm{Ar} = \frac{\rho_g \cdot (\rho_p - \rho_g) \cdot g \cdot d_p^3}{\mu^2}\right)$

The value of the empirical constants C_1, C_2 can be found experimentally as (Grace, 1982):

$C_1 = 27.2$ and $C_2 = 0.0408$.

Hence, the minimum fluidisation velocity will be:

$$U_{mf} = \frac{\mu}{d_p \cdot \rho_g} \cdot [(739.84 + 0.0408 Ar)^{0.5} - 27.2] \quad \text{..... 3-34}$$

3.7.3. Application of the Theory to Experimental Rig

The study includes an isothermal bubbling fluidised bed gasifier with 800mm height and 83mm inner diameter and four different perforated distributors as described in section 3.2. The

specifications for each distributor are shown in table 3-5. The geometrical designs for the isothermal BFBG and the four air distributors are illustrated with the dimensions in figures 3.9 and 3.10 respectively.

Table 3-5. The specifications of the BFBG distributors.

Type	Distributor	Working diameter (mm)	Orifice diameter d_o (mm)	Holes arrangement	Pitch, P (mm)	Number of Holes
A	Perforated Disc	83	2	Square	7.5	97
B	Perforated Disc	83	2	Triangular	7.5	109
C	Perforated Disc	83	1	Square	6.35	137
D	Perforated Disc	83	1	Triangular	6.35	151

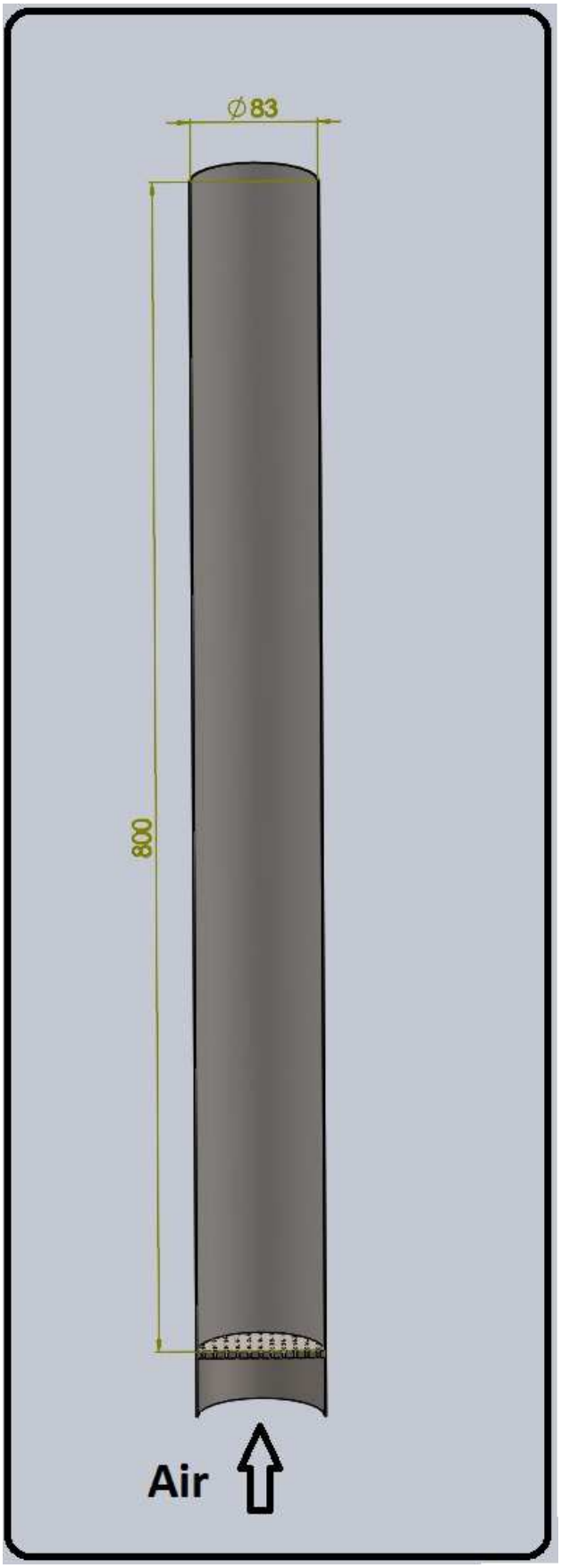

Figure 3.9. Section of the geometrical design of the isothermal BFBG.

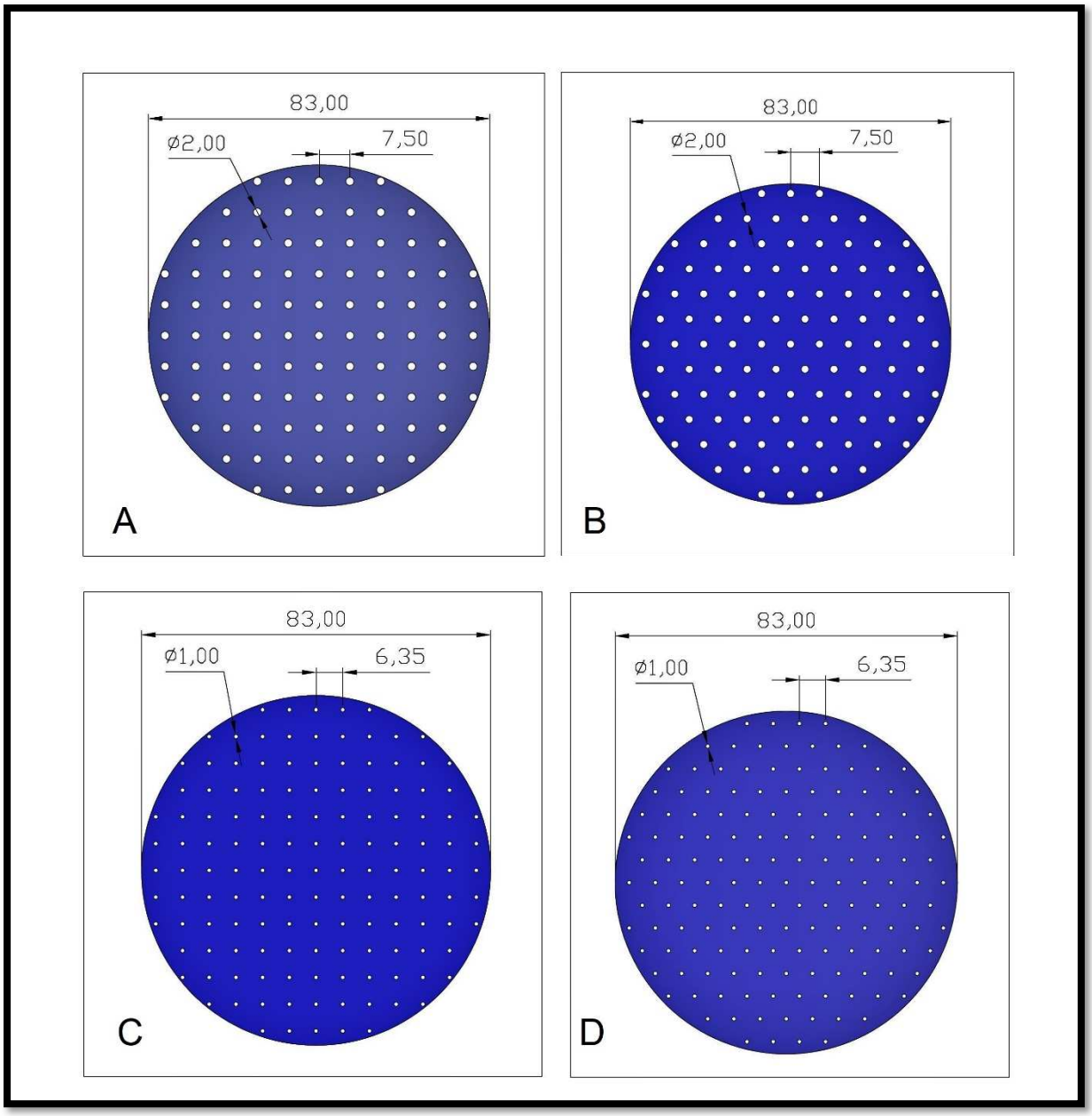

Figure 3.10. Geometrical designs for the perforated plate distributors:

A – 2mmϕ, square arrangement, 7.5mm pitch and 97 holes.

B – 2mmϕ, triangular arrangement,7.5mm pitch and 109 holes.

C – 1mmϕ, square arrangement, 6.35mm pitch and 137 holes.

D – 1mmϕ, triangular arrangement,6.35mm pitch and 151 holes.

3.7.4. Simulation Parameters

The isothermal bubble fluidised bed gasifier used in this simulation has silica sand particles as a solid phase and air as a fluid phase. The properties of each substance are presented in table 3-6.

Table 3-6. The properties of simulation parameters.

Parameters	Material	Unit	Value
Solid phase	Silica Sand	(-)	(-)
Total (particles) mass	Silica Sand	kg	0.5
Particle size, d_p	Silica Sand	µm	(425 - 500)
Particle density, ρ_p	Silica Sand	kg/m^3	2650
Particle sphericity,ϕ	Silica Sand	(-)	1
Particles injection mode	Silica Sand	(-)	Batch injection
Fluid phase	Air	(-)	(-)
Fluid flow rate	Air	SLPM	(100 -150)
Gas temperature, T	Air	^oC	20
Gas pressure, p	Air	Pa	101325
Gas density, ρ_g	Air	kg/m^3	1.2
Gas dynamic viscosity, µ	Air	$^{kg}/_{m \cdot s}$	1.82 x 10-5
Gas kinematic viscosity, υ	Air	$^{m^2}/_{s}$	1.56 x 10-5
Gravitational acceleration, *g*	(-)	$^{m}/_{s^2}$	9.81

3.7.5. Simulation Procedure

The simulation involves three main stages which are the design of the control volume geometry, mesh generation, and solving the model respectively.

3.7.5.1. Control Volume Geometrical Design

The region where the gas (air) and solid (silica sand) are flowing and forming the fluidised bed has been represented geometrically by using the open – source software SALOME 7.7.1 (CASCADE, 2005-2018). Figure 3.11 shows the system geometrical representation in the SALOME 7.7.1 platform.

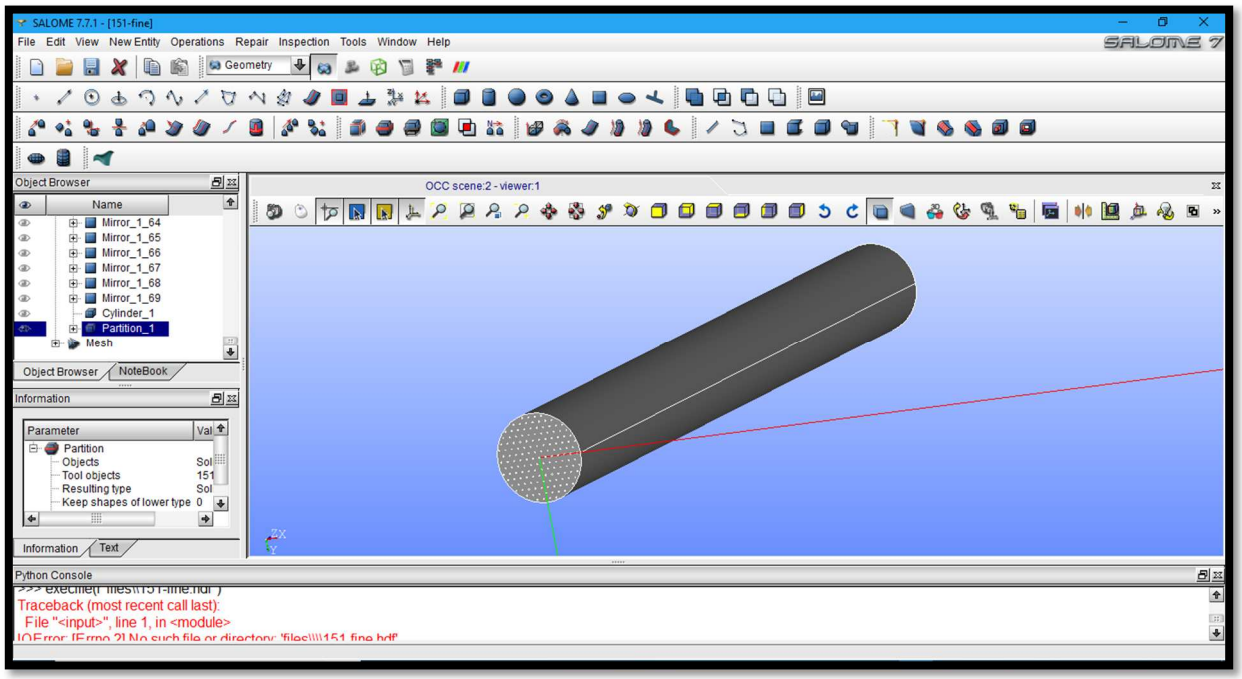

Figure 3.11. System control volume in the SALOME7.7.1 platform.

3.7.5.2. Mesh Generation

In the same software platform (SALOME 7.7.1), the system mesh has been generated with NETGEN_2D3D algorithms with approximately 30,000 to 60,000 nodes depending on the distributor type. The mesh for the whole control volume and for the distributor side are illustrated in figures 3.12 and 3.13 respectively.

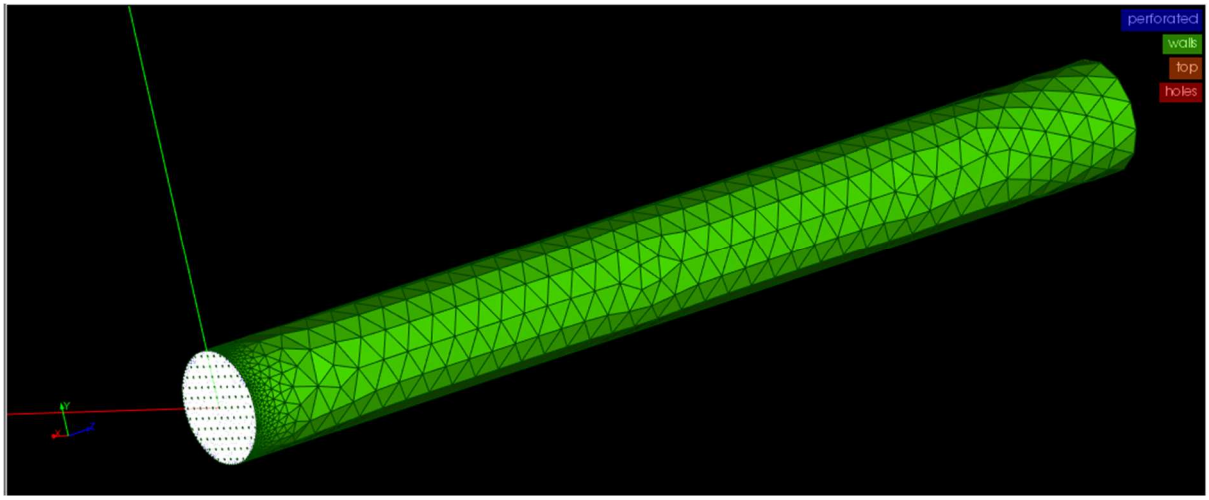

Figure 3.12. The system control volume mesh.

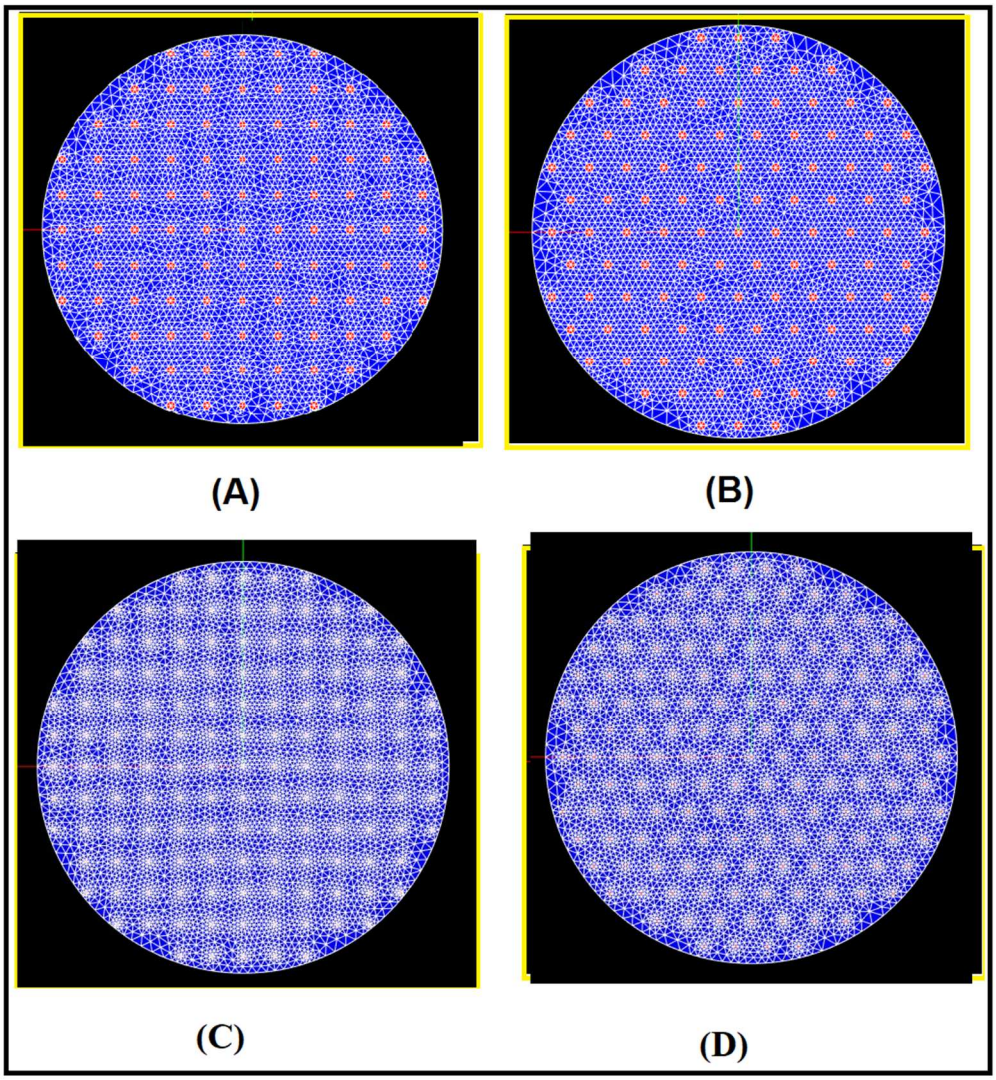

Figure 3.13. The mesh of the distributor side: A – 2mmϕ - square arrangement. B - 2mmϕ - triangular arrangement. C - 1mmϕ - square arrangement. D - 1mmϕ - square arrangement.

The choosing of mesh generation method and quality was subjected to many factors such as the complexity and the shape of the system. However, the BFBG system with the air distributors forms a complex structure as shown in figure 3.13 which cannot be applied to the other mesh types such as the hexahedron mesh. Moreover, the size of the elements is not the same for all the system as shown in figures 3.12 and 3.13, the distributor zone has fine elements and the rest of the BFBG body has coarse elements. Three different types of mesh have been studied and a mesh sensitivity analysis has been done to choose the suitable mesh type for the simulation as shown in figure 3.14 and 3.15 for type A distributor. In spite of the high computational time of the fine mesh compared to the moderate and coarse mesh (1706 sec, 823 sec and 383 sec respectively per 0.01 sec time step), the fine mesh was chosen in this modelling due to the convergence with experimental data as shown in figure 3.14.

The final files of the system mesh are exported to the model solver after changing their format from (HDF) of the SALOME 7.7.1 to the (UNV) format.

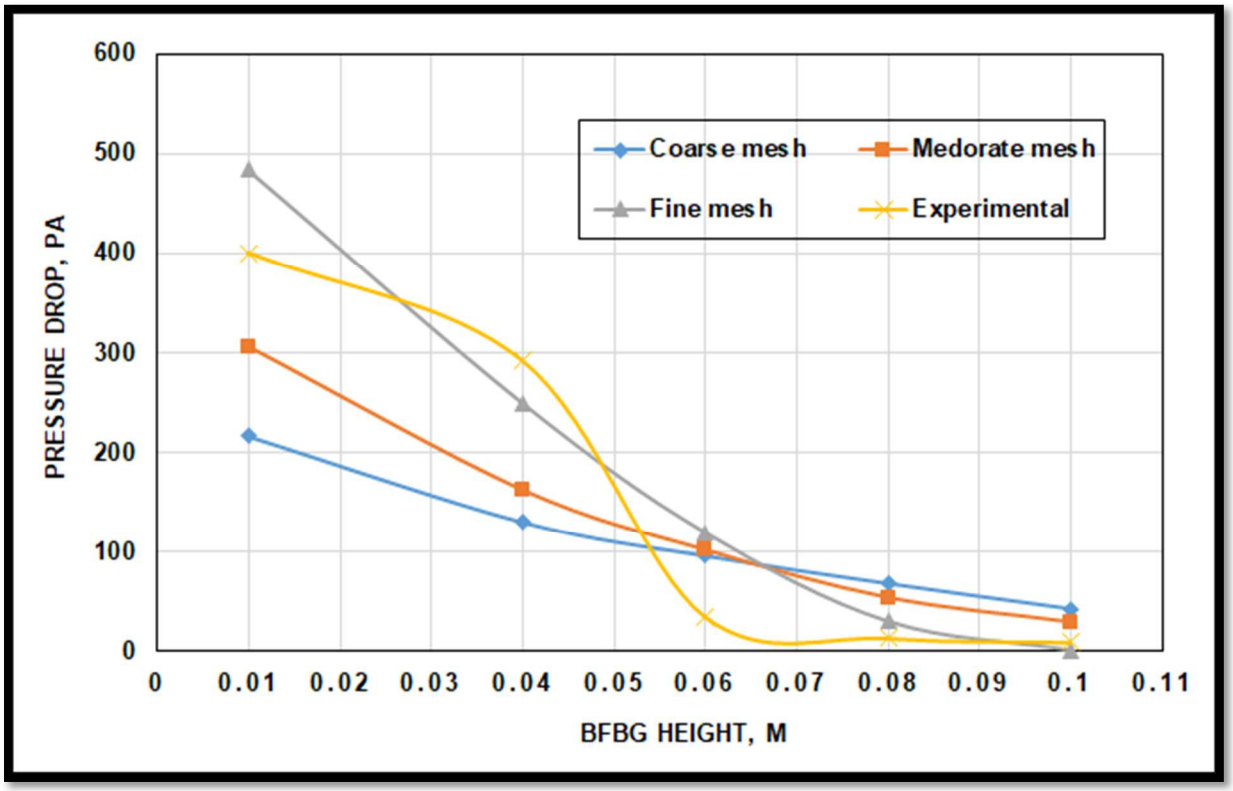

Figure 3.14. Comparison between the three mesh types with the experimental pressure drop in type A distributor.

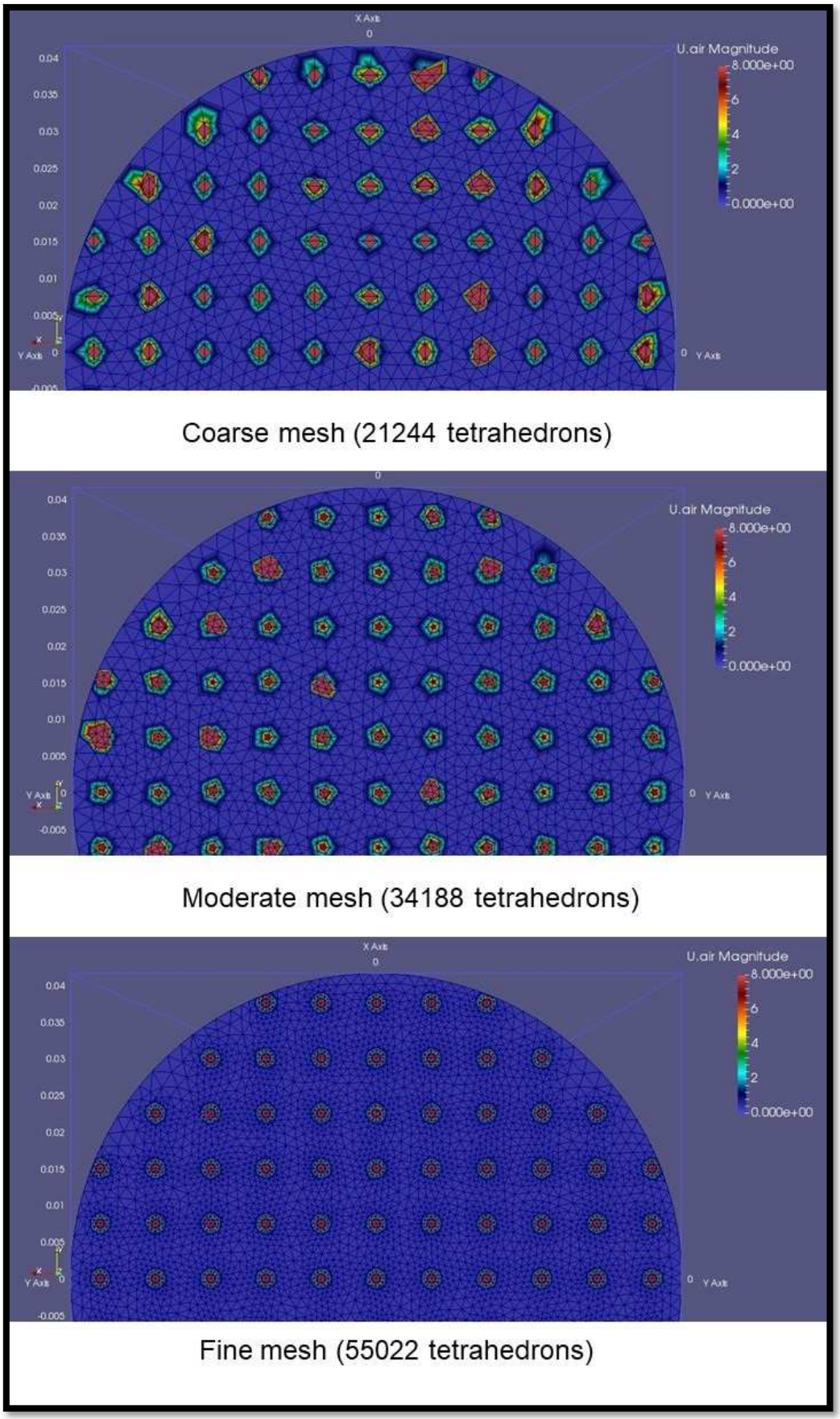

Figure 3.15. The effect of mesh type on the velocity patron in type A distributor.

3.7.5.3. The Model Solver

The final step in the simulation procedure is using the model solver with the exported UNV files from SALOME 7.7.1. The model solver in this simulation is the open source software OpenFOAM.

3.7.6. OpenFOAM®

OpenFOAM® is open source software developed by OpenCFD Ltd at ESI Group and distributed by the OpenFOAM Foundation. The word OpenFOAM® stands for Open Source Field Operation and Manipulation (ESI-OpenCFD, 2018).

OpenFOAM® has a C++ library used primarily to create executables (Applications). The applications in OpenFOAM are divided into two categories:

1- The solvers: solvers are the specific parts designed to solve a specific problem in the continuum mechanics.
2- The Utilities: the parts which are designed to improve the tasks that need data manipulation.

The OpenFOAM software involves large numbers of solvers and utilities covering a wide range of different engineering and scientific problems. OpenFOAM has pre- and post-processing environments which help in handling the consistent data across all environments. The overall structure of OpenFOAM is illustrated in Figure 3.16.

3.7.6.1. MPPICFoam Solver

In 2014, OpenFOAM® introduced the OpenFOAM - 2.3.0 version. This version has many new solvers such as the (DPMFoam) solver used for solving the Discrete Particle Methods (DPM) for the dense flow of particles and the (MPPICFoam) solver for the Discrete Particle Methods

(DPM) to resolve collisional exchange, implementing the Multiphase Particle-in-Cell (MP-PIC) method.

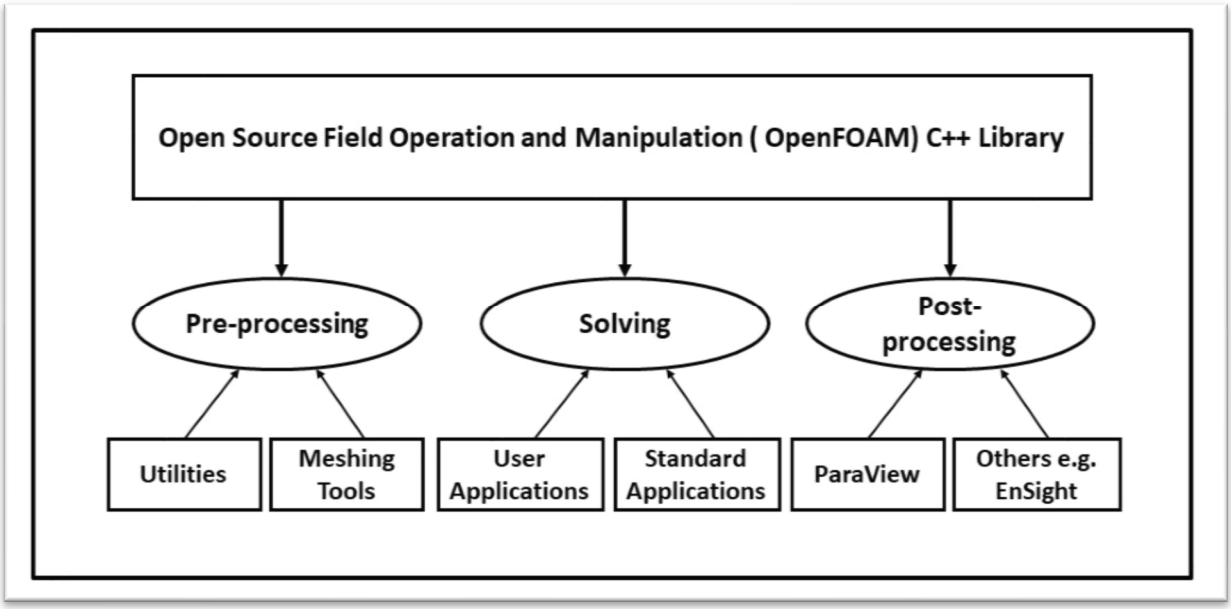

Figure 3.16. OpenFOAM structural overview.

3.7.6.2. Simulation of The Study Cases

To simulate the study cases in OpenFOAM 2.3.x, some of the OpenFOAM 2.3.x dictionaries need to be modified to meet the conditions of system distributors real cases. However, to run one case of the system for a specific superficial air velocity in the normal 5 cores computer for a 0.01 sec time step, a normal computer needs almost 6 hours to finish one-time step. Thus, 4800 working hours are needed to simulate just 8 seconds of one case with one specific superficial air velocity. Therefore, using the High-Performance Computing (HPC) cluster (RAVEN) of the Cardiff University with 2048 cores was the best choice to do the simulation for the all cases to reduce the computation time.

3.8. Post – Gasification Microwave Improvements

Biomass gasification produces a product gas with different compositions. This mainly depends on the biomass type and gasification mechanisms. However, this product gas can be improved to syngas with low greenhouse gases and high hydrogen and carbon monoxide yields.

However, in this part of the thesis the already dynamically improved BFBG was having further improvement. This modification starts after the gasification stage ended in which even more syngas would be generated from the greenhouse gases of the BFBG products. The activity of this process and power requirements were studied by using a kinetically simulation model via ASPEN PLUS® software (Plus, 2009).

To understand the improvement mechanism in the product gas, the kinetics of the most possible reactions should be explained.

3.8.1. Reaction Kinetics

The study of reaction rates for chemical processes in different environments and conditions is called chemical reaction kinetics. There are two main goals for which the study of chemical reaction kinetics is carried out (Vallance, 2018):

1- Study the reaction mechanism: Analyse the elementary step sequences bringing over the overall reaction.
2- Calculate the absolute rate for the overall reaction or for individual elementary steps or for both.

3.8.1.1. Reaction Rate of Methane Reforming

In chemical reactions, the rate at which the reactants are consumed (or products materials are forming) is called the reaction rate. The reaction rate for methane reforming in the presence of a metallic catalyst material has been studied widely in different temperatures and

catalyst loading (Lewis et al., 1949, Bodrov and Apel'baum, 1967, Richardson and Paripatyadar, 1990, Mark and Maier, 1996, Abbas et al., 2017, Zhang et al., 2008)**.**

3.8.1.2. Power law model

The rate of a reaction related to the chemical species concentrations present in the reaction is called rate law or power law. The general form of the power law is (Muller, 1994):

$$r = k \cdot [A]^a \cdot [B]^b \cdot [C]^c \cdot [D]^d \quad \text{..... 3-35}$$

Where:

[A], [B], [C], and [D] – are the concentrations or partial pressure of the species in the reaction (species may contain reactants, products, and catalysts).

a, b, c, and d – are the partial orders of reaction for the species (A, B, C, and D) respectively and the sum of all these exponents is the overall reaction order. However, the value of the exponents (a, b, c, and d) may vary for different catalysts.

k – is the rate constant of the reaction (or reaction rate coefficient) and it depends on temperature, ionic strength, the surface area of an adsorbent, or light irradiation. The value of the rate constant (*k*) can be calculated by Arrhenius equation (Arrhenius, 1889):

$$k = A \cdot e^{-\frac{E_a}{RT}} \quad \text{..... 3-36}$$

Where:

A - is the pre-exponential factor and it is constant for each reaction.

E_a – is the activation energy for the reaction ($J \cdot mol^{-1}$).

R – is the universal gas constant ($R = 8.314\, J \cdot K^{-1} \cdot mol^{-1}$).

Hence, the reaction rate for dry reforming of methane according to the power law can be written as (Zhang et al., 2008):

$$r_{DRM} = k \cdot P_{CH4}^{x} \cdot P_{CO2}^{y} \quad \text{..... 3-37}$$

Where:

P_{CH4}, P_{CO2} – are the partial pressure of CH_4 and CO_2 respectively.

x, y – are the partial orders of CH_4 and CO_2 in the DRM reaction for the specific catalyst. The empirical value of x and y for DRM with different nickel-based catalysts for some different references are shown in the table 3-7.

Table 3-7. Empirical power law indices for different nickel-based catalysts.

Reference	Catalyst	*x* (CH_4)	*y* (CO_2)	Notes
(Osaki et al., 1997)	Ni/SiO_2	- 0.3	0.16	
(Bradford and Vannice, 1996)	Ni/MgO^{*} Ni/TiO_2^{**} Ni/SiO_2^{***} Ni/C^{***}	0.52 – 1.22±0.18 0.13 – 1.76 0.18 – 0.49 0.33 – 1.03	- 0.54±0.06 – 0.36 -0.61 – 1.55 0.11 – 0.64 -0.05 – 0.77	Temperature: *773K-823K **673K-723K ***723K
(Zhang et al., 2008)	Ni-Co/Al-Mg-O	0.483	0.291	
(Özkara-Aydınoğlu and Aksoylu, 2013)	Pt – Ni/Al_2O_3	1.0† 1.09††	0.87† 1.40††	† 0.3Pt – 10Ni †† 0.2Pt – 15Ni

3.8.1.3. Langmuir Hinshelwood Hougen Watson (LHHW) Model

The LHHW kinetic model for heterogeneous catalysis was proposed by (Hougen and Watson, 1943). The reaction rate expression according to this model consists of three terms that have been represented in the following equation:

$$r = \text{Kinetic factor term} \frac{\text{Driving force term}}{\text{Adsorption term}} \quad \text{..... 3-38}$$

1- The kinetic factor term which represents the surface reaction of the reactants to produce the products. This term is calculated by the equation:

$$\text{Kinetic factor} = k\left(\frac{T}{T_o}\right)^n \cdot e^{-\left[\frac{E_a}{R}\left(\frac{1}{T}-\frac{1}{T_o}\right)\right]} \quad \text{3-39}$$

Or

$$\text{Kinetic factor} = k \cdot e^{-\left[\frac{E_a}{RT}\right]} \quad \text{3-40}$$

Where T and T_o are the reaction temperature and the reference temperature respectively. The equation 3-40 is used when the reference temperature, T_o is not specified.

2- The driving force term represents the desorption of the products from the catalyst surface to the surrounding environment, which is proportional directly to the reaction overall rate. The driving force term can be expressed by the equation:

$$\text{Driving force expression} = k_1 \cdot \sum_{i=1}^{N} C_i^{x_i} - k_2 \cdot \sum_{j=1}^{M} C_j^{y_j} \quad \text{3-41}$$

Where:

k_1, k_2 – The driving force rate constants for reactants and products respectively.

C_i, C_j – The concentration of reactants and products species for the reaction.

x_i, y_j – The reaction order reactants and products species respectively.

3- The adsorption expression represents the adsorption of reactants to the catalyst surface, which is proportionally indirect to the overall rate of the reaction. The adsorption expression can be written as:

$$\text{Adsorption expression} = \left[\sum_{i=1}^{N} k_i \left(\prod_{j=1}^{M} C_j^{v_j}\right)\right]^m \quad \text{3-42}$$

The equilibrium constants k_i for the driving force and adsorption terms can be evaluated by the following equation:

$$\ln(k) = A + \frac{B}{T} + C \cdot \ln(T) + D \cdot T \quad \text{3-43}$$

The parameters A, B, C, and D in equation 3-43 are experimental values.

3.8.2. Case Study

The optimum product gas from the gasification of olive kernel biomass in the experimental bubbling fluidised bed gasifier has been used in this modification process. The composition of this product gas is shown in table (3-8), previously obtained by others (Al-Farraji, 2017).

Table 3-8. Optimum product gas composition of olive kernel gasification in BFBG (Al-Farraji, 2017).

Product components	CH_4	CO_2	CO	H_2
State	gas	gas	gas	gas
Mole fraction	0.1385	0.3037	0.4008	0.1570

3.8.3. Aspen Plus® Simulation

Aspen Plus® is a market-leading process modelling tool for conceptual design, optimization, and performance monitoring for the chemical, polymer, speciality chemical, metals, minerals, and coal power industries (Plus, 2009). The comparison between the real process and ASPEN PLUS® simulation principles are shown in figure 3.17. This simulation can help in several aspects such as reducing the design time and improving the current process.

By using Aspen Plus for the post- gasification process, the CH_4 and CO_2 conversion, H_2 and CO yields and reaction heat duty for different reaction temperatures can be predicted.

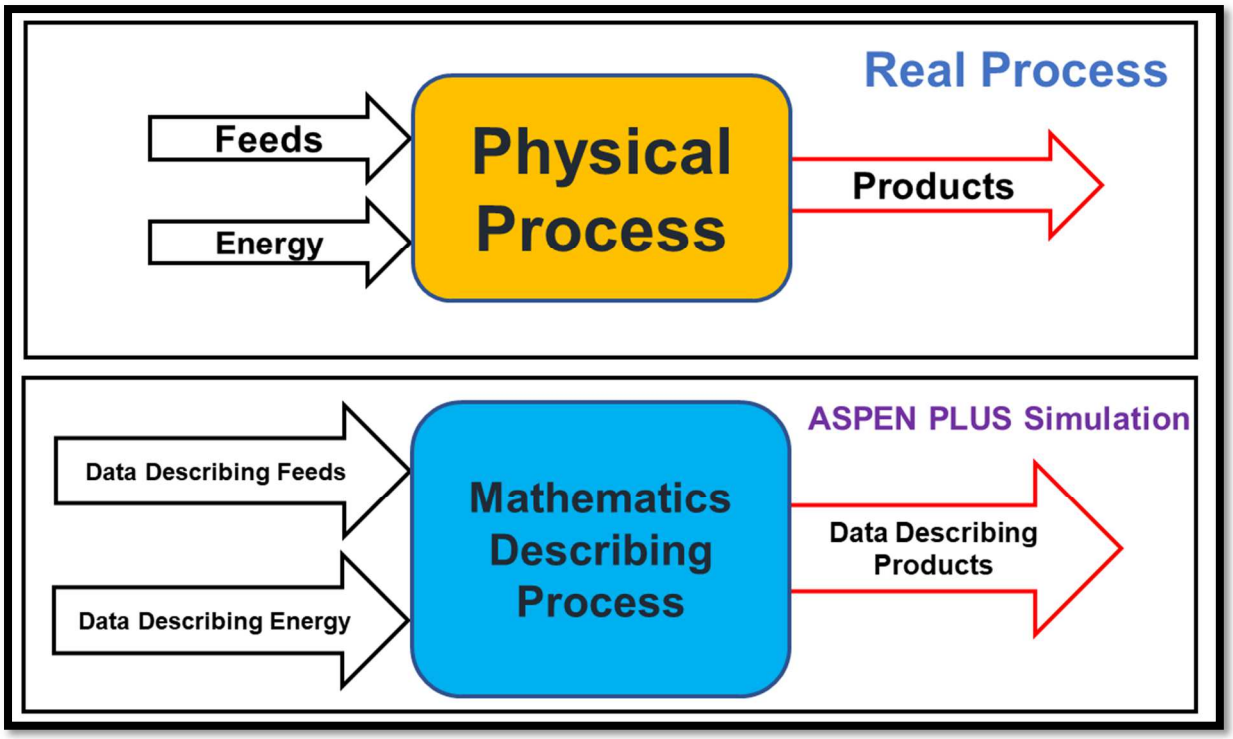

Figure 3.17. The real and ASPEN PLUS® simulation principles.

The reactions of methane through reforming has been assumed to be the dominated controller in the Aspen Plus model. The combined reforming of methane consists of the following main reactions (Park et al., 2014):

1- Dry reforming of methane reaction (DRM):

$$CH_4 + CO_2 \leftrightarrow 2CO + 2H_2 \quad \text{3-44}$$

2- First order steam reforming of methane reaction (SRM1):

$$CH_4 + H_2O \leftrightarrow CO + 3H_2 \quad \text{3-45}$$

3- Second order steam reforming of methane reaction (SRM2):

$$CH_4 + 2H_2O \leftrightarrow CO_2 + 4H_2 \quad \text{3-46}$$

4- Water gas shift reaction (WGS):

$$CO + H_2O \leftrightarrow H_2 + CO_2 \quad \text{3-47}$$

These reactions have the following reaction rates:

$$r_{DRM} = \frac{k_{DRM}\left(P_{CH_4}\cdot P_{CO_2} - {P_{H_2}^2\cdot P_{CO}^2}/{K_{pDRM}}\right)}{\left(1+K_{CH_4}\cdot P_{CH_4}+K_{CO}\cdot P_{CO}\right)\left(1+K_{CO_2}\cdot P_{CO_2}\right)} \quad \text{3-48}$$

$$r_{SRM1} = \frac{k_{SRM1}\left(P_{CH_4}\cdot P_{H_2O} - {P_{H_2}^3\cdot P_{CO}}/{K_{pSRM1}}\right)\Big/ P_{H_2}^{5/2}}{\left(1+K_{CH_4}\cdot P_{CH_4}+K_{CO}\cdot P_{CO}+K_{H_2}\cdot P_{H_2}+K_{H_2O}.{P_{H_2O}}/{P_{H_2}}\right)^2} \quad \text{3-49}$$

$$r_{SRM2} = \frac{k_{SRM2}\left(P_{CH_4}\cdot P_{H_2O}^2 - {P_{H_2}^4\cdot P_{CO}}/{K_{pSRM2}}\right)\Big/ P_{H_2}^{7/2}}{\left(1+K_{CH_4}\cdot P_{CH_4}+K_{CO}\cdot P_{CO}+K_{H_2}\cdot P_{H_2}+K_{H_2O}.{P_{H_2O}}/{P_{H_2}}\right)^2} \quad \text{3-50}$$

$$r_{WGS} = \frac{k_{WGS}\left(P_{CO}\cdot P_{H_2O} - {P_{H_2}\cdot P_{CO_2}}/{K_{pWGS}}\right)\Big/ P_{H_2}}{\left(1+K_{CH_4}\cdot P_{CH_4}+K_{CO}\cdot P_{CO}+K_{H_2}\cdot P_{H_2}+K_{H_2O}.{P_{H_2O}}/{P_{H_2}}\right)^2} \quad \text{3-51}$$

Where:

k_i – The reaction rate constant for species i.

K_i – The adsorption equilibrium constant for species i.

K_p – The reaction equilibrium constant.

P_i – The partial pressure of species i.

The kinetic parameters of the proposed methane combined reforming reactions are listed in table 3-9.

Table 3-9. CRM reactions kinetic parameters.

Parameter	Equation	Units	Reference
k_{DRM}	$2.91 \times 10^{-7} e^{\left[\frac{-234.851}{R}\left(\frac{1}{T}-\frac{1}{T_o}\right)\right]}$	$mole \cdot g_{cat}^{-1} \cdot h^{-1} \cdot Pa^{-2}$	(Park et al., 2014)
k_{SRM1}	$4.72 \times 10^{6} e^{\left[\frac{-232.477}{R}\left(\frac{1}{T}-\frac{1}{T_o}\right)\right]}$	$mole \cdot Pa^{0.5} . g_{cat}^{-1} \cdot h^{-1}$	(Park et al., 2014)
k_{SRM2}	$1.89 \times 10^{3} e^{\left[\frac{-267.76}{R}\left(\frac{1}{T}-\frac{1}{T_o}\right)\right]}$	$mole \cdot Pa^{0.5} . g_{cat}^{-1} \cdot h^{-1}$	(Park et al., 2014)
k_{WGS}	$1.06 \times 10^{-3} e^{\left[\frac{-71.537}{R}\left(\frac{1}{T}-\frac{1}{T_o}\right)\right]}$	$mole \cdot g_{cat}^{-1} \cdot h^{-1} \cdot Pa^{-1}$	(Park et al., 2014)
K_{CO_2}	$5.97 \times 10^{-7} e^{\left[\frac{52670}{RT}\right]}$	Pa^{-1}	(Park et al., 2014)
K_{CO}	$8.23 \times 10^{-10} e^{\left[\frac{70650}{RT}\right]}$	Pa^{-1}	(Xu and Froment, 1989)
K_{H_2}	$6.12 \times 10^{-14} e^{\left[\frac{82900}{RT}\right]}$	Pa^{-1}	(Park et al., 2014)
K_{CH_4}	$6.65 \times 10^{-9} e^{\left[\frac{38280}{RT}\right]}$	Pa^{-1}	(Park et al., 2014)
K_{H_2O}	$1.77 \times 10^{5} e^{\left[\frac{-88680}{RT}\right]}$	-	(Park et al., 2014)
K_{pSMR1}	$e^{\left(2.48-\frac{22920.6}{T}+7.19\times \ln T-2.95\times 10^{-3}\cdot T\right)}$	Pa^2	(Park et al., 2014)
K_{pWGS}	$e^{\left(-12.11-\frac{5318.69}{T}+1.01\times \ln T+1.14\times 10^{-4}\cdot T\right)}$	-	(Park et al., 2014)
K_{pDRM}	K_{pSMR1} / K_{pWGS}	Pa^2	(Park et al., 2014)
K_{pSMR2}	$K_{pSMR1} \times K_{pWGS}$	Pa^2	(Park et al., 2014)

Where: T_o – The reference temperature (K) and R – The universal gas constant (kJ/kmol·K).

A 9 mm ϕ x 40 mm length plug flow reactor PFR (as shown in figure 3.18) was used in this simulation. The BFBG product gas flow rate in the reactor was set to be (100 ml/min) at an inlet temperature of 293 K and a pressure of 1 atm. The 10% Ni/90%Al_2O_3 was used as a catalytic material in this process. The Aspen Plus® calculations were done for reaction temperature ranges from 773 K to 1273 K for different catalyst loading from 2.5 mg_{cat}.min/ml to 10 mg_{cat}.min/ml.

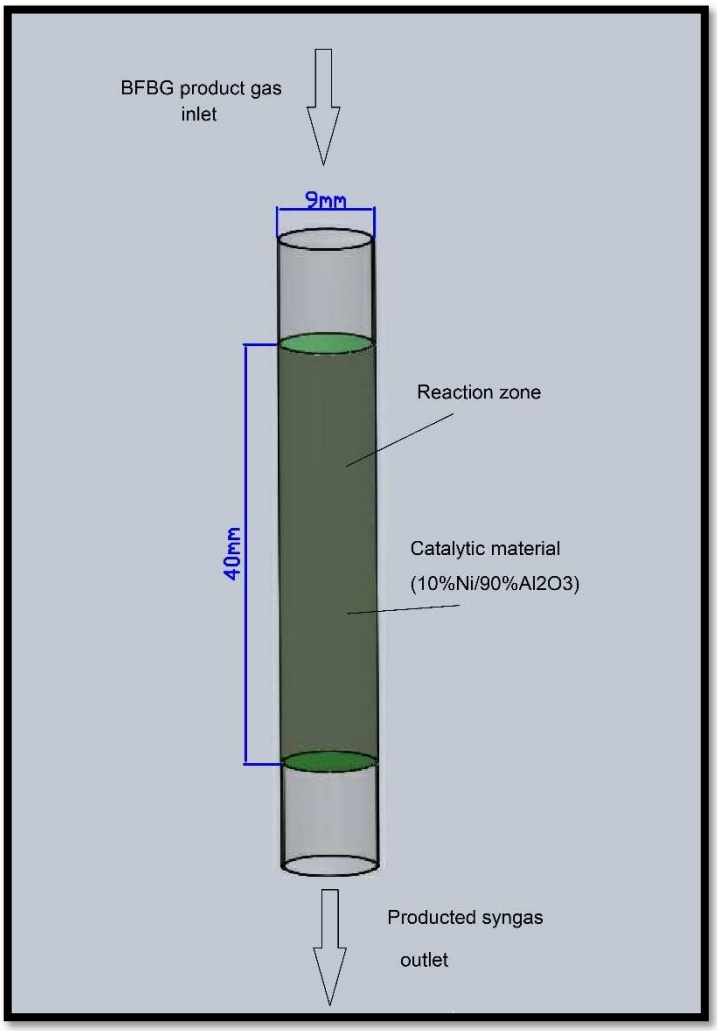

Figure 3.18. The plug flow reactor used in Aspen plus simulation.

Chapter Four: Experimental Study of BFBG Hydrodynamics

4.1. Introduction

This chapter focuses on the hydrodynamic behaviour of the isothermal BFBG with four perforated distributor types, will be studied in depth experimentally and later under three-dimensional CFD simulations (chapter five).

4.2. Rig Description

A bespoke experimental rig was built at Cardiff School of Engineering combustion lab and it is shown in figure 4.1. Four perforated distributors, shown in figure 4.2, were used to study the flows inside the rig. Compressed air was injected into the system at different flow rates controlled by a gate valve and regulated by a digital gas flowmeter. When the compressed air passes through the distributor holes toward the packed sand bed, the sand particles will move throughout the BFBG free space forming a fluidised bed environment. The size of bed expansion depends mainly on the distributor type and the air flow rate. The height of the sand particles as a packed bed before fluidisation was 60 mm as shown in figure 4.3.

The size of air bubbles and their movements inside the BFBG with the different distributor was examined by using a Photron (FASTCAM-APX RS) High-Speed Video Camera shown in figure 3.4 in chapter 3. The frame rate used in this process is 125 fps for all cases. The measured bubble size and velocity were then compared with the bubble size and velocity predicted by OpenFOAM simulation (chapter five). The bubble size and movement have been measured by using the image processing and analysis in Java software, ImajeJ (NIH, 2018).

The aim of building this rig was to study the effect of the perforated distributor orifice size (2mmϕ and 1mmϕ), the distance between orifices (7.5mm and 6.35mm) and the orifices

arrangement (square or triangular) on the hydrodynamic behaviour of the BFBG. This study can improve the performance of the bubbling fluidised bed gasifier by choosing the right distributor that provides uniform fluidised bed inside the gasifier.

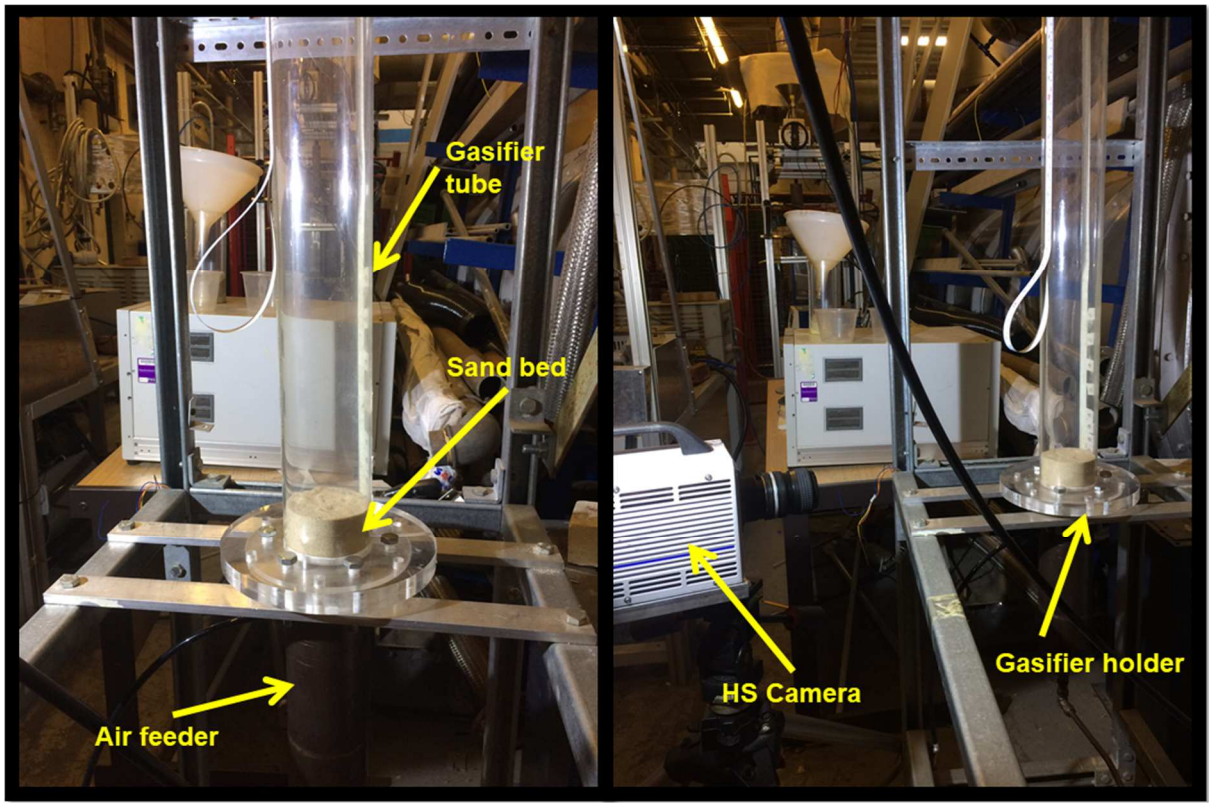

Figure 4.1. The prototype isothermal BFBG.

4.3. Pressure Distribution in BFBG

The pressure drop in the BFBG inside wall was measured in five different positions along the BFBG as shown in figure 4.3. The five positions are located at 10 mm, 40 mm, 60 mm, 80 mm and 100 mm above the perforated distributor. The average pressure reading was taken for each position and flow rate. The pressure drop was measured by the digital gas pressure meter model (Digitron PM-20) as mentioned in chapter three. This pressure meter has two ports with two hoses, the right hose for the datum level and the left hose for the position in which pressure drop to be measured as shown in figure 4.3. This procedure was done for all positions and repeated three times for each position to make sure it is the right reading.

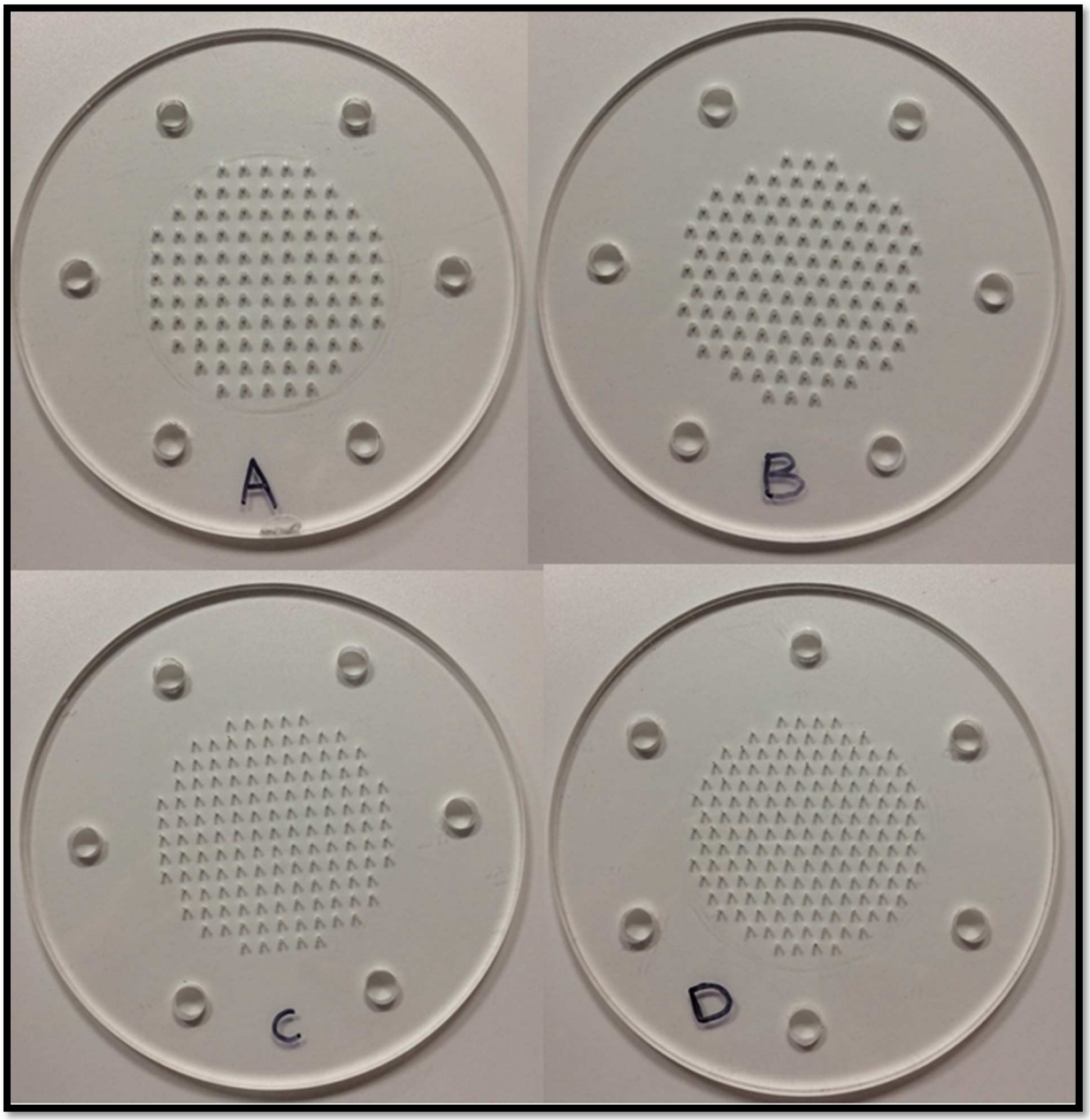

Figure 4.2. The four case study perforated distributors :

Type (A) distributor – 2mmϕ & 7.5mm square pitch.

Type (B) distributor – 2mmϕ & 7.5mm triangular pitch.

Type (C) distributor – 1mmϕ & 6.35mm square pitch.

Type (D) distributor – 1mm ϕ & 6.35mm triangular pitch.

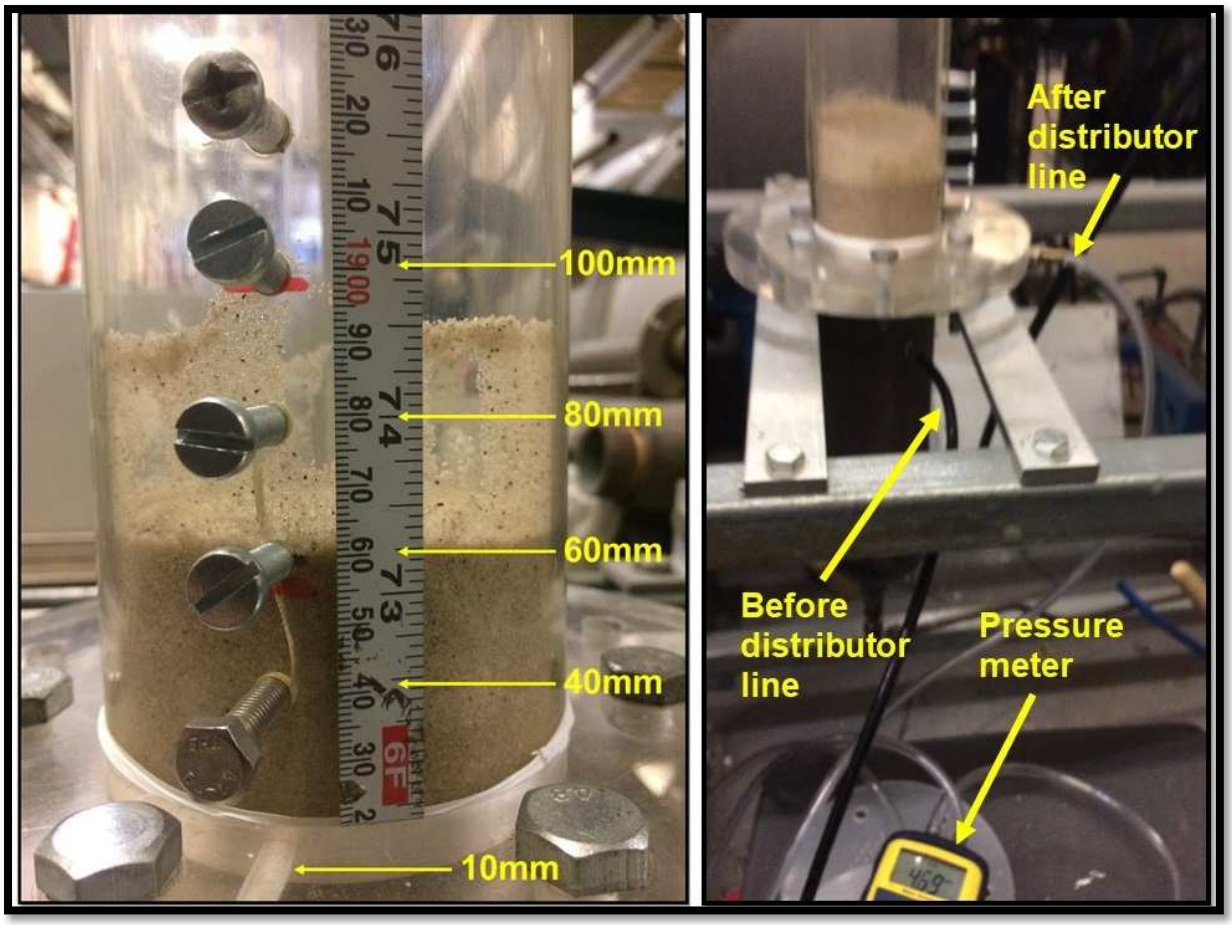

Figure 4.3. Pressure measurement positions in the BFBG prototype.

4.4. Pressure Drop Results

4.4.1. Pressure Drop at 10 mm Level

In figure 4.4 the variation of pressure drop at different air flow rates for the four distributor types in the 10 mm level is illustrated. In all cases, the pressure drop increases linearly with the air flow rate until the minimum fluidisation flow rate (minimum fluidisation velocity, U_{mf}). Beyond this flow rate the pressure drop increases only marginally. This is due to the sand bed transition from a packed condition to a fluidised condition (Kunii and Levenspiel, 1991).

The minimum fluidisation flow rates for the four distributors are between 76 to 94 SLPM and the minimum fluidisation velocities are between 23.4 to 28.9 cm/sec.

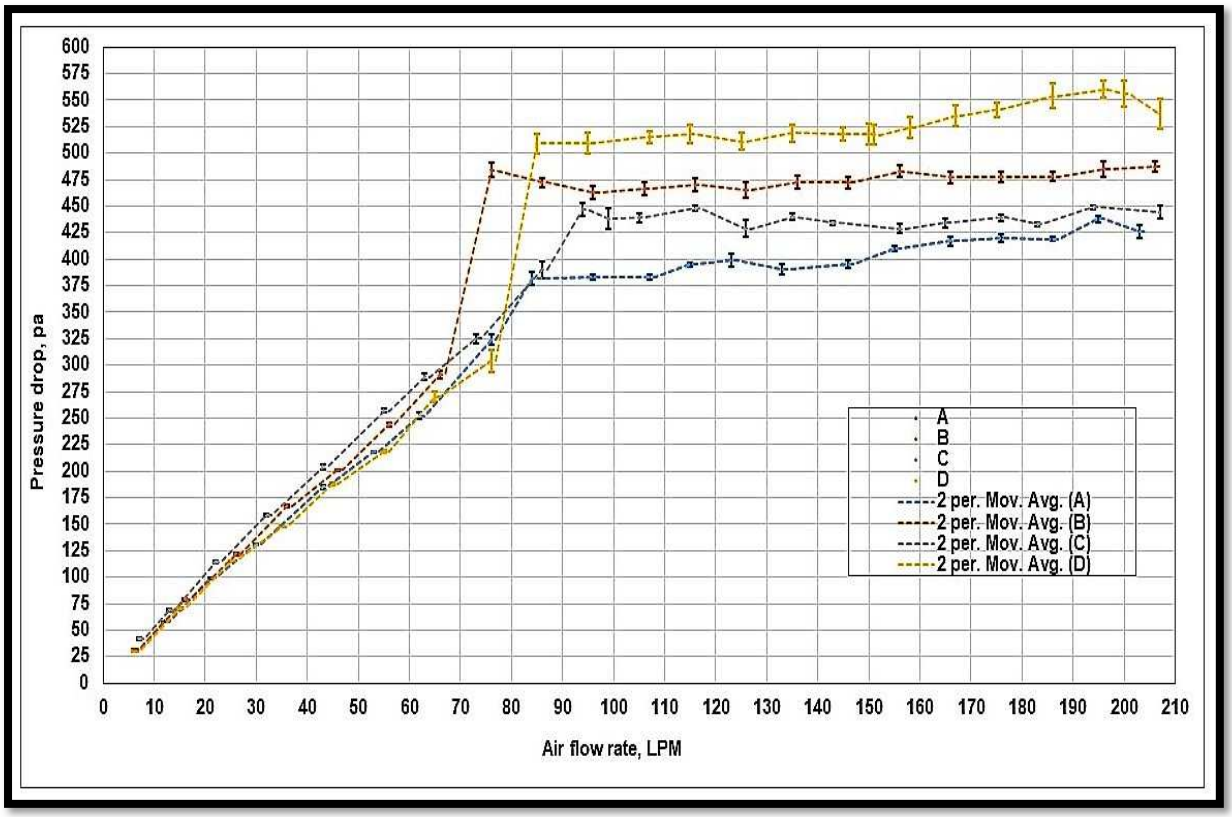

Figure 4.4. The pressure drop variation at 10 mm height level in the isothermal BFBG with the four perforated distributor types A, B, C and D.

The fluidisation velocity in the isothermal BFBG with triangular arrangement distributors B and D showed experimentally lower minimum fluidisation air flow rates than the BFBG with square arrangement distributors A and C by 10.5% and 10.6% respectively.

Regarding the pressure drop, the type D distributor produced the highest pressure drop in the fluidised bed stage, while the lowest pressure drop was observed with the A distributor. However, the second largest pressure drop is observed with the type B distributor, this means that triangular arrangement distributors provide a larger pressure drop in the fluidised bed stage than the square arrangement distributors. This maybe due to the better distributon of air at this position provided by the triangular distributors as they have a larger number of holes per unit area than the square arrangement distributors.

4.4.2. Pressure Drop at 40 mm Level

At the position 40 mm above the distributor, pressure drop decreased from between (370 to 560 pa) at 10 mm level to between (250 to 375 pa) for the four distributors as shown in figure 4.5. The profile of the fluidisation pressure drop at this position tends to increase linearly. This maybe due to the decrease in bed thickness above this position. The pressure drop observed with the type D distributor still has the largest values among the other distributors in this position at the fluidisation flow rates. However, the type C distributor showed the second largest while the lowest pressure drop was produced by type B. The distributor orifice size probebly has the major effect on this position as the small orifice distributor (C and D) provides the largest pressure drop comares to the large orifice distributors (A and B).

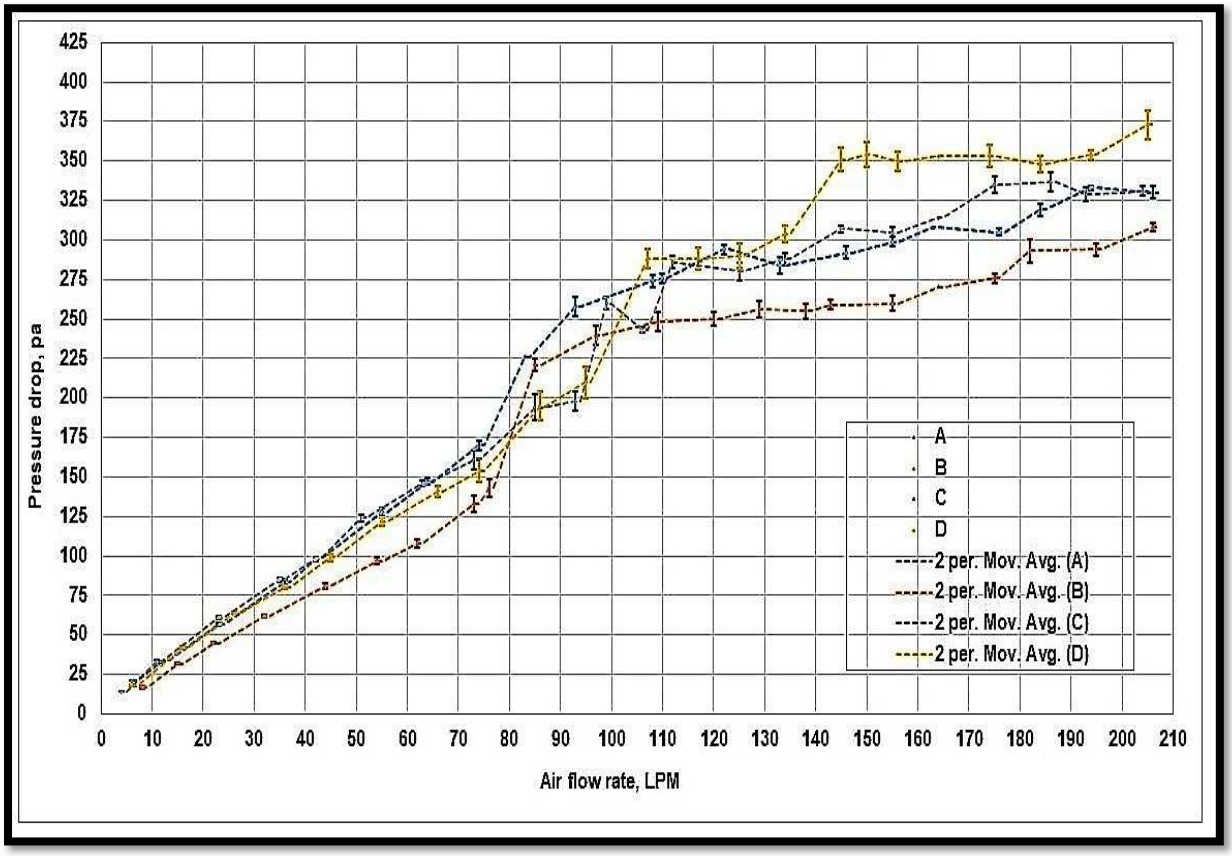

Figure 4.5. The pressure drop variation at 40 mm height level in the isothermal BFBG with the four perforated distributor types A, B, C and D.

4.4.3. Pressure Drop at 60 mm Level

At this position, the pressure drop has a further reduction than in the previous positions, as previously explained. However, the type D distributor has the greatest pressure drop throughout all distributors and flowrates. Type C distributor followed, figure 4.6. Type A and B distributors have produced the lowest pressure drop in this position. This was caused by the low sand particles column above this point especially above the minimum fluidisation velocity. The effect of distributor orifice size in this position was greater than the effect of orifice distribution (square or triangular).

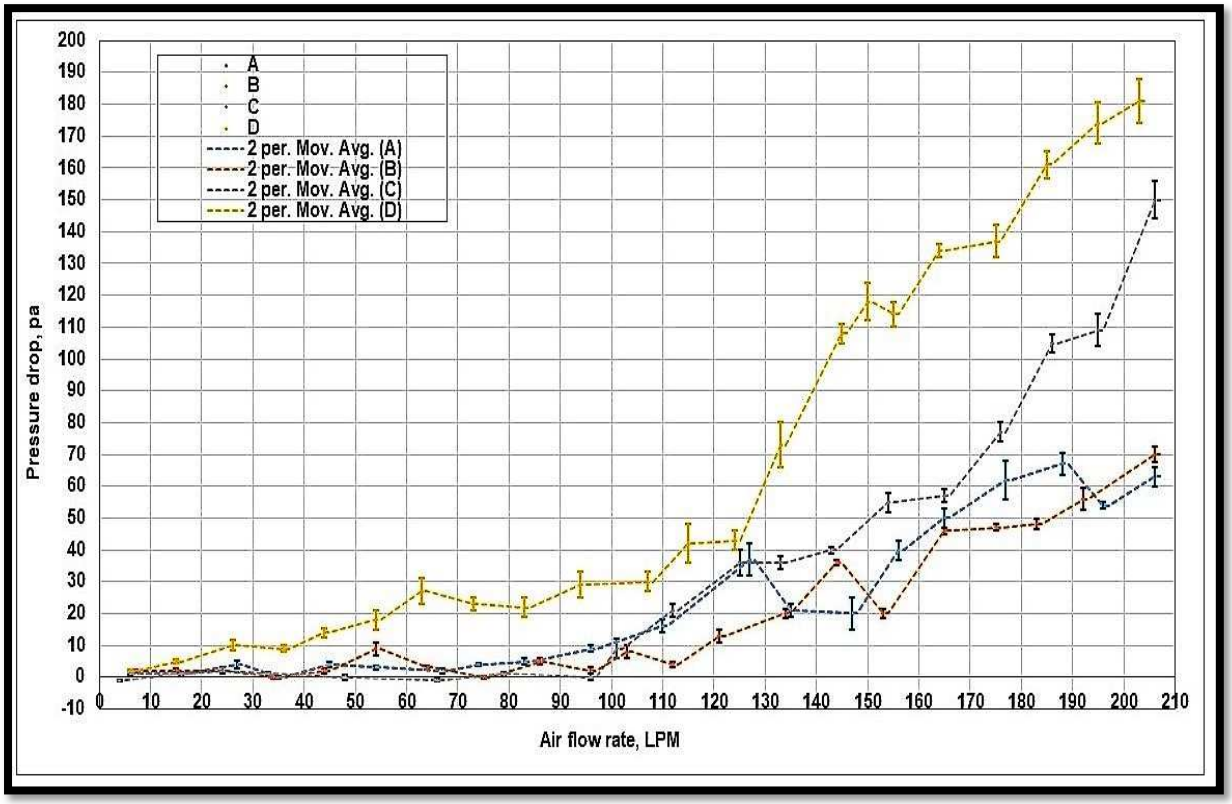

Figure 4.6. The pressure drop variation at 60 mm height level in the isothermal BFBG with the four perforated distributor types A, B, C and D.

4.4.4. Pressure Drop at 80 mm Level

The packed bed height of the sand bed in the BFBG was 60 mm as illustrated in figure 4.3. The increase in bed height above the packed bed level (60 mm) represents the fluidised bed expansion. The 80 mm level port is located in the fluidised bed expansion

zone and the pressure drop in this position reflects the actvity of the fuidised bed at this level. The more pressure drop at this level the more fluidised bed activity observed.

Further reduction in pressure drop can be seen at this position and type D distributor has the greatest values as previously, as demonstrated in figure 4.7. Type B distributor showed the second greatest pressure drop in the all set. This means the effects of orifice distribution in this position was greater than the orfice size effect as the distributors with triangular distrbution (D and B) have a greater effect than the square ones.

Moreover, the pressure drop has showed fluctuations under the high air flow rates. This maybe due to the low concetration of sand particles in this postion which makes the pressure readings fluctaute as the column changes consequance of the movement caused by the air bubbles and relocation of sand.

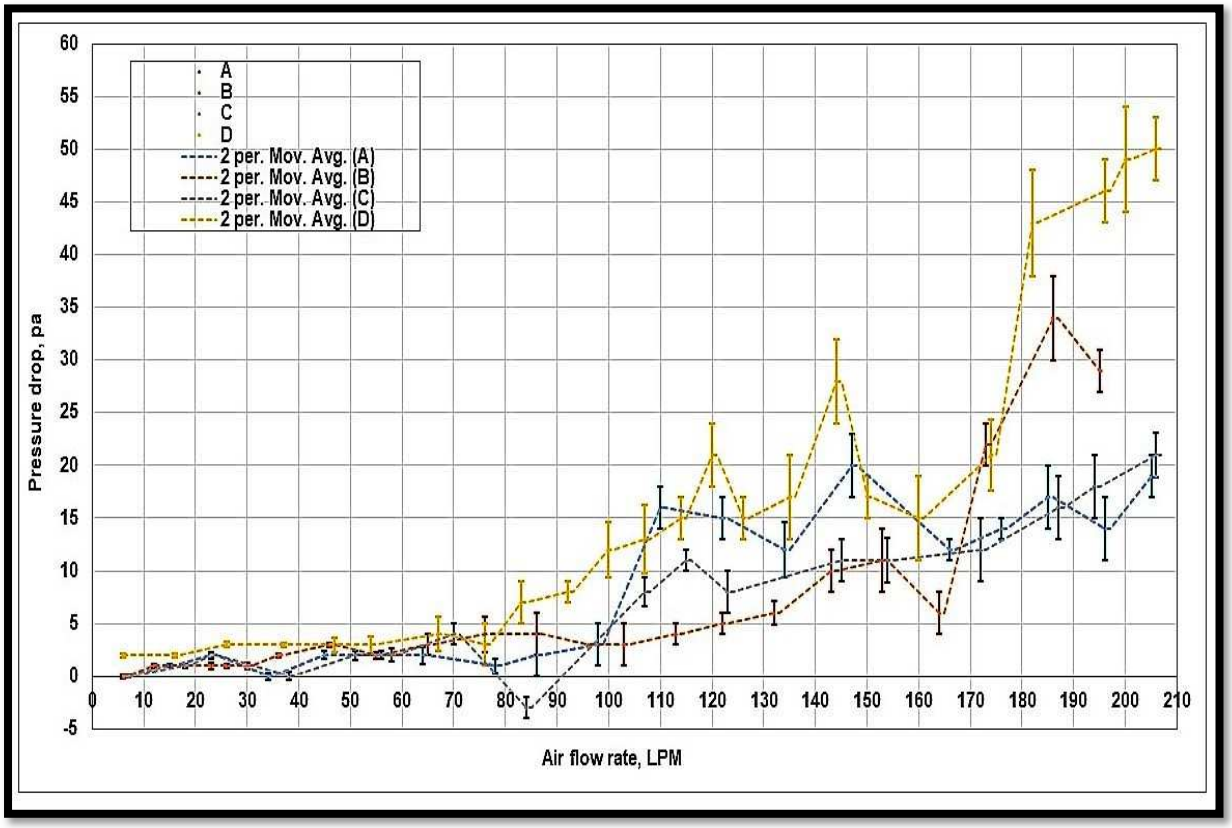

Figure 4.7. The pressure drop variation at 80 mm height level in the isothermal BFBG with the four perforated distributor types A, B, C and D.

4.4.5. Pressure Drop at 100 mm Level

The fluctuation of pressure drop was very clear at the level 100 mm above the BFBG distributor with a significant reduction among all previous positions. The type D distributor has the greatest values especially at high air flow rates, while the other distributors nearly having the same performance. Figure 4.8 shows the pressure drop at the 100 mm position for the four distributors.

The fluctuation in measured pressure together with the non zero pressure drop indicates the existance of floating sand particles (fluidised sand particles) at this level, as the sand particles are responsible for creating the pressure drop (Wang et al., 2007).

The variation of pressure drop for the five positions of each distributor (A, B, C and D) are shown in figure 4.9.

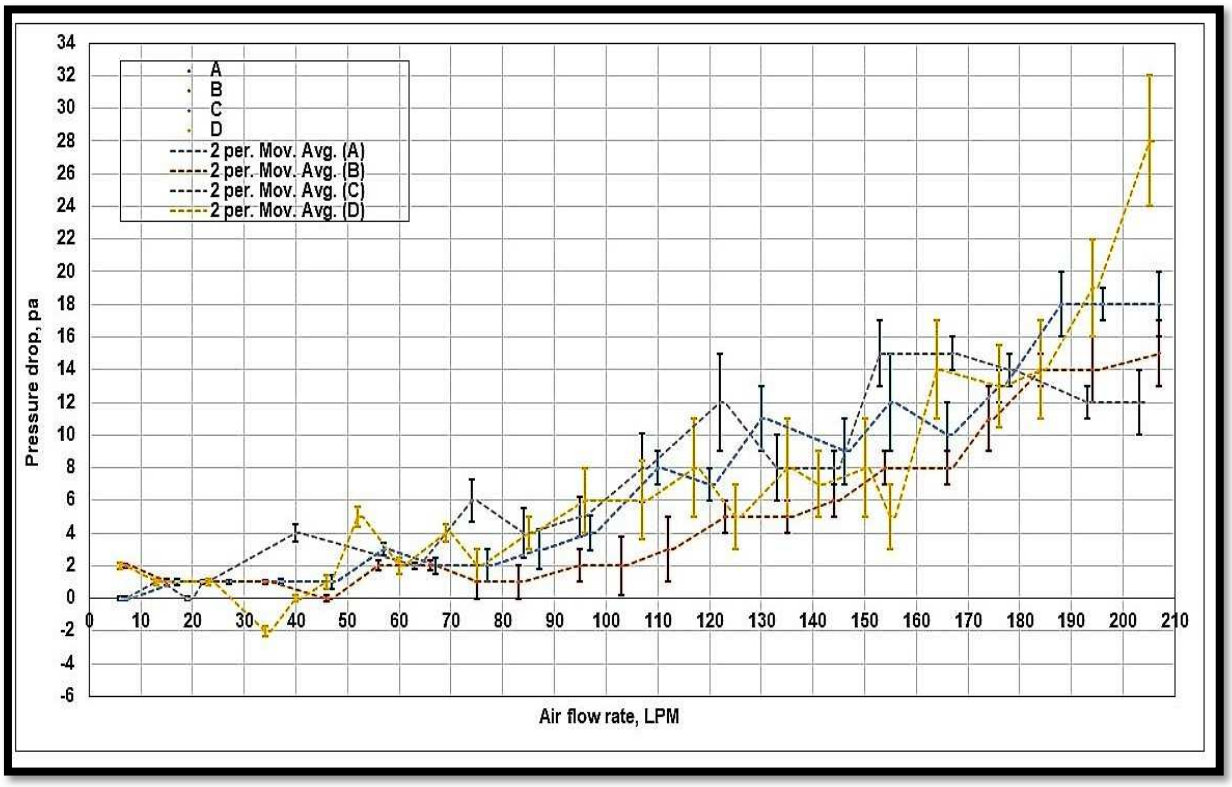

Figure 4.8. The pressure drop variation at 100 mm height level in the isothermal BFBG with the four perforated distributor types A, B, C and D.

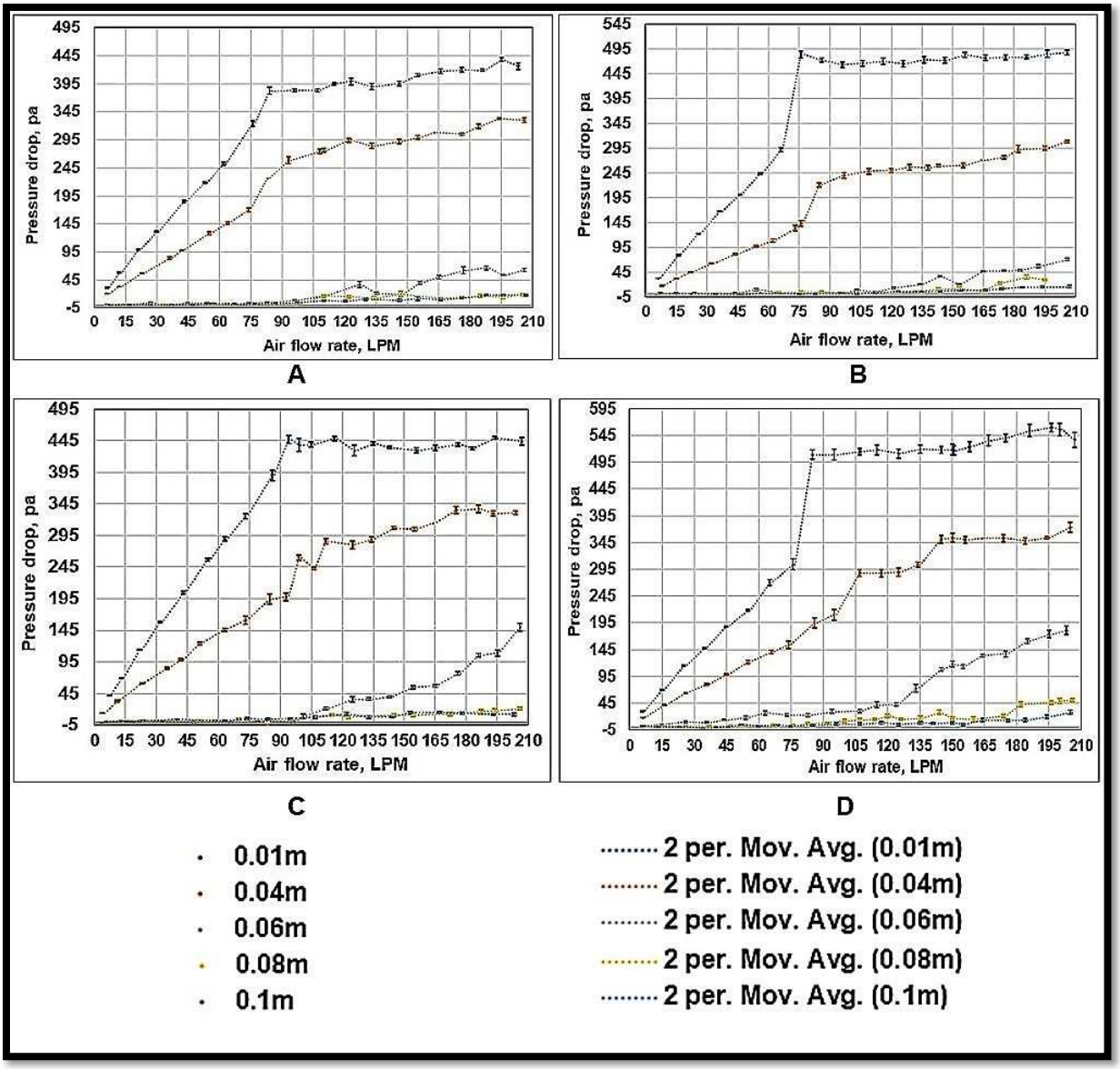

Figure 4.9. The variation of pressure drops with air flow rate in the 5 positions of each distributor (A, B, C and D).

4.5. Bubbles Size and Velocity in The BFBG

The bubble size and position were measured by using the open source software (ImageJ) by making a calbratition to the BFBG width in the images from the value in pixels to 83 mm. Then the front distances including the bubble size and the bubble height are measured accordingly. Figure 4.10 shows the BFBG width (diameter) calbration in the ImageJ software. The

measuring of bubble height starts from the upper surface of the gasifier holder shown in figure 4.10. The height of this gasifier holder is 20 mm which means adding 20 mm for each measured height.

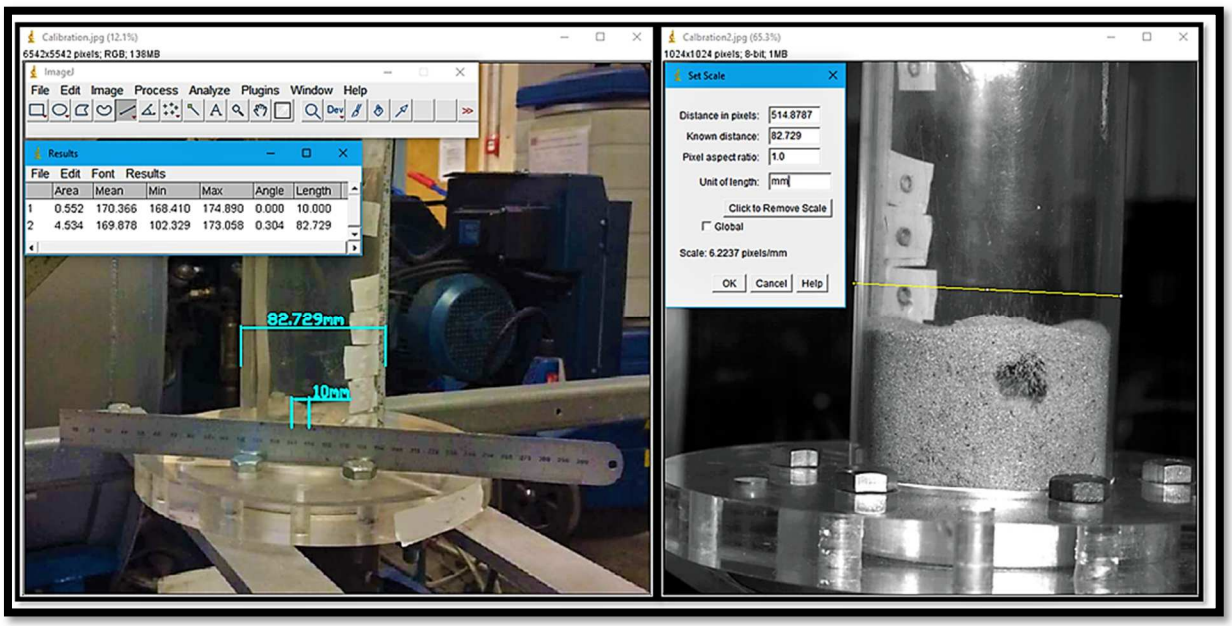

Figure 4.10. The calibration of the BFBG image dimensions in the ImageJ software.

4.5.1. Bubble Size and Movement in BFBG with Type (A) Distributor

The tracking of bubbles formation and upward movement in the BFBG with type A perforated distributor by using the high-speed camera provided a good visualisition to each case. In figure 4.11 the experimental bubble size and upward movement in the prototype BFBG with type A distributor at low superficial velocity (U = 0.33 m/s) is shown while the time variation of the upward bubble position in the same case is illustrated in figure 4.12. The bubble motion in this case followed an exponential trend rather than linear as shown in figure 4.12.

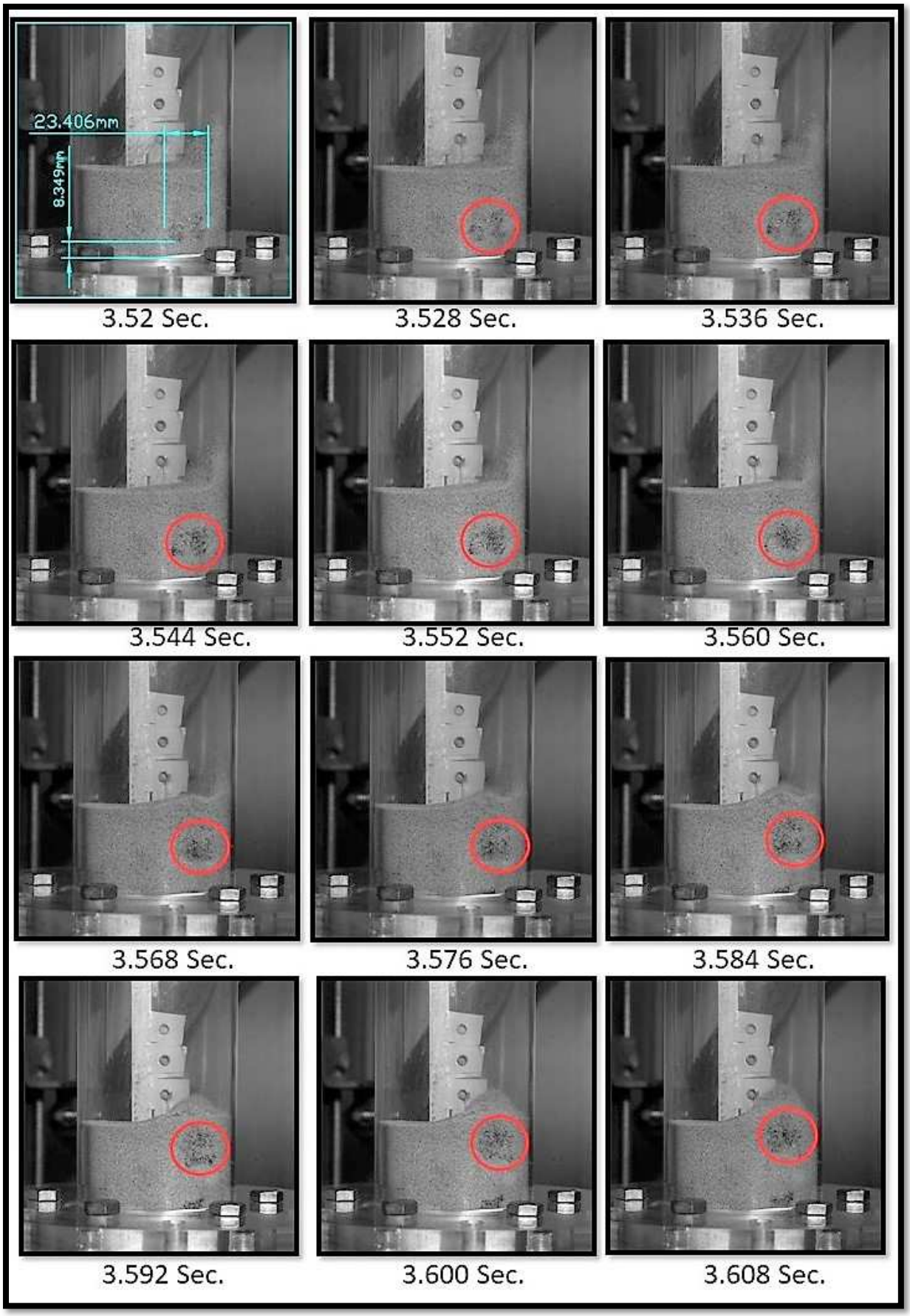

Figure 4.11. Bubble size and movement in the BFBG with type A distributor at U = 0.33 m/s.

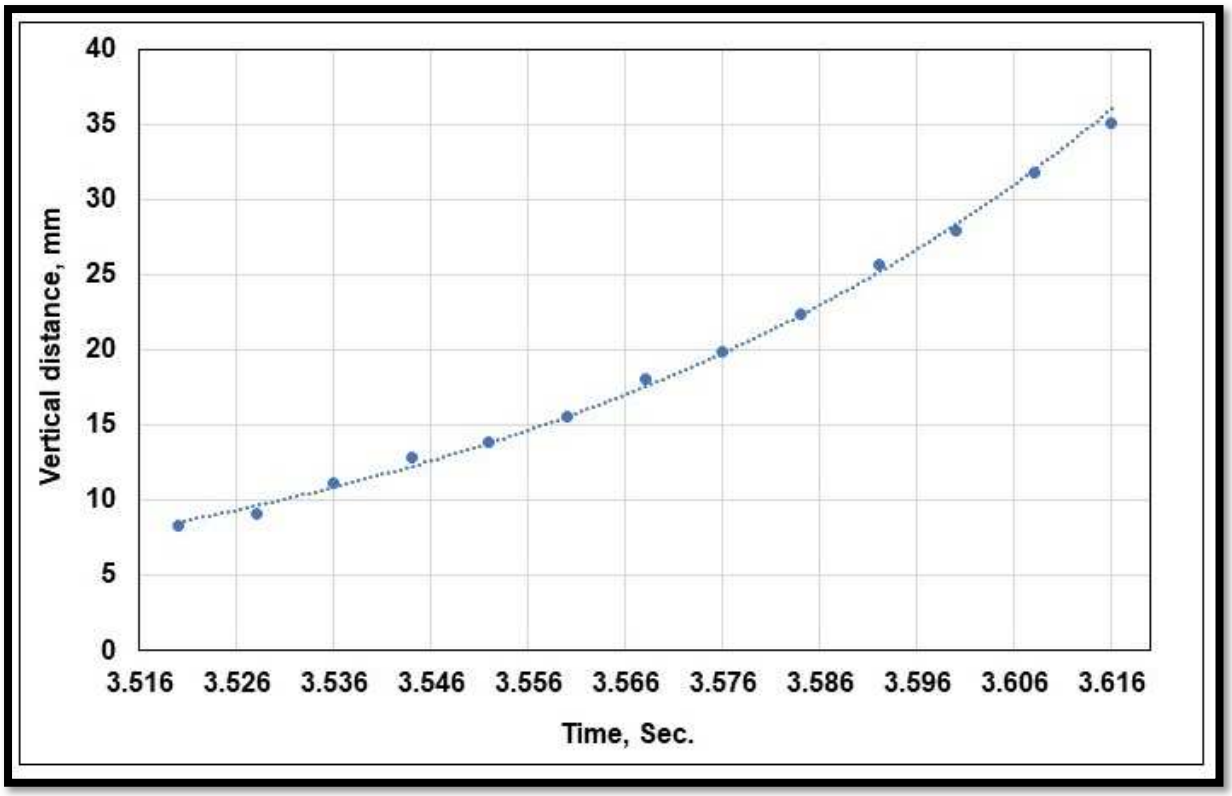

Figure 4.12. Experimental time variation of bubble movement in BFBG with type A distributor at U = 0.33 m/s.

In the high superficial velocity case (U = 0.45 m/s), the bubble was larger and faster than in the previous case as shown in figure 4.13 and 4.14 respectively. The average bubble velocity in this case is 416.6 mm/sec while it was 278.5 mm/sec in the previous case and the bubble size in the high velocity case is 42.6 mm while in the low velocity case is 23.4 mm. The bubble motion was linear in the high velocity case as shown in figure 4.14.

The expansion of the bed in the BFBG with the type A distributor was not full in both low and high velocity cases. The experiments show that only about one third of the sand bed is fluidised while the other two thirds have stayed packed with some bubbles showing up from time to time. However, at high velocity the fluidised bed covers about half of the total bed.

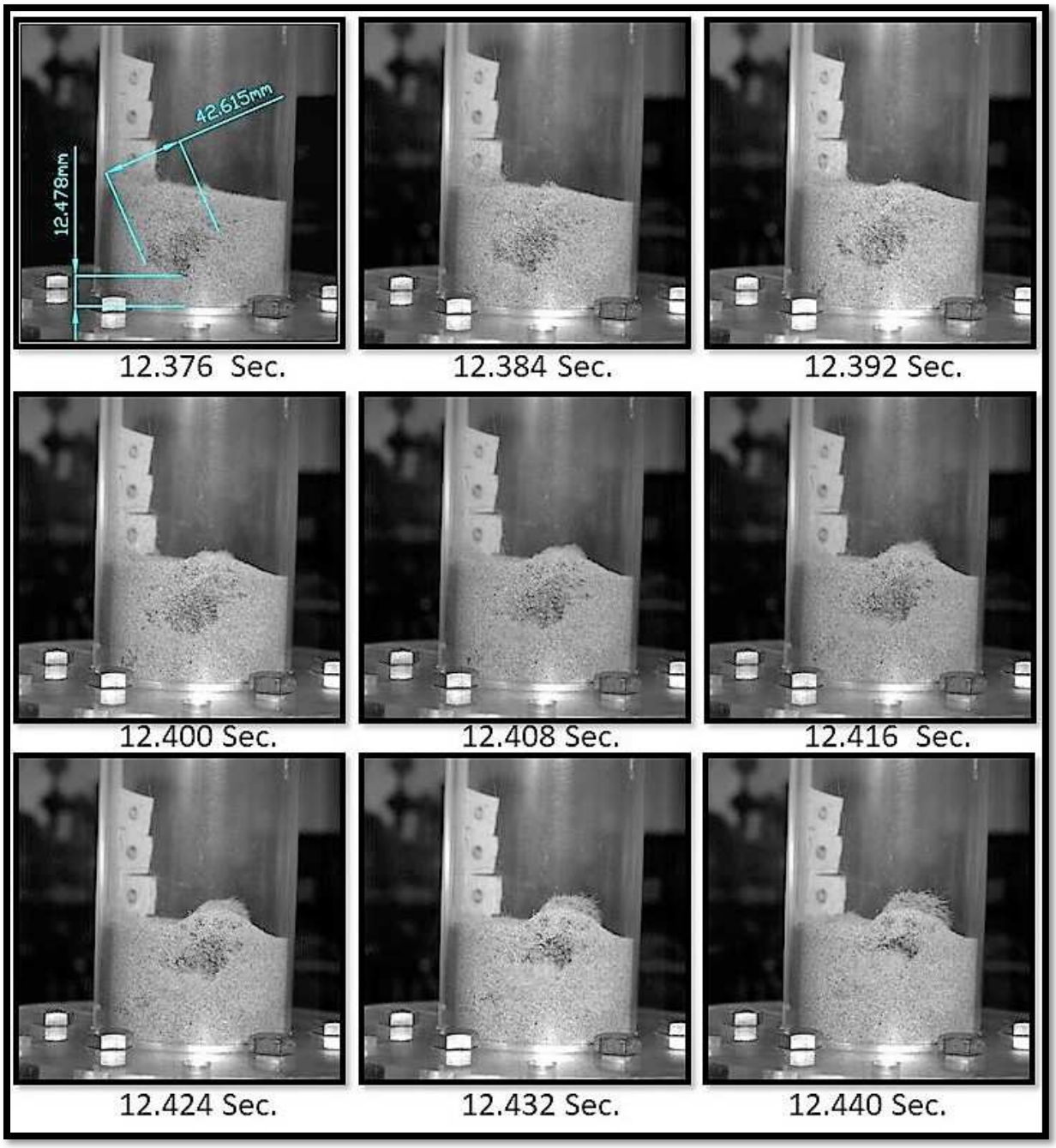

Figure 4.13. Bubble size and movement in the BFBG with type A distributor at U=0.45 m/s.

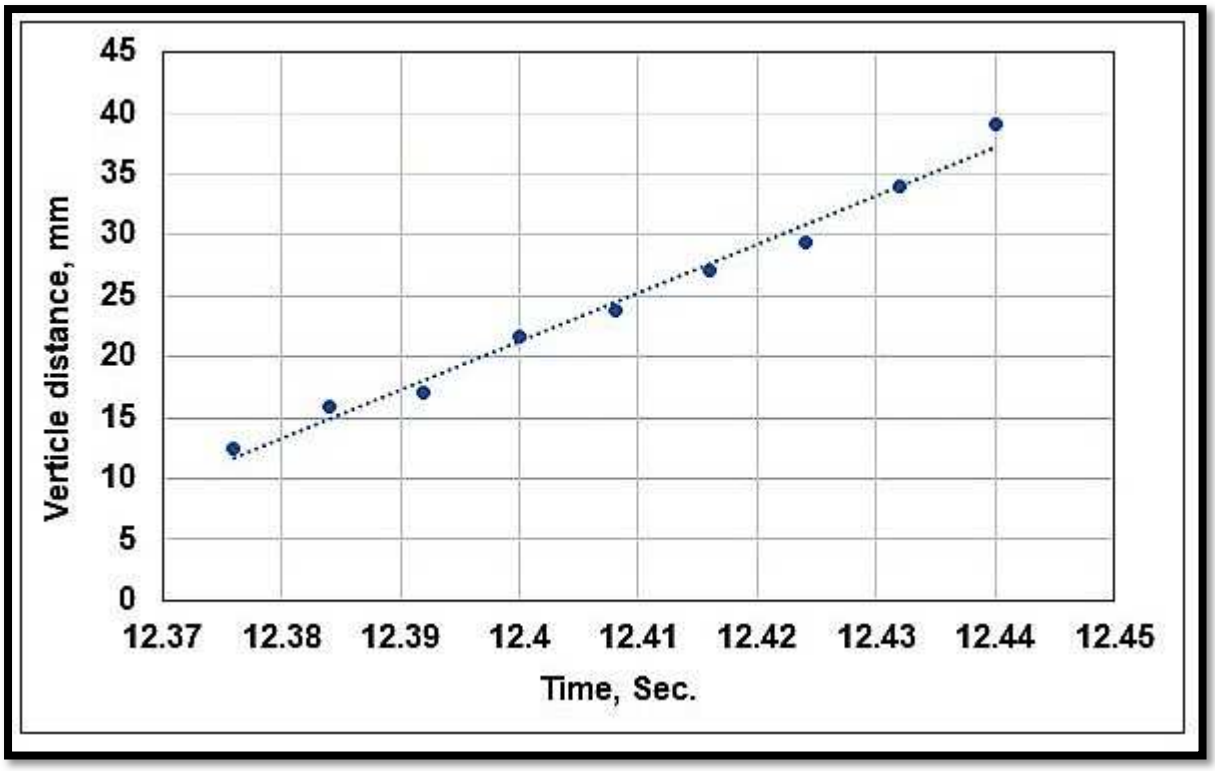

Figure 4.14. Experimental time variation of bubble movement in BFBG with type A distributor at U = 0.45 m/s.

4.5.2. Bubble Size and Movement in BFBG with Type (B) Distributor

The isothermal BFBG with type (B) distributor has a good bed transition from packed to fluidised conditions at both high and low superficial velocities. In figure 4.15 the experimental upward bubble movement in the BFBG with type B distributor at low superficial velocity is shown. The average bubble upward velocity in this case is 278 mm/sec which is very close to the bubble velocity in type A case. The bubble size in this case is 23.8 mm as shown in figure 4.16 which presents a very little difference to the bubble size at the previous case.

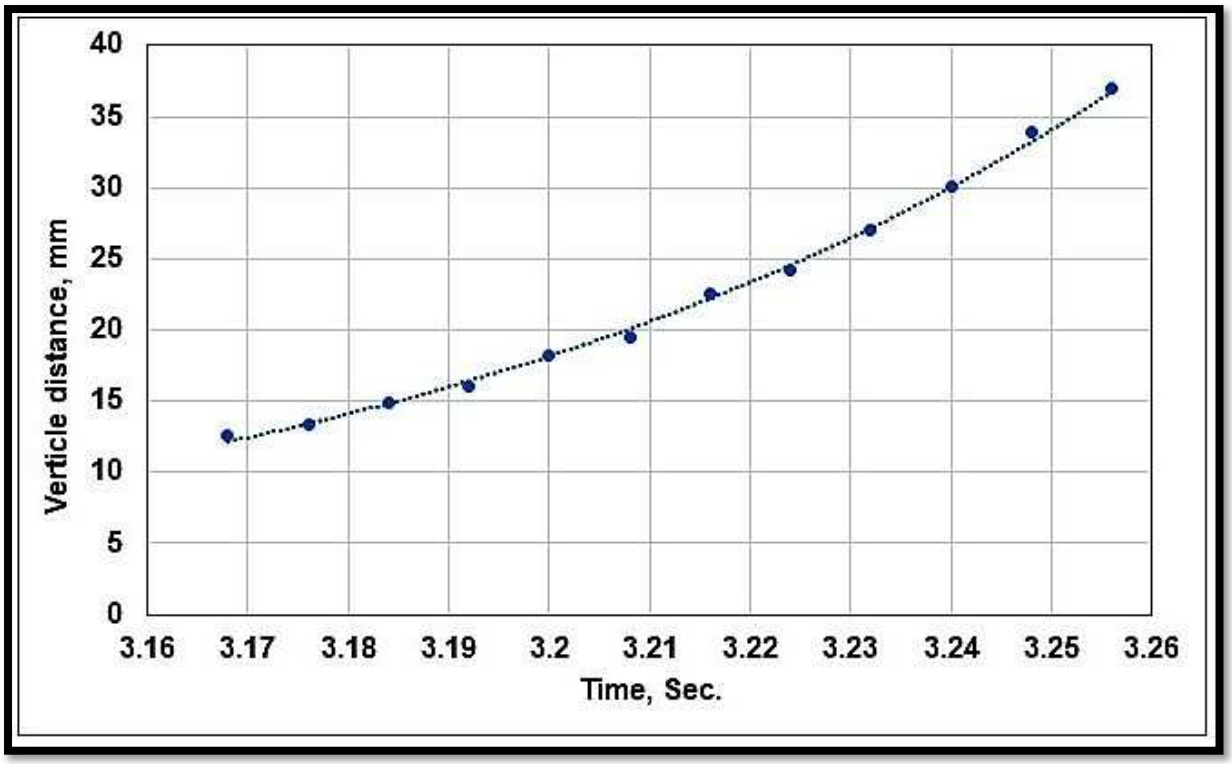

Figure 4.15. Experimental time variation of bubble movement in BFBG with type B distributor at U = 0.32 m/s.

Under high velocity, the bubble size was 23.4 mm and then expands to be more than 44 mm in 0.088 seconds at an average bubble velocity of 185.7 mm/sec which is lower by more than three times the velocity of the same case with the type A distributor. The partial fluidisation in the type A case has an impact on the bubble velocity as the air flow will be faster in the fluidised bed zone than in the packed bed zone due to the high drag in the packed zone which makes more air flows throgh the fluidised bed zone. Figure 4.17 shows the bubble size variation with time in the BFBG with type B distributor at high velocity.

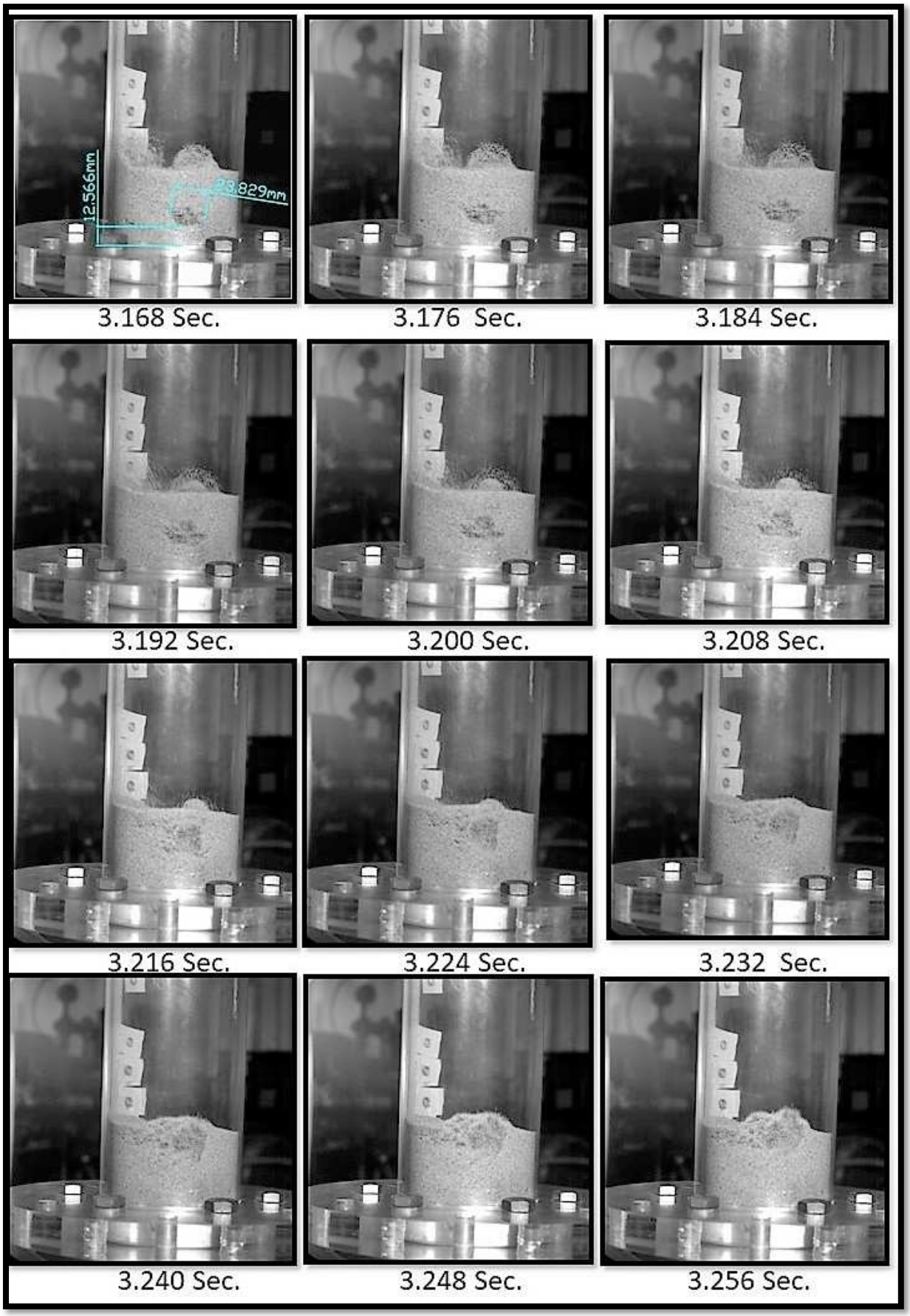

Figure 4.16. Bubble size and movement in the BFBG with type B distributor at U = 0.32 m/s.

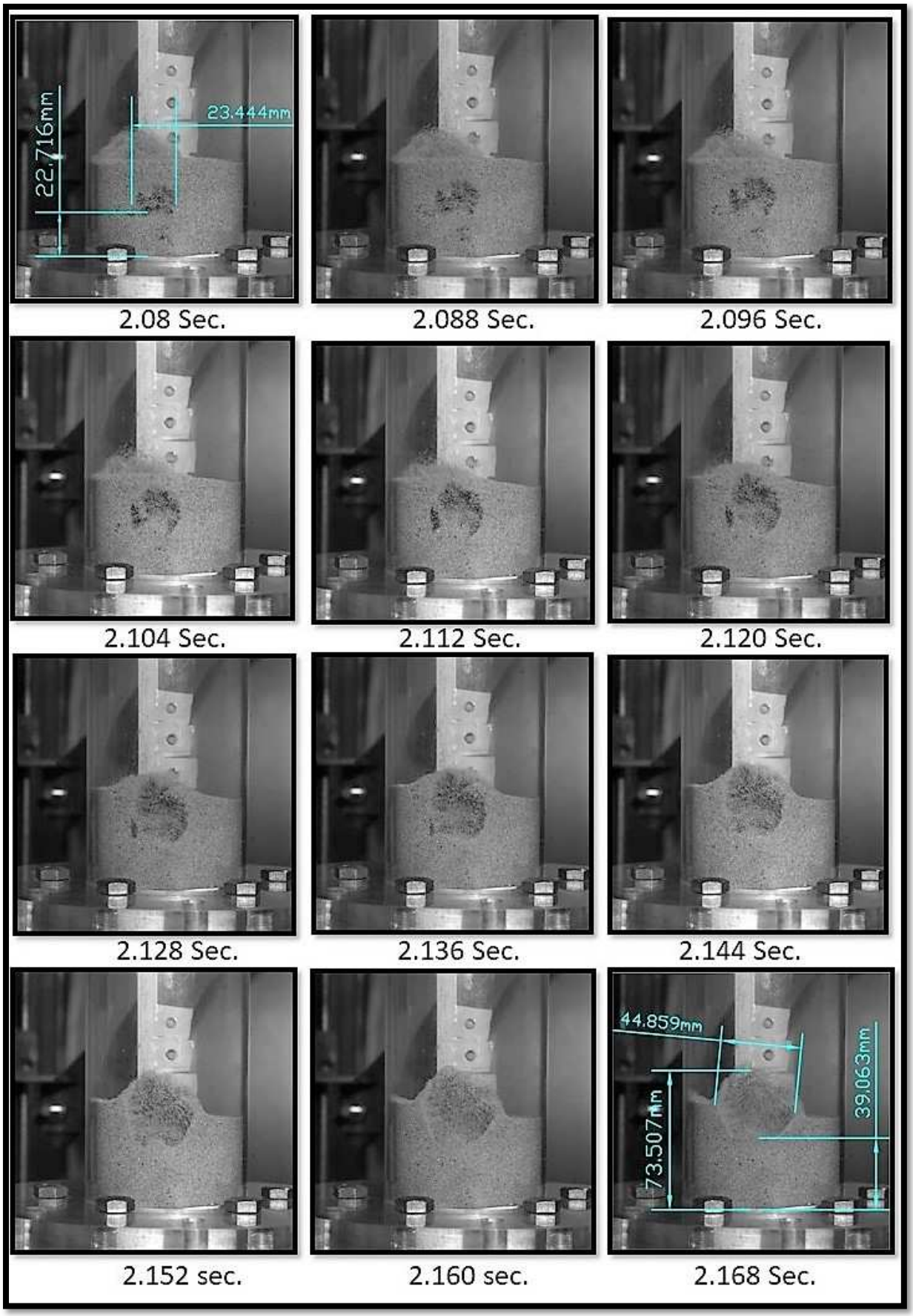

Figure 4.17. Bubble size and movement in the BFBG with type B distributor U = 0.44 m/s.

The upward movement of the selected bubble in the BFBG with the type B distributor at high velocity is illustrated in figure 4.18. Although the average superficial velocity is high in this case the bubble movement is slow compared to the low velocity case. This is probably due to the large wake fraction in the bubble as shown in figure 4.17 which dissipates the gas energy (Surma, 1985).

The maximum bed expansion in the high velocity case is 73.5 mm (maximum expansion from the distributor is 93.5 mm) after the bubble bursting as shown in figure 4.17.

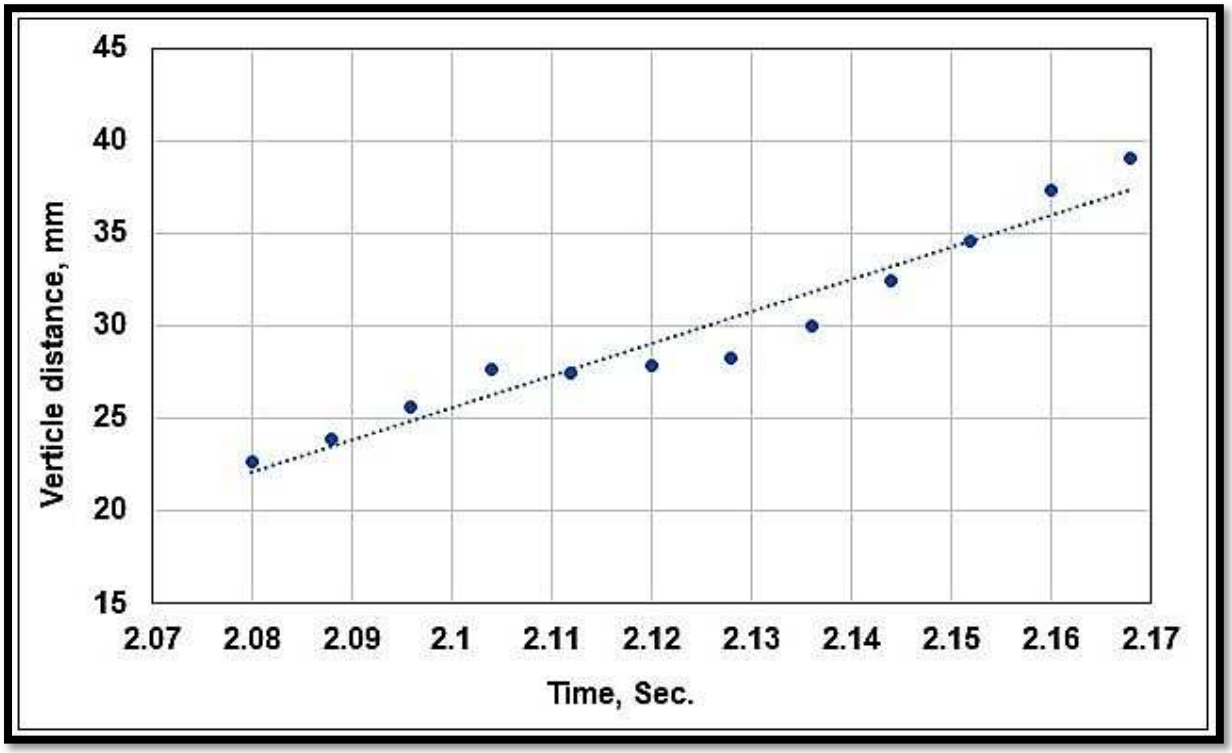

Figure 4.18. Experimental time variation of bubble movement in BFBG with type B distributor at U = 0.44 m/s.

4.5.3. Bubble Size and Movement in BFBG with Type (C) Distributor

The average bubble velocities in BFBG with a type C distributor are 215.5 mm/sec for the low velocity case and 318 mm/sec for the high velocity case. In figures 4.19 and 4.20 the upward movement of the formed bubble inside the BFBG at low and high average superficial velocities, respectively, is presented, and the bubbles size and their upward movement

patterns are shown in figures 4.21 and 4.22. The sand bed in the BFBG with type C distributor has totally fluidised in both high and low velocity conditions. This total fluidisation maybe due to the large number of orifices in this distributor (137 holes) with small pitch distance (6.35 mm) and small orifice diameter which provides uniform air flow through the sand bed.

Although the fluidisation in this case was full, the observed bed expansion was lower than type B. The maximum bed expansion in the high velocity case was 68 mm (maximum expansion from the distributor is 88 mm) as shown in figure 4.22. This is maybe due to the effect of triangular arrangement in type B distributor which provides fewer dead zones in the bed.

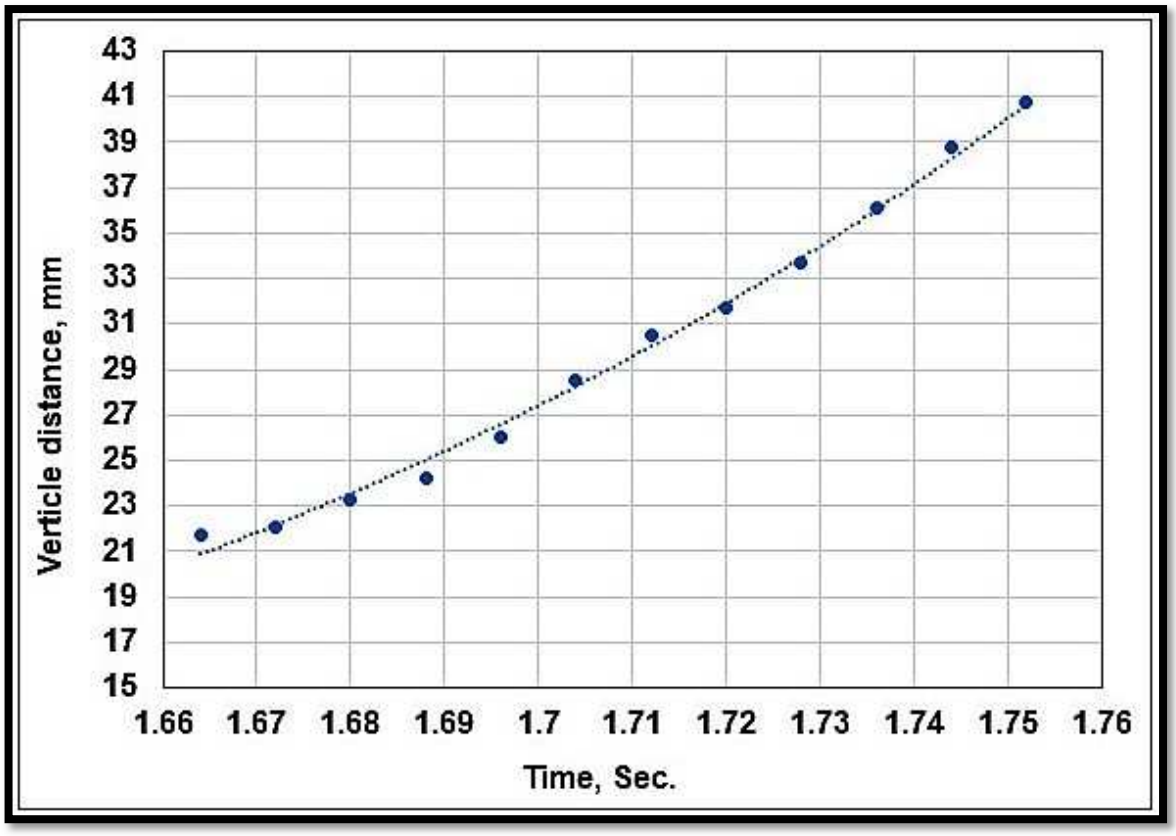

Figure 4.19. Experimental time variation of bubble movement in BFBG with type C distributor at U = 0.32 m/s.

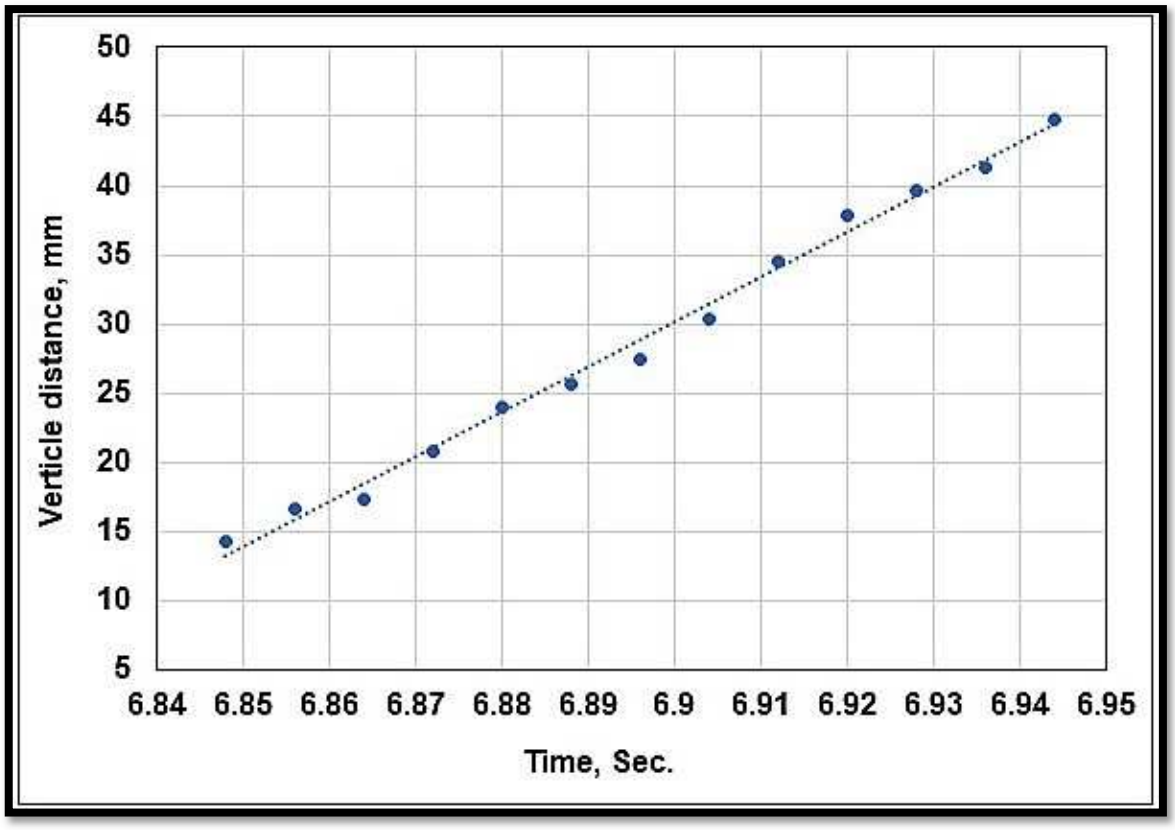

Figure 4.20. Experimental time variation of bubble movement in BFBG with type C distributor at U = 0.44 m/s.

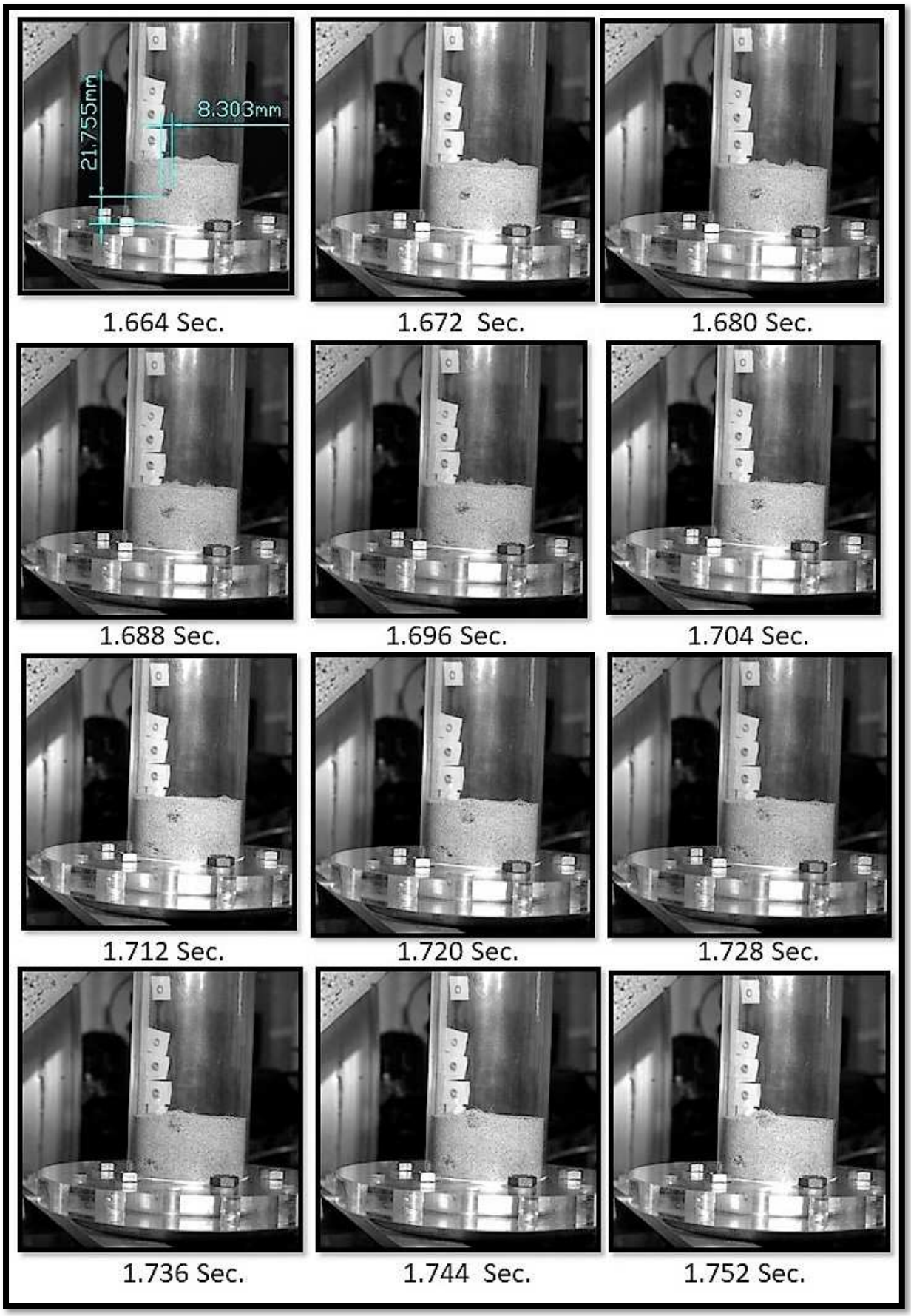

Figure 4.21. Bubble size and movement in the BFBG with type C distributor at U = 0.32 m/s.

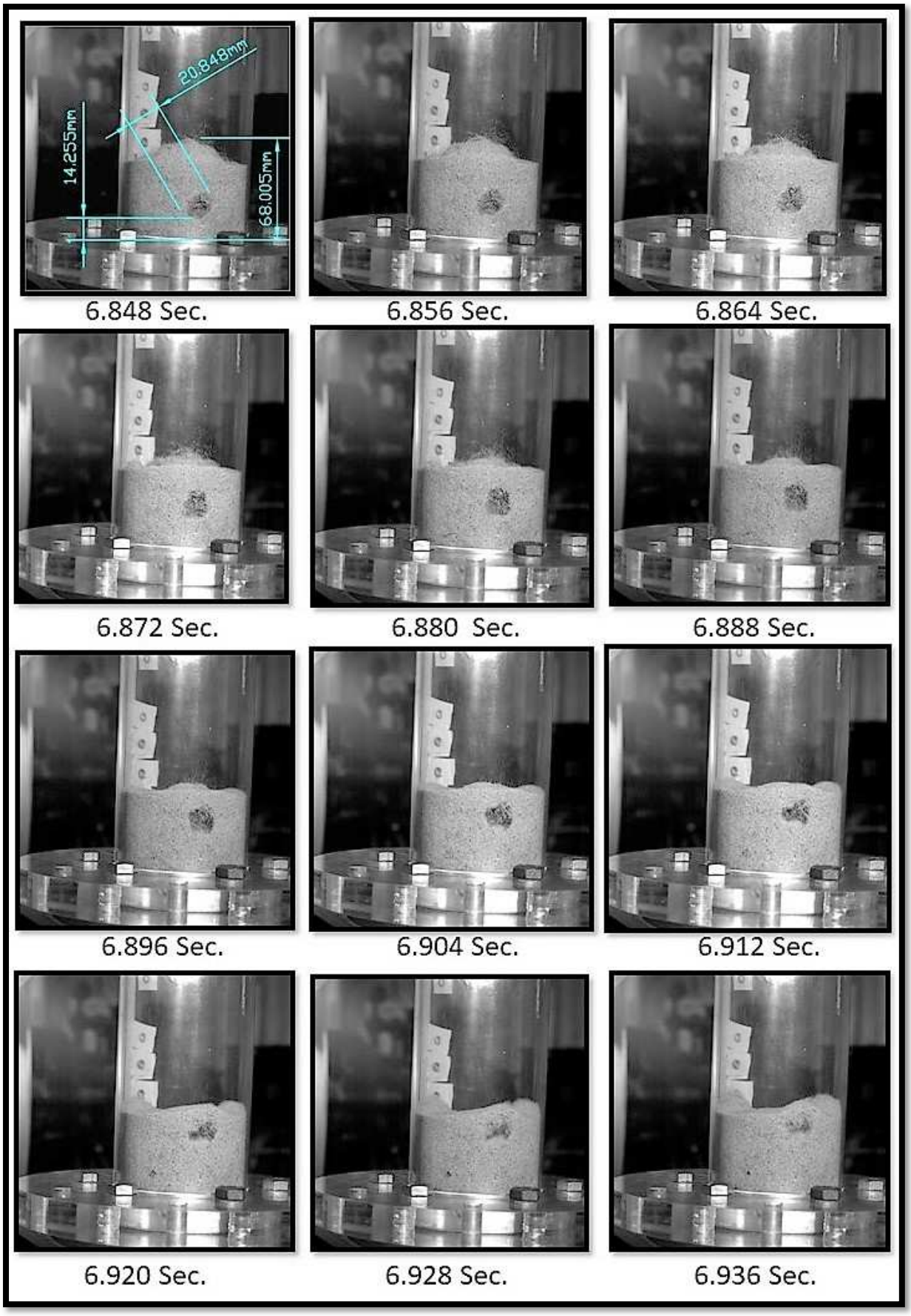

Figure 4.22. Bubble size and movement in the BFBG with type C distributor at U = 0.44 m/s.

4.5.4. Bubble Size and Movement in BFBG with Type (D) Distributor

The sand bed in the BFBG with the type D distributor has fluidised totally with many bubbles of different shapes and sizes. The expansion of the bed with this distributor was the largest among the other distributor cases providing an opportunity for good bed mixing. In figure 4.23 the bubble upward motion with the type D distributor at a low air velocity is presented. The average bubble velocity in this case is 260.7 mm/sec for a bubble size of 10.3 mm as shown in figure 4.24.

Under high velocity, more bubbles have formed at the same time as shown in figure 4.25. These bubbles have different sizes and velocities distributed throughout the sand bed. The bed height reaches more than 93 mm as shown in figure 4.25 (the bed height from the distributor is 113 mm) which is the largest bed expansion among all distributors. This high performance maybe due to the large number of small orfices (151 holes) with a small pitch distance (6.35 mm) in addition to the triangular arrangement which reduces the bed dead zones.

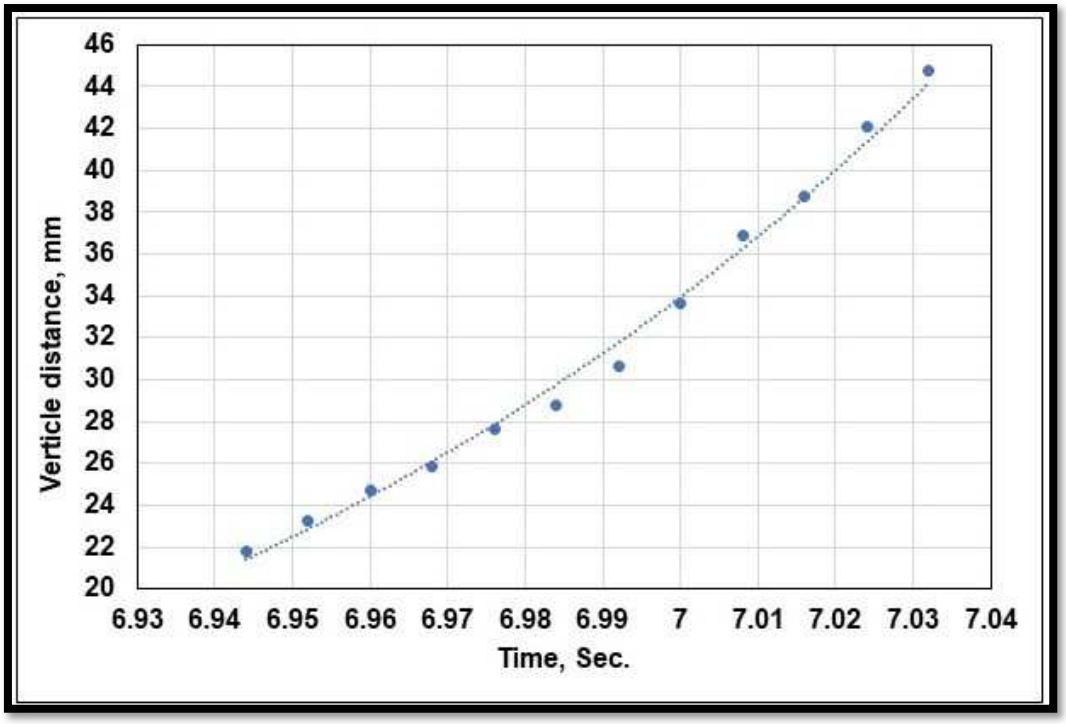

Figure 4.23. Experimental time variation of bubble movement in BFBG with type D distributor at U = 0.33 m/s.

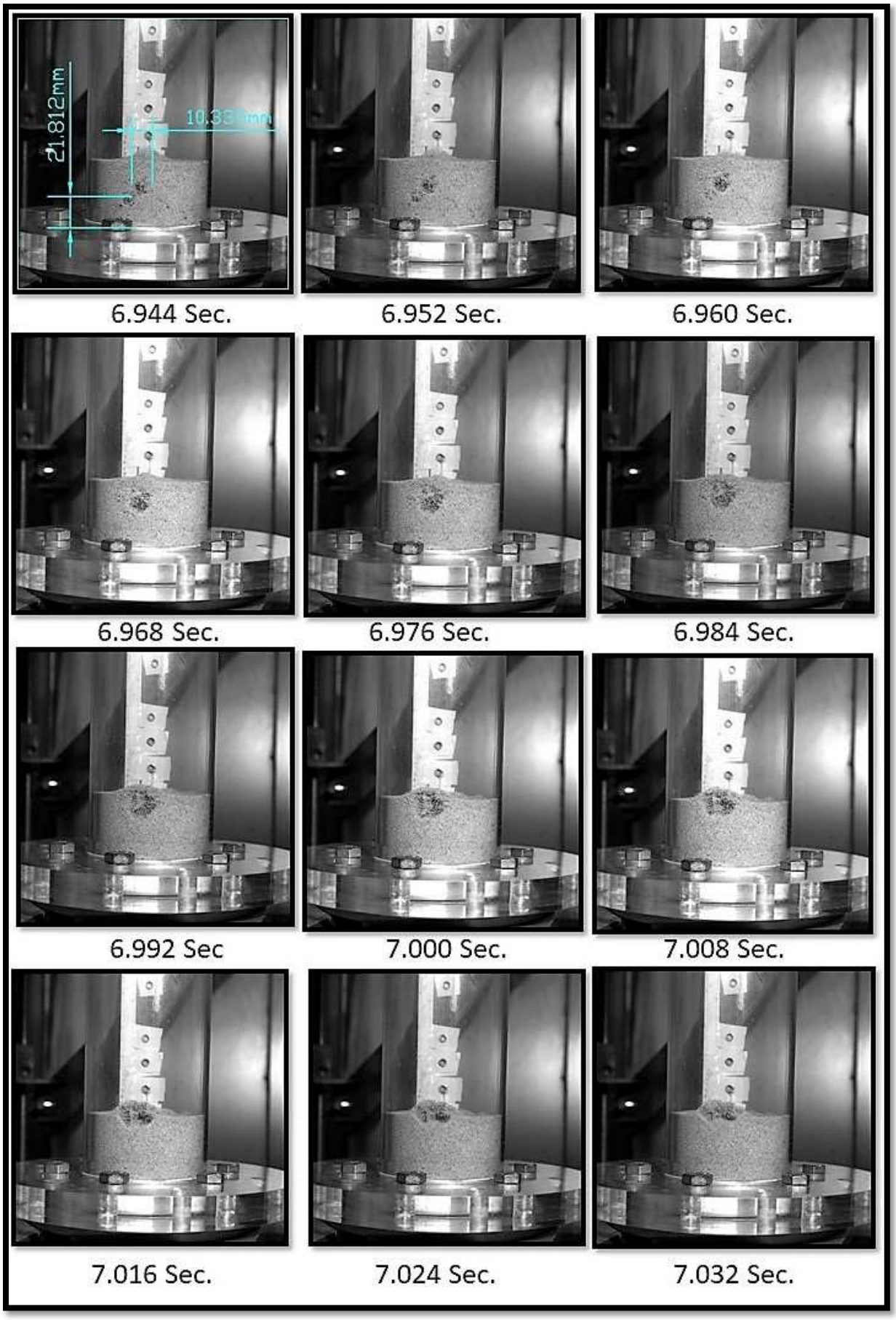

Figure 4.24. Bubble size and movement in the BFBG with type D distributor at U = 0.33 m/s.

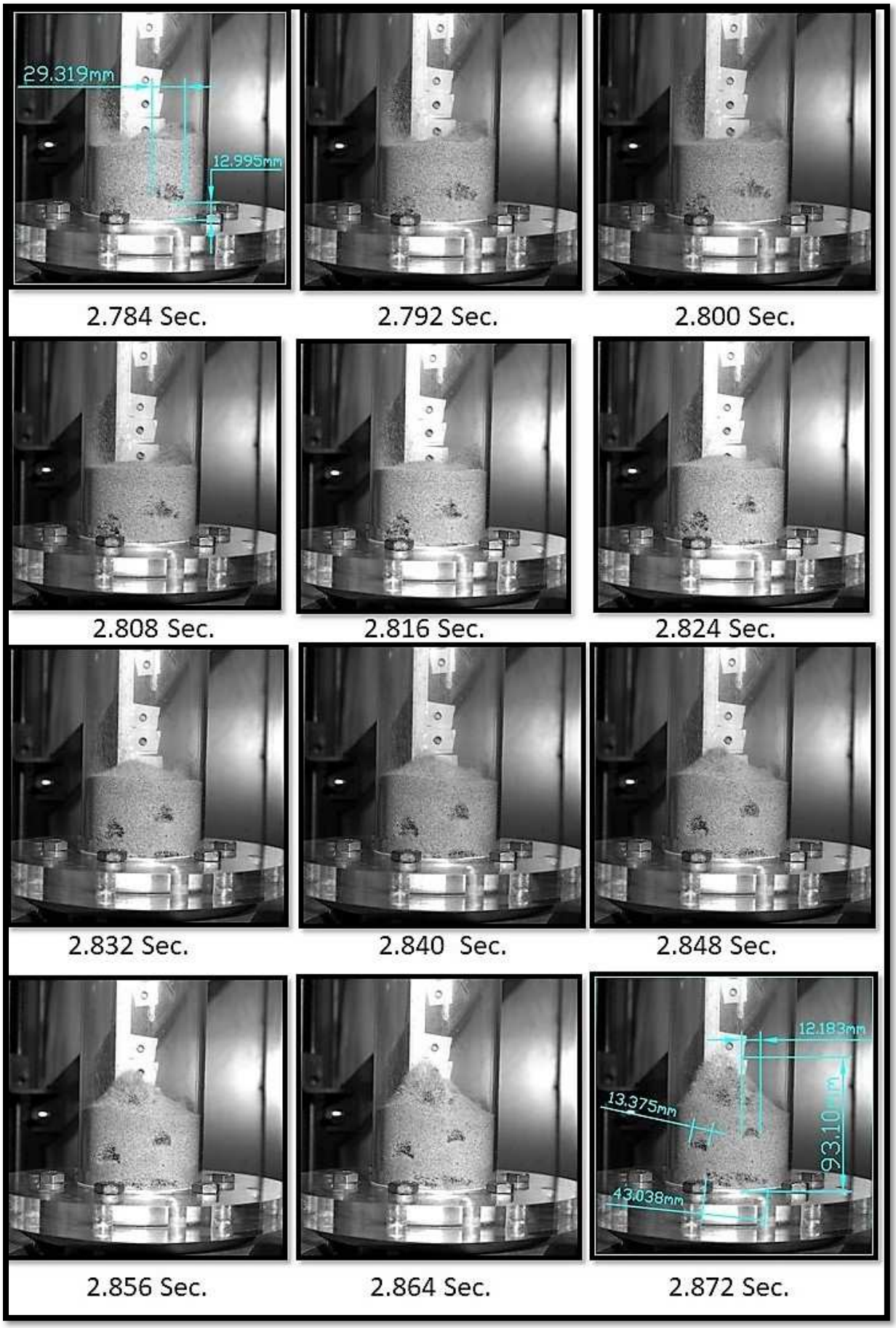

Figure 4.25. Bubble size and movement in the BFBG with type D distributor at U = 0.44 m/s.

The average bubble velocity in the high velocity case is 285.5 mm/sec, while the bubble motion is shown in figure 4.26.

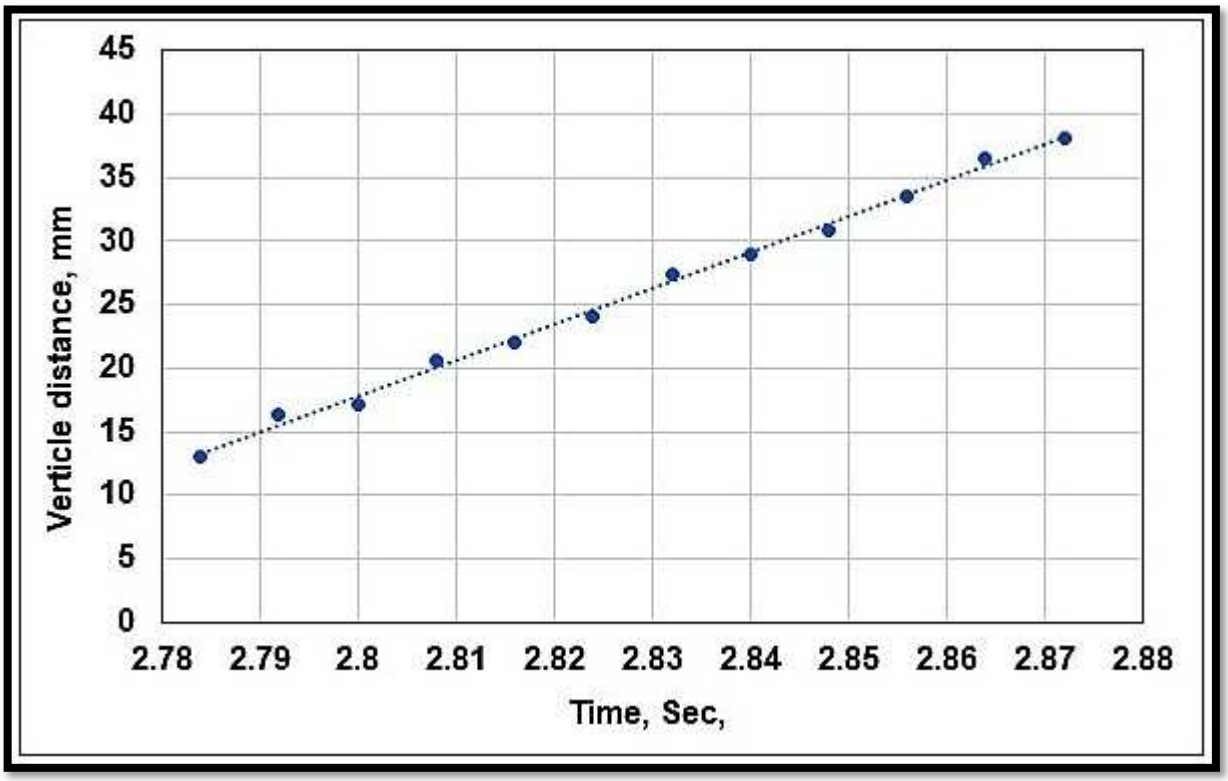

Figure 4.26. Experimental time variation of bubble movement in BFBG with type D distributor at U = 0.44 m/s.

A comparision between bubble movement in the low and high velocities for each distributor is illustrated in figure 4.27 and the comparisin between bubble movements in the four distributors in the low and high velocities are shown in figure 4.28 and 4.29 respectvily.

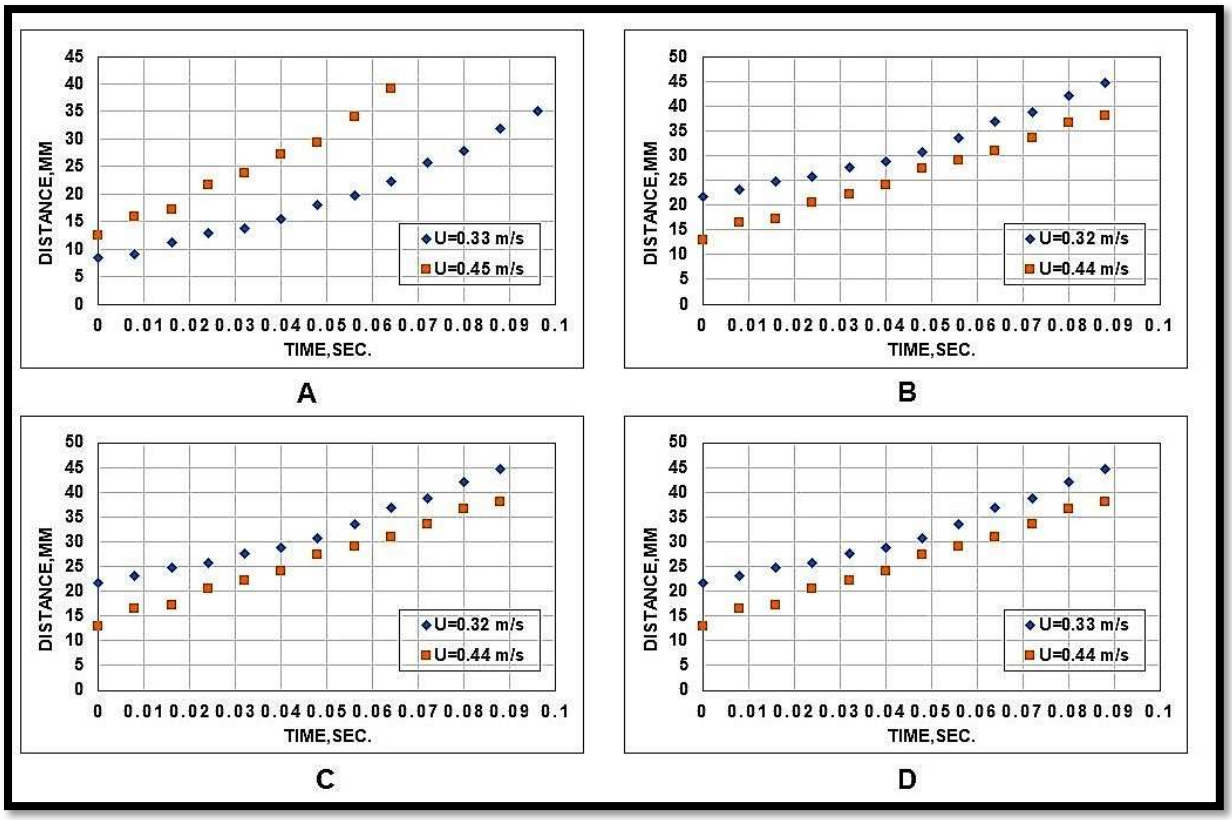

Figure 4.27. The variation of bubble movement with superficial velocity for the A, B, C and D distributors.

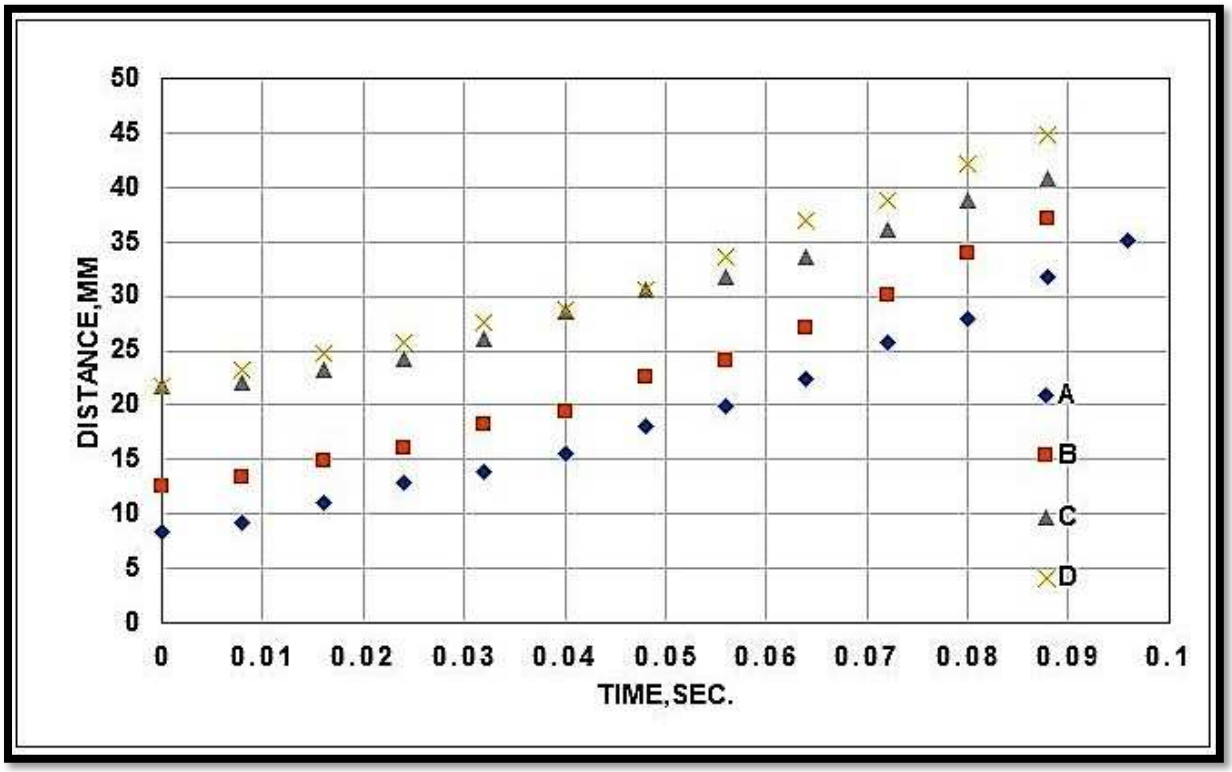

Figure 4.28. The variation of bubble movement with distributor type at low velocities.

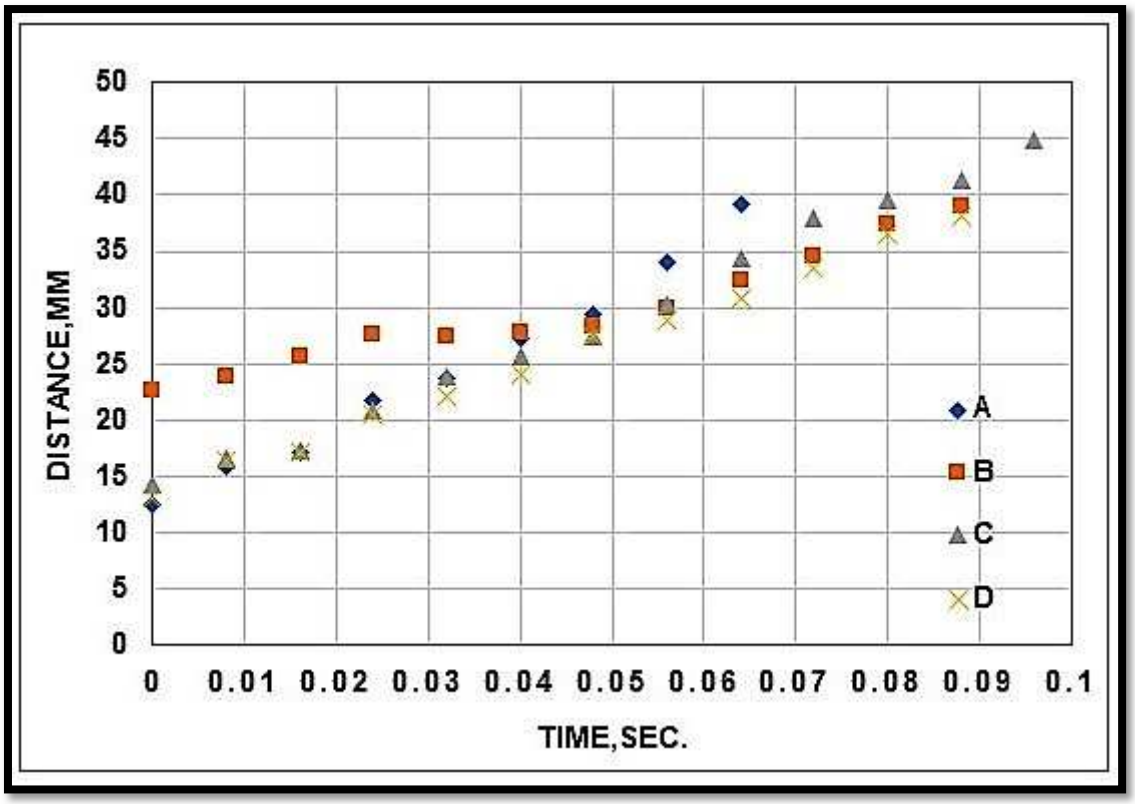

Figure 4.29. The variation of bubble movement with distributor type at high velocities.

4.6. Conclusion

The hydrodynamic behaviour of the isothermal BFBG has been studied experimentally for four different perforated distributors in terms of pressure drop and bubble characteristics. The performance of the BFBG with these distributors has been tested for different air flow rates and at different bed heights.

The experiments showed that all four perforated distributors have succeeded in producing bubbling fluidised bed inside the BFBG. However, the produced fluidised bed is not the same for all distributors. Type A distributor for example, partially fluidised the sand bed lifting a large pat of the packed bed. On the other hand, the type D distributor has fluidised the sand bed entirely with a large number of bubbles being formed. The expansion of the bed was the largest among the other distributors with a bed height reaching more than 113 mm under high velocity. Moreover, the minimum fluidisation velocity in the BFBG with D distributor was the lowest

among the other distributors at 234 mm/sec while the highest minimum fluidisation velocity was 289.5 mm/sec produced by type C distributor.

Regarding the pressure drop, all distributors have produced a uniform pressure drop throughout the BFBG sand bed with the preference to type D distributor as it showed a large pressure drop at high levels due to the bed expansion. Overall hydrodynamic behaviour of those four perforated distributors outweighs the triangular pitch distributor with 151 x 1mm ϕ holes (type D) to use it in the BFBG.

To conclude, the design of perforated plate distributor depends mainly on the orifice size and distribution pattern of the orifices. The distributors with small and triangular arrangement orifices form a fluidised bed regime with hydrodynamic specifications better than the distributors with large and square arrangement orifices.

Furthermore insight into the fluidised bed was only possible with highly advanced CFD which is detailed in chapter 5.

Chapter 5: CFD Analysis of BFBG Hydrodynamics

5.1. Introduction

CFD can be considered as a third approach in the philosophical study and development of the fluid dynamics discipline in addition to the purely experimental and the purely theoretical (mathematical) approaches (Anderson and Wendt, 1995).

Computational fluid dynamics solves and analyses fluid mechanics problems that involve fluid flows including fluidisation by using numerical analysis and data structures. The technical booming in computing speed and data storage has a major impact on CFD development (Alhussan, 2013).

In this chapter a CFD simulation with the open source software (OpenFOAM) was carried out for the isothermal BFBG with the four different distributors mentioned in chapter four. The aim of this CFD study is to provide a comprehensive visualisation of the hydrodynamics activities inside the BFBG which cannot be measured experimentally.

5.2. Isothermal BFBG Modeling

The OpenFOAM solver MPPICFoam was used in the modelling of the isothermal BFB gasifier with silica sand and air as solid-gas working materials. The properties and quantities of these materials are listed in table 3-2 in chapter three. However, the geometry and mesh generation for the isothermal reactor was created by the open source software (SALOME 7.7.1) as cited in chapter 3.

The modelling was carried out for the isothermal reactor with four different distributors which are the same configurations studied experimentally in chapter four. The simulation was carried out for two different air flow rates or superficial velocities for each distributor, average low superficial velocities and average high superficial velocities as shown in table 5-1. The reason

behind choosing just two velocity cases for each distributor, is the simulation requirements of time and data storage. For example, the computation time required to simulate one of the velocity cases is between 2 weeks and 1 month in the high-speed computer and generates about 250 GB of data. The air flow conditions for the eight cases are illustrated in table 5-1.

Table 5-1. Air flow conditions for the eight cases of the isothermal BFB reactor.

Case No.	Distributor specifications	Orifice air velocity (m/s)	Total air flowrate (SLPM)	Average superficial velocity (m/s)	Type
1	97 x 2mm ϕ x 7.5mm pitch (Square arrangement)	6	109.704	0.338	A
2	97 x 2mm ϕ x 7.5mm pitch (Square arrangement)	8	146.273	0.450	A
3	109 x 2mm ϕ x 7.5mm pitch (Triangular arrangement)	5	102.73	0.316	B
4	109 x 2mm ϕ x 7.5mm pitch (Triangular arrangement)	7	143.822	0.443	B
5	137 x 1mm ϕ x 6.35mm pitch (Square arrangement)	16	103.296	0.318	C
6	137 x 1mm ϕ x 6.35mm pitch (Square arrangement)	22	142.031	0.437	C
7	151 x 1mm ϕ x 6.35mm pitch (Triangular arrangement)	15	106.736	0.329	D
8	151 x 1mm ϕ x 6.35mm pitch (Triangular arrangement)	20	142.314	0.438	D

5.3. Modelling Results

The modelling of the isothermal BFB gasifier was carried out in the RAVEN supercomputing cluster of the Advanced Research Computing at Cardiff (ARCCA) in Cardiff University (ARCCA, [no date]). Data for each case simulation was between 230 and 300 GB. This data includes information about most of the hydrodynamic parameters throughout the isothermal bubbling fluidised bed gasifier such as particle size distribution, pressure drop, instantaneous velocity, and porosity (void fraction).

The minimum fluidisation velocity, U_{mf} for the isothermal BFB gasifier model was calculated using the equation 3-8 along with the properties in the table 3-2 of chapter three. Hence, the minimum fluidisation velocity for the system is $U_{mf} = 0.21574\ {}^{m}/_{S}$ and the minimum fluidisation flowrate is $Q_{mf} = 70\ SLPM$.

Therefore, all the eight study cases for the isothermal bubbling fluidised bed gasifier are in the fluidisation zone.

5.4. Simulation Results Validation

The simulation results presented in this chapter has been compared with the experimental data illustrated in chapter four in order to validate the simulation process in terms of pressure drop and bubble formation characterstics. The pressure drop from the simulation is calculated along the inner wall of the BFBG and the experimental pressure drop was measured in five positions along the BFBG inner wall as illustrated in chapter four. The second valdiation of the results is between the predicated bubble size in this simulation with results of the bubble size from literature.

5.4.1. Pressure Drop in BFBG with Type (A) Distributor

The comparison between experimental and simulated pressure drops along the inner wall of the isothermal BFBG with type A distributor is shown in figure 5.1 and the difference between the averge measured and predicted pressure drops in the five positions for the high and low velocity cases for type A distributor are listed in table 5-2. The variance between the predicated and experimantal results in table 5-2 can be related to many reasons such as the assumption of constant density and viscosty of air in the simulation. The experimental errors were too small compared to the total pressure range as shown in figure 5.1.

Table 5-2. The difference between experimental and calculated pressure drop in the BFBG with type A distributor.

Position (mm)	Low velocity case			High velocity case		
	Simulated (pa)	Experimental (pa)	percentage differences (%)	Simulated (pa)	Experimental (pa)	percentage differences (%)
10	525.69	390 ± (2.9)	25.81 ± (0.55)	483.45	400 ± (4.1)	17.26 ± (0.84)
40	245.73	276 ± (3.05)	-12.32 ± (1.24)	249.45	292 ± (4.4)	-17.06 ± (1.76)
60	61.90	16 ± (2.3)	74.15 ± (3.71)	119.41	35 ± (3)	70.69 ± (2.51)
80	10.04	16 ± (2.1)	-59.39 ± (20.91)	29.84	13 ± (2.8)	56.44 ± (9.38)
100	8.57	8 ± (0.9)	6.64 ± (10.5)	0.830	9 ± (0.8)	-90.77 ± (8.88)

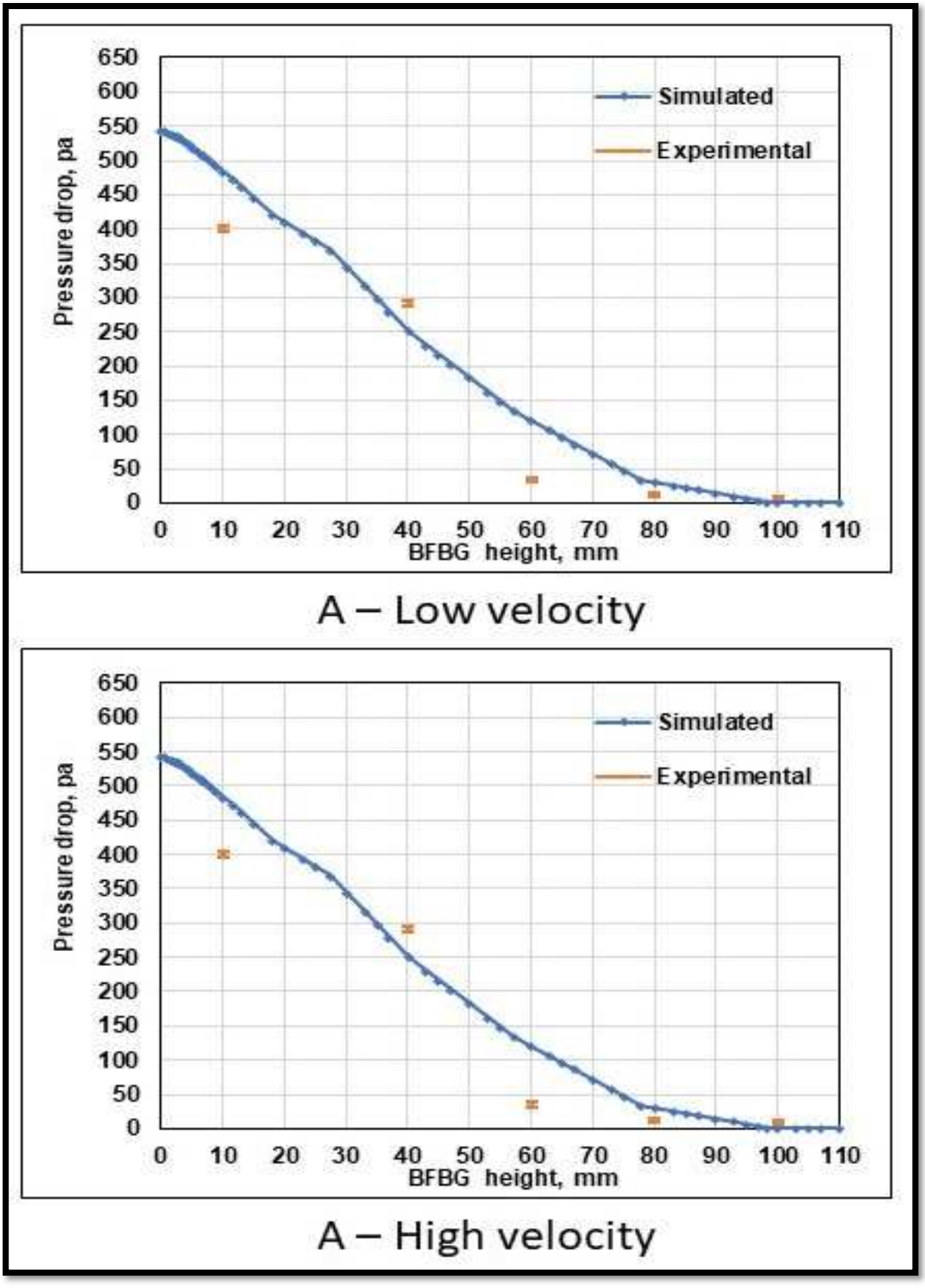

Figure 5.1. The comparison between experimental and simulated pressure drop in the BFBG with type (A) distributor.

5.4.2. Pressure Drop in BFBG with Type (B) Distributor

In table 5.3 shows the calculated and measured data in the five positions with the percentage of differences and in figure 5.2 the experimental and theoretical pressure drops in BFBG with type B distributor is shown.

Table 5-3. The difference between experimental and calculated pressure drop in the BFBG with type B distributor.

Position (mm)	Low velocity case			High velocity case		
	Simulated (pa)	Experimental (pa)	percentage differences (%)	Simulated (pa)	Experimental (pa)	percentage differences (%)
10	506.75	466 ± (5.3)	8.04 ± (1.13)	499.14	475 ± (6.01)	4.83 ± (1.26)
40	203.07	248 ± (6)	-22.12 ± (2.41)	266.99	259 ± (5)	2.99 ± (1.87)
60	55.77	8 ± (1.95)	85.66 ± (3.5)	102.52	36 ± (1.21)	64.89 ± (1.18)
80	8.13	3 ± (1.8)	63.1 ± (22.14)	19.93	10 ± (2.0)	49.83 ± (10)
100	6.00	2 ± (1.7)	66.71 ± (28.33)	4.77	6 ± (1.0)	-25.54 ± (16.66)

A general comparison between A and B distributors shows type B has less error than type A in the most positions with the minimum value of 3% error at 40 mm position at the high velocity case.

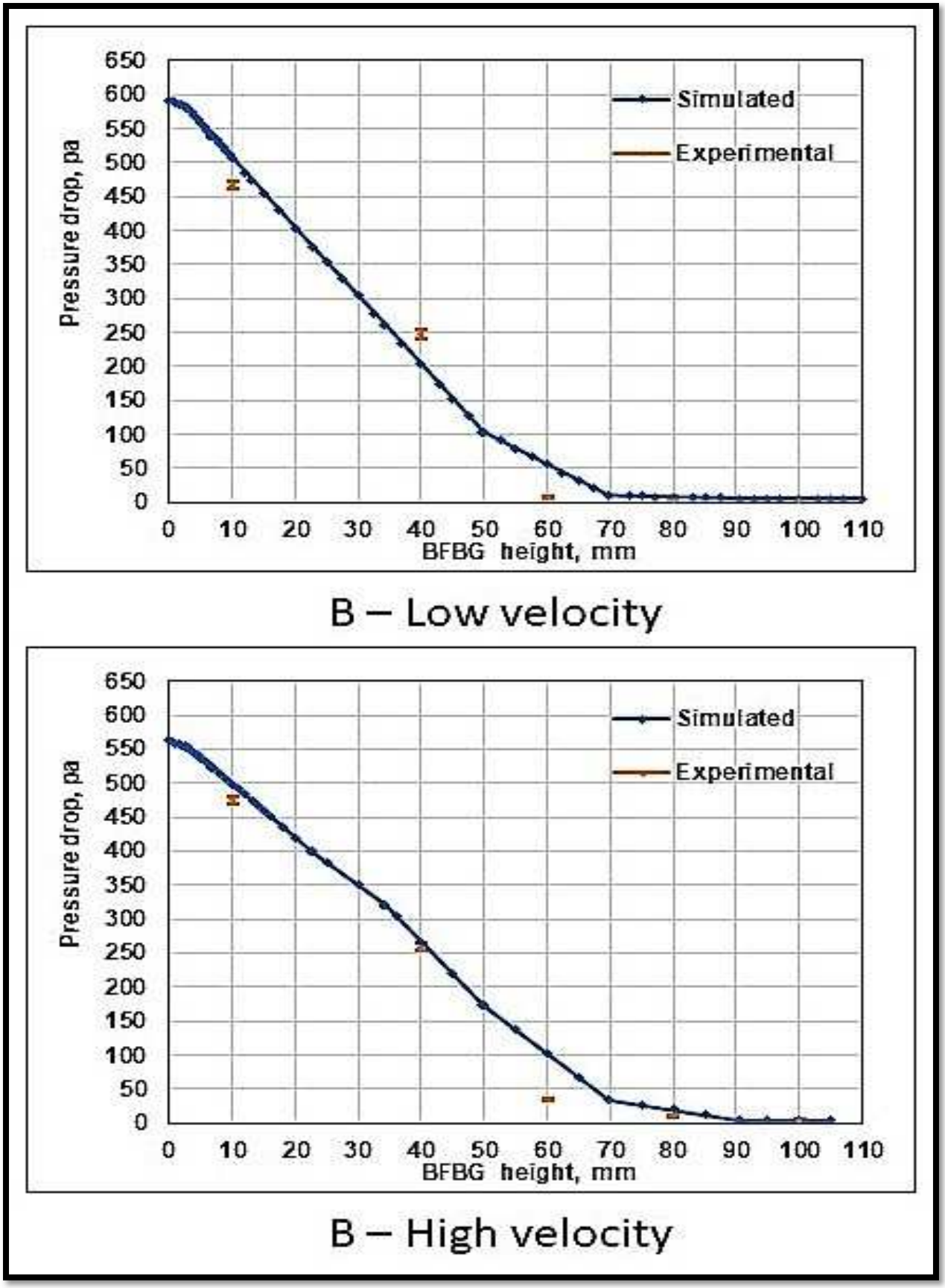

Figure 5.2. The comparison between experimental and simulated pressure drop in the BFBG with type (B) distributor.

5.4.3. Pressure Drop in BFBG with Type (C) Distributor

In type C cases the mostly higher than type B distributor and lower than type A as shown in table 5-4 and figure 5.3. The distributor holes arrangement and size may influence the accuracy of the simulation as the square arrangement distributors have more error than the triangular distributors and the small orifice distributor showed more converge between the experimental and simulated results.

Table 5-4. The difference between experimental and calculated pressure drop in the BFBG with type C distributor.

Position (mm)	Low velocity case			High velocity case		
	Simulated (pa)	Experimental (pa)	percentage differences (%)	Simulated (pa)	Experimental (pa)	percentage differences (%)
10	456.66	440 ± (4.0)	3.65 ± (0.87)	504.07	445 ± (5)	11.72 ± (0.99)
40	225.54	243 ± (2.0)	-7.74 ± (0.82)	229.88	290 ± (2.65)	-26.15 ± (0.91)
60	62.32	16 ± (1.51)	74.33 ± (2.59)	84.10	42 ± (1.32)	50.07 ± (1.57)
80	5.03	8 ± (1.4)	-58.81 ± (17.5)	18.93	11 ± (2.1)	41.91 ± (11.05)
100	2.64	8 ± (2.1)	-66.9 ± (26.25)	3.67	8 ± (1.1)	-54.04 ± (13.75)

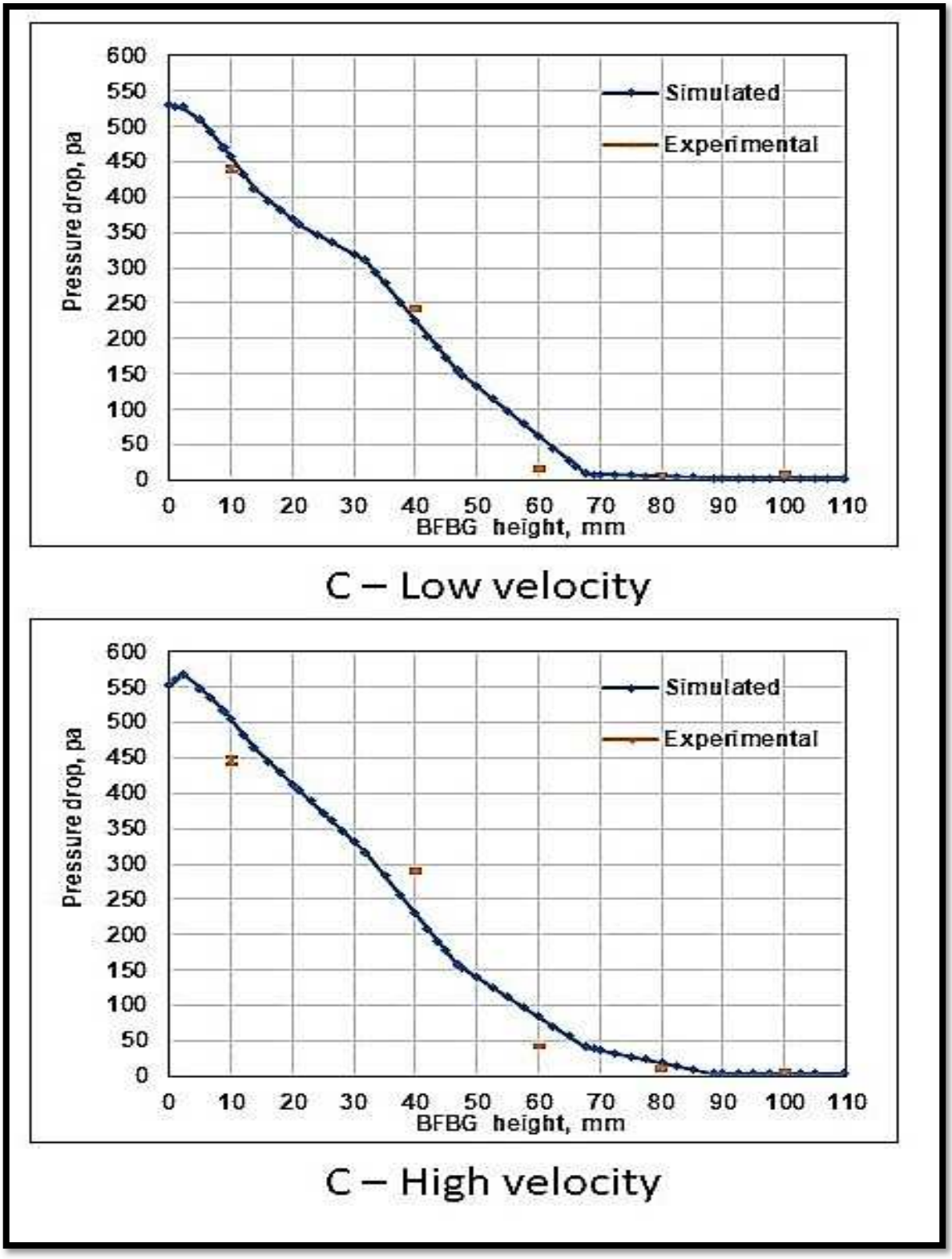

Figure 5.3. The comparison between experimental and simulated pressure drop in the BFBG with type (C) distributor.

5.4.4. Pressure Drop in BFBG with Type (D) Distributor

The percentage of error for the isothermal BFBG with the type D distributor in each position is listed in table 5-5 and the value of pressure drop along the inner wall of the BFBG is shown in figure 5.4.

Table 5-5. The difference between experimental and calculated pressure drop in the BFBG with type D distributor.

Position (mm)	Low velocity case			High velocity case		
	Simulated (pa)	Experimental (pa)	percentage differences (%)	Simulated (pa)	Experimental (pa)	percentage differences (%)
10	525.73	515 ± (6.07)	2.04 ± (1.15)	493.70	518 ± (6.42)	-4.92 ± (1.23)
40	244.01	288 ± (4.8)	-15.27 ± (1.66)	331.62	354 ± (8)	-6.74 ± (2.25)
60	61.80	30 ± (2.98)	51.46 ± (4.83)	106.37	118 ± (6)	-10.93 ± (5.08)
80	7.32	13 ± (3.3)	-43.68 ± (25.38)	20.65	17 ± (2)	17.68 ± (9.70)
100	3.56	6 ± (2.4)	-40.55 ± (40)	13.23	8 ± (3.02)	39.54 ± (22.82)

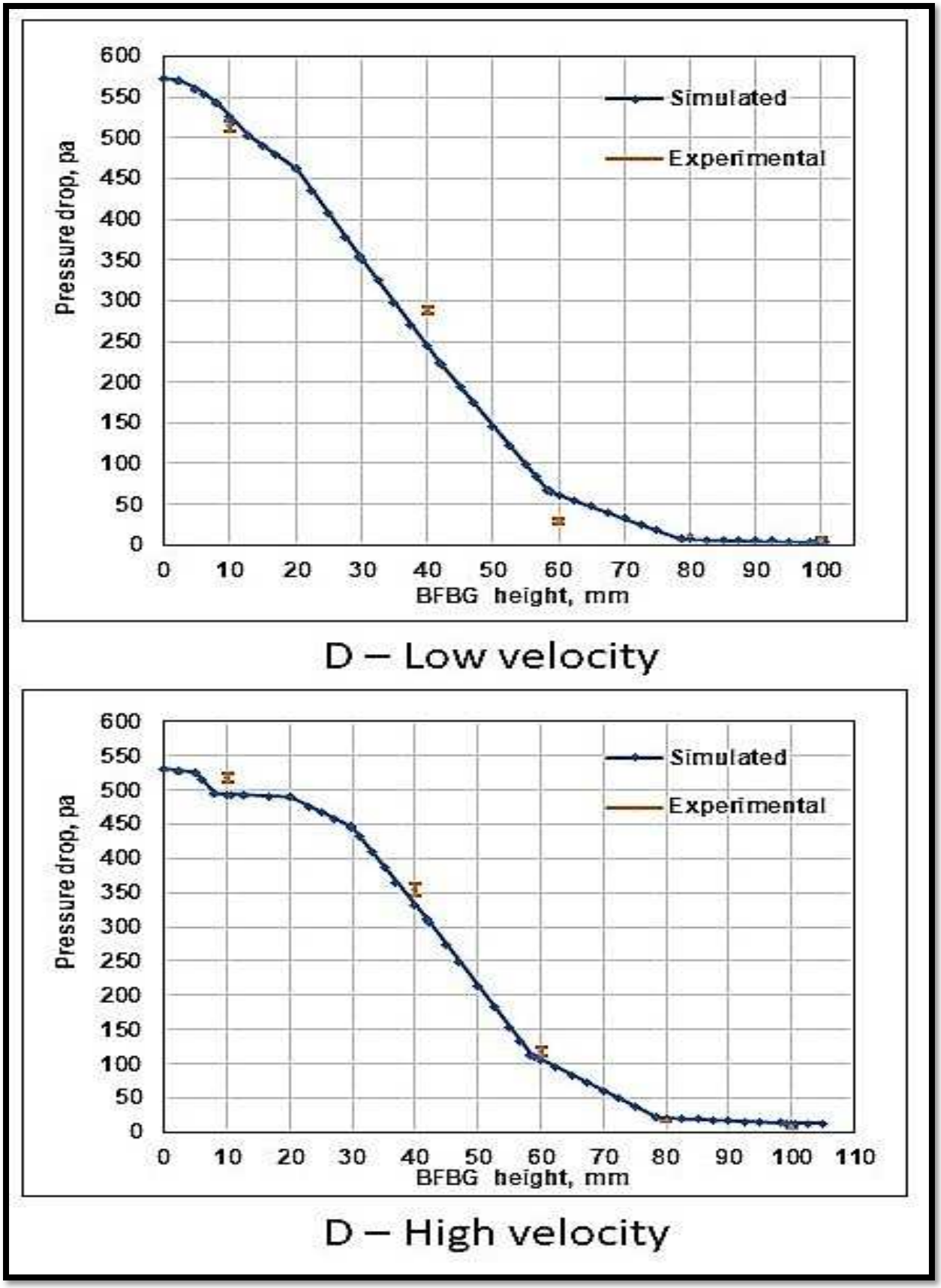

Figure 5.4. The comparison between experimental and simulated pressure drop in the BFBG with type (D) distributor.

he overall comparison between the experimental and the simulated results shows that type D distributor has the best matching in most of the height positions among the other distributors as shown in figure 5.5. The orifice size and pitch arrangement of the type D distributor may cause this preference in comparison as mentioned before.

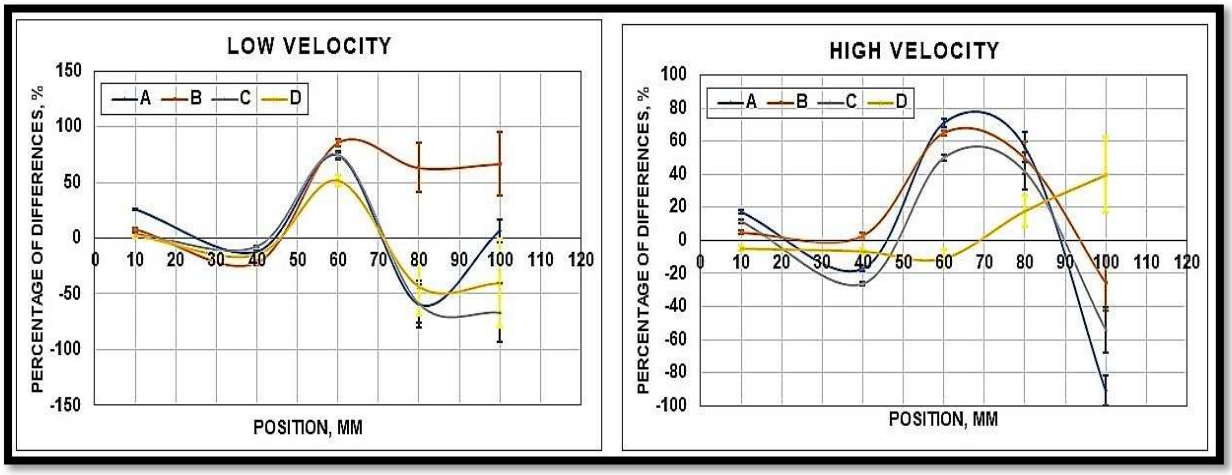

Figure 5.5. Comparison of the pressure drop percentage differences in the four distributors (A, B, C and D).

5.5. Bubble Size Comparison

Comparison of recent simulation results with previous literature is a crucial issue to validate the work. The sizes of fluidised bed bubbles formed in this simulation have been compared with the bubble size calculated from three different correlations.

5.5.1. Chiba Correlation

The Chiba correlation for the bubble size in a fluidised bed reactor with a perforated distributor depends on the difference between superficial and minimum fluidisation velocities, reactor cross sectional area and inversely on orifices number (Chiba et al., 1972).

$$d_b = 0.431 \left(\frac{A_c \cdot (U_s - U_{mf})}{n}\right)^{0.4} \quad \text{..... 5-1}$$

Where:

d_b – Bubble diameter (cm).

A_c – Reactor cross-sectional area (cm^2).

U_s – Instantons superficial gas velocity (cm/sec).

U_{mf} – Minimum fluidisation velocity (cm/sec).

n – orifices number.

5.5.2. Cranfield Correlation

In Cranfield correlation, the bubble height has an important effect on bubble size. However, there is no effect of the area and holes number in Cranfield correlation (Cranfield and Geldart, 1974).

$$d_b = 0.0326 \cdot (U_s - U_{mf})^{1.11} \cdot h_b^{0.81} \quad \text{..... 5-2}$$

Where:

h_b – Bubble height (cm).

5.5.3. Geldart Correlation

The holes number and the gravity in addition to the bubble height has been included in Geldart correlation (Geldart, 1972).

$$d_b = 1.43 \left(\frac{U_s - U_{mf}}{n}\right)^{0.4} \cdot \frac{1}{g^{0.2}} + 0.027 \cdot h_b \cdot (U_s - U_{mf})^{0.94} \quad \text{..... 5-3}$$

Where:

g – Gravitational constant, g = 981 cm/s^2.

The instantaneous superficial velocity at the bubble centre has been used instead of the average superficial velocity in the validation of the above three correlations which gives more reality to the bubble size calculations. In table 5-6 the comparison between bubbles sizes predicted by the recent simulation and the three empirical correlations are shown.

The results of the recent simulation have a good approach with the empirical correlations of Cranfield (Cranfield and Geldart, 1974) and Geldart (Geldart, 1972). On the other hand, the results of the Chiba correlation (Chiba et al., 1972) were far from the simulation results. This disparity is also present between the results of Chiba correlation and the results of the other two correlations. This may due to the absence of the bubble height effect in the Chiba correlation. However, this fact has been mentioned in the literature (Karimipour and Pugsley, 2011). The error between the simulated bubble size and Cranfield and Geldart correlation was between 9.92% and 58.81, while the error between the recent simulation and Geldart correlation was between 4.83% and 37.65% as shown in table 5-7.

Table 5-6. Bubble size comparison for the eight simulation cases.

Distributor type		A		B		C		D	
Velocity case		Low	High	Low	High	Low	High	Low	High
Number of orifices, n		97	97	109	109	137	137	151	151
Bubble height, h_b (cm)		2.71	3.06	3.42	1.07	1.14	1.62	2.82	2.80
Instantaneous local superficial velocity, U_s (cm/s)		50.40	86.34	36.17	25.79	30.79	61.95	71.46	85.13
Time (Sec.)		2.64	1.23	2.51	1.30	3.32	1.11	0.89	5.78
Minimum fluidisation velocity, U_{mf} (cm/s)		21.57	21.57	21.57	21.57	21.57	21.57	21.57	21.57
Bubble diameter, d_b (cm)	Recent simulation	2.68	5.23	1.92	0.48	0.92	3.37	5.20	5.12
	(Chiba et al., 1972)	0.55	0.72	0.38	0.23	0.29	0.52	0.54	0.6
	(Cranfield and Geldart, 1974)	3.47	8.09	1.72	0.44	1.04	5.35	5.80	7.53
	(Geldart, 1972)	2.15	4.37	1.3	0.46	0.87	3.21	3.24	4.00

Table 5-7. The difference between (Cranfield and Geldart, 1974) and (Geldart, 1972) correlations and recent simulation in terms of bubble size.

Distributor type	Velocity case	Percentage differences (%)	
		(Cranfield and Geldart, 1974)	(Geldart, 1972)
A	LOW	29.14	19.83
	HIGH	54.69	16.37
B	LOW	10.17	31.99
	HIGH	9.92	5.99
C	LOW	13.43	5.24
	HIGH	58.81	4.83
D	LOW	11.55	37.65
	HIGH	47.06	21.88

5.6. Simulation Results Analysis

5.6.1. Particles Size Distribution

The sand particles used in the simulation process of the eight cases have different sizes. The size of these particles starts from 425 µm to 500 µm and all particles are assumed to have a spherical shape, i.e. unity sphericity, $\phi = 1$. In figure 5.6 the batch injection of sand particles inside the BFBG with type (A) distributor and 0.338 m/s superficial velocity is presented. The particle size distribution through the injection time can be seen clearly in figure 5.6. The batch injection of sand particles was synchorised with the upward flow of air streams from the distrbutor holes. The injection sequence of sand particles shows that the large particles 500

μm (red colour) reach the BFBG bottom before the small particles 425 μm (blue colour) which stay on the rest of the batch, as expected. This is due to the gravity and the bouncy effect in low gas velocities (Chen and Keairns, 1975, Soria-Verdugo et al., 2011).

More details about the effects of each distributor type and superficial velocity on bed height and particles distribution can be seen in figure 5.7 and figure 5.8. The fluidised bed height or bed expansion showed a clear influence by the distributor type. Types A, B and C distributors produce fluidised beds with heights of about 60 cm for the low superficial gas velocity (as shown in figure 5.7) or about 65 to 70 cm for the high superficial gas velocity (as shown in figure 5.8).

On the other hand, type D distributor produced a fluidised bed with about 70 cm height for the low superficial gas velocity and more than 75 cm for the high superficial gas velocity.

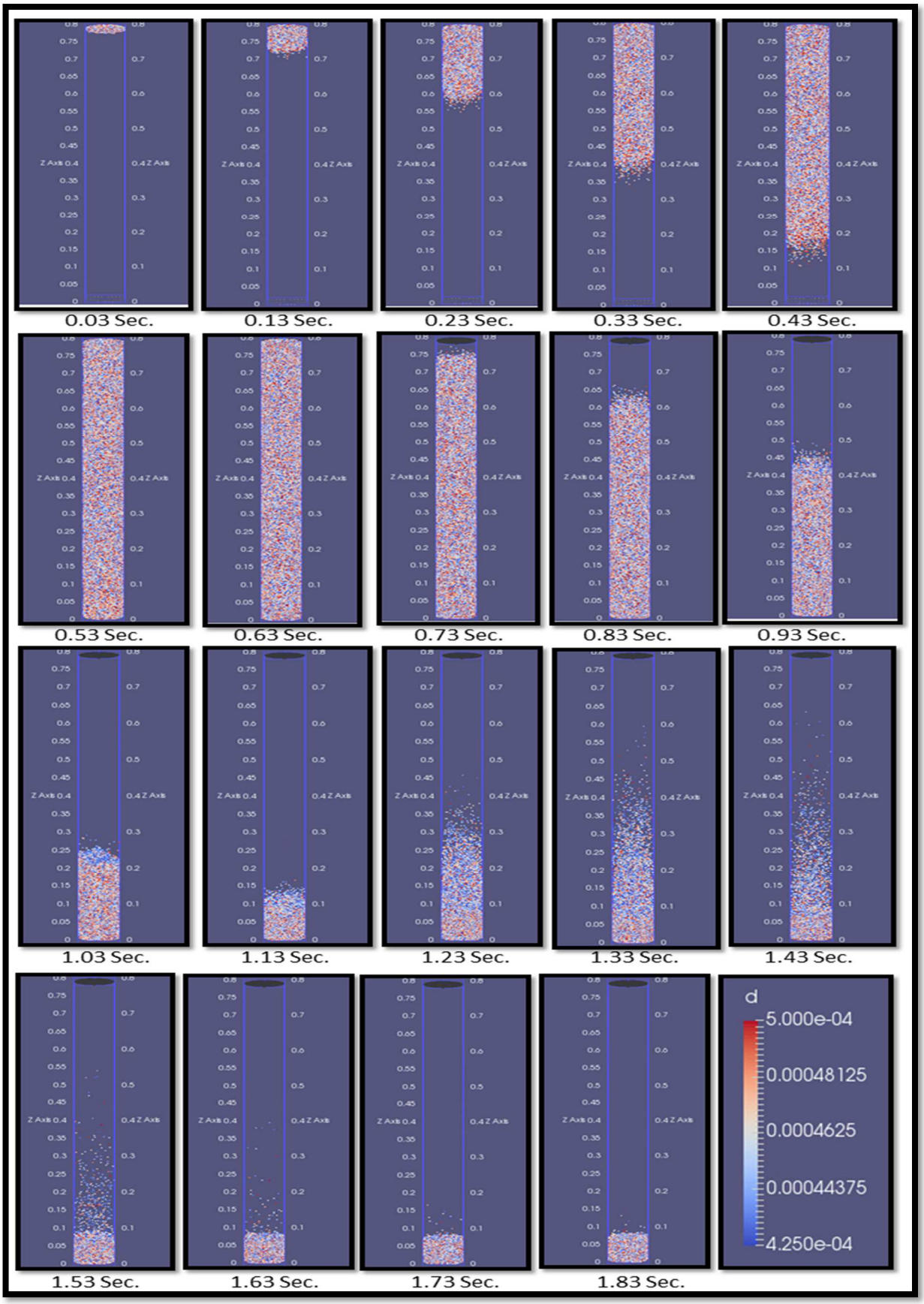

Figure 5.6. The time sequence of the sand particles batch injection through an isothermal BFBG with type A distributor.

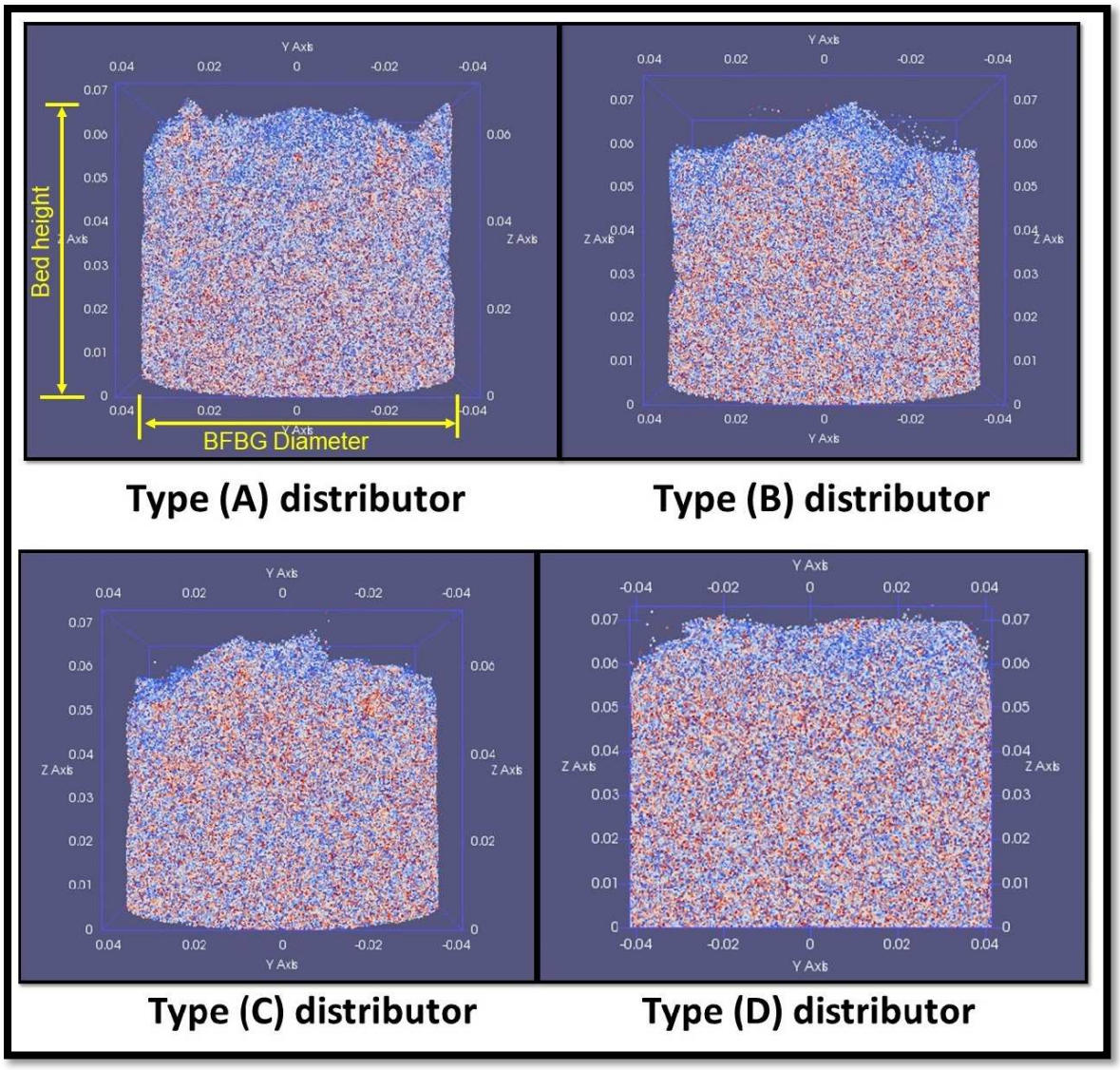

Figure 5.7. The effect of distributor type on the bed height and particles distribution for low superficial velocity.

Regarding particles distribution, the triangular arrangement distributors B and D showed more uniform particles distributed throughout the bed compared to the square arrangement distributors A and C. Moreover, high superficial velocities produced more uniform fluidised beds particles distribution than low superficial velocity beds. However, the particles distribution can be viewed and evaluated for any section in the BFBG at any specific time.

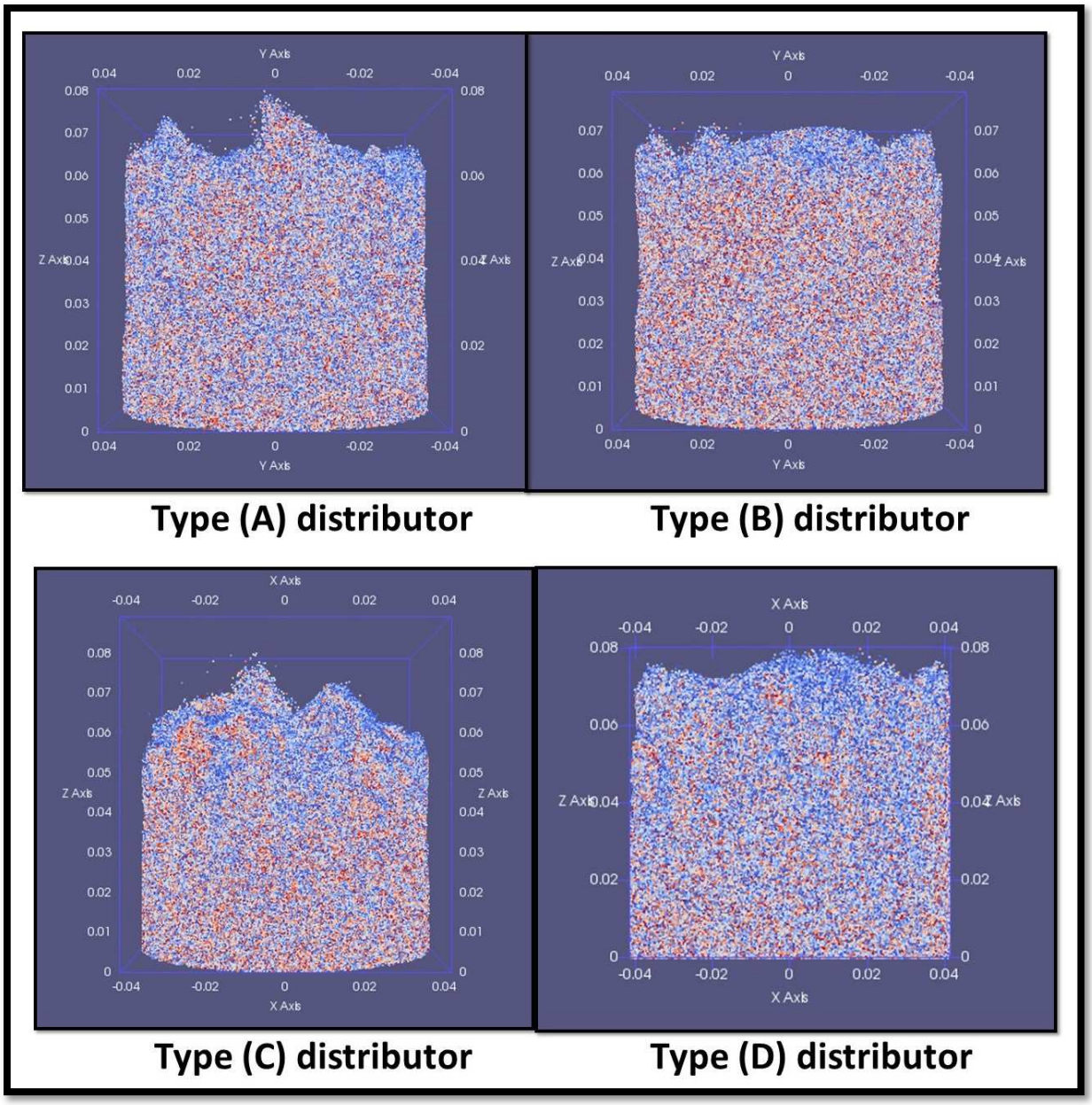

Figure 5.8. The effect of distributor type on the bed height and particles distribution for high superficial velocity.

In figures 5.7 and 5.8 the formed gas bubbles can be seen barely in the BFBG sides as small gaps between the BFBG walls and the particles bed. However, this is not enough to provide a comprehensive vision of the bubbles inside the fluidised bed. More details about the bubbles can be extracted from the bed void factor (voidage).

5.6.2. Void Fraction (Voidage) (ε)

The ratio between the volume of gas voids formed between solid particles and the total volume is called voidage or porosity. The value of voidage at the free gas zones and bubbles is unity while it is zero or a little above in particles agglomerate in the bed.

The time sequence of voidage variation at type D distributor with high gas superficial velocity when the batch injection starts is shown in figure 5.9. Figure 5.9 shows that particles reach the BFBG bottom from two sides at first then they cover the centre of the bottom (distributor's face). This may be due to the pre-injection of air which makes a fast air stream in the centre of the BFBG pushing the solid particles to the sides.

The variation of the void fraction on the bottom of the BFBG for the four distributors is shown in figure 5.10. The voidage variation was taken for low and high air superficial velocities. Figure 5.10 shows that the voidage highest values are concentrated above the distributor holes (the red spots). On the contrary, the lower values are concentrated in the zone between the holes (the blue spots). However, the concentrations of sand particles are not the same in all the zones between distributor holes. Generally, square arrangement distributors have more dark blue spots (particles agglomerates) than the triangular arrangement distributors. This may be related to the air distribution patterns as the triangular distributors have more holes than the square distributors for the same unit area. This provides more opportunity to scavenge the sand particles from the dead zones (between holes).

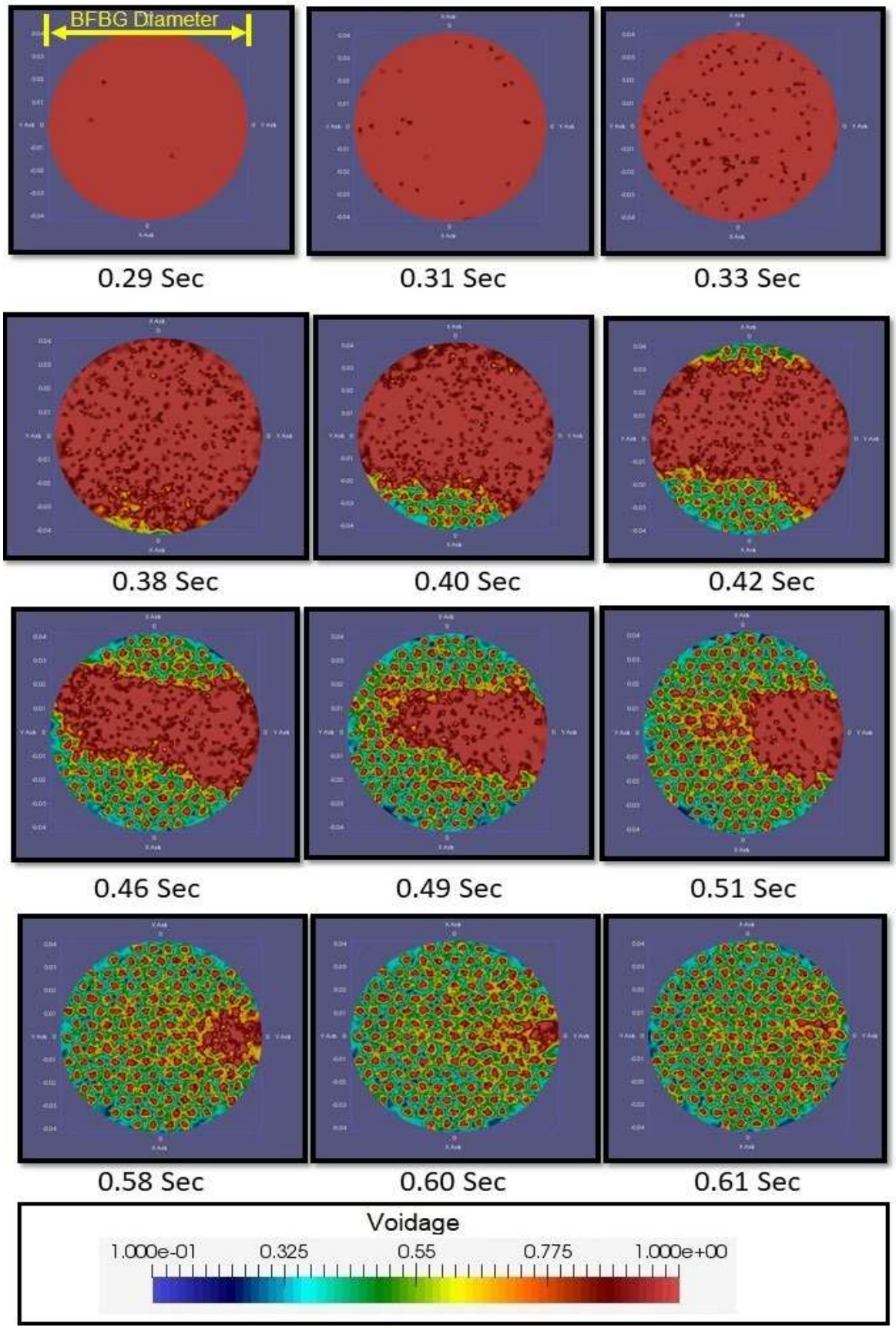

Figure 5.9. The time sequence of falling the sand particles to the bottom of BFBG in terms of voidage.

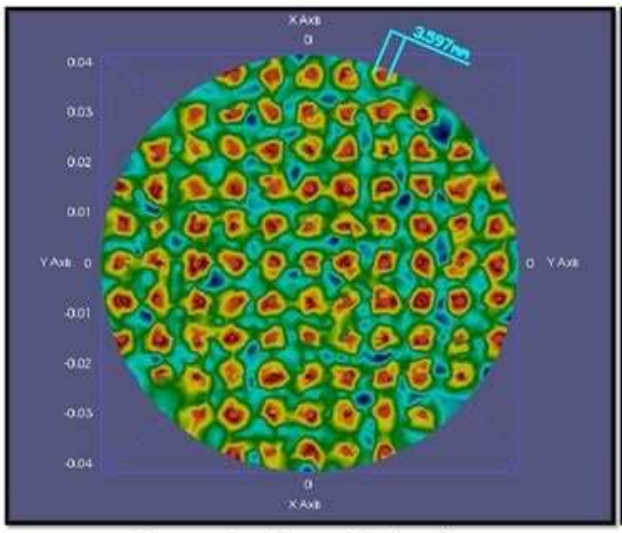

Type A - Low Velocity

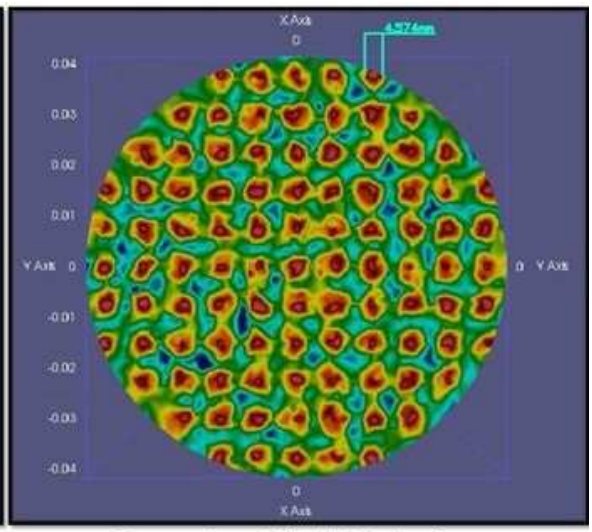

Type A – High Velocity

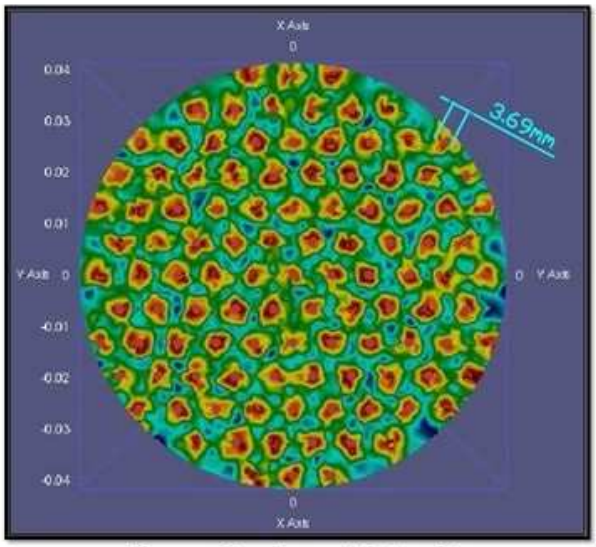

Type B - Low Velocity

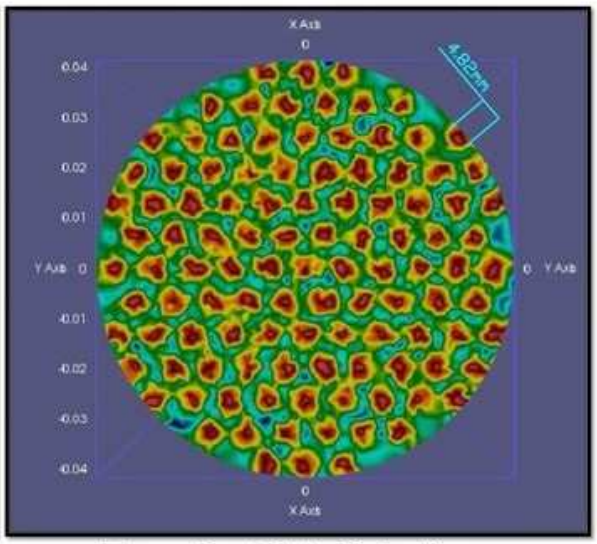

Type B – High Velocity

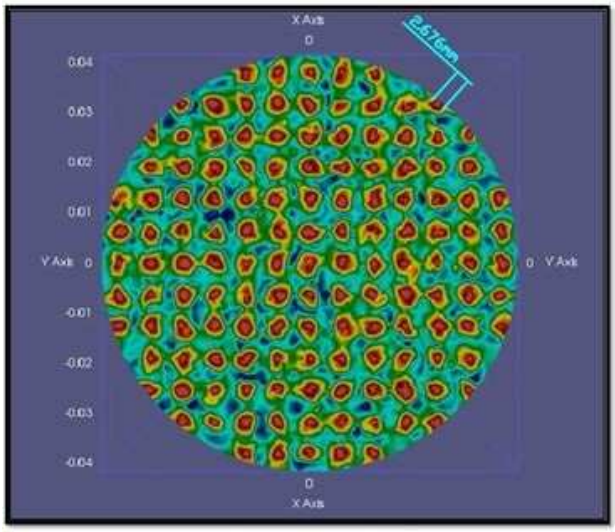

Type C – Low Velocity

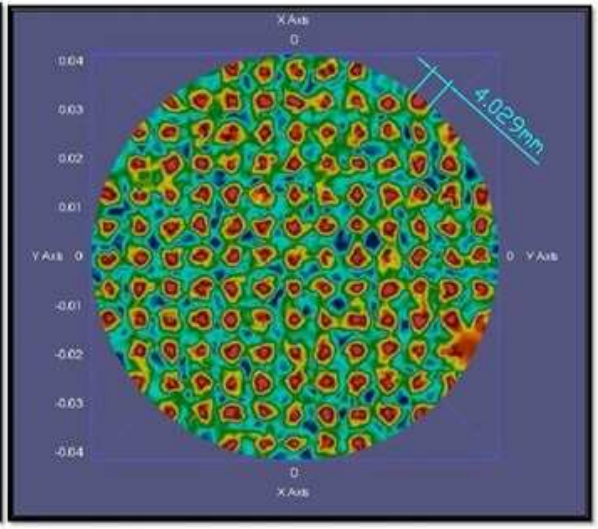

Type C – High Velocity

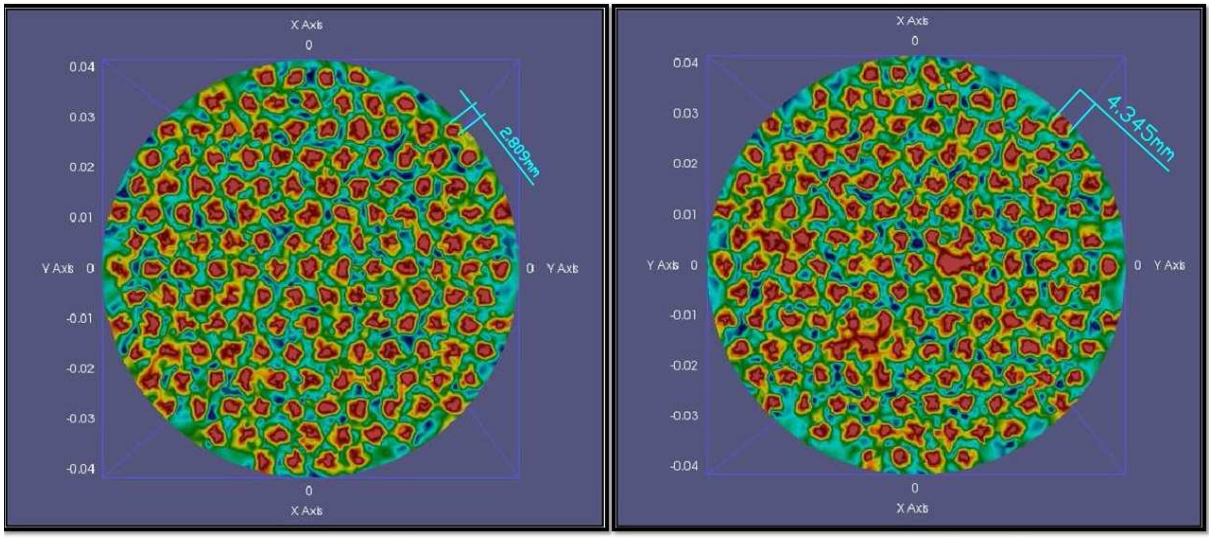

Figure 5.10. Voidage variation at the BFBG bottom for the four distributors A, B, C and D.

The high voidage zones (the dark red spots) above the distributor holes are varying from type to type and from the low to high superficial velocities as shown in figure 5.10. The average voidage diameter for the type A distributor is 3.597 mm for the low velocity case and 4.574 mm, while the value reaches 3.69 mm and 4.82 mm for type B at low and high velocity, respectvily. Moreover, the voidage diameters for type C and D distributors are 2.676 mm, 4.029 mm, 2.809 mm and 4.345 mm for low and high velocites, respectvily, as shown in figure 5.10.

The expansion ratio of the free zone above the orifice can be calculated be the following equation:

$$\text{Expansion ratio} = \frac{\text{Free zone area } (\text{mm}^2)}{\text{Orifice area } (\text{mm}^2)} \quad \text{..... 5-4}$$

The comparison between the expansion ratio of free air area above the orifice to the orifice area for the eight cases is illustrated in table 5-8.

Table 5-8. The free air expansion ratio (voidage ≅ 1) above the orifices for the two superficial velocities.

Distributor type	Superficial velocity	Orifice diameter (mm)	Orifice area $(mm)^2$	Free air zone diameter (mm)	Free air zone area $(mm)^2$	Expansion ratio
A	Low	2	3.1416	3.597	10.161	3.234
A	High	2	3.1416	4.574	16.431	5.230
B	Low	2	3.1416	3.69	10.694	3.404
B	High	2	3.1416	4.82	18.246	5.808
C	Low	1	0.7854	2.676	5.624	7.161
C	High	1	0.7854	4.029	12.749	16.232
D	Low	1	0.7854	2.809	6.197	7.890
D	High	1	0.7854	4.345	14.827	18.879

Table 5-8 shows the clear difference between the performance of large and small holes distributors and the square and triangular arrangement distributors. Generally, small holes distributors C and D provided much more expanding ratio than the large holes distributors A and B. Moreover, the triangular distributors provided expansion ratio a little larger than the square arrangement distributors. The small orifice distributors provided free air area ratio of more than two times the ratio in the large orifice distributors for the low superficial velocity cases and more than three times for the high superficial velocity cases.

This may happen due to the high air velocity in the small orifices which can scavenge more sand particles above these orifices due to high air momentum. However, this action is very important for particle fluidisation and mixing.

5.6.3. Voidage and bubble size and velocity

The formation of gas bubbles in the BFBG is crucial to provide better hydrodynamic conditions. The bed voidage has the ability to reveal the bubbles inside the bed and determining their size and velocity.

5.6.3.1. BFBG with Type A Distributor

Bubble formation in this type has been recorded with an average bubble diameter of 16.64 mm in the low superficial velocity case and 52.26 mm for the high superficial velocity case, see figures 5.11 and 5.13 respectively. For the low-velocity case, the bubble diameter has increased to be 26.8 mm in just 0.04 sec with an average upward bubble velocity of 339 mm/sec. However, the upward movement of the air bubble is not constant all the time but generally, the bubble velocity increased as it goes up. This may be due to the decrease in the pressure with the bed height. Figure 5.12 shows the variation of the upward bubble movement through the BFBG bed with time for the low superficial velocity conditions.

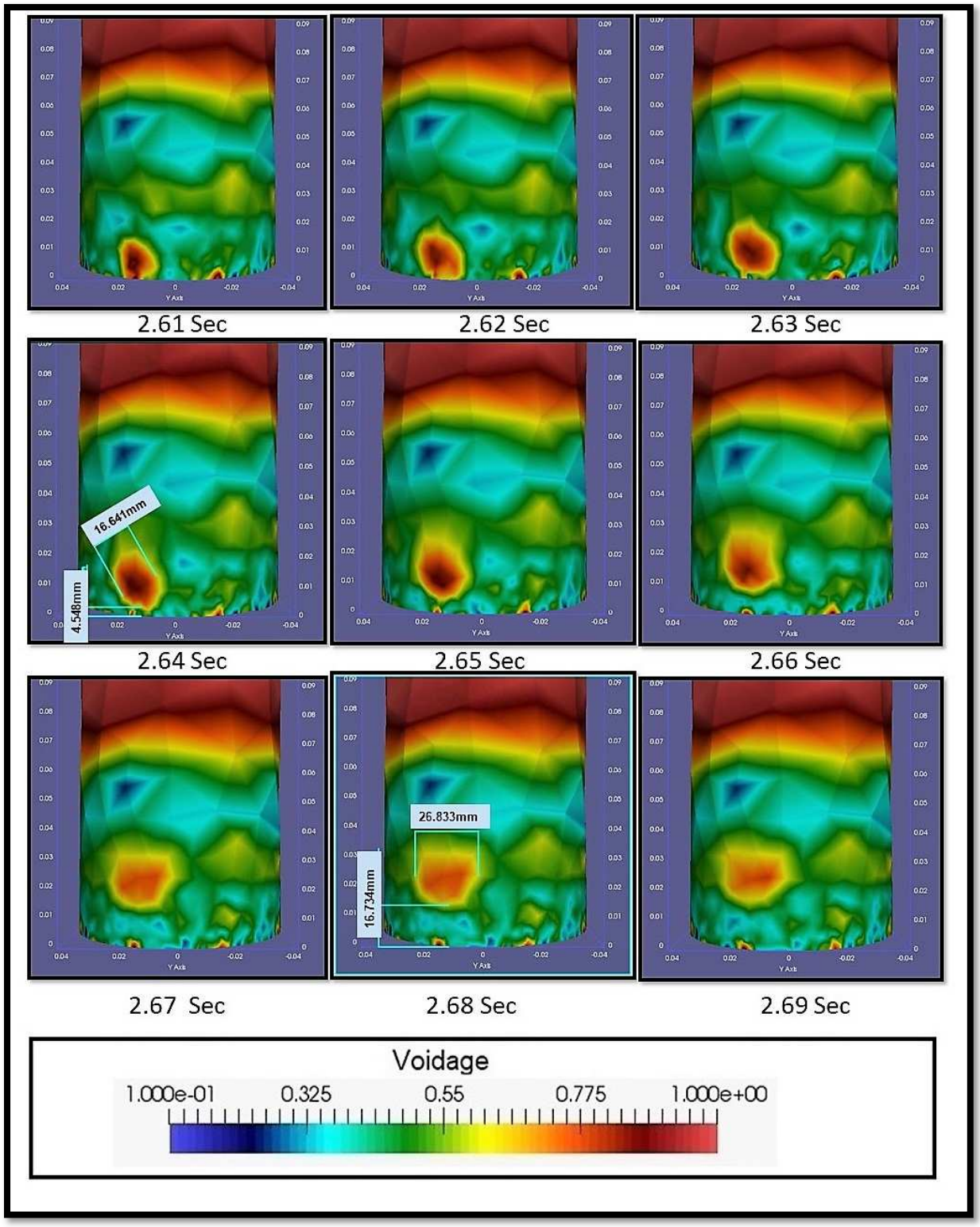

Figure 5.11. Bubble size and upward movement in BFBG with type A distributor and low superficial air velocity.

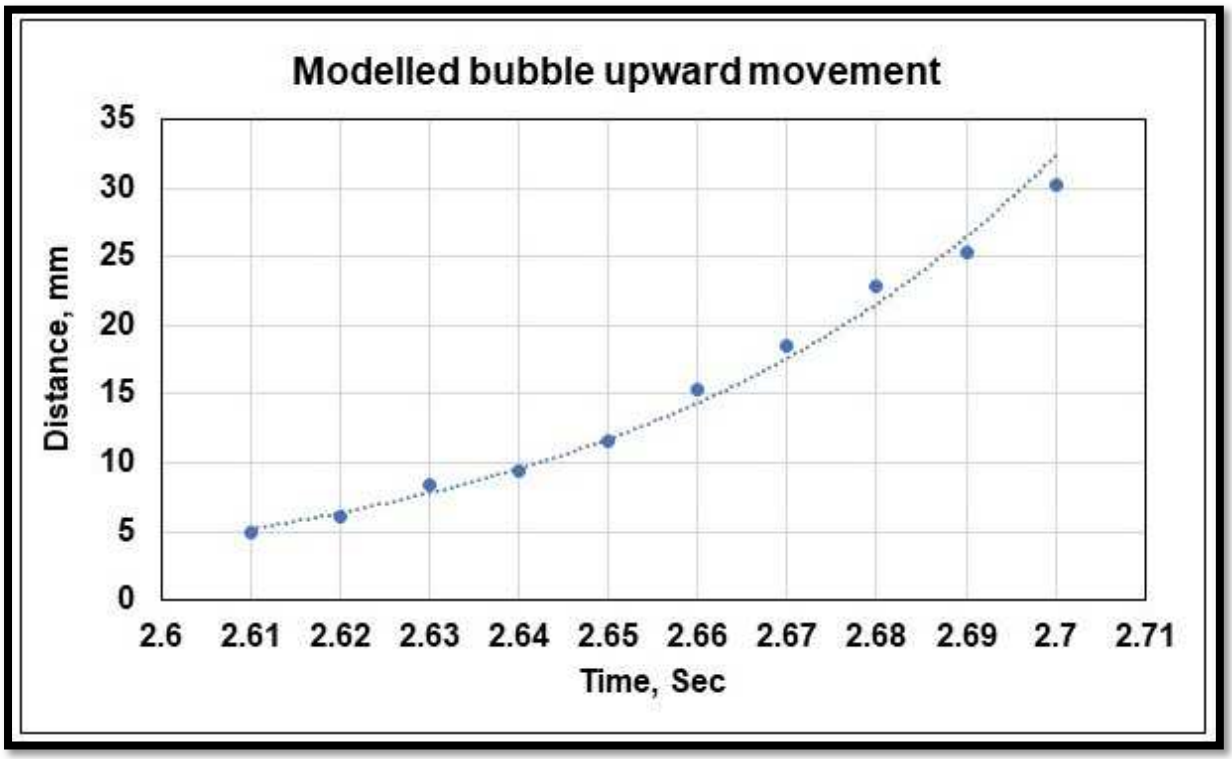

Figure 5.12. Modelled time variation of air bubble motion through the bed of BFBG with type (A) distributor at low superficial velocity.

In the high-velocity case, the size of the big bubble shown in figure 5.13 has slightly increased when the bubble rises to the bed surface and then bursts. The bubble diameter has increased by less than 2 mm in 0.04 sec with an average upward bubble velocity of 495 mm/sec. Figure 5.14 shows the variation of the upward bubble movement through the BFBG bed with time for the high superficial velocity conditions.

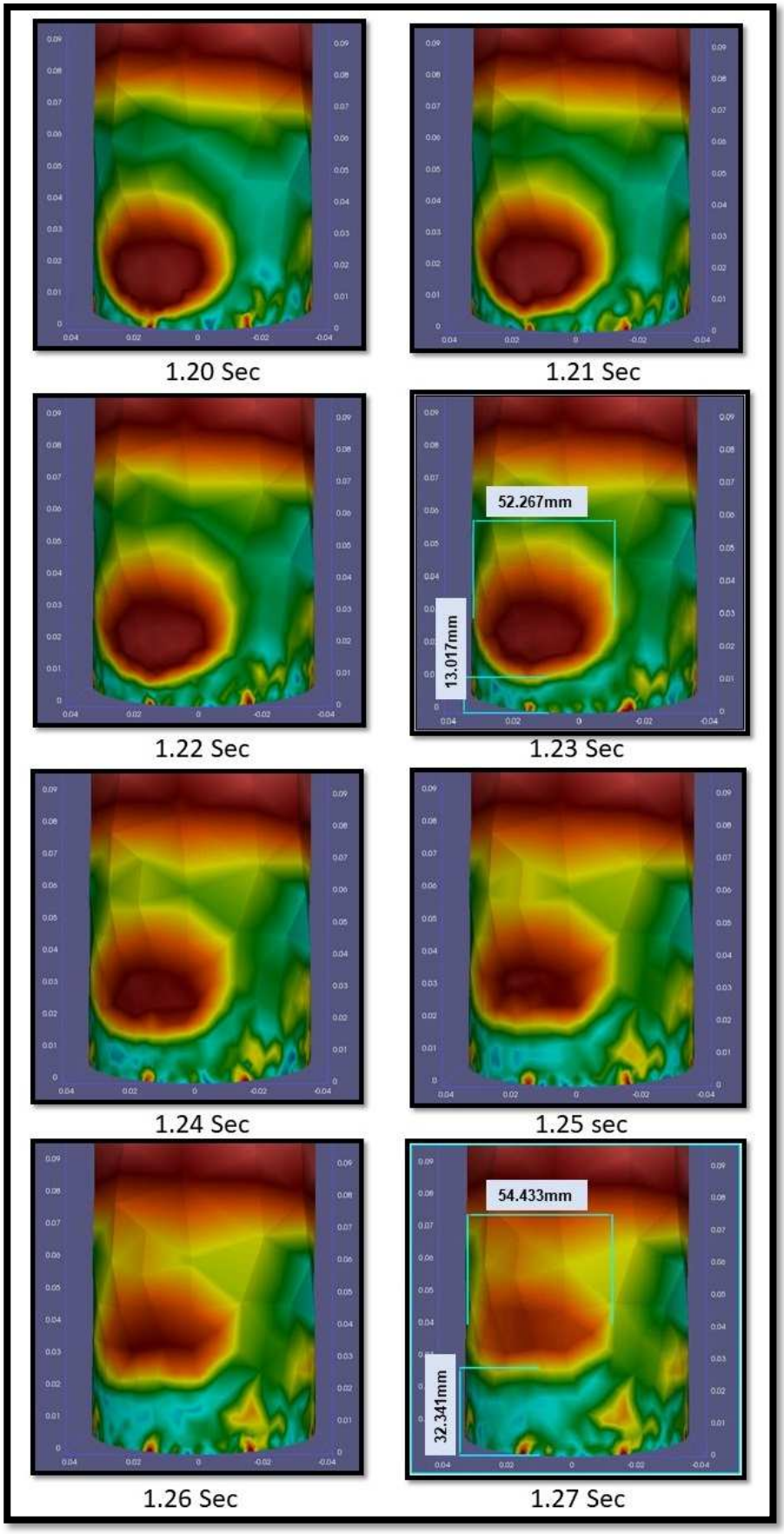

Figure 5.13. Bubble size and upward movement in BFBG with type A distributor and high superficial air velocity.

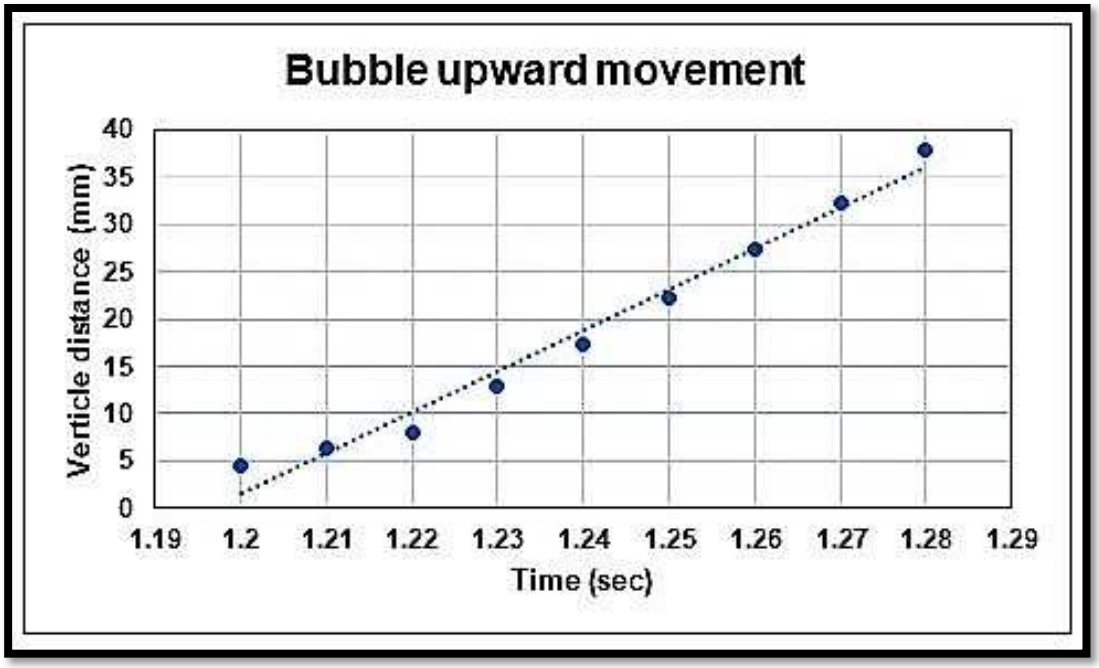

Figure 5.14. Modelled time variation of air bubble movement through the bed of BFBG with type (A) distributor at high superficial velocity.

5.6.3.2. BFBG with Type B Distributor

In type B distributor, bubbles formation has also been noticed in the eight-seconds simulation. For the low superficial velocity case, the bubble size is relatively smaller than the bubble formed in type A for the low velocity, see figure 5.15. This bubble has very low upward velocity compared to the type A bubble.

However, in the high superficial velocity case, a larger void cloud has been noticed covering almost the entire BFBG width with a 23.7 mm maximum height. The cloud formation and fading in the bed is 0.016 seconds. Figure 5.16 shows the formation and fading of a void cloud in the BFBG with type B distributor.

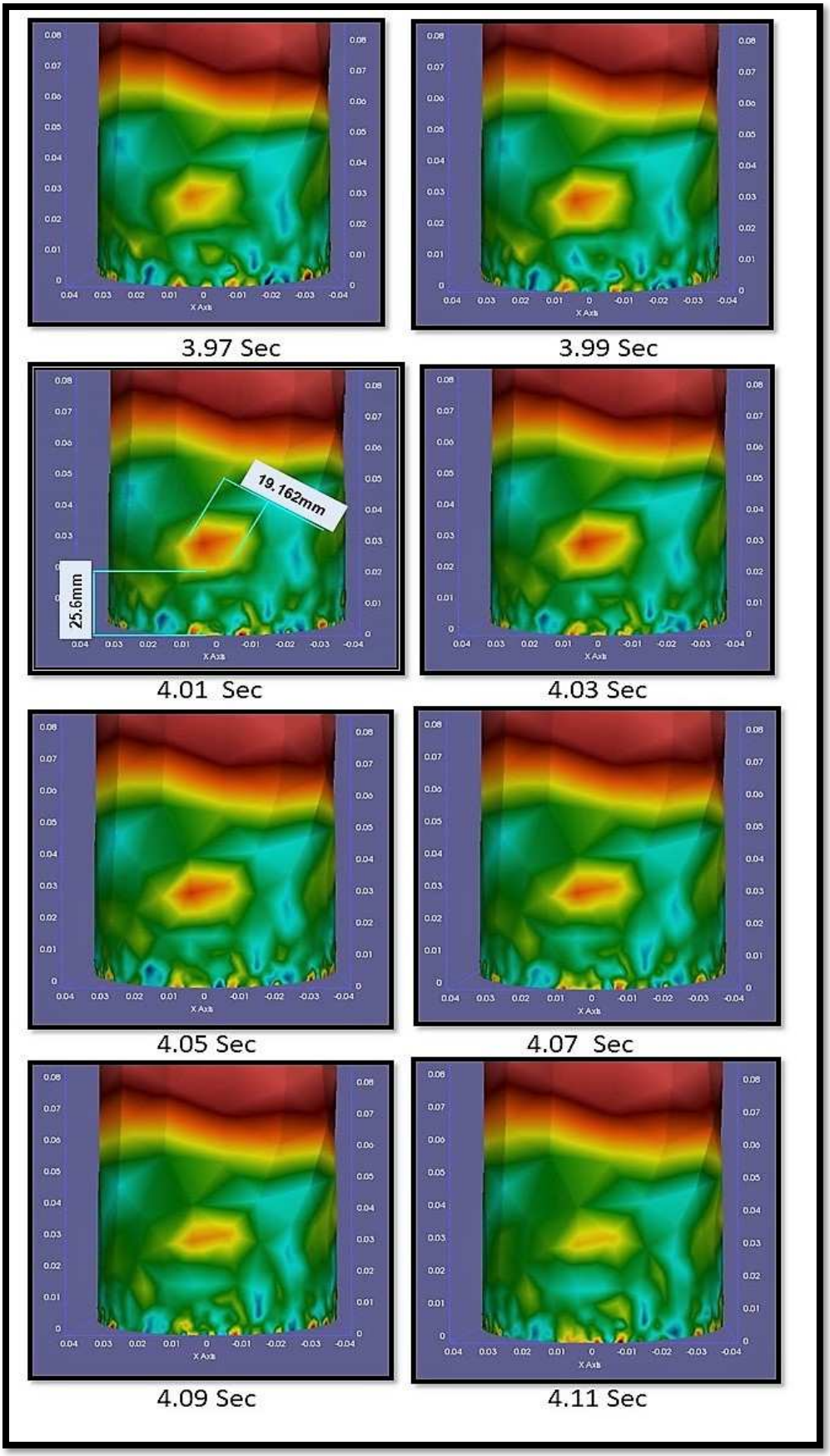

Figure 5.15. Bubble size and upward movement in BFBG with type B distributor and low superficial air velocity.

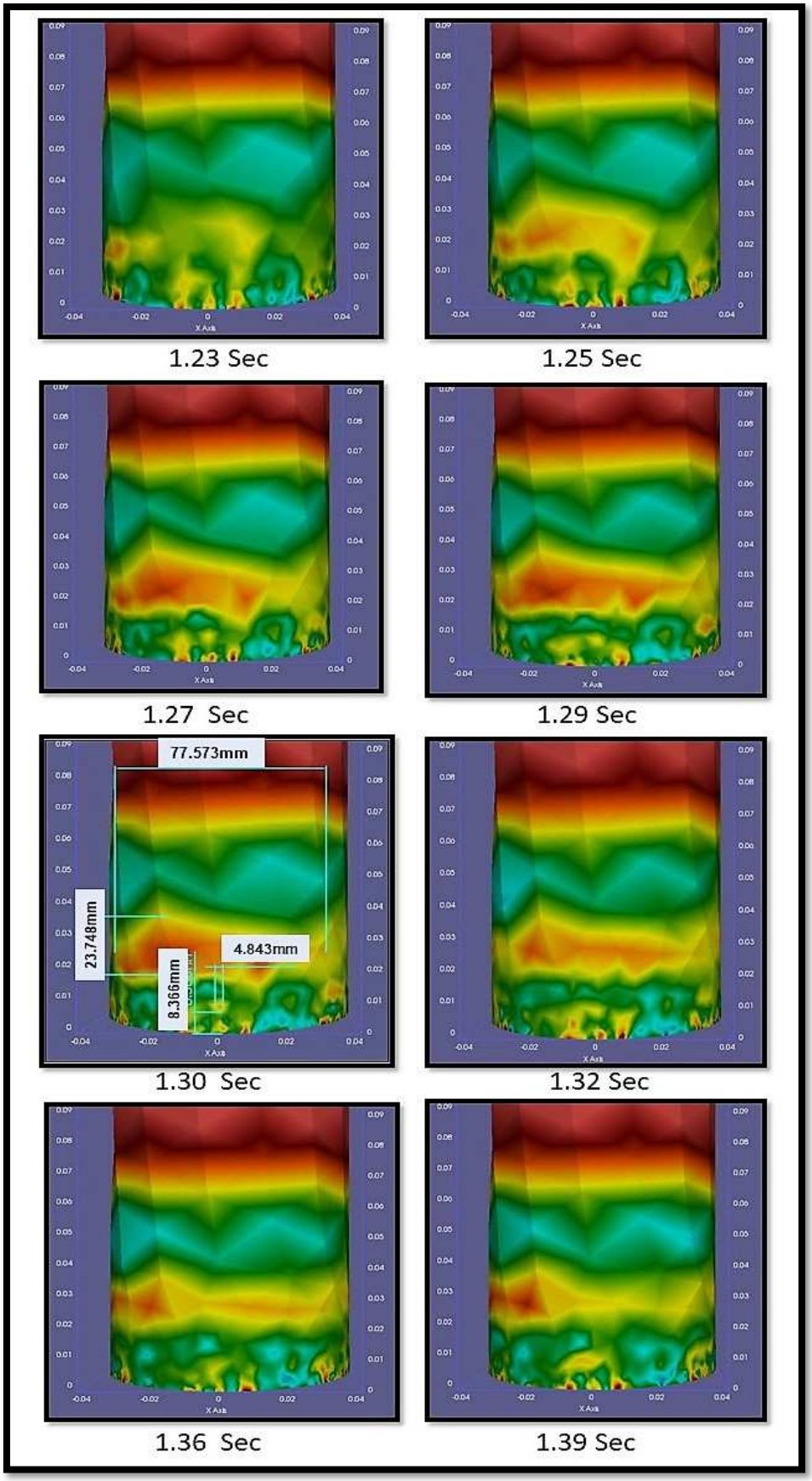

Figure 5.16. Void cloud formation and fading in BFBG with type B distributor and high superficial air velocity

5.6.3.3. BFBG with Type C Distributor

The BFBG with this distributor also showed a bubble formation in the eight seconds simulation. In the low-velocity case a medium size bubble 9.3 mm with an average bubble velocity of 192 mm/sec formed. This bubble size and velocity are comparatively lower than in the type A distributor for the same low-velocity case. This may be due to the difference in orifice diameter as type A has the large orifice which injects a large amount of air compared to the C type orifice. However, the number of bubbles in type C is more than that in type A. Moreover, there is an agglomeration of particles of about 18.5 mm size which has been captured in the bed near the wall. Figure 5.17 shows the formation of a bubble and particles agglomerate in the BFBG with type C distributor at low superficial velocity.

The bubble in the high superficial velocity case with type C distributor is also smaller than in the type A distributor and slower. The average size and velocity of this bubble are 36 mm and 275 mm/sec respectively. In figure 5.18 the bubble formation and fading time sequence in BFBG with type C distributor at high velocity have illustrated. However, figure 5.19 shows the time variation of the bubble upward movement in the BFBG with type C distributor at high superficial velocity.

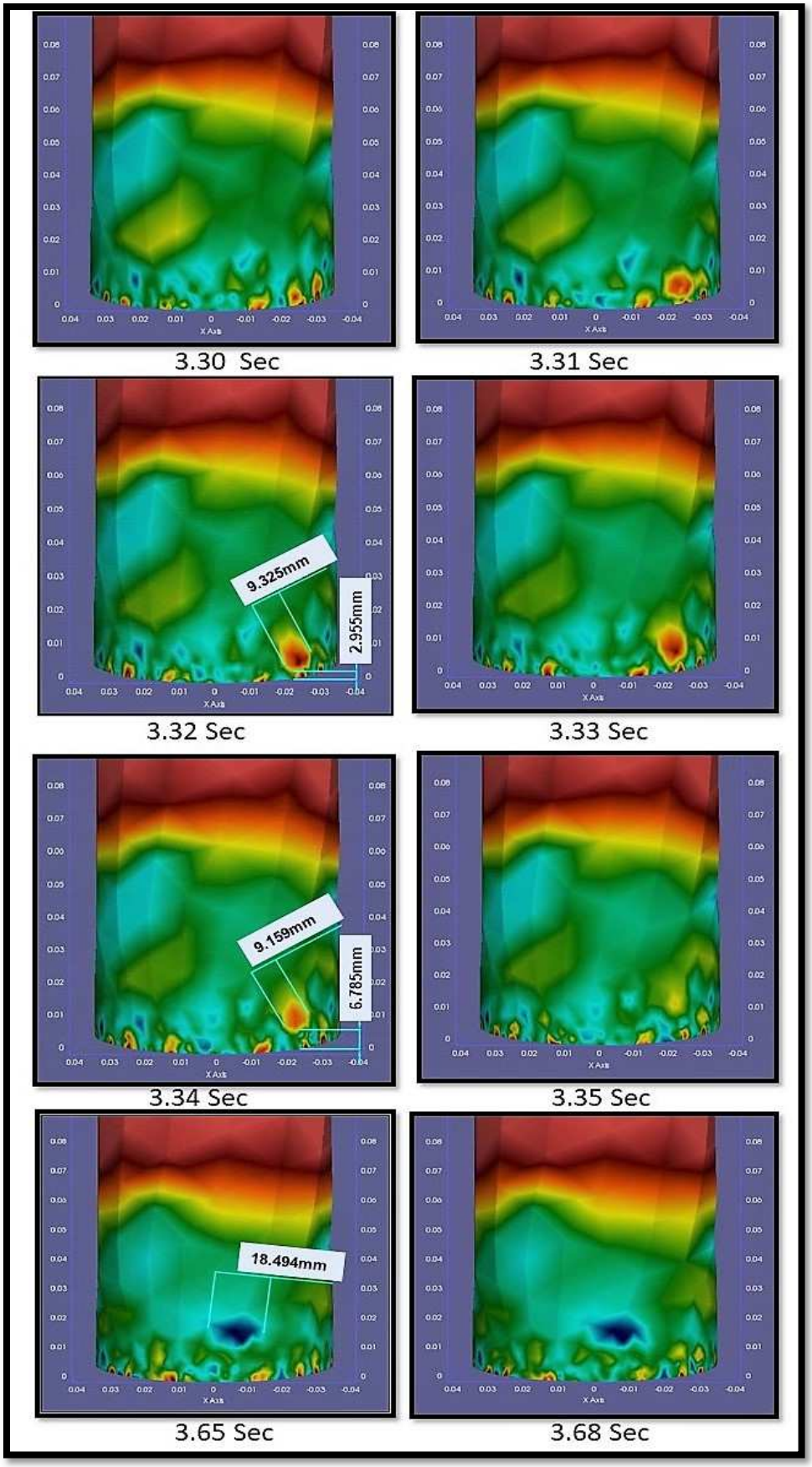

Figure 5.17. Bubble and particles agglomerate formation in BFBG with type C distributor at a low superficial air velocity.

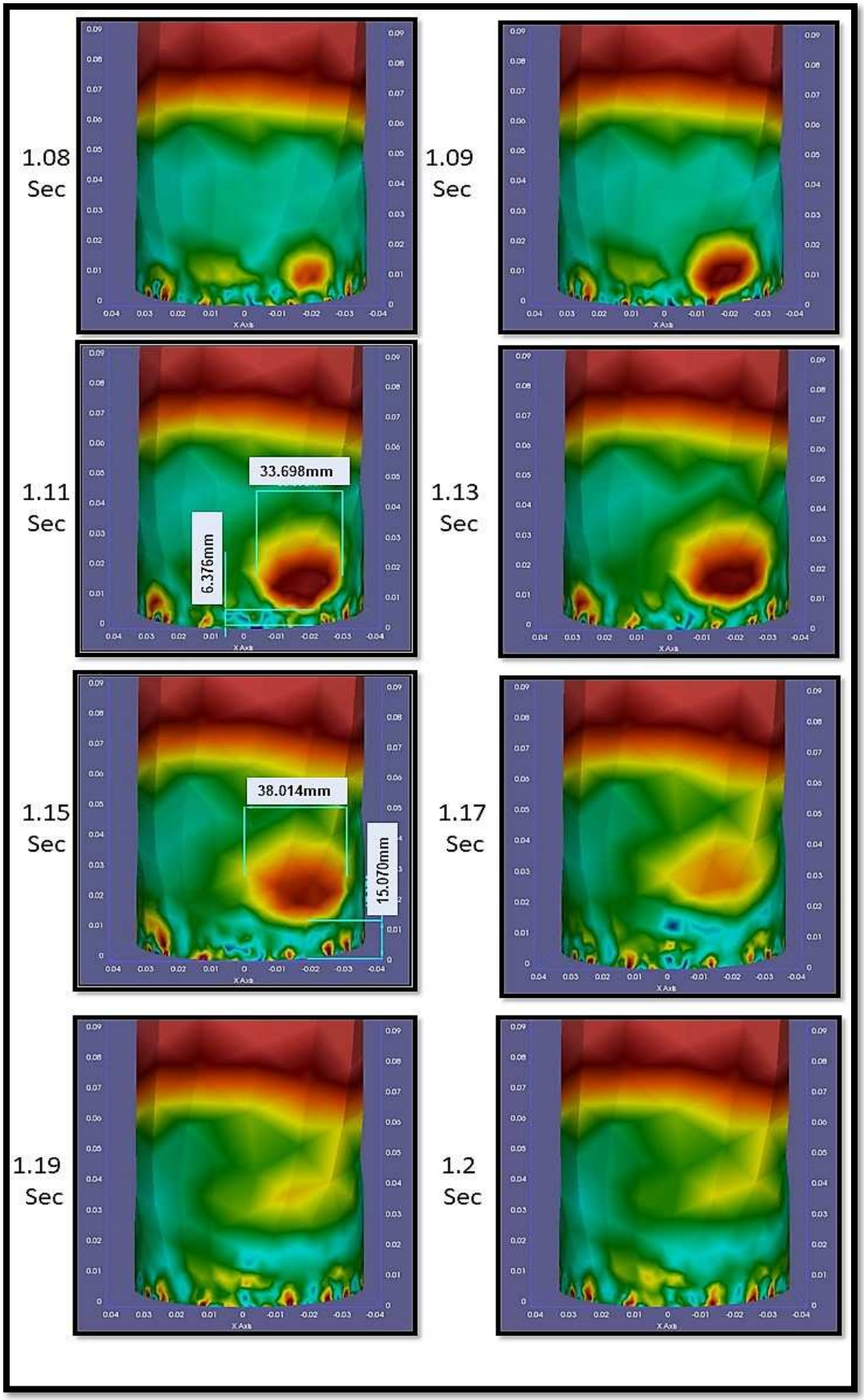

Figure 5.18. Bubble size and upward movement in BFBG with type C distributor and high superficial air velocity.

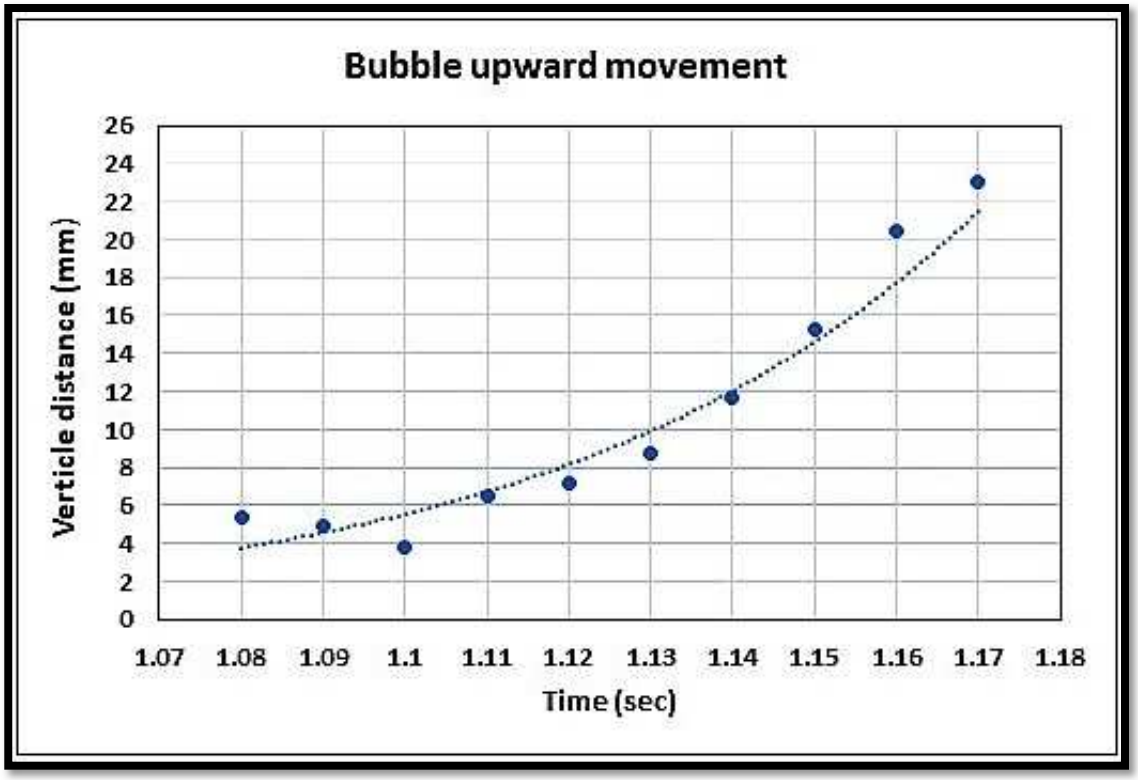

Figure 5.19. Modelled time variation of air bubble movement through the bed of BFBG with type (C) distributor at high superficial velocity.

5.6.3.4. BFBG with Type D Distributor

The eight seconds simulation for the BFBG with type D distributor discloses a large number of bubble formation in different sizes and positions for both low and high superficial velocity cases as shown in figure 5.20 and 5.23.

In the low superficial velocity case, the formation and bursting of a large bubble have been presented in figure 5.21 and the time changing of bubble position is illustrated in figure 5.22. The average velocity of the bubble shown in figure 5.21 is 391 mm/sec which is higher than the velocity of bubbles in the other distributors in terms of low superficial velocity.

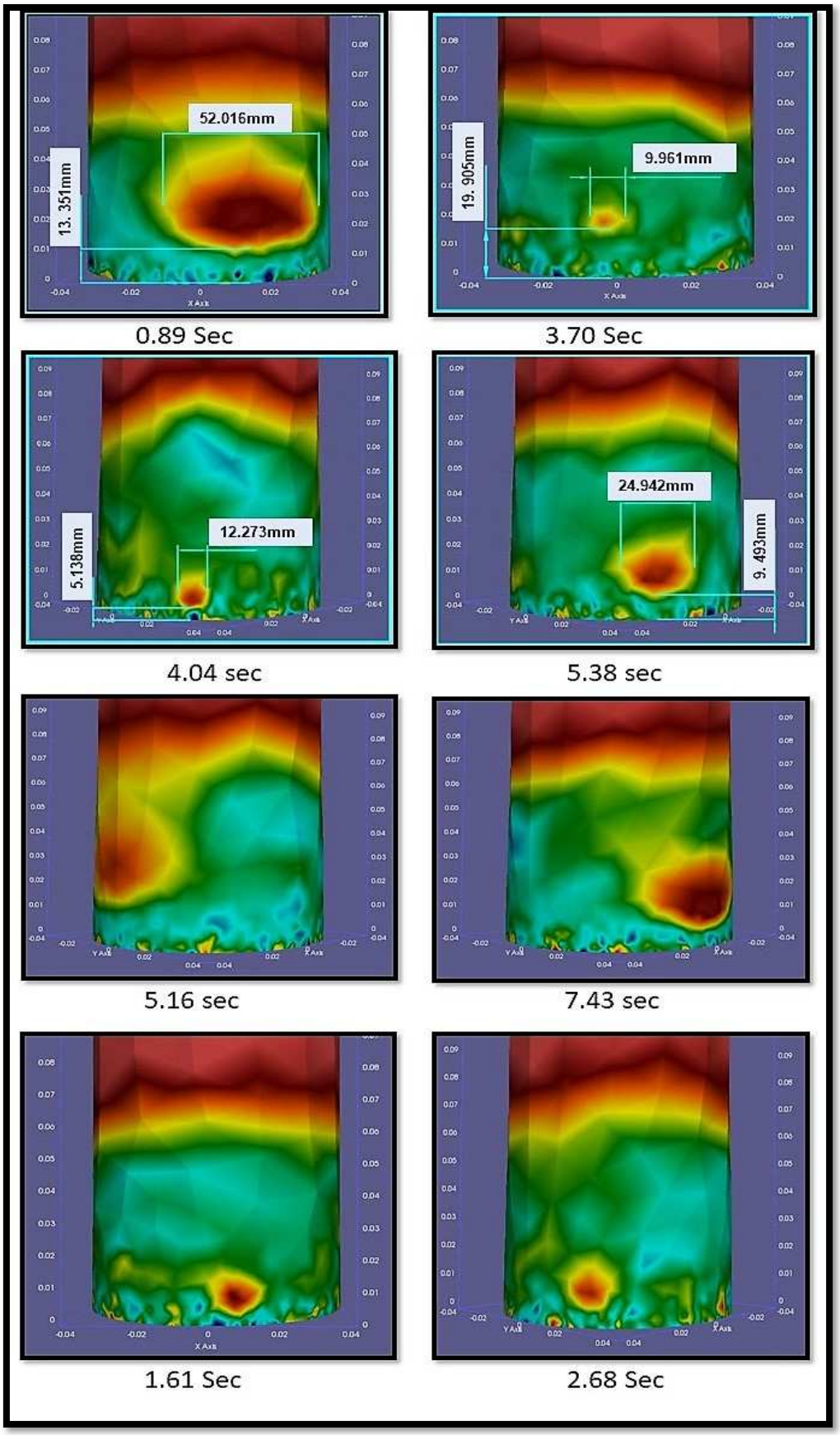

Figure 5.20. Different bubbles size and position in BFBG with type D distributor and low superficial velocity.

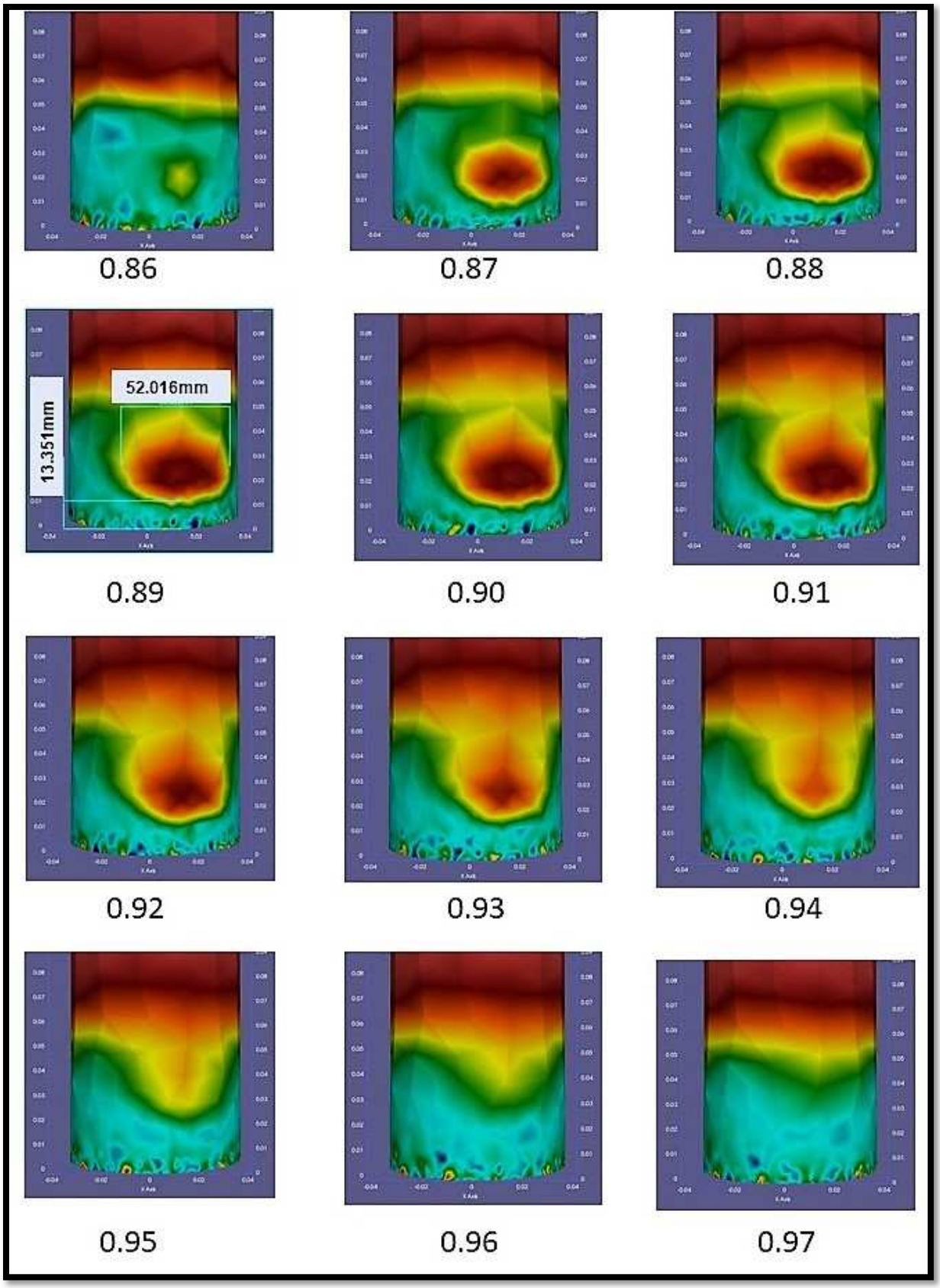

Figure 5.21. Large bubble formation and fading in the BFBG with type D distributor at the low superficial velocity.

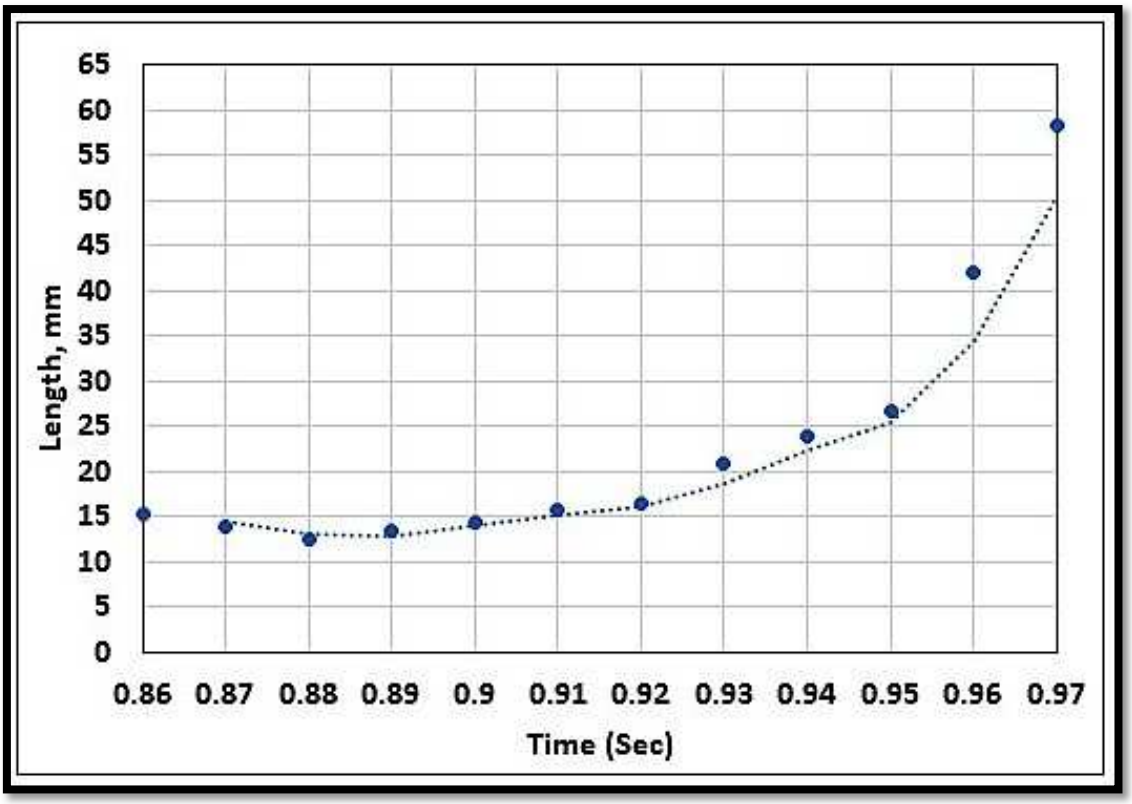

Figure 5.22. Time variation of the bubble position through the BFBG with type D distributor at low superficial velocity.

Regarding the high superficial velocity case, the number of formed bubbles is more than in the low-velocity case and the bubble velocity is higher see, figure 5.23. The formation and bursting stages of a large bubble in the high-velocity case are shown in figure 5.24. The average bubble velocity, in this case, is 437 mm/sec.

The time variation of the bubble size and upward movement for the bubble are shown in figures 5.24 and 5.25. In figures 5.22 and 5.25 the bubble size rapidly decreases as the bubble reach the bed surface and burst. While the bubble upward movement (velocity) increases as the bubble reach the bed surface. This happens due to the decrease in pressure drop which decreases the drag force on the bubble.

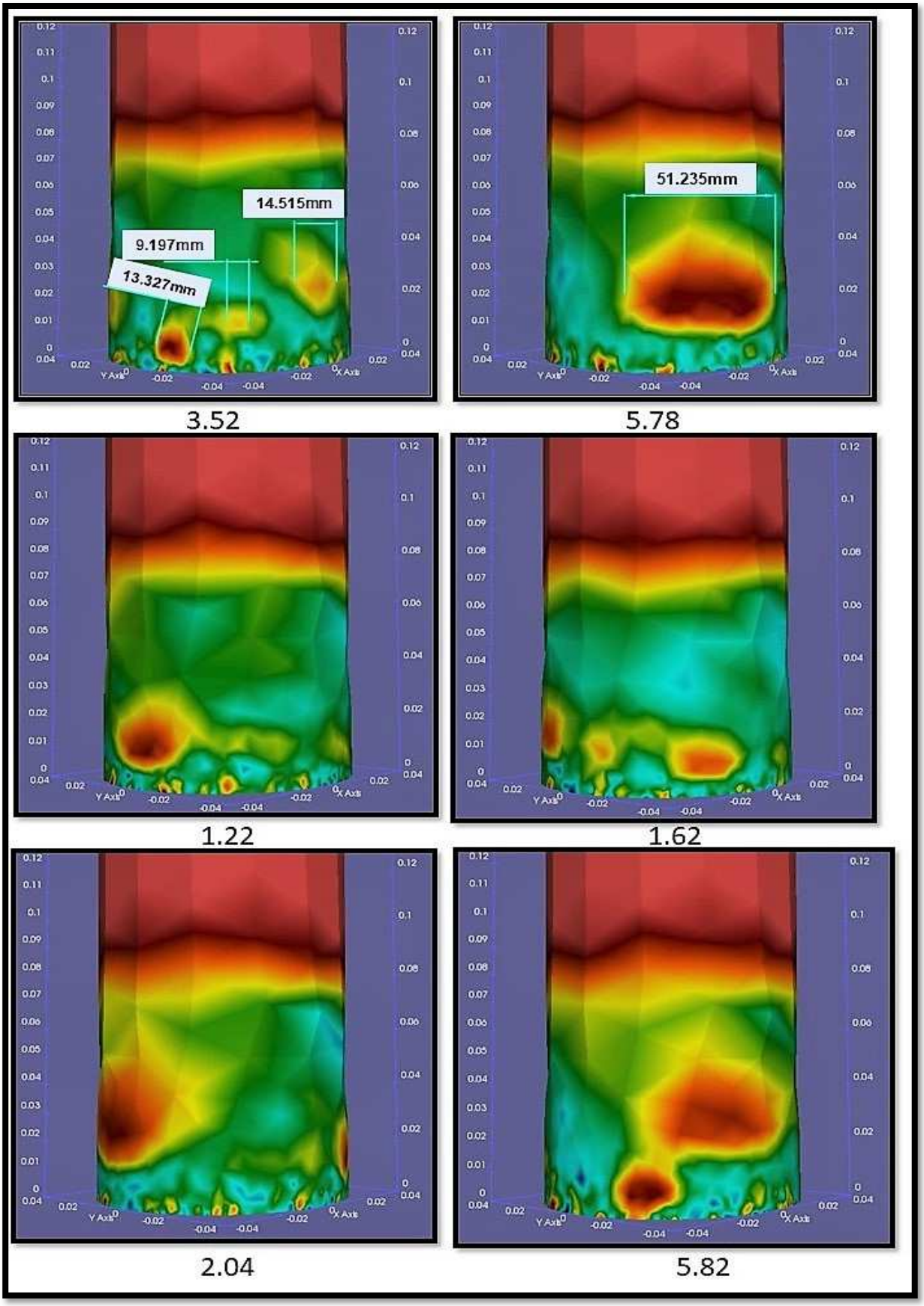

Figure 5.23. Different bubbles size and position in BFBG with type D distributor and high superficial velocity.

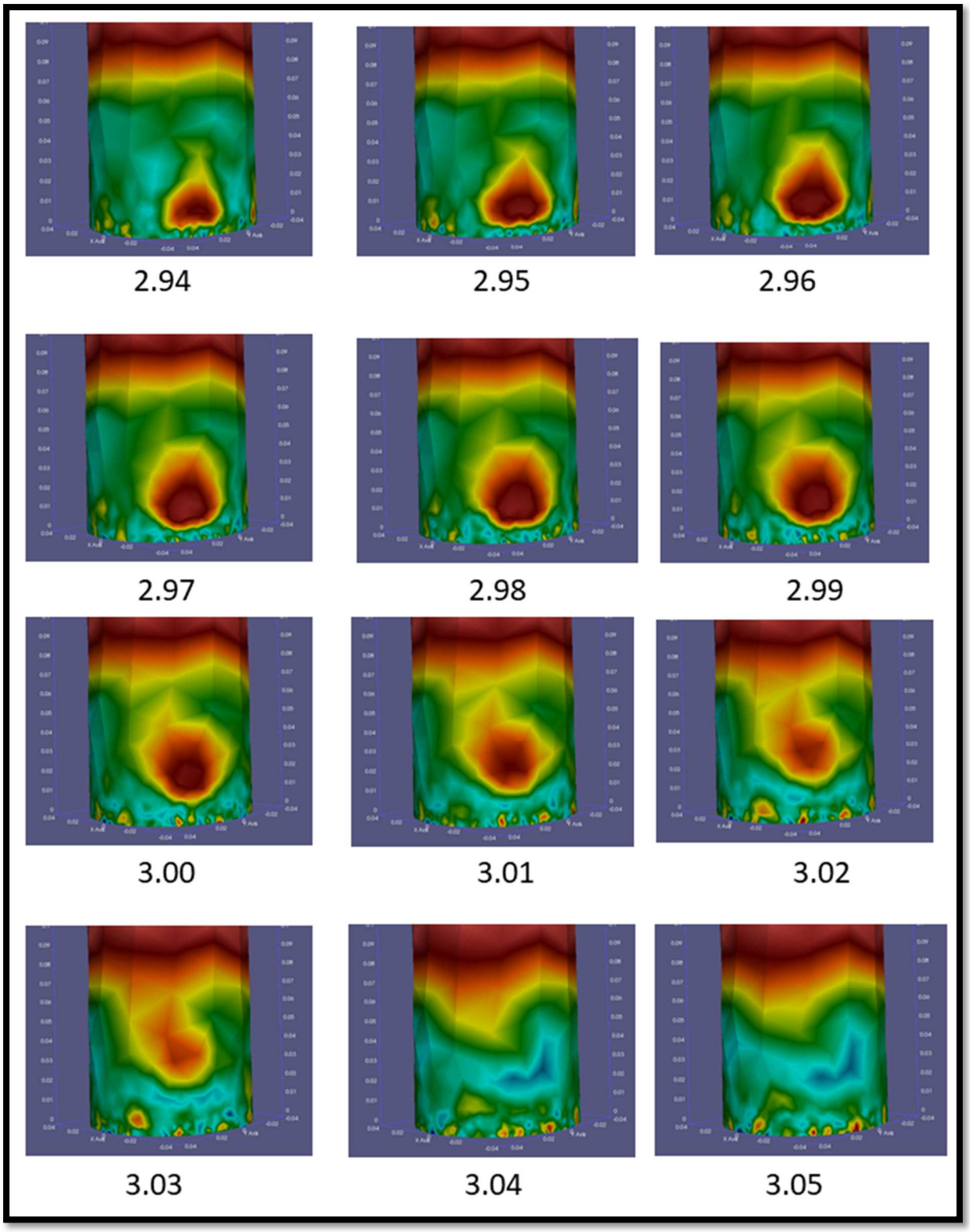

Figure 5.24. Large bubble formation and fading in the BFBG with type D distributor at the high superficial velocity.

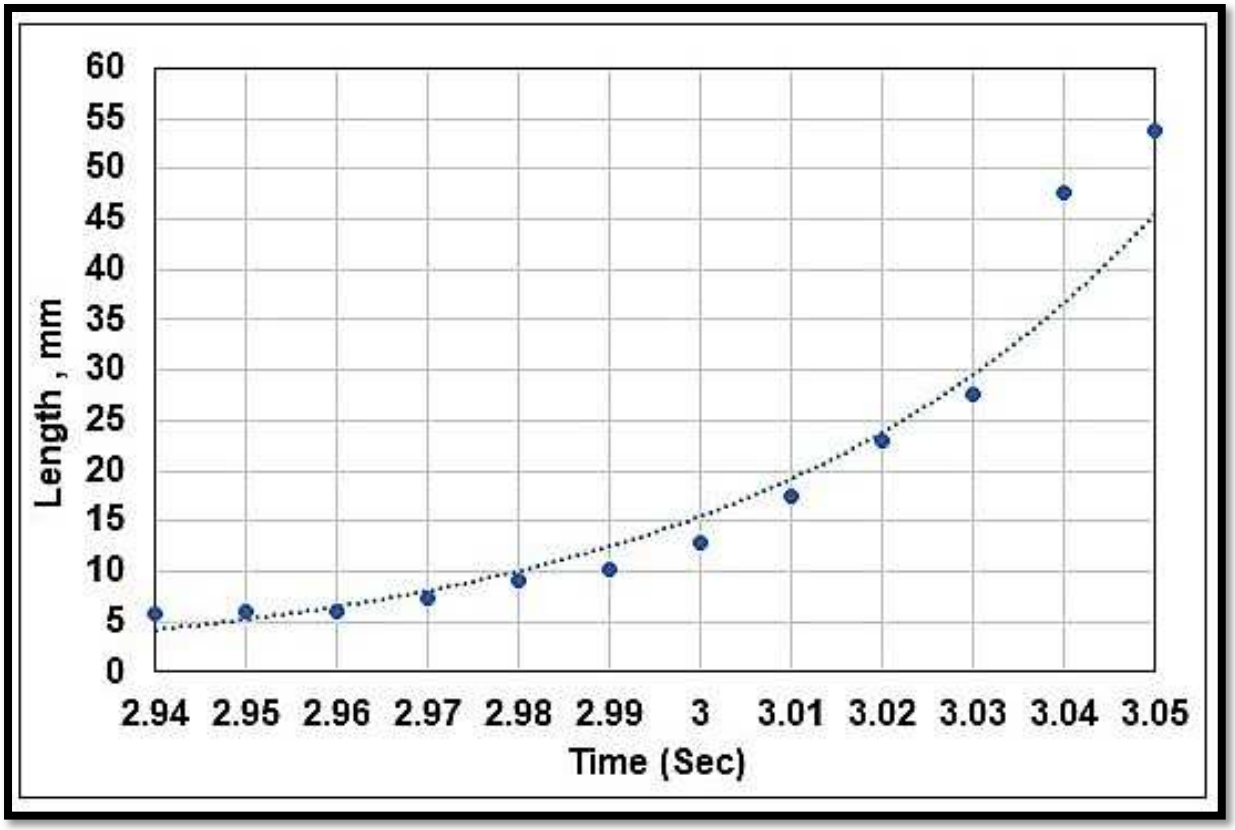

Figure 5.25. Time variation of the bubble position through the BFBG with type D distributor at high superficial velocity.

Generally, the simulation can provide more details about the bubble size and movement in every section of the BFBG and at any time of the simulation.

5.6.4. Pressure Drop (Δp)

The pressure drop is an important hydrodynamic factor in the fluidised bed reactors which is one of the distinguishing characteristics between the fluidised bed and the packed bed. Generally, the pressure drop at any point inside the BFBG is caused by the weight of the particles column above this point. Hence, it is high at the points located in dense particles zones and low in the void zones. The present simulation provides the opportunity to determine the pressure drop at any position inside the BFBG and at any time through the simulation.

5.6.4.1. BFBG with Type A Distributor

The pressure drop contours in the BFBG with type A distributor for the low and high superficial velocities are illustrated in figures 5.26 and 5.27. These pressure contours are the average among all the contours in the eight-second simulation. Each layer of the contour represents a pressure drop range starting from the bottom (the dark red) which represents the high-pressure zone to the highest point of the bed (the dark blue) which represents the lower pressure zone. A closer look at the two contours shows the difference in the spacing between the pressure drop layers. The high-velocity case has large spacing compares to the low-velocity case. This is related to the bed expansion, the high-velocity case has larger bed expansion than the other case which can provide better contact between the gas and solid particles.

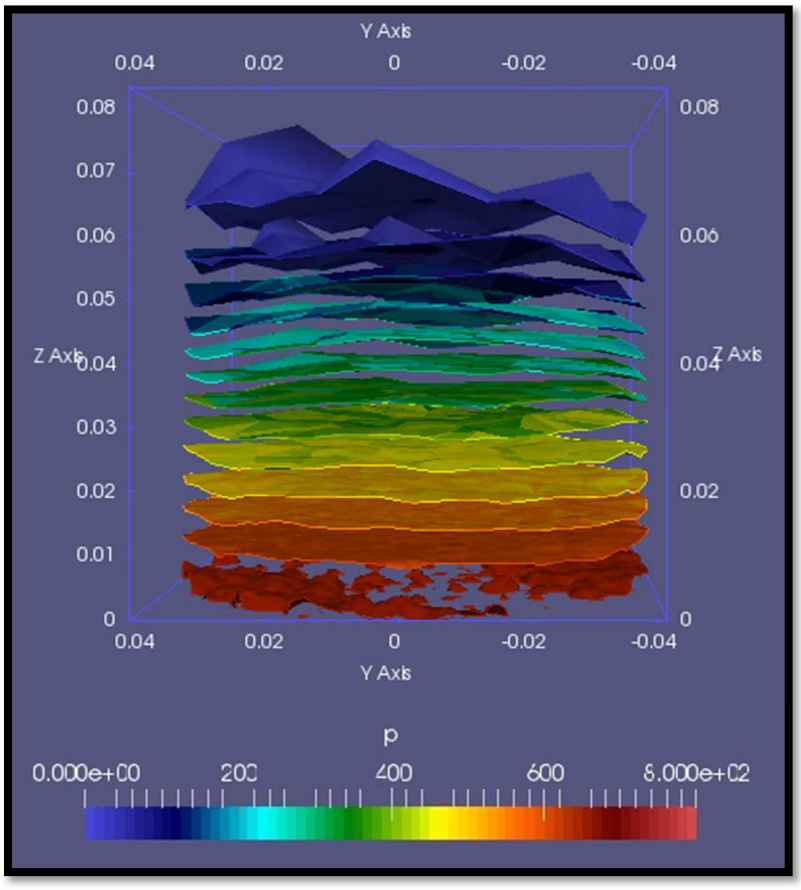

Figure 5.26. Pressure drop contour in the BFBG with type A distributor at low superficial velocity.

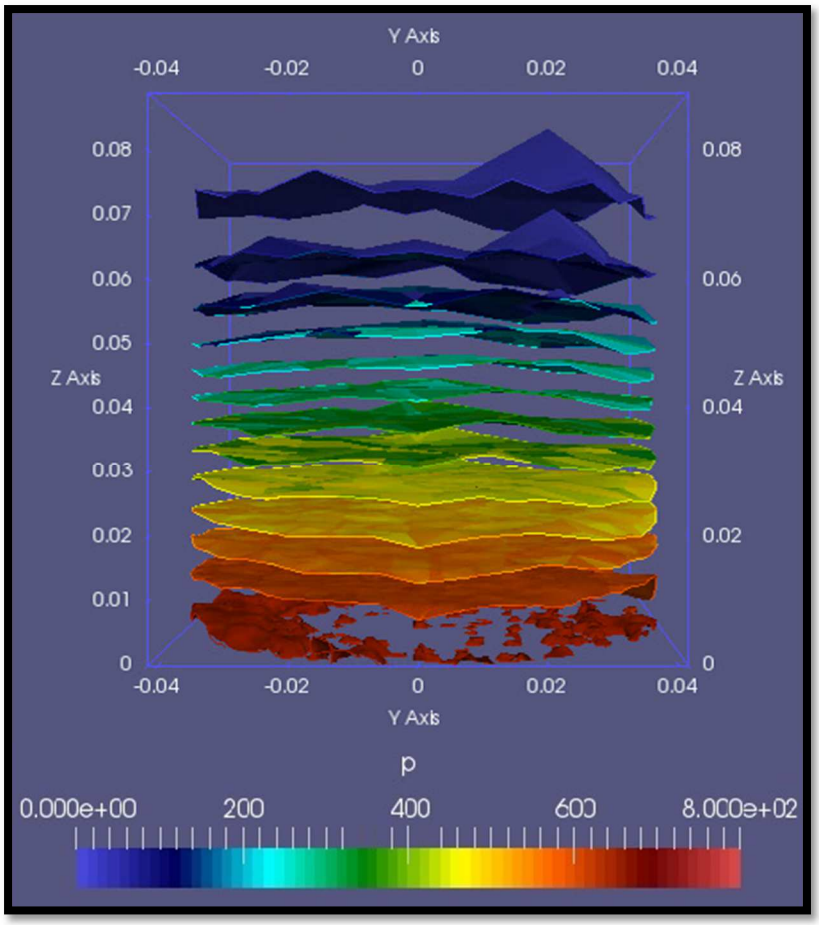

Figure 5.27. Pressure drop contour in the BFBG with type A distributor at high superficial velocity.

The effect of bed expansion on pressure drop can be seen in figures 5.28 and 5.29. In figure 5.28, the pressure drops at a point located 20 mm above the centre of type A distributor for the low and high-velocity cases are presented for the eight second simulation time. The low expansion of bed in the low-velocity case raises the pressure drop at this point more than the other case. However, this fact reversed at 80 mm above the centre of the distributor, i.e. the pressure of the high-velocity case is higher than in the low-velocity case. This is caused as more solid particles reach this level in the high-velocity case which raises the pressure drop as shown in figure 5.29.

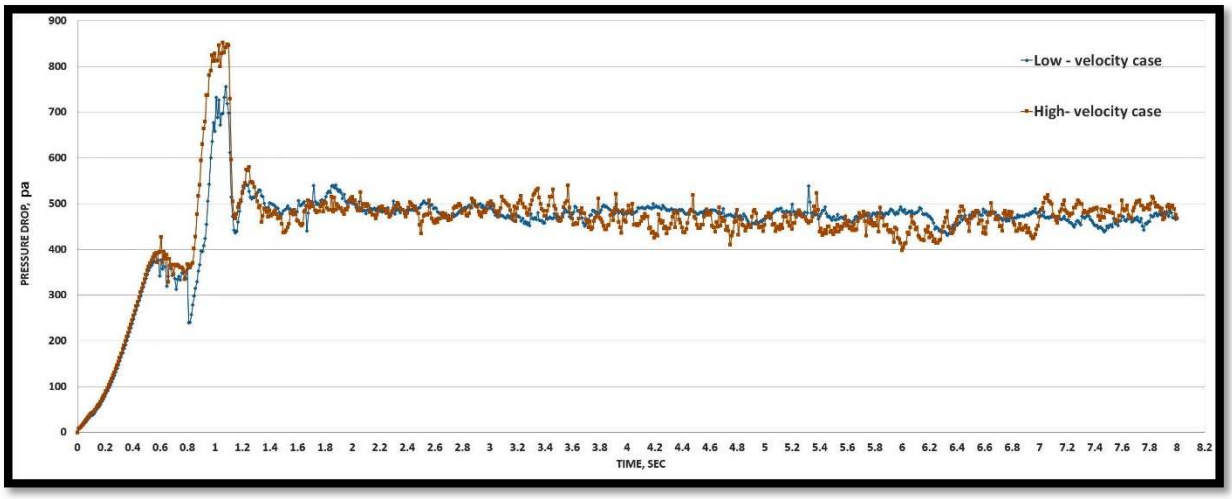

Figure 5.28. The time variation of pressure drop at a point located 20 mm above the centre of type A distributor.

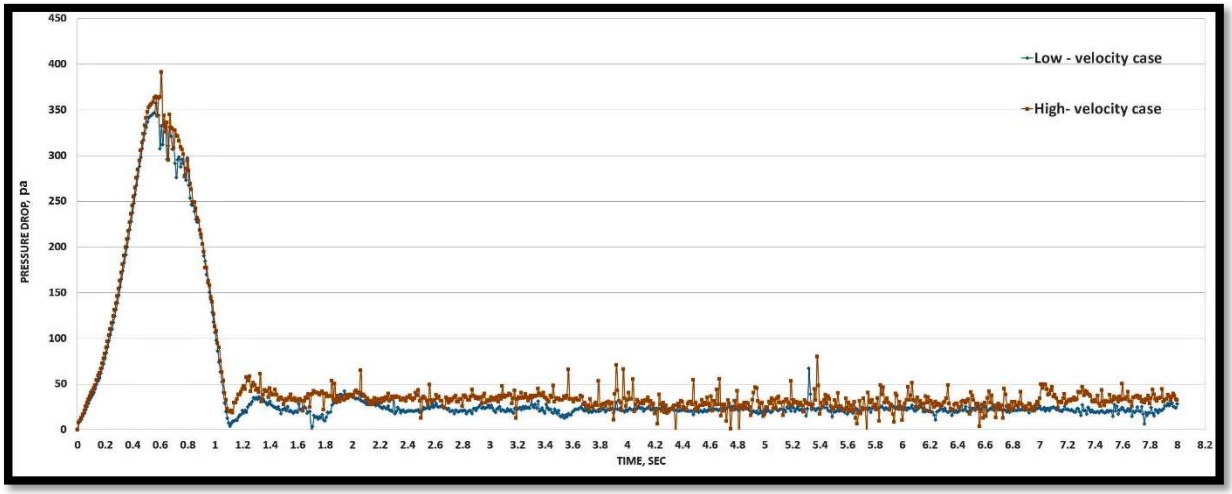

Figure 5.29. The time variation of pressure drop at a point located 80 mm above the centre of type A distributor.

5.6.4.2. BFBG with Type B Distributor

In the type B distributor, the same happens regarding the bed expansion, i.e. the high superficial velocity case has more expansion than the low superficial velocity case. Figures 5.30 and 5.31 show the pressure drop contours in the low and high-velocity cases in the BFBG with type B distributor.

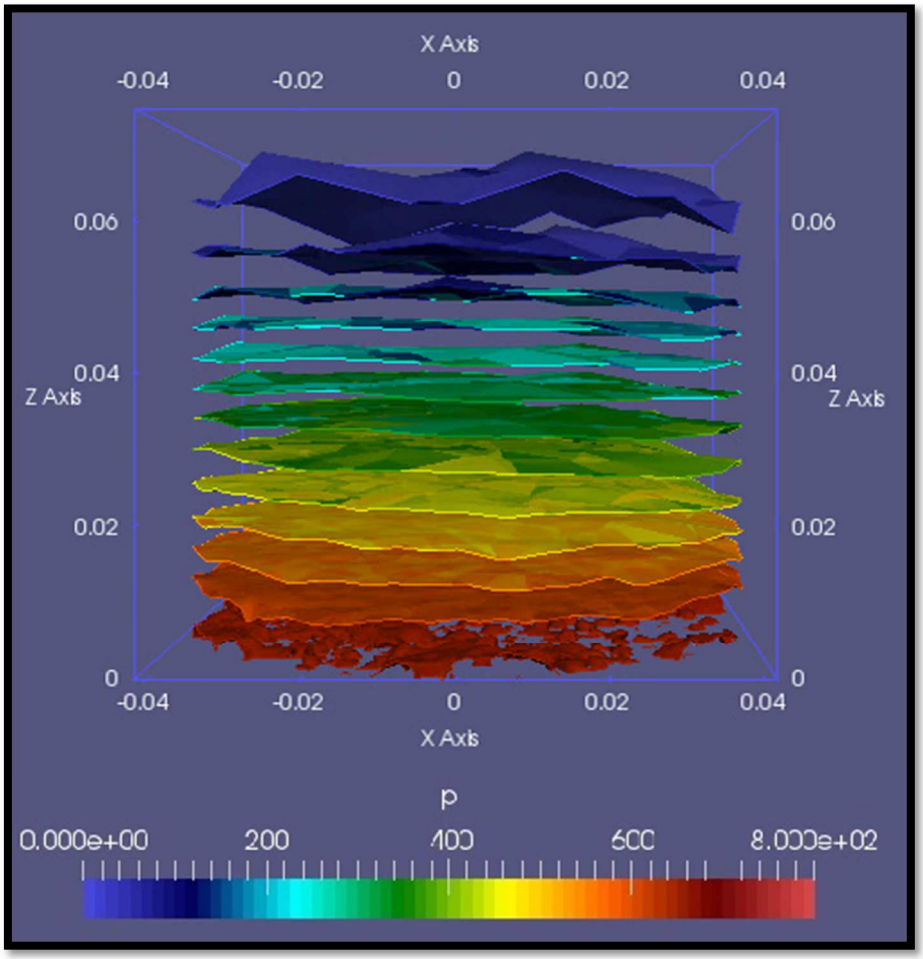

Figure 5.30. Pressure drop contour in the BFBG with type B distributor at low superficial velocity.

However, type B distributor provides a higher pressure drop in the high-velocity case than the low-velocity case in both low and high level above the distributor. Figures 5.32 and 5.33 illustrate the time variation of pressure at level 20 mm and 80 mm above the centre of the type B distributor respectively. The peaks in these graphs represent the pressure rise at the batch injection of sand particles.

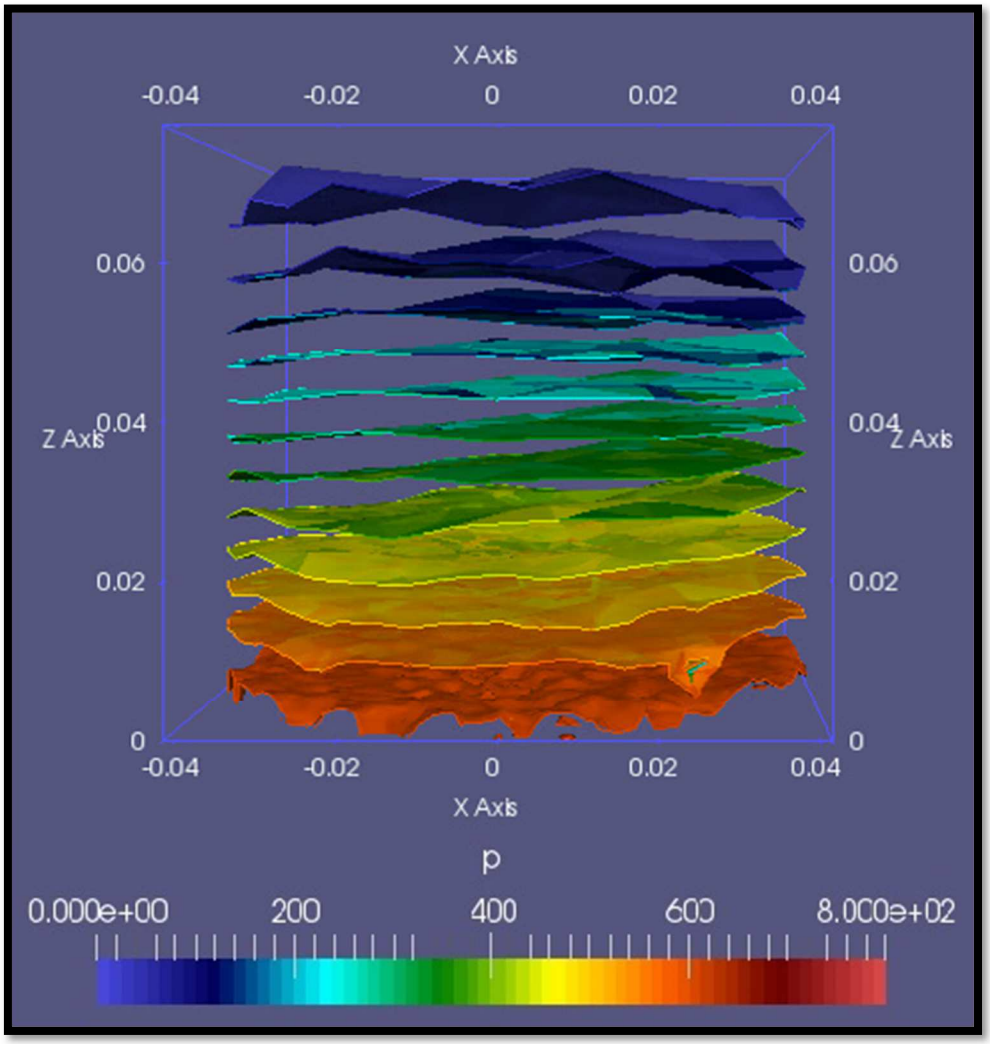

Figure 5.31 Pressure drop contour in the BFBG with type B distributor at high superficial velocity.

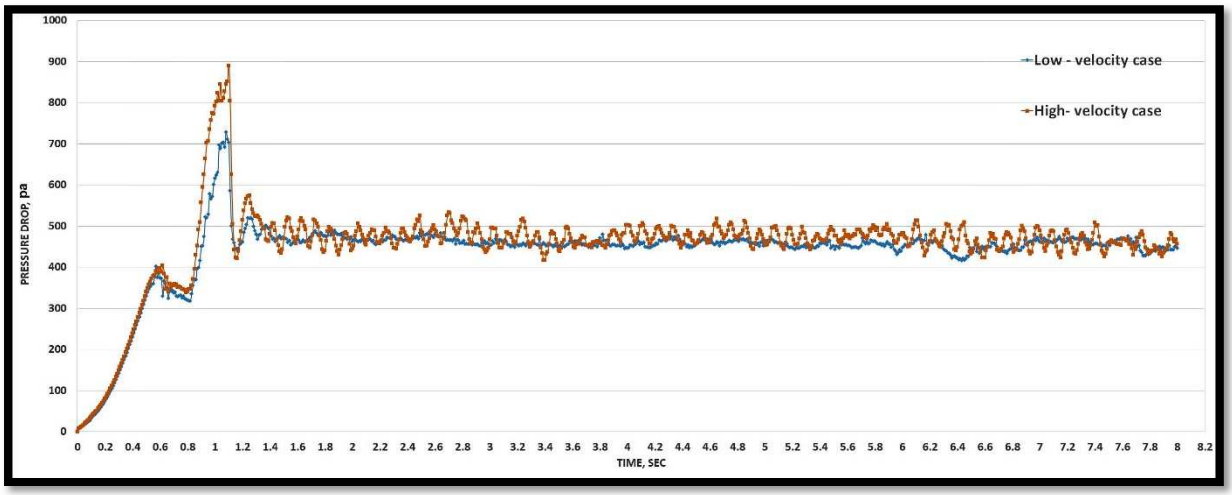

Figure 5.32. The time variation of pressure drop at a point located 20 mm above the centre of the type B distributor.

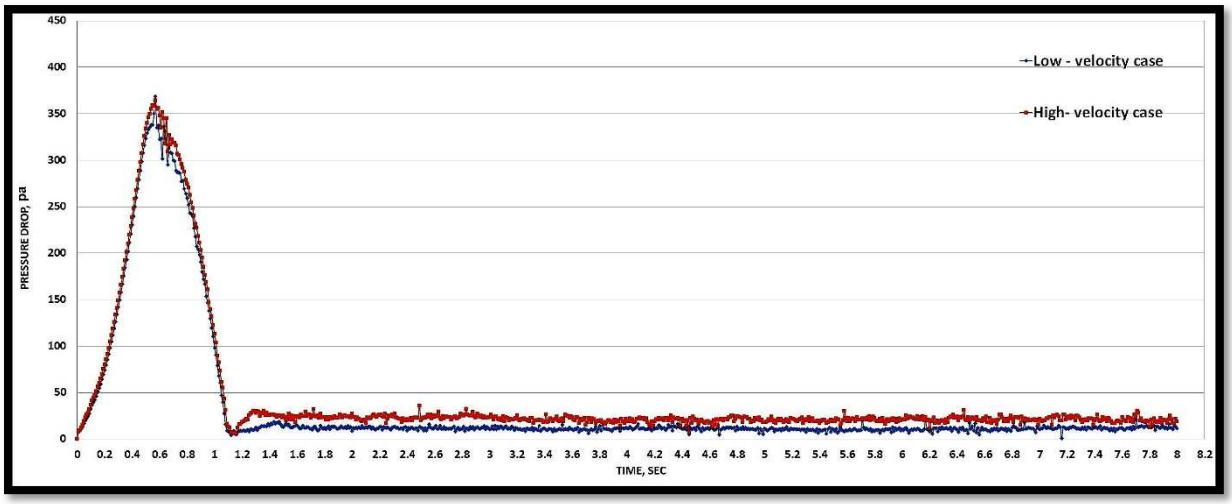

Figure 5.33. The time variation of pressure drop at a point located 80 mm above the centre of the type B distributor.

5.6.4.3. BFBG with type C Distributor

The pressure drop in the BFBG with the type C distributor also shows more expansion for the high-velocity case than the low-velocity case. In figures 5.34 and 5.35 the pressure drops contours in the BFBG with type C distributor at low and high average superficial velocities respectively.

On the other hand, the overall bed expansion in the BFBG with type C distributor was found to be relatively highest than in the previous two types A and B for both low and high superficial velocity cases. This may due to the large number of orifices in the C distributor compares to the number of orifices in type A and B distributors which provide a uniform air pressure throughout the BFBG bed.

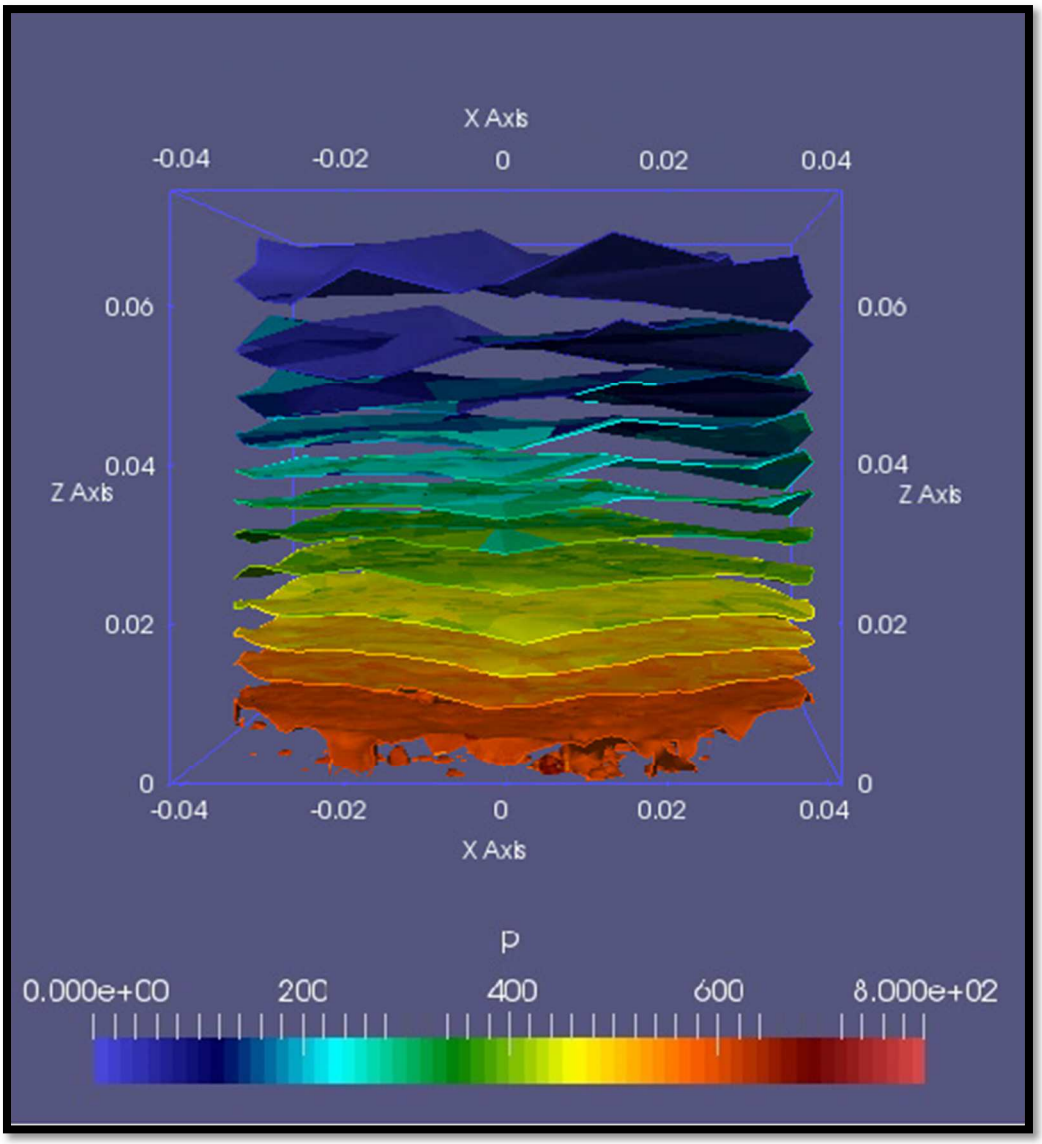

Figure 5.34. Pressure drop contour in the BFBG with type C distributor at low superficial velocity.

In the BFBG with type C distributor, the pressure drop for the high-velocity case is higher than the pressure in the low-velocity case in the low and high level above the centre of the distributor which is the same case in type B distributor. However, the type C cases have much more pressure fluctuation through the simulation time. This fluctuation was caused by the rapid movement of the sand particles which leads to good contact between the particles and air. Figures 5.36 and 5.37 illustrate the pressure variation in the BFBG with type C distributor at low and high-level points respectively.

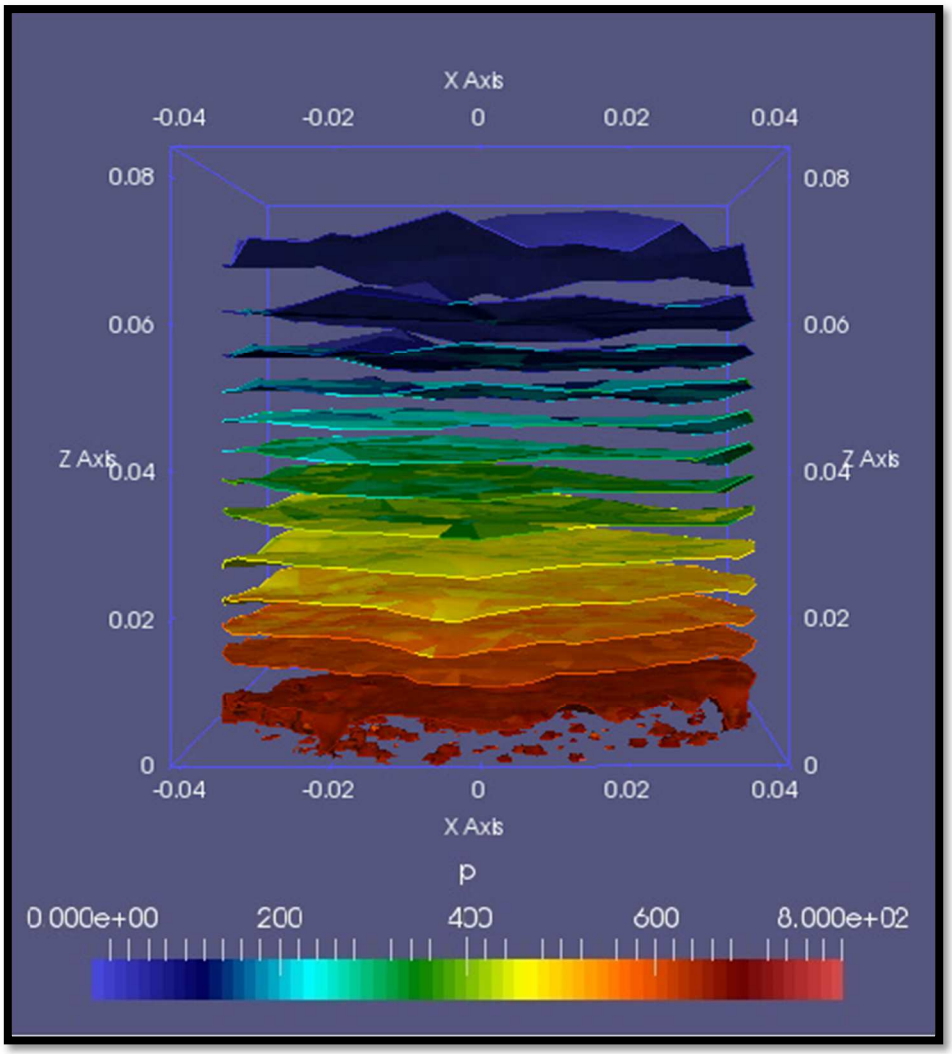

Figure 5.35. Pressure drop contour in the BFBG with type C distributor at high superficial velocity.

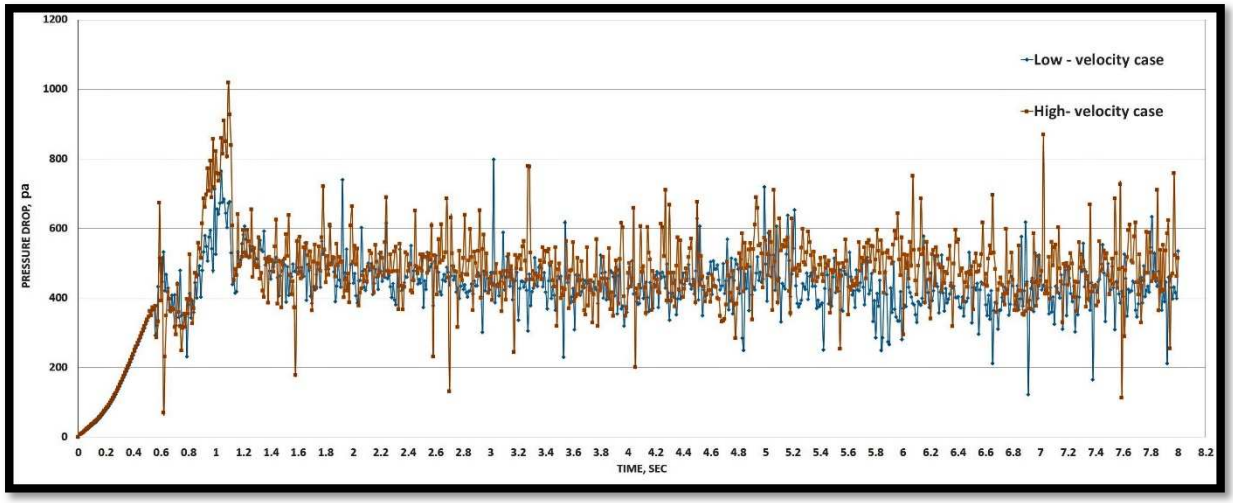

Figure 5.36. The time variation of pressure drop at a point located 20 mm above the centre of the type C distributor.

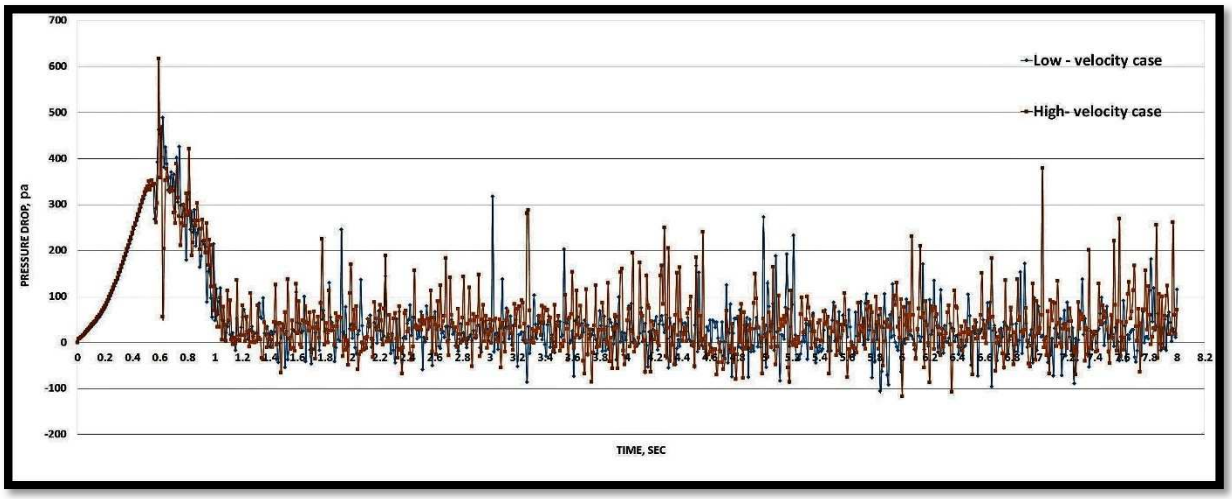

Figure 5.37. The time variation of pressure drop at a point located 80 mm above the centre of the type C distributor.

5.6.4.4. BFBG with type D Distributor

The simulation of the BFBG system with type D distributor shows a big bed expansion compared to all other three distributors A, B and C for the high and low superficial velocities. The bed height reaches more than 80 mm in the low superficial velocity case and hits the 100 mm in the high superficial velocity case. Figures 5.38 and 5.39 show the pressure drop contours in the BFBG with type D distributor for the low and high superficial velocities respectively.

The triangular arrangement of type D distributor and the small orifice diameter provides more orifices and better air distribution which gives uniform bouncy forces lifting the solid particles higher.

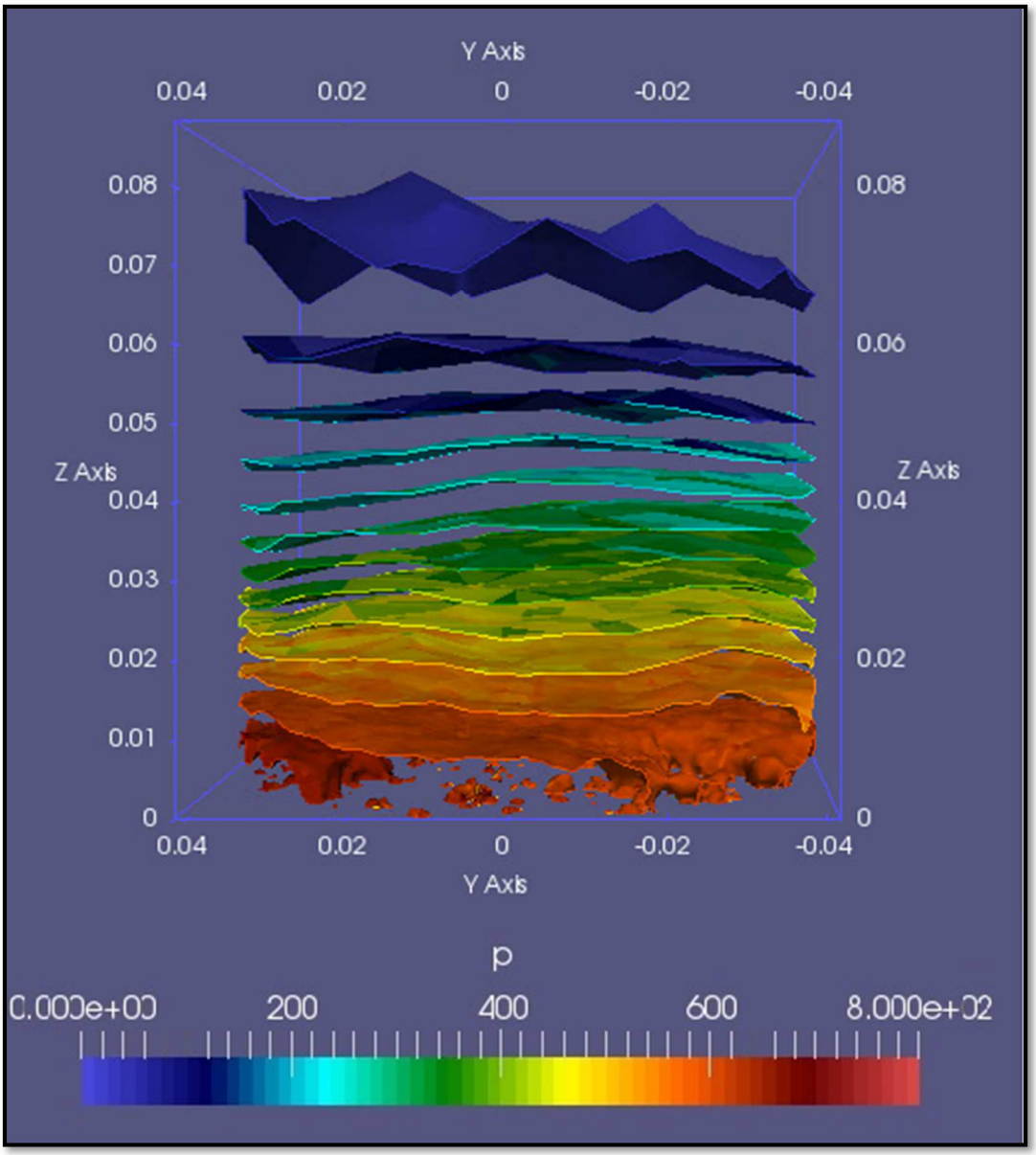

Figure 5.38. Pressure drop contour in the BFBG with type

D distributor at low superficial velocity.

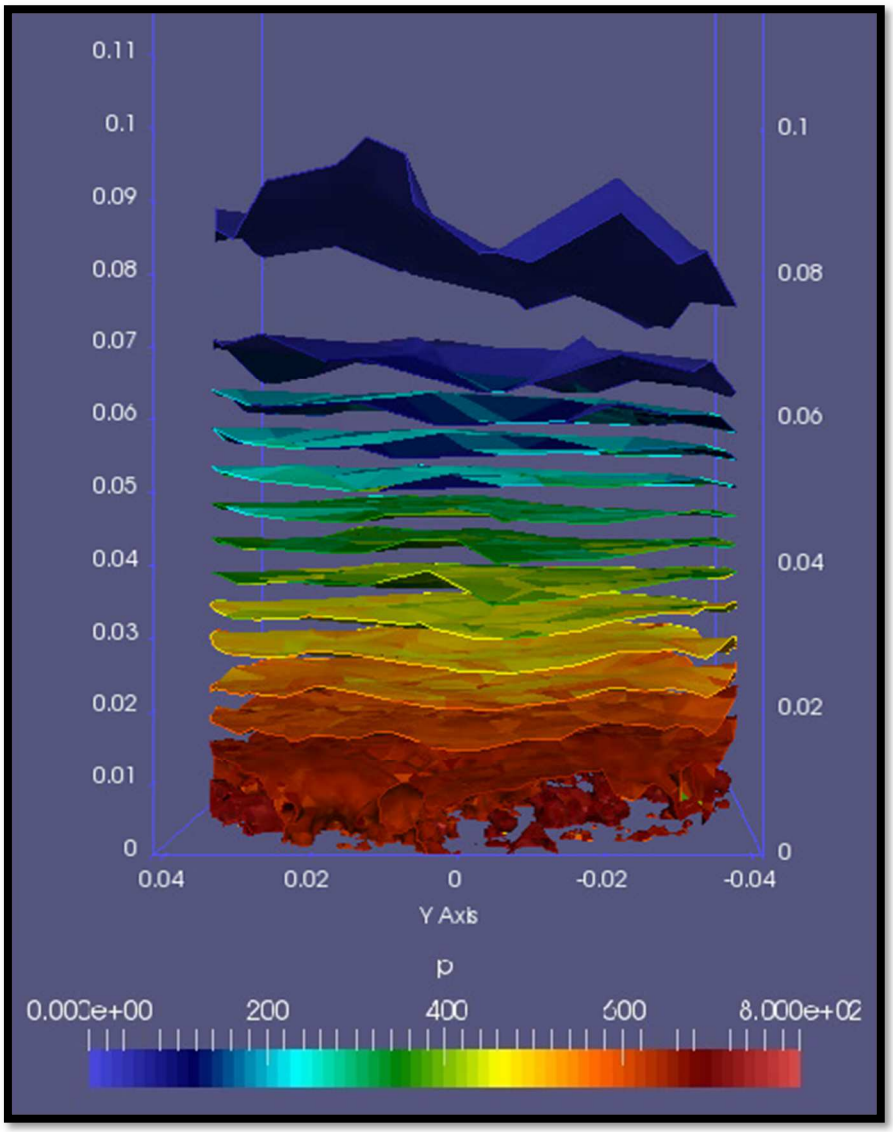

Figure 5.39. Pressure drop contour in the BFBG with type D distributor at high superficial velocity.

In figures 5.40 and 5.41, the pressure fluctuation throughout the eight seconds has increased rapidly in the BFBG with the using of type D distributor. The rapid fluctuation can be considered as a sign of active fluidised bed compared to the static packed bed.

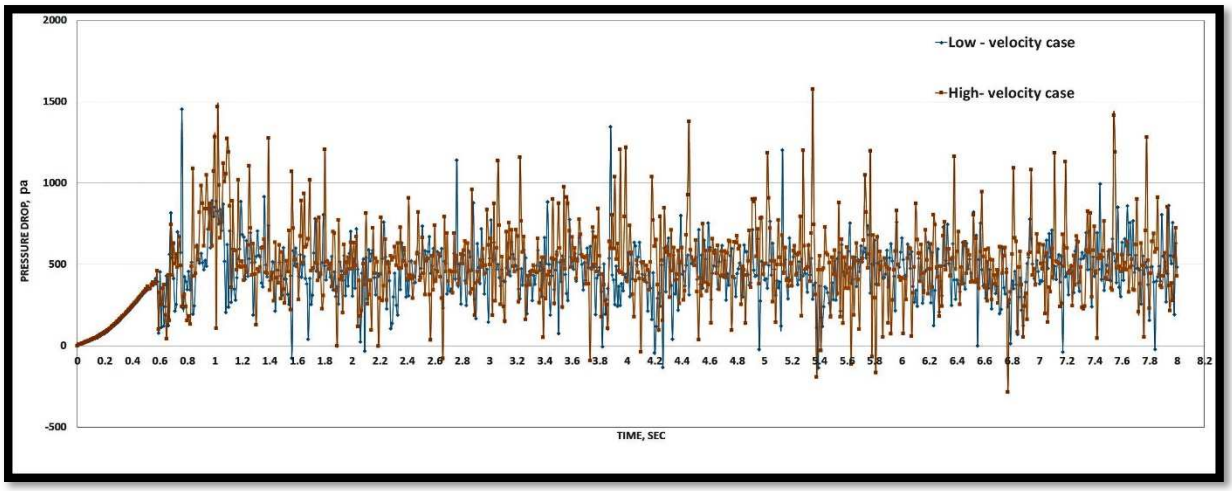

Figure 5.40. The time variation of pressure drop at a point located 20 mm above the centre of the type D distributor.

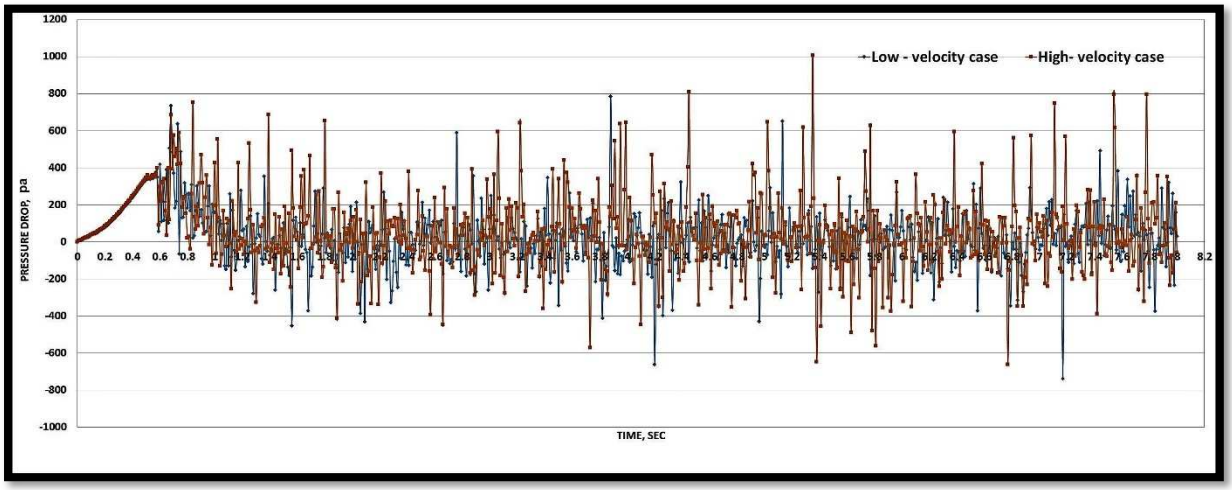

Figure 5.41. The time variation of pressure drop at a point located 80 mm above the centre of the type D distributor.

5.6.5. Local Superficial Velocity

The gas velocity of at a specific position and time inside the fluidised bed regime is called the instantaneous local superficial gas velocity. The superficial gas velocity is an important indicator of the fluidised bed activity inside the BFBG. However, the low and high superficial velocities mentioned earlier represent the average superficial velocity which was calculated

by dividing the air flow rate to the BFBG cross-sectional area. The local superficial velocity can affect other factors such as pressure drop, voidage and bubbles formation.

5.6.5.1. BFBG with Type A Distributor

The local superficial velocity for a central cross-section of the BFBG with type A distributor is shown in figure 5.42. The local superficial velocity distribution for the high-velocity case was wider and contains more high-velocity spots than the low-velocity case. This increases the pressure drop and the bed expansion.

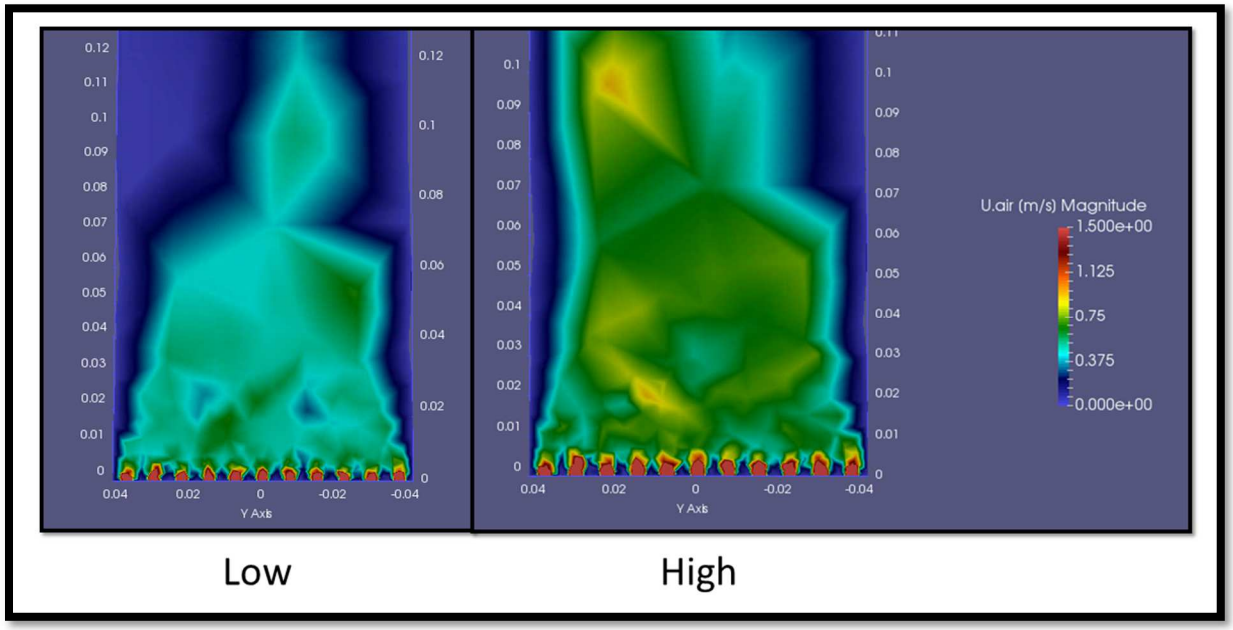

Figure 5.42. Instantaneous superficial velocity distribution in a central cross-section of the BFBG with type A distributor for low and high average superficial velocity.

5.6.5.2. BFBG with Type B Distributor

In figure 5.43 the BFBG central cross-section, which shows the local superficial velocity, has taken from a different angle. The number of orifices that appear in this section is seven dues to the triangular arrangement of type B distributor. Although the velocity distribution in this section is slightly lower than the distribution in the type A distributor section shown in figure 5.42, the cross section of type B distributor has more high local superficial velocity spots.

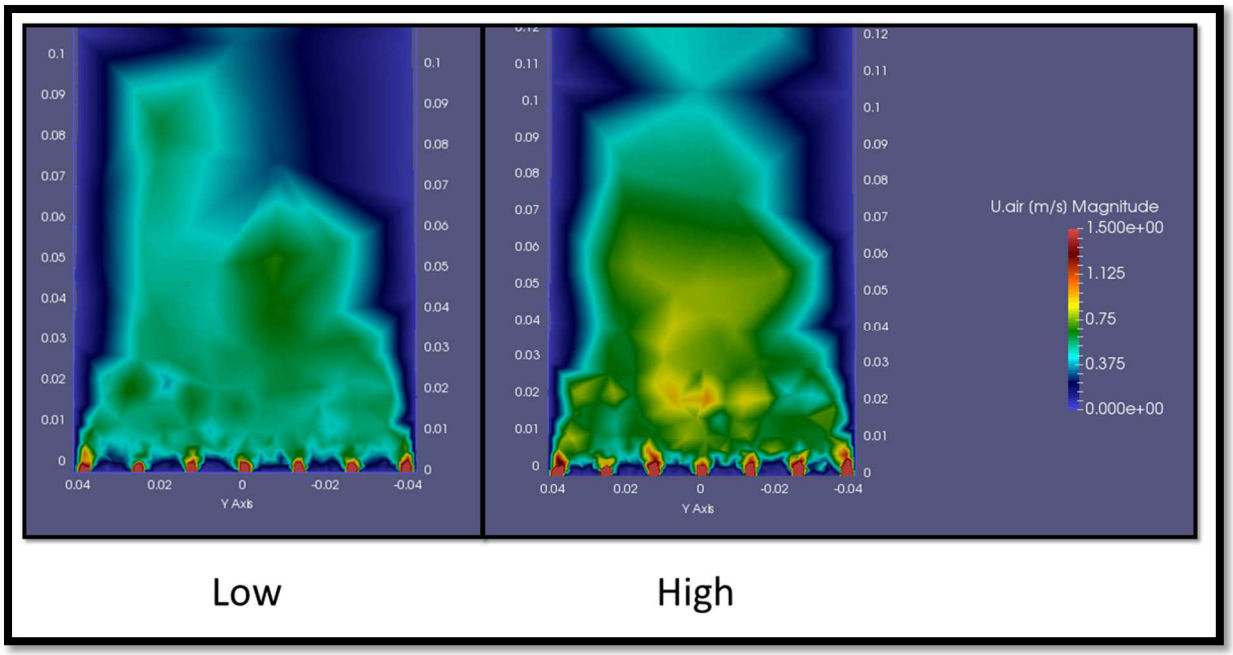

Figure 5.43. Instantaneous superficial velocity distribution in a central cross-section of the BFBG with type B distributor for low and high average superficial velocity.

5.6.5.3. BFBG with Type C Distributor

The local superficial velocity distribution in a central cross-section of the BFBG with type C distributor is wider than the previous types and has more high-velocity spots which mean more bed expansion and more air – solid particles contact. This is maybe due to the uniform distribution of air from these 137 small orifices. Figure 5.44 shows the local superficial velocity distribution in the cross section of BFBG with type C distributor.

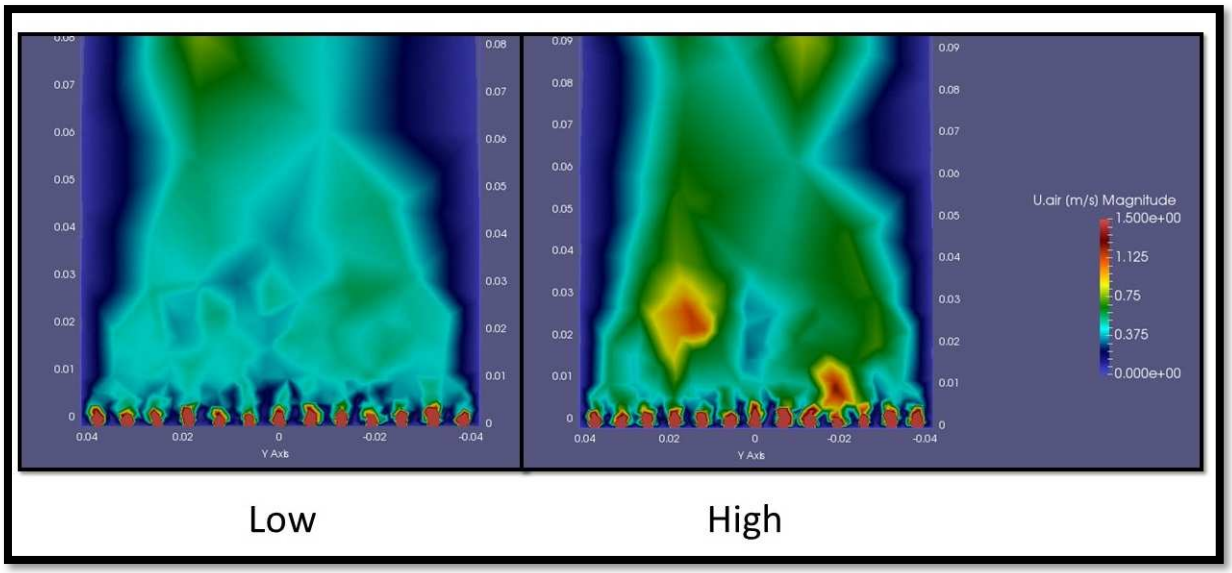

Figure 5.44. Instantaneous superficial velocity distribution in a central cross-section of the BFBG with type C distributor for low and high average superficial velocity.

5.6.5.4. BFBG with Type D Distributor

Type D distributor has a great effect on the distribution of the local superficial velocity as shown in figure 5.45. Despite the different BFBG central cross section which shows seven orifices, large local superficial velocity distribution with many and large high-velocity spots can be seen in this section which refers to high bed expansion and more bubbles generation.

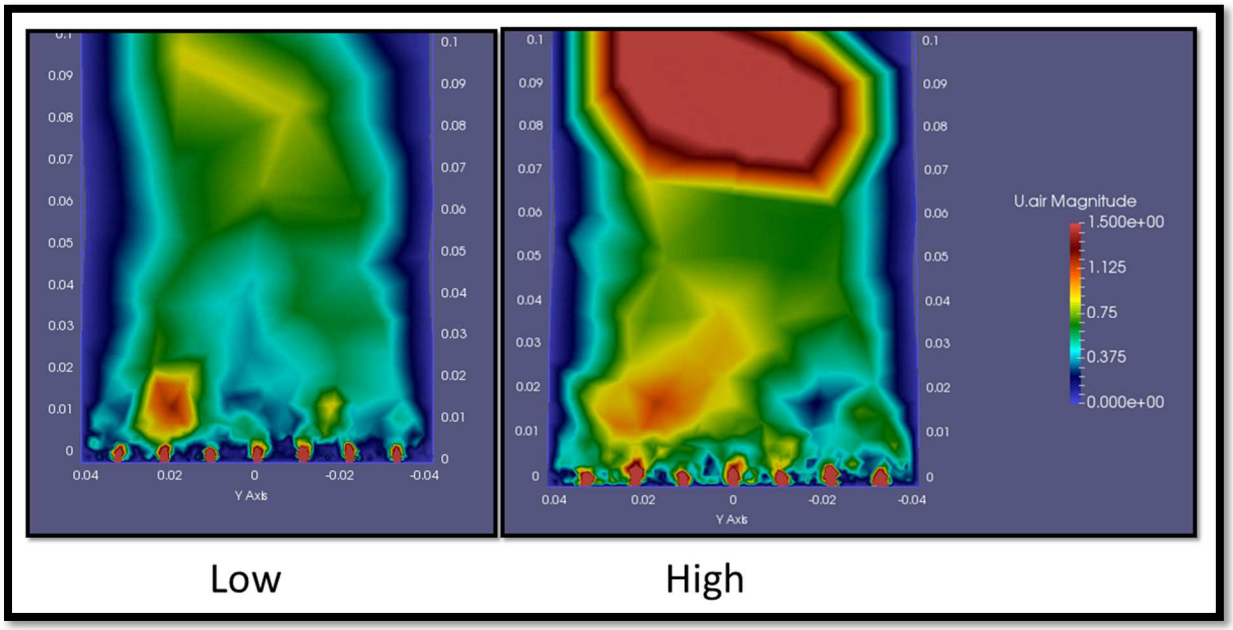

Figure 5.45. Instantaneous superficial velocity distribution in a central cross-section of the BFBG with type D distributor for low and high average superficial velocity.

5.6.5.5. Local Superficial Velocity Comparison

The effect of distributor type on the local superficial velocity was been tested by choosing a test point (S) locates at x=30.9 mm, y=0 mm and z=80 mm inside the BFBG as shown in figure 5.46. This point locates above the packed bed zone (packed bed height = 60 mm) which reflects the fluidised bed status. The time variation of the local superficial velocity at this point for each distributor case has been compared in figure 5.47.

In a nutshell, type D distributor provided the highest local superficial velocity in both high and low-velocity cases among all distrubtors which indicates the high activity of fluidised bed using this distributor.

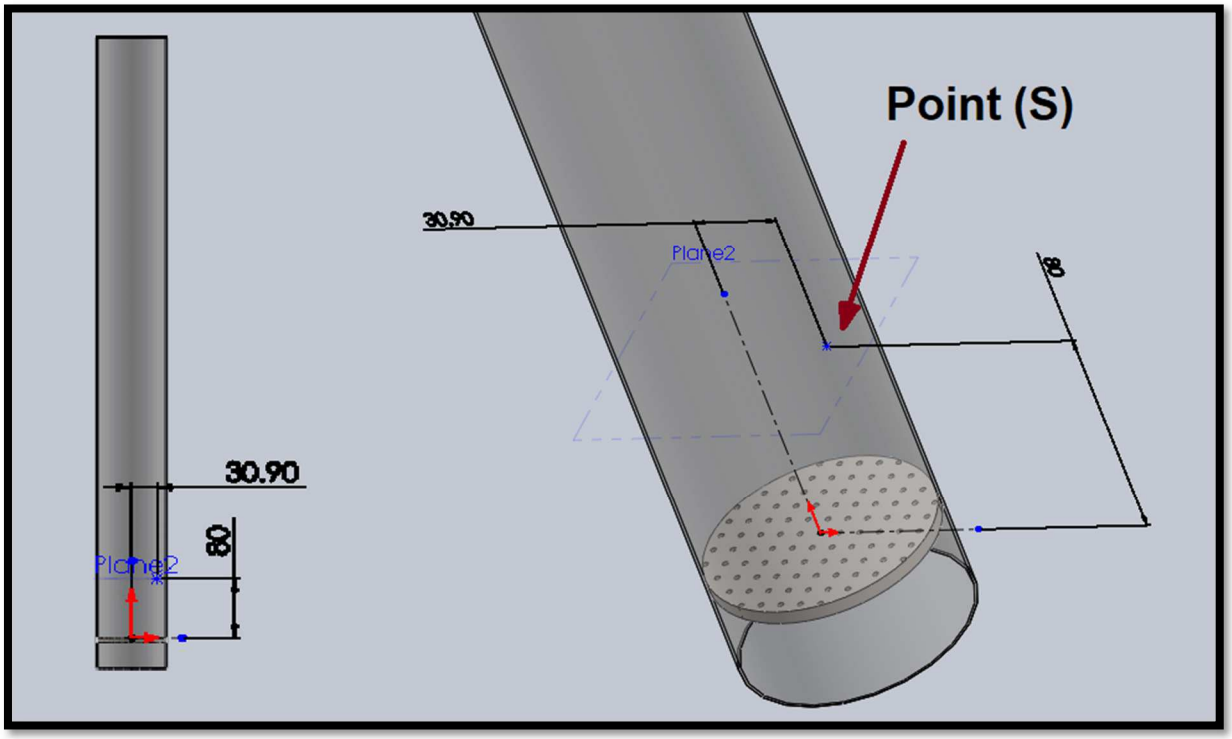

Figure 5.46. The test point (S) location in the BFBG.

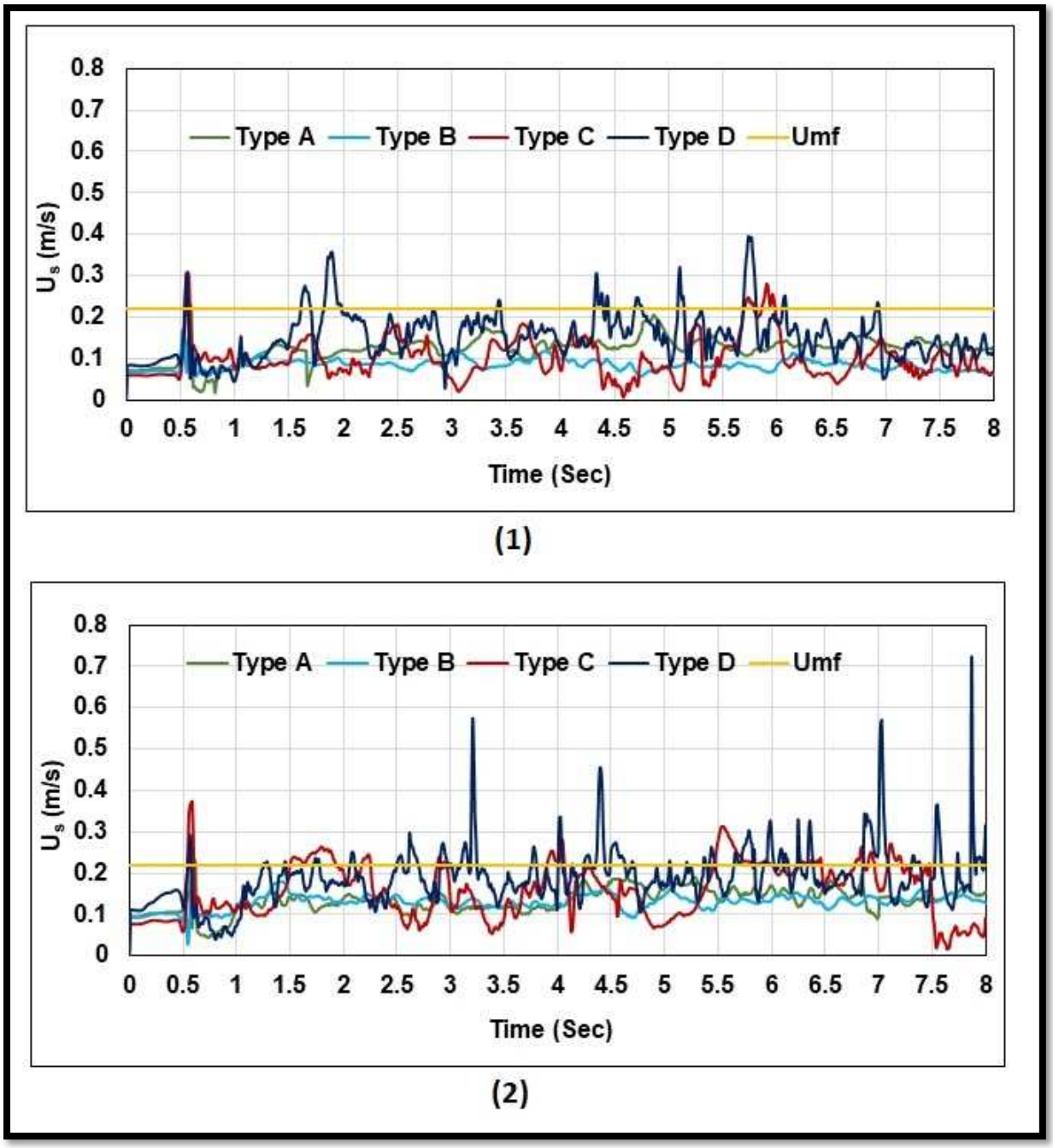

Figure 5.47. The time variation of the local superficial velocity in point (S) inside the BFBG at (1) Low velocity, (2) High velocity.

5.7. Conclusion

In this chapter, a visualisation for the isothermal BFBG has been illustrated. The open source software (OpenFOAM) has been used to simulate the BFBG with four different perforated plate distributors for low and high average superficial velocity cases. More than 2000 Gigabit of data for the different hydrodynamic properties of the BFBG with the four different distributors has been produced.

Particle distribution, bed voidage, bubble formation, pressure drop and local superficial velocity are all tested inside the BFBG. All 4 distributors have produced bubbles in different sizes and velocities. Generally, the triangular arrangement of holes showed better performance than the square pitch arrangement for all hydrodynamic properties. Moreover, the small orifice distributors presented a uniform fluidised bed. However, the type D distributor showed a good performance among the other three distributors in terms of hydrodynamic properties. The fluidised bed produced by the type D distributor was more uniform with the largest bed expansion with a uniform pressure drop.

The uniform bed height reached more than 75 mm in the type D distributor while it is 65 mm in the other distributors under the same conditions. Moreover, the number of formed bubbles in the BFBG with the type D distributor is more than the other distributors.

The simulation was validated with an experimental data and literature. The comparison showed a good approach with the experimental data with approximately 2% error for type D, 3% for type B, 3.65% for type C and 6.64% for type A distributors. Comparison of bubble size with literature showed a good approach between the recent simulation results with two of the empirical correlations. The correlation of Geldart was the closet to the recent results with a minimum error of 4.83%.

A conference paper was published containing a part of this work (Al-Akaishi et al., 2017).

Chapter 6: Post - Gasification Improvement

6.1. Introduction

Biomass gasification in the BFBG produces a product gas with varied molecular composition. The composition of this product gas depends on different factors such as the biomass type and the BFBG hydrodynamics. The main composition of the BFBG product gas is based on the molecules CH_2, H_2, CO and CO_2. However, the percentage of each component depends on inlet conditions, flowrates, temperatures profiles, etc. In this chapter, results using the optimal distributor in a BFBG located at Cardiff University are presented in combination with some further modifications numerically analyzed to improve even further the production of highly valuable gases (i.e. H_2 and CO).

6.2. Improved gasification using the Optimal Distributor

As demonstrated in previous chapters, the best air distributor (D) was determined after complex numerical simulations and experimental trials. It was noted that the hydrodynamics of the latter considerably improved the fluidic performance of the fluidized bed, with pressures and bubble formation that demonstrated a superior behavior, which eventually needed to be evaluated in a real gasifier.

In order to achieve this task, works were conducted in parallel to another research project (Al-Farraji, 2017) whose objective was to evaluate the performance of the new BFBG developed at Cardiff University. As stated, the previously mentioned project aimed to characterize this new rig, while the current project under discussion was responsible to assess the improvement in biomass gasification using the new distributor here developed.

Olive kernel biomass, a widely available agro-industrial residue of Mediterranean origin, were received as coarse particles with an approximate size of less than 5 mm (Al-Farraji, 2017). The initial moisture content of the olive kernel was measured as 13.3%. The samples were dried to 5.3% moisture content and stored in sealed sacks.

As demonstrated, Distributor D provided the best results across flow distribution, bubble formation, pressure decay and hydrodynamics, thus this distributor was used for biogas production. The BFBG system employed, depicted in figure 6.1 below (Al-Farraji, 2017).

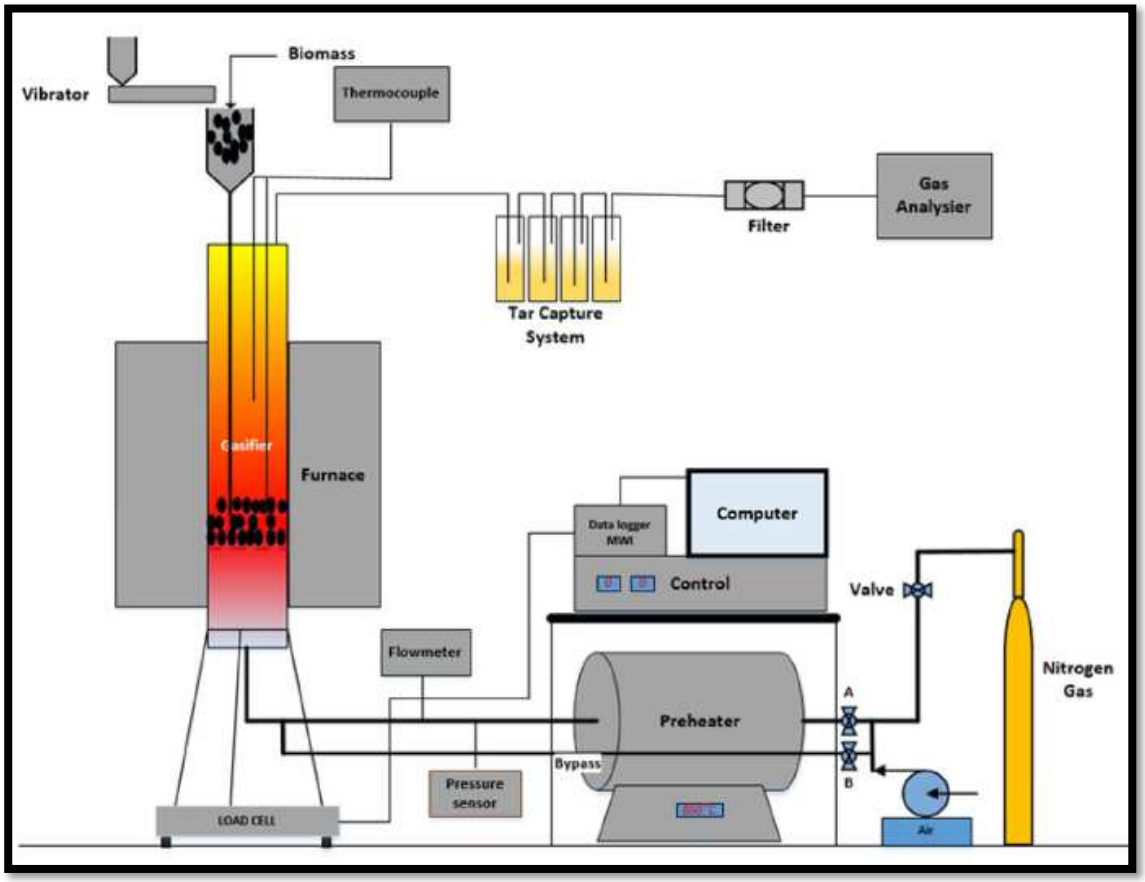

Figure 6.1. BFBG system employed to characterize the production of biogas using type D perforated distributor (Al-Farraji, 2017).

The overall experimental preparation procedures undertaken for the operation of the fluidised bed gasifier were as follows:

1. The day before gasification testing the freezer was switched on and 100ml of isopropanol was poured into each of the 250ml dreschel bottles in the tar capture unit located inside the freezer. The freezer was set to -10°C and this was verified with a thermocouple.

2. Prior to testing, the gas analyser was zero calibrated on N2 and then with span gas mixture supplied by Air Products. The standard gas mixture used for gas analyser calibration was composed of CO, CO_2, H_2, and CH_4 with concentrations of 15%, 15%, 15%, and 5% respectively. The balance was N_2.

3. Depending on the (Hs/D) ratio, a required amount of silica sand with a density of 2650 kg/m^3 was used and added as bed material to the gasifier; its particle size was 500-600µm.

4. The preheater, split furnace and air blower were activated and the temperatures monitored using a data logger. The superficial velocity was constant at 40l/min, twice the value of Umf.

5. The computer was switched on and the data logger and multifunction weight indicator were activated.

6. The vibrating feeder was then calibrated gravimetrically for each mass flow rate depending on ER by direct weighing of the biomass for 5 minutes. The biomass was fed at 80mm above the distributor, through a tube made of stainless steel with 1" i.d. from a hopper by a vibration feeder. The mass flow rate of biomass was varied based on the selected ER and the other condition (air flow rate) was held constant. It should be mentioned that the feeding rate to obtain a desired ER was not the same for torrefied biomass due to the stoichiometry being different. This procedure was repeated three times to ensure repeatability was achieved. The hopper was filled with biomass ready for the gasification test.

Experiments demonstrated that high conversion ratios were obtained using such a system. Temperatures above 400ºC generally showed conversation of >80% biomass, Figure 6.2.

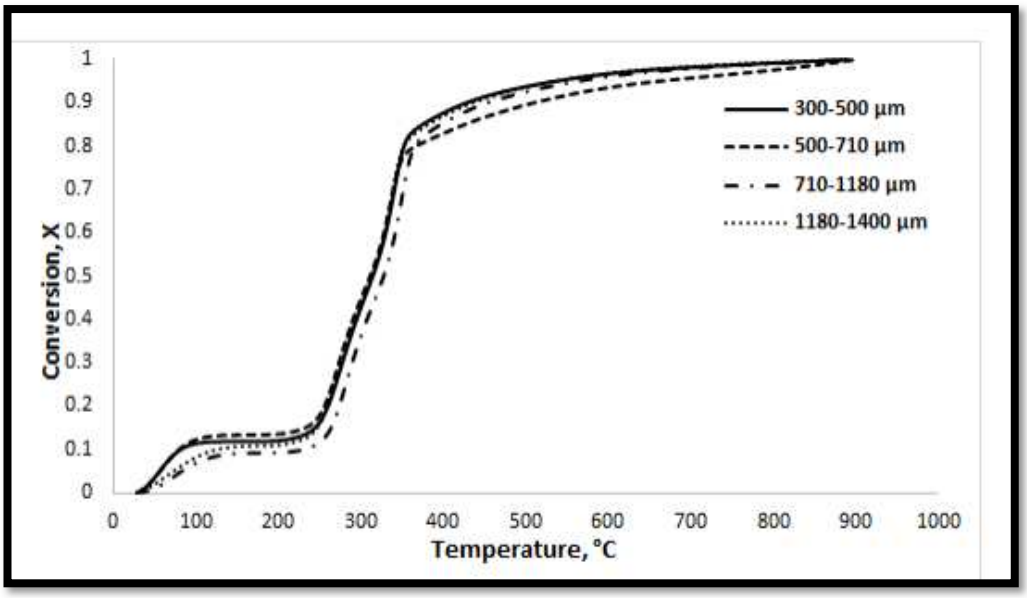

Figure 6.2. Relationship between mass conversion and temperature for olive kernels of different particle sizes. Heating rate 20°C/min (Al-Farraji, 2017).

6.3. Gasification Product Gas Composition

The product gas obtained from the previously mentioned studies was then assessed for further improvement of the gasification process. The mixture used in this modification was the optimum product of the gasification of olive kernels in the BFBG using the type D distributor. The composition is, as determined somewhere else (Al-Farraji, 2017), as follows,

- Methane = 13.85%, Hydrogen = 15.7%, Carbon monoxide = 40.08%, Carbon dioxide = 30.37 % (mole fraction).

This gas blend was used as the feed of the modification system in the following simulations.

6.4. High Temperature Reformer

In order to increase the amount of high valuable gases (i.e. hydrogen and carbon dioxide) obtained from gasification of biomass, a new post-process was conceptualized. The process is based on the rapid increase of temperature, thus allowing the reforming of species such as carbon dioxide and water to generate H_2 and CO. Some ideas on the device that can be potentially used for reforming of these gases will be discussed in the next chapter. The addition of inert gases such as Argon and Nitrogen at different concentrations in combination with greater reaction temperatures and catalytic materials was assessed. These innovative additions, that to the knowledge of the author have never been assessed before, could potentially be implemented in combination with highly efficient distributors such as the one developed in this work to obtain high amounts of high valuable gases for industrial use, with its inherent benefits and flexibility.

In order to determine the effectiveness of the post – gasification improvement process, the commercial software Aspen Plus was employed. The main components of the improved cycle are shown in figure 6.3.

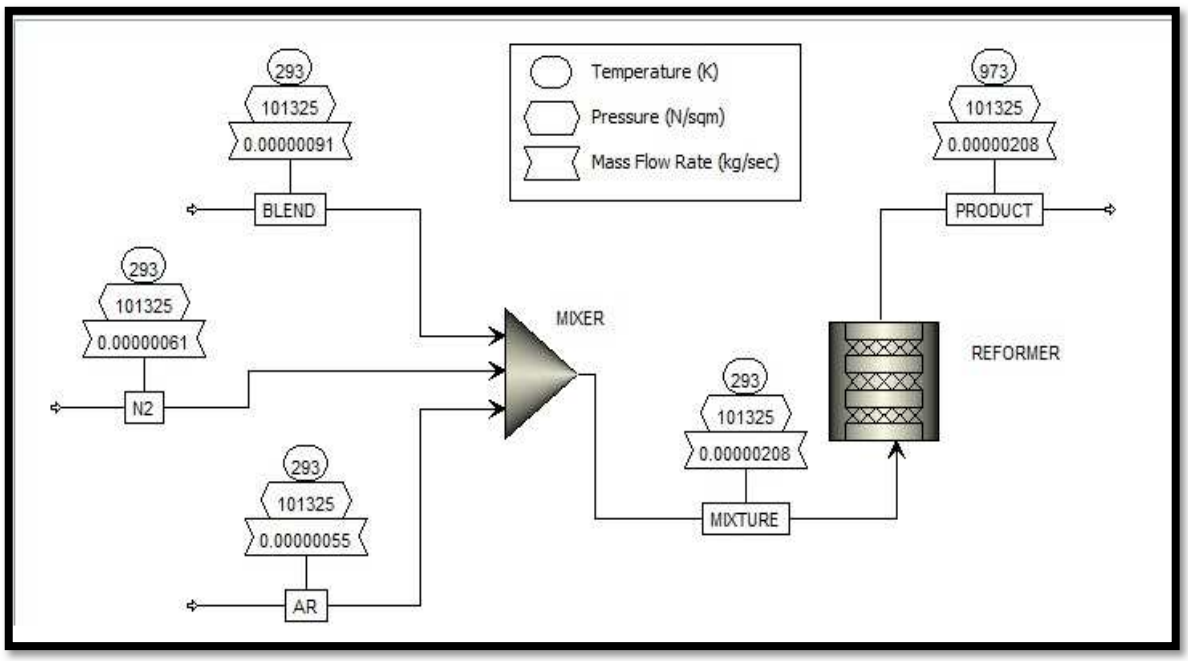

Figure 6.3. Aspen plus flowsheet for the case study.

The system consists of the following components:

6.4.1. Feeding Lines and Mixer

Three gas lines carry the feeding gases at ambient conditions. Table 6-1 shows the specifications of the three gas lines. The total flow rate of the gases is 100 mL/min. A mixer was then used to adiabatically mix all fed gases.

Table 6-1 Feeding lines in the system.

Line No.	Line component	Mole Fraction (%)	Pressure (kpa)	Temperature (K)	Note
1.	BFBG product gas blend	48.4	101.325	293	Main component
2.	N_2	31.6	101.325	293	Optional
3.	Ar	20	101.325	293	Optional

6.4.2. Reformer

This component is the main part of the system (the reactor) in which all gas conversions occur. A plug flow tubular reactor (PFR), RPLUG was used. The specifications of this reactor are shown in table 6-2. The reactor contains a catalyst material to enhance the reaction process. The type of catalyst was used in this reactor is 10% Ni with 90% Al_2O_3 as a dilution material. RPLUG reactor was tested in different reaction temperature and catalyst loading.

Table 6-2. The specifications of system reactor.

Specifications	Value	Unit	Note
Reactor type	RPLUG	-	
Diameter	9	mm	
Length	40	mm	
Reactions nature	Solid - catalysed reactions	-	
Catalyst type	10%Ni / 90%Al_2O_3	-	
Catalyst loading	2.5 - 10	mg_{cat}.min/ml	Catalyst loading step = 2.5
Gas mixture flow rate	100	mL/min	
Reactor pressure	101.325	kpa	
Reactor temperature	773 - 1273	K	Temperature step = 50 K
Reaction Model	Langmuir-Hinshelwood-Hougen-Watson (LHHW)	-	

The kinetic parameters of the presumed reaction are listed in table 3-9 in chapter three.

6.5. Model Validation

The Aspen Plus® model has been validated with another mathematical model (Jokar et al., 2018) and with experimental data from literature (Jokar et al., 2016). The validation was obtained in a CRM reactor with the following conditions shown in table 6-3. The recent Aspen Plus® model has a good agreement with both the experimental data and mathematical model in literature as shown in figure 6.4.

Table 6-3. The validation conditions of the Aspen Plus® model (Jokar et al., 2018).

Reactor Conditions	Value	Unit
Reaction temperature	723	K
Reaction pressure	1.5 - 3.5	Bar
Steam to Carbon ratio, S/C	2.64	-
Sweep fraction, $SF = \frac{N_2\ Moles}{CH_4\ Moles}$	1.2	-
Catalyst type	Ni-based catalyst	-

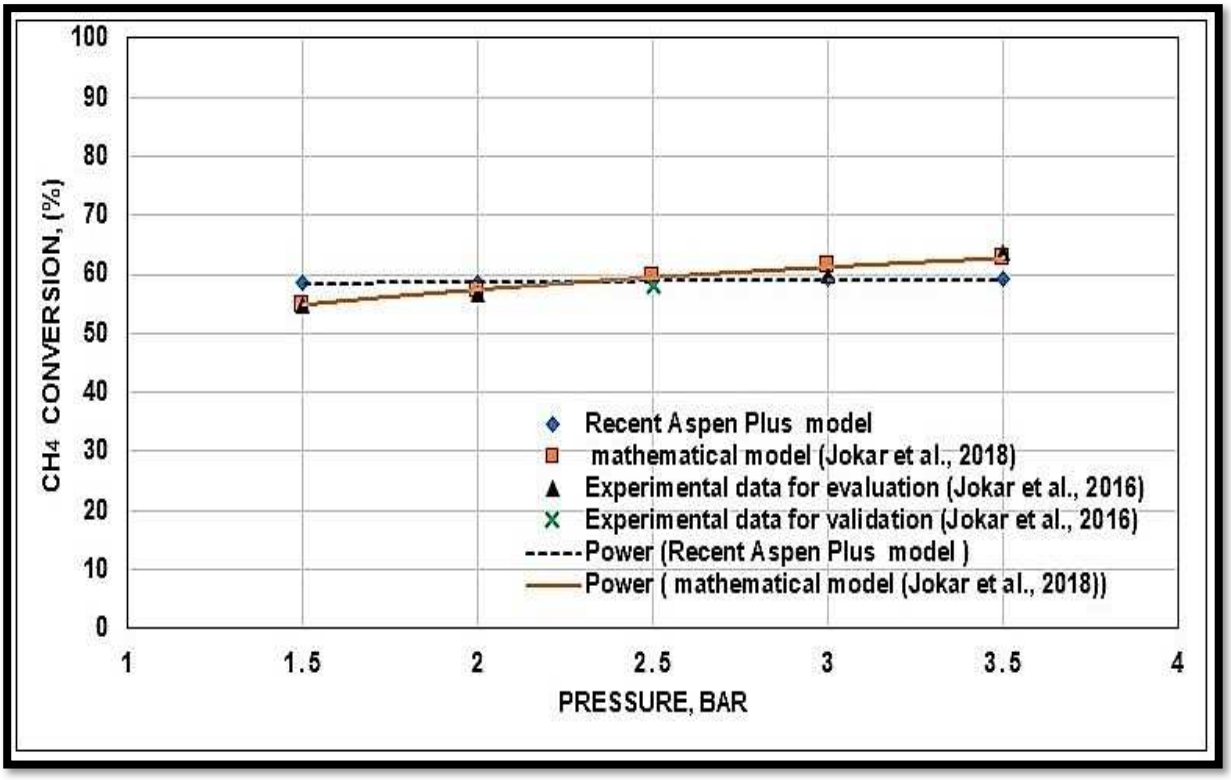

Figure 6.4. The validation of Aspen Plus model in terms of CH_4 conversion.

6.6. Simulation Results

The simulation was performed for 3 different cases, Table 6-4,

1- Case one (light feeding): BFBG blend, Argon and Nitrogen gas mixture.

2- Case two (medium feeding): BFBG blend and Nitrogen gas mixture.

3- Case three (heavy feeding): BFBG blend gas mixture.

Table 6-4. The molar and mass fractions of the three gas mixtures components.

Feeding case	Components	CH_4	CO_2	CO	H_2	Ar (Dilution gas)	N_2 (Dilution gas)
Case one (light feeding)	Molar fraction (%)	6.7	14.7	19.4	7.6	20	31.6
	Mass fraction (%)	3.58	21.58	18.13	0.51	26.65	29.53
Case two (medium feeding)	Molar fraction (%)	9.47	20.77	27.42	10.74	-	31.6
	Mass fraction (%)	5.54	33.35	28.021	0.79	-	32.297
Case three (heavy feeding)	Molar fraction (%)	13.85	30.37	40.08	15.7	-	-
	Mass fraction (%)	8.18968	49.2643	41.3795	1.16655	-	-

6.6.1. Case One Results

Composition variation of the gas mixture along the reactor at 100mL/min feeding rate and 700^{o}C reaction temperature is shown in figure 6.5. The simulation predicts the formation of a small amount of H_2O in the product gases and a rapid conversion of CH_4 and CO_2 to H_2 and CO at the beginning of the reactor, with low conversion along the rest of the reactor length.

The selectivity of H_2 and CO can be calculated by using the Hao equations 6-1 and 6-2 (Hao et al., 2009) and the molar compositions of the gases before and after the RPLUG reactor.

$$H_2 \text{ selectivity} = \frac{H_{2.out} - H_{2.in}}{2(CH_{4.in} - CH_{4.out})} (\text{in moles}) \times 100\% \quad \text{..... 6-1}$$

$$H_2 \text{ selectivity} = \frac{0.177162 - 0.076}{2(0.067 - 0.00435094)} \times 100\% = 80.7\%$$

$$CO \text{ selectivity} = \frac{CO_{out} - CO_{in}}{(CH_{4.in} + CO_{2.in} - CH_{4.out} - CO_{2.out})} (\text{in moles}) \times 100\% \quad \text{..... 6-2}$$

$$CO \text{ selectivity} = \frac{0.259789 - 0.194}{0.067 + 0.147 - 0.00435094 - 0.0745788} \times 100\% = 66.6\%$$

Changes in molar composition along the reactor are shown in figure 6.5. Decreasing in N_2 and Ar mole fractions in figure 6.6 is related to the increase in total numbers of moles due to the formation of H_2O at constant pressure and temperature. The total heat duty of this process is 1.121 W under these conditions and the actual residence time is 0.391 seconds as shown in figure 6.7.

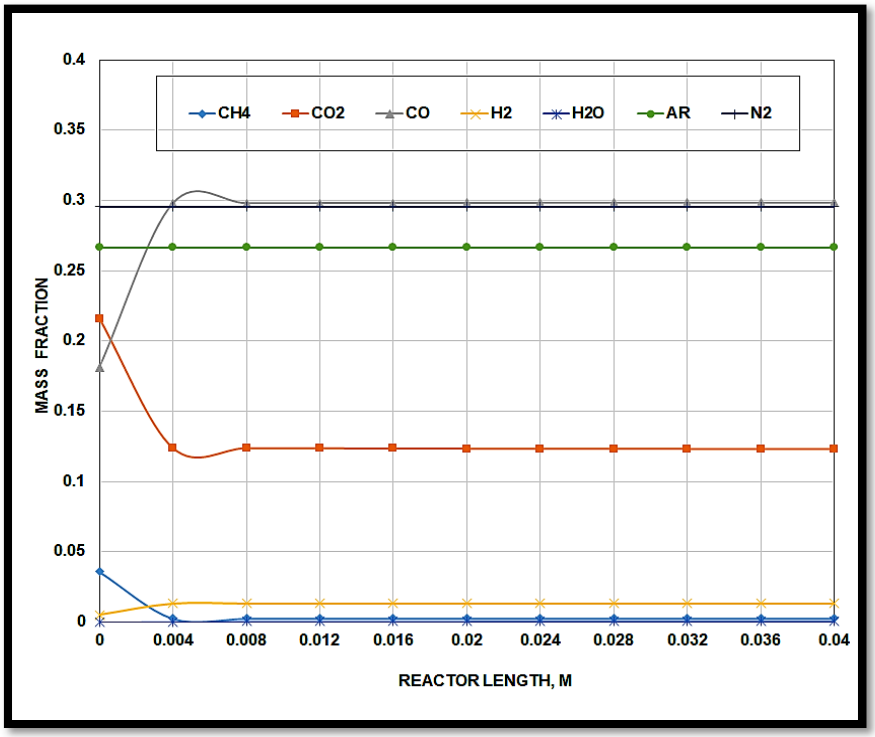

Figure 6.5. Mixture conversion along the reactor at temperature 973K.

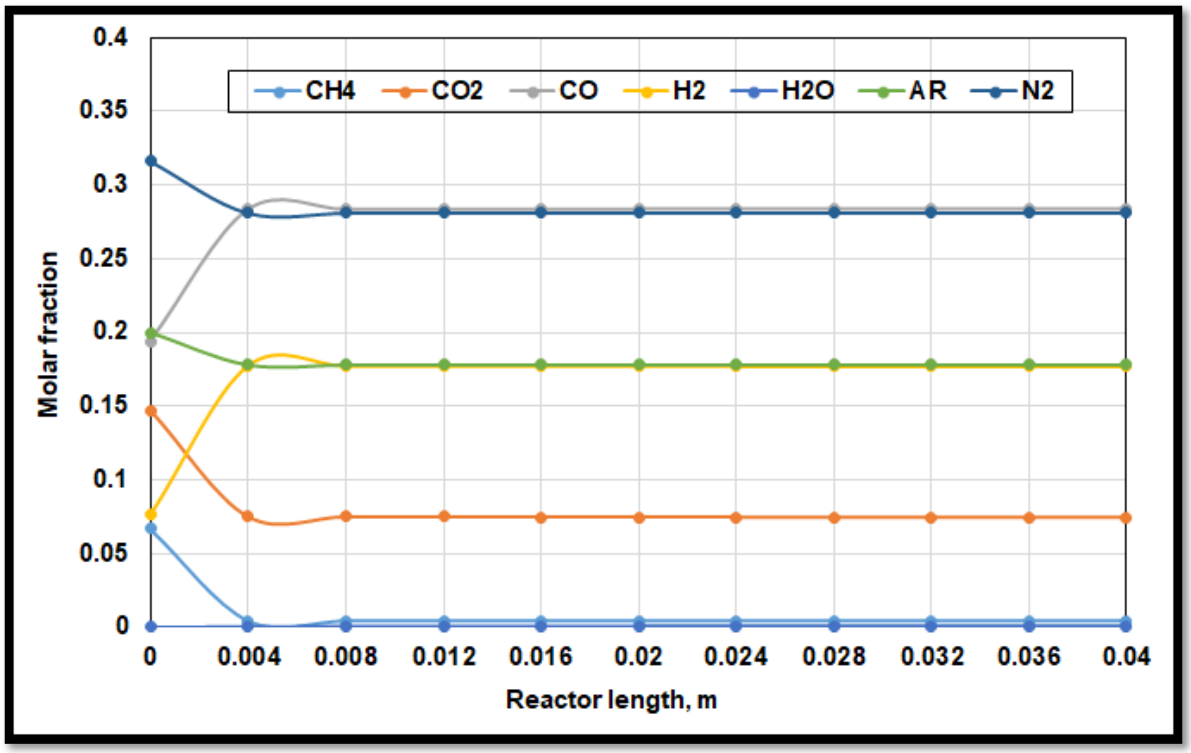

Figure 6.6. Molar fraction of the gases along the reactor at temperature 973K.

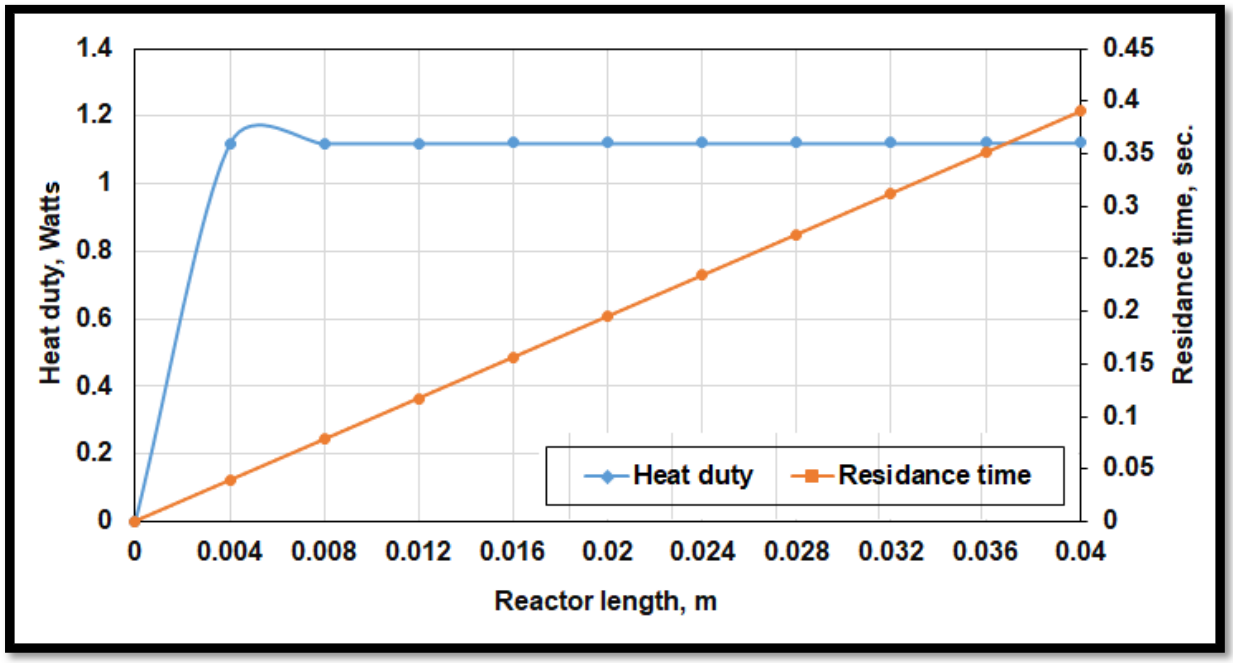

Figure 6.7. Reaction heat duty along the reactor at temperature 973K.

6.6.1.1. The Effect of Reaction Temperature in Case One

The effect of reaction temperature on the composition of each gas component in the mixture has also been studied. Figure 6.8 shows the variation of the concentration of product gases with the reaction temperature. The conversion of gases increases rapidly with the increase of temperature until the reaction temperature reaches 700 ^{o}C, then the reactions slow down to be nearly constant between 750 to 1200 ^{o}C as shown in figure 6.8. In addition, the amount of H_2O in the product gas was increased at the low temperatures, especially at 550 ^{o}C. The fraction of H_2O then drops rapidly to stop at nearly 0.0005 at temperatures above 800 ^{o}C. This variation of the H_2O fraction is maybe related to the effectivity of the reverse water gas shift reaction at different temperatures (Oshima et al., 2014).

The mass fraction variation of H_2O, H_2, CH_4, CO and CO_2 with reaction temperatures along the reactor length are shown in figures 6.9, 6.10, 6.11, 6.12 and 6.13 respectively.

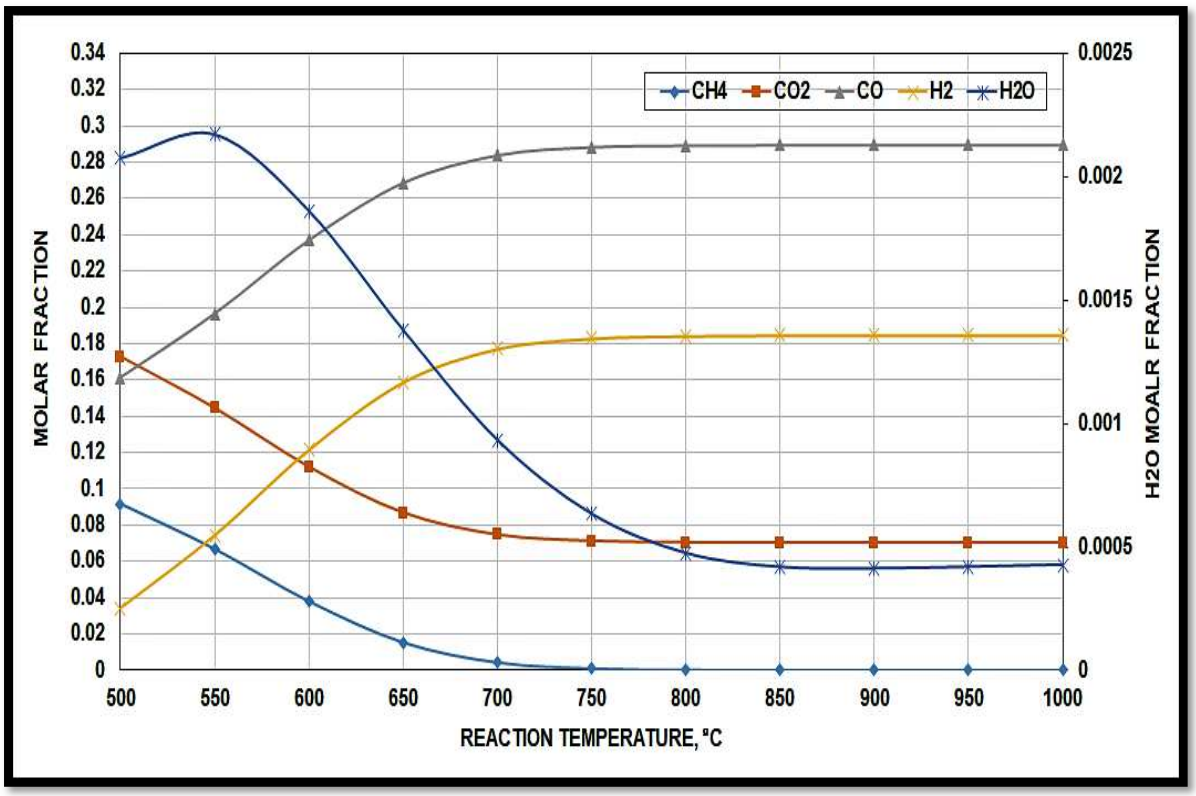

Figure 6.8. The effect of reaction temperature on the product gas molar composition.

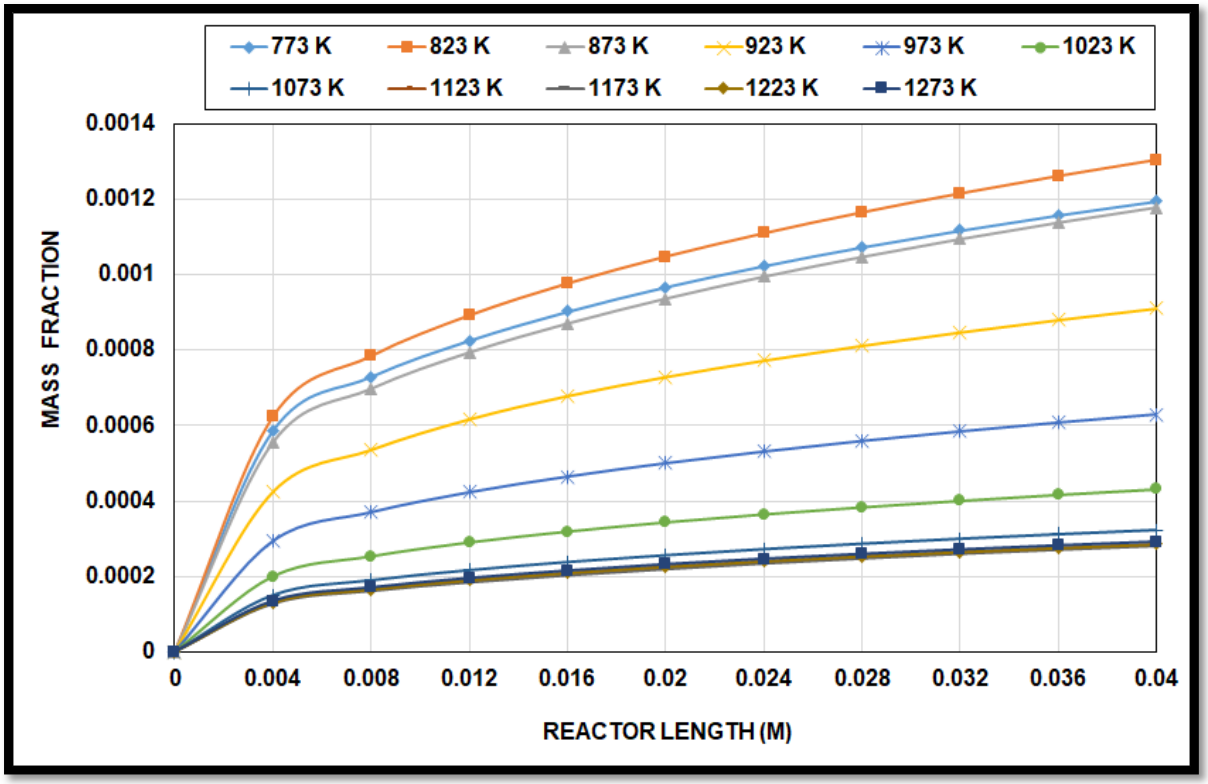

Figure 6.9. The variation of formed H_2O mass fraction along the RPLUG reactor for different reaction temperatures.

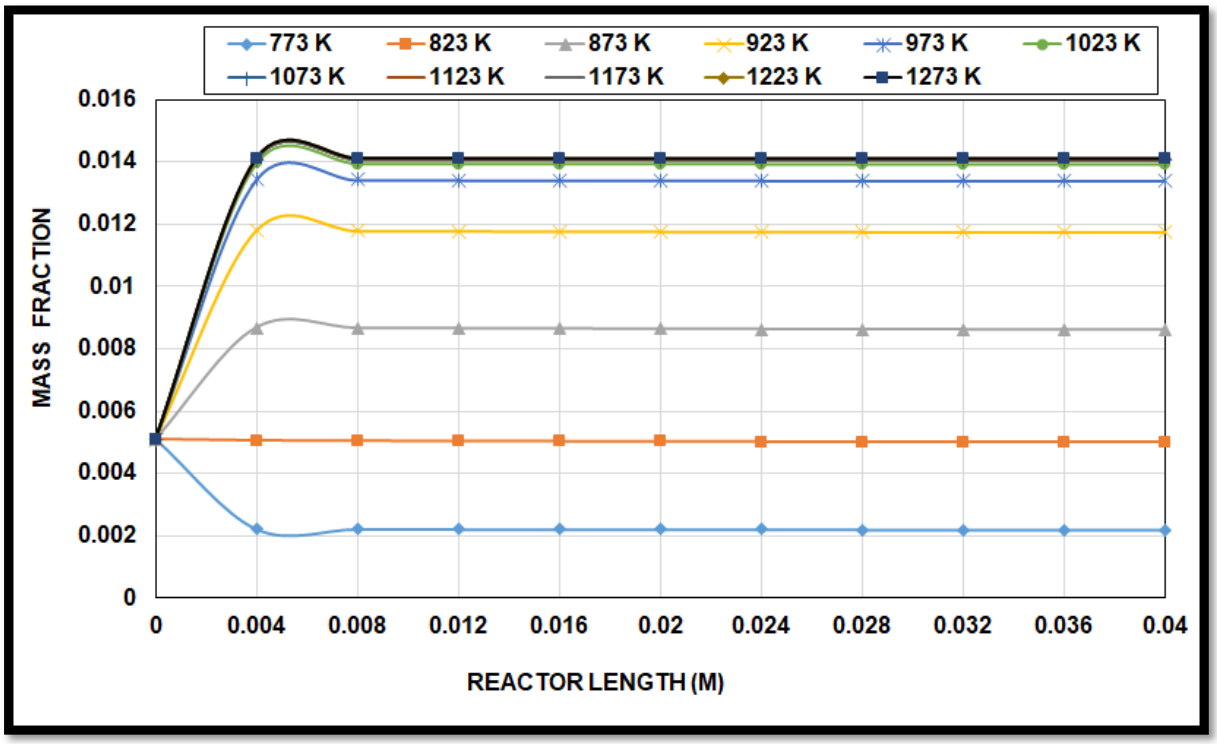

Figure 6.10. The variation of H_2 mass fraction with reaction temperature along the RPLUG reactor.

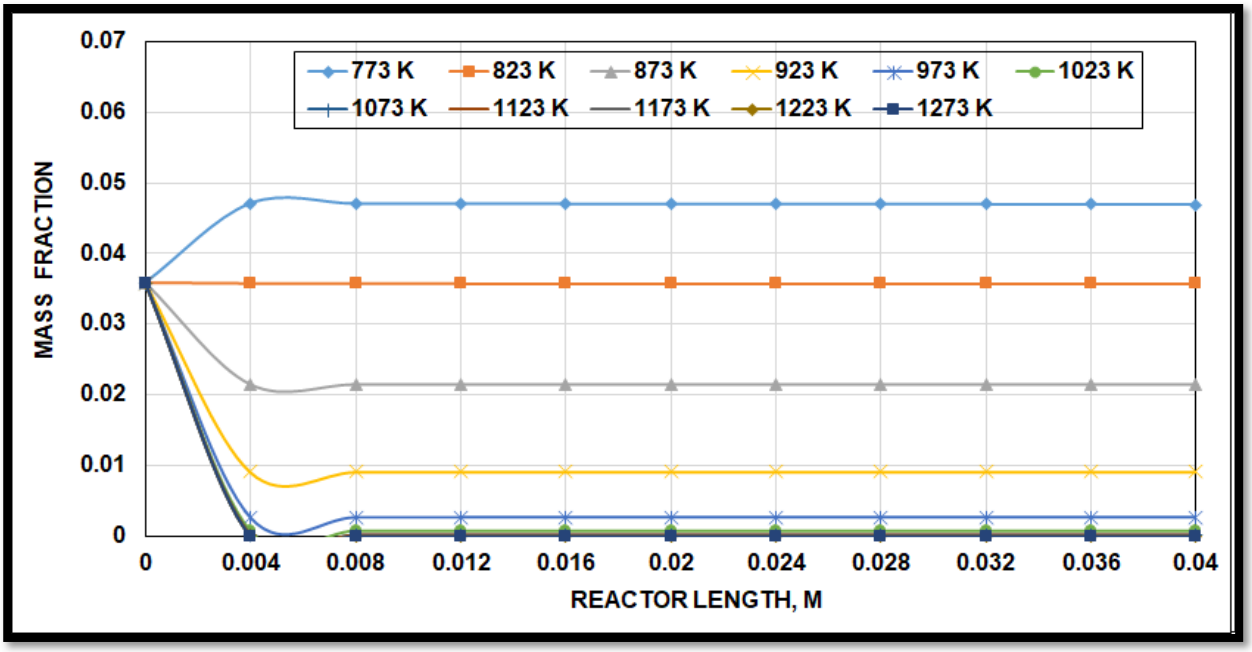

Figure 6.11. The variation of CH_4 mass fraction with reaction temperature along the RPLUG reactor.

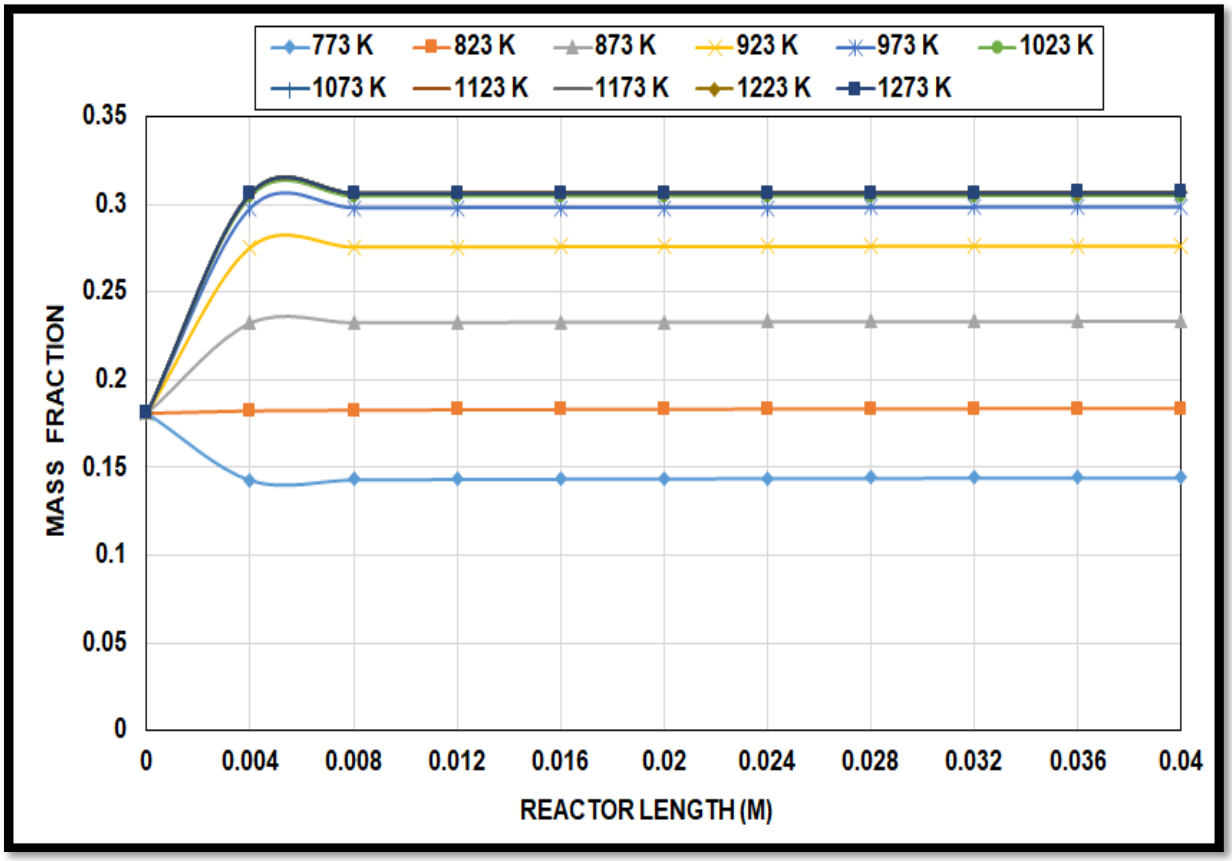

Figure 6.12. The variation of CO mass fraction with reaction temperature along the RPLUG reactor.

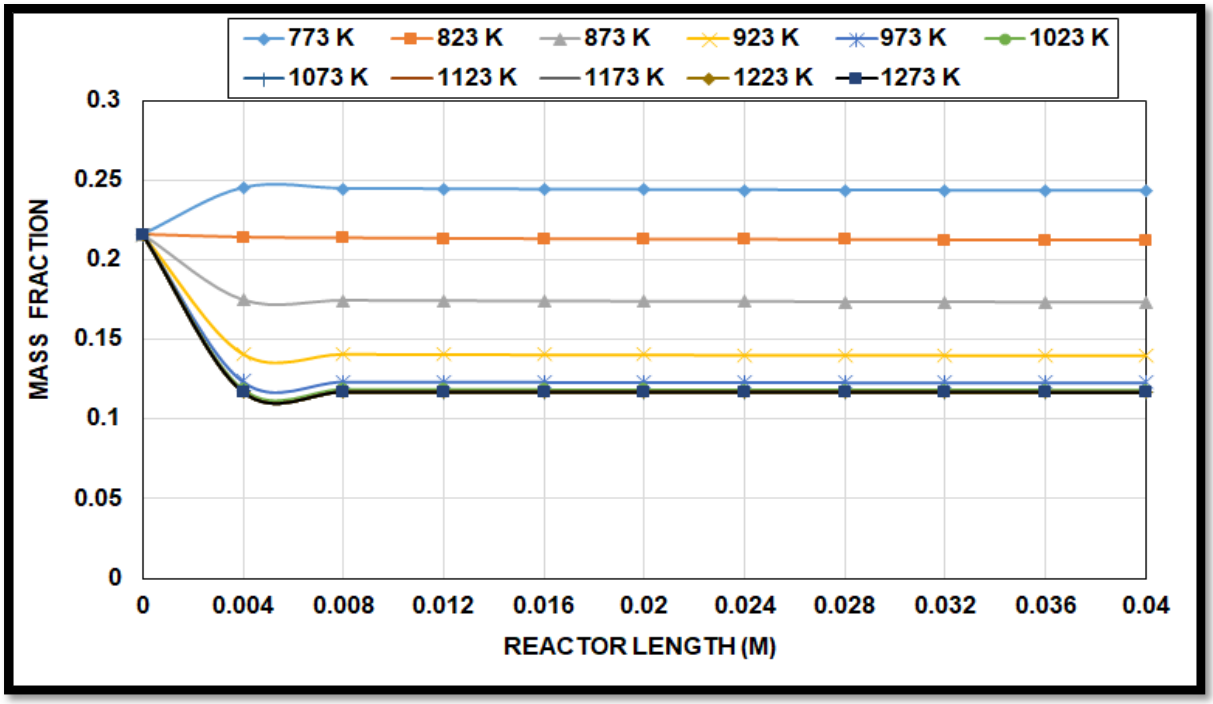

Figure 6.13. The variation of CO_2 mass fraction with reaction temperature along the RPLUG reactor.

In the same context, the selectivity of H_2 and CO are also varied with the reaction temperature. However, the selectivity of H_2 and CO at low reaction temperatures 500 and 550 ^oC are negative here as the conversion of CH_4 and CO_2 are negative as shown in figure 6.8. The variation of H_2 and CO selectivity through the 600 to 1000 ^oC temperature range is shown in figure 6.14. The reason for the decrease in CO selectivity and the increase in H_2 selectivity with the raise of the reaction temperature is the behaviour of CH_4, CO_2, CO and H_2 mole fractions to temperature and recombination between molecules. The reduction of CO_2 mole fraction was higher than CH_4 and the raise in H_2 mole fraction was greater than CO as shown in figure 6.15.

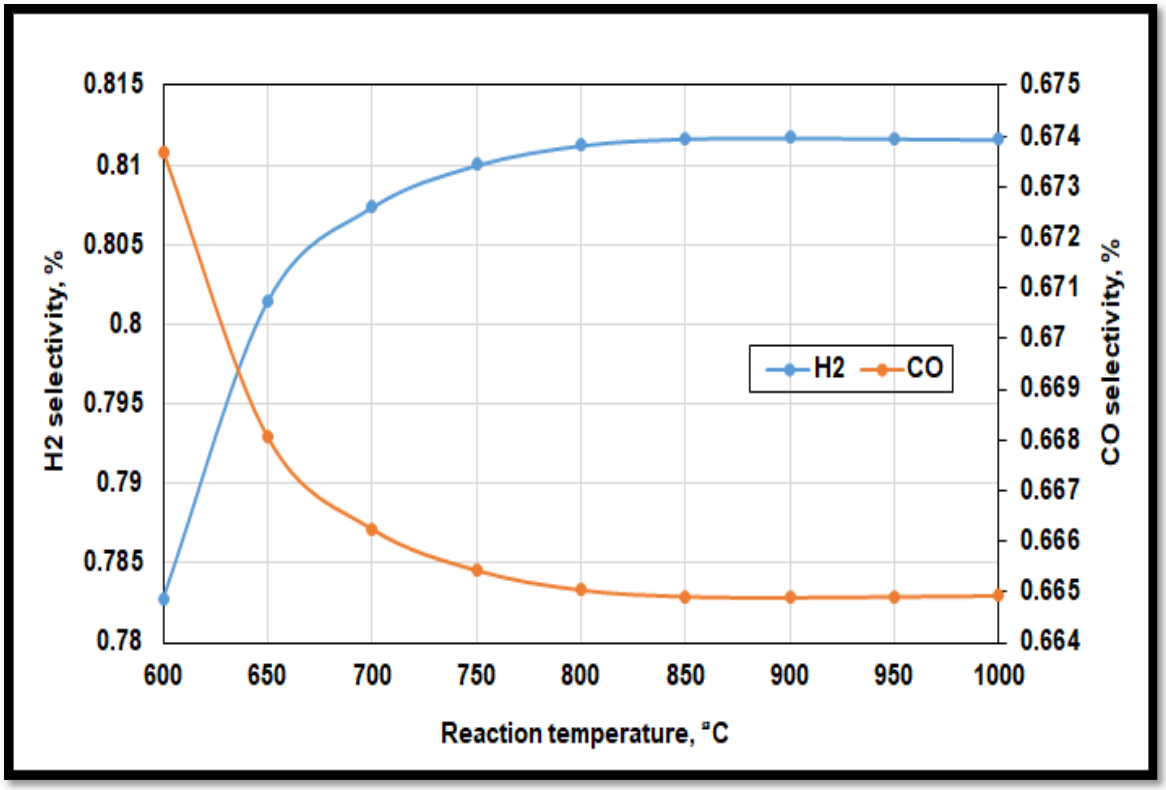

Figure 6.14. The effect of reaction temperature on the selectivity of H_2 and CO.

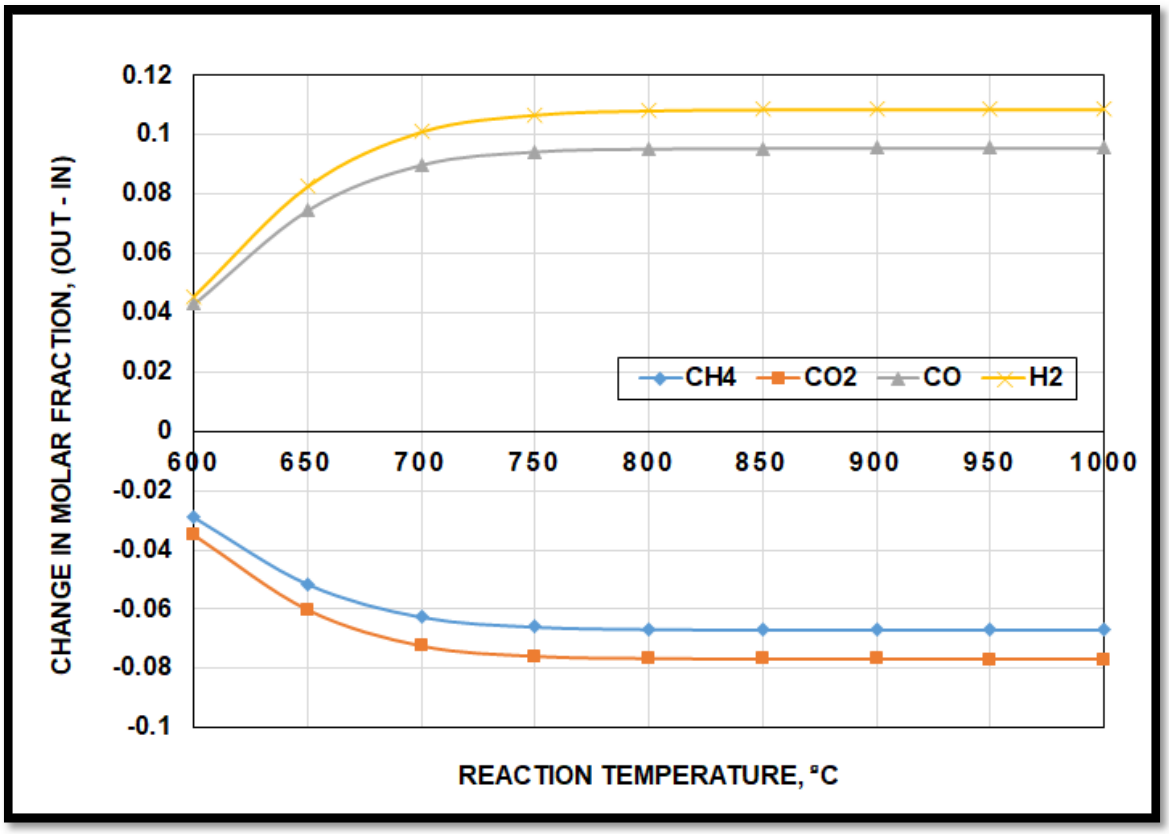

Figure 6.15. The effect of reaction temperature on the difference of molar fraction between the reactor outlet and inlet gases.

The effect of reactor temperature on the reaction heat duty and residence time are shown in figure 6.16. The negative and low heat duty in the low temperatures is related to the activity of the exothermic reaction methanation or the reverse steam reforming ($CO + 3H_2 \leftrightarrow CH_4 + H_2O$) at these temperatures (Gao et al., 2013).

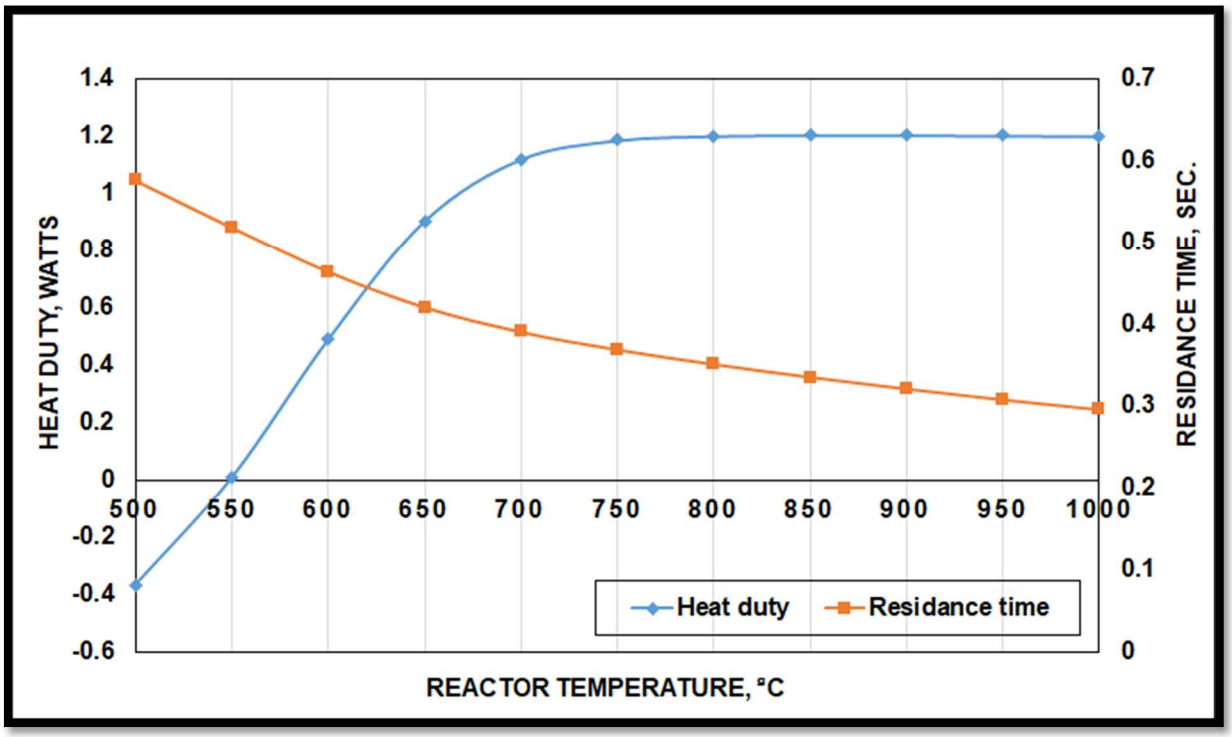

Figure 6.16. The effect of reactor temperature on the reaction heat duty and residence time.

6.6.1.2. The Effect of Catalyst Loading in Case One

The influence of the catalysts was also assessed towards the production of the final gas composition. Figure 6.17 shows the variation of the product gas mass fraction with different catalyst loading. The increase in catalyst loading causes an increase in the mass fraction of CH_4 and CO and a decrease in CO_2 and H_2 mass fraction. However, these changes are very small compared to the effect of temperature. The catalyst loading has also a little effect on the reaction heat loading and residence time as shown in figure 6.18.

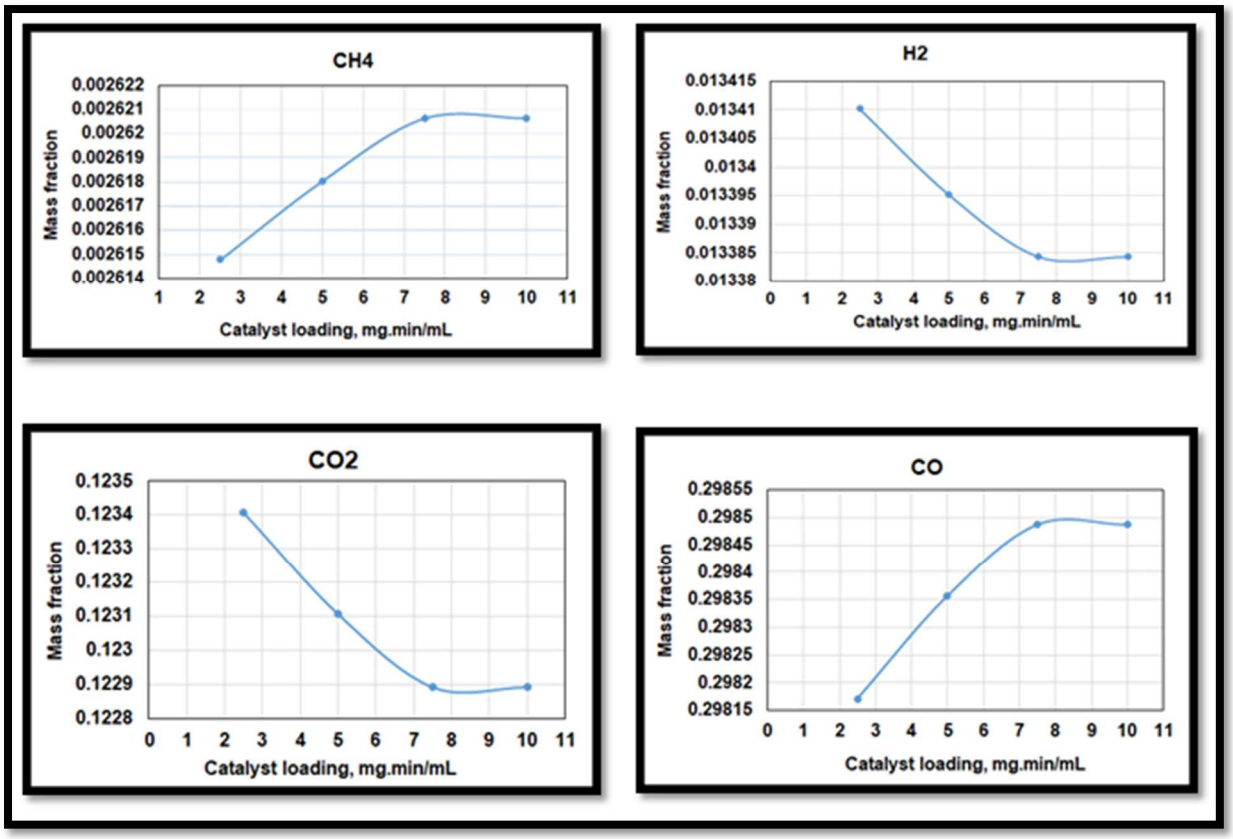

Figure 6.17. The effect of catalyst loading on product gases mass fraction.

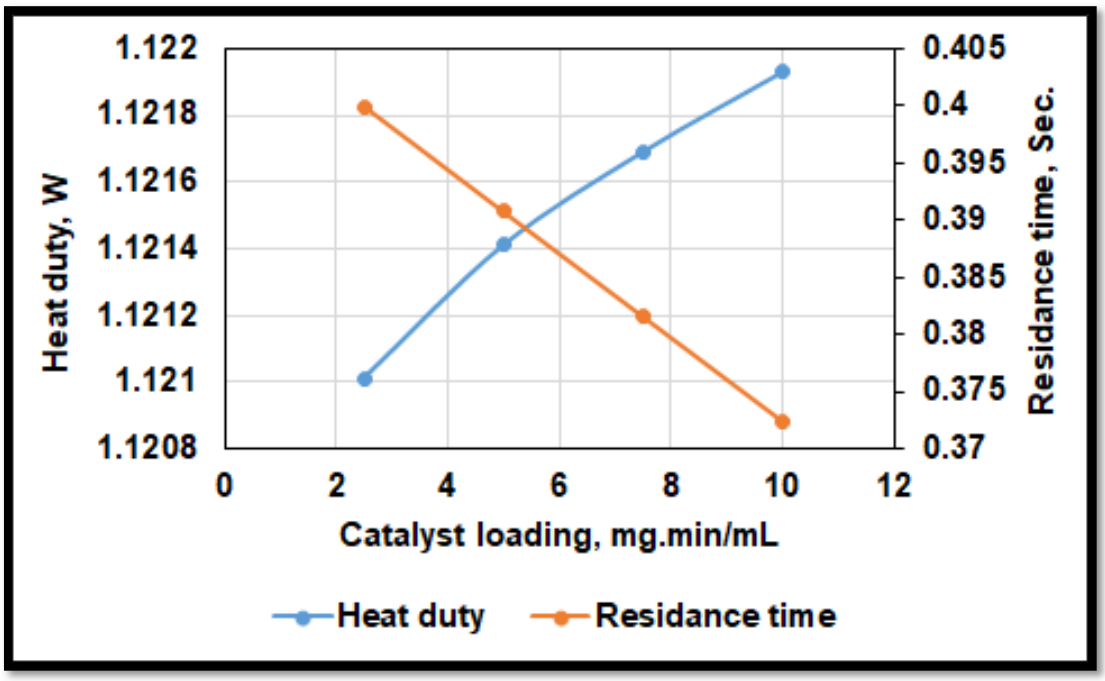

Figure 6.18. The effect of catalyst loading on the reaction heat duty and residence time.

6.6.2. Case Two Results

In this case, only nitrogen was used as a dilute gas with the BFBG blend. The reaction conditions are the same, i.e. feeding flow rate set at 100 mL/min at a pressure of 101.325 kpa. At 700^{o}C reaction temperature and 5 mg.min/mL catalyst loading, the gas mass fraction along the reactor is shown in figure 6.19. The effect of removing the Ar can be seen in the BFBG gases peaks and H_2O formation. Although the concertation of gases has increased, the selectivity of H_2 and CO decreased. The H_2 selectivity is 74.3 % and CO selectivity is 56.03%. This is due to the increase of the denominator of selectivity equations 6-1 and 6-2.

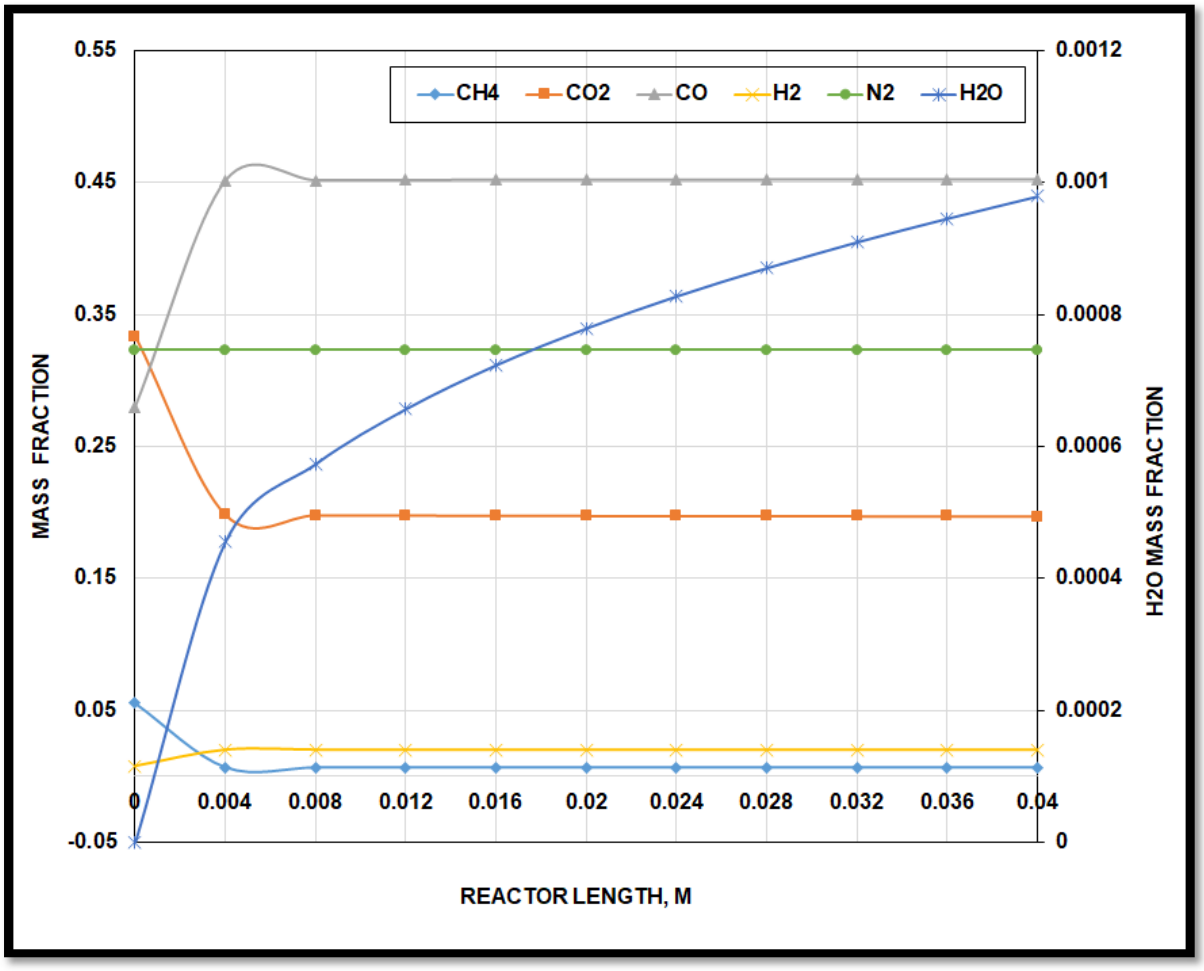

Figure 6.19. Mass fraction variation of the case two gases along the RPLUG reactor.

In addition, the heat duty of the reaction has increased in case two to be 1.508 Watt and the residence time decreased slightly to be 0.376 seconds. Figure 6.20 shows the variation of reaction heat duty and residence time along the reactor for case two.

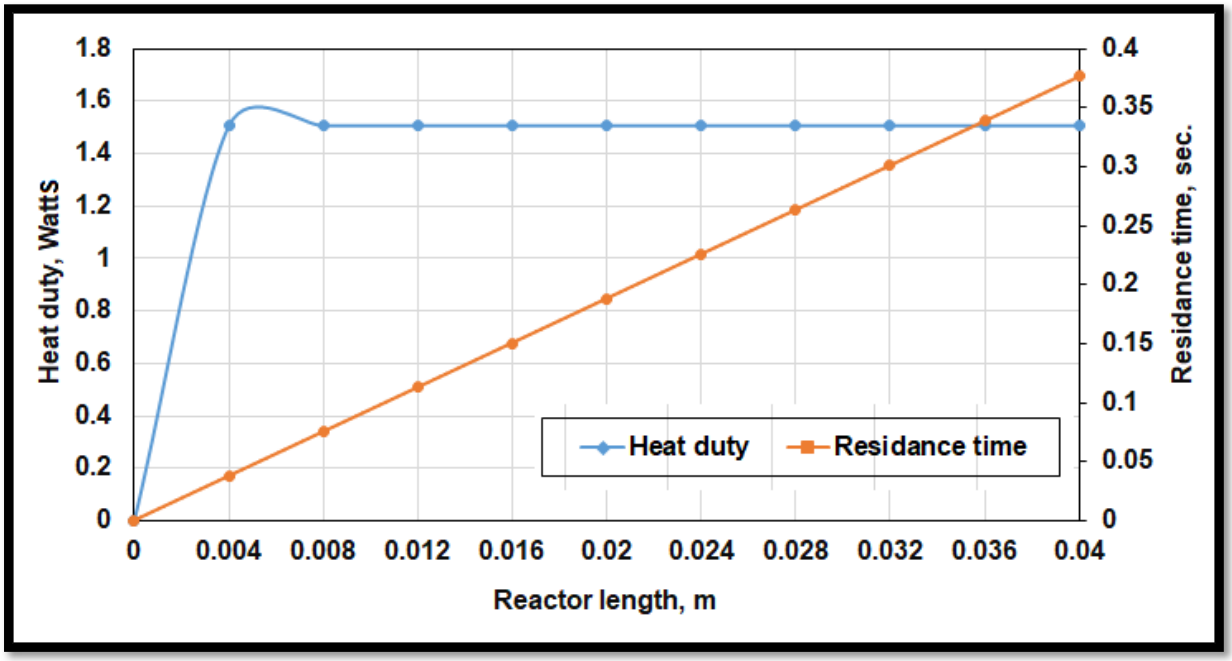

Figure 6.20. The variation of heat duty and residence time along the RPLUG reactor for case two gas mixture.

6.6.2.1. The Effect of Reaction Temperature in Case Two

The effect of the reactor temperature on the mass fraction of the different species is shown in figure 6.21. The gases have mostly the same behaviour as in case one with a noticeable high mass fraction for all BFBG blend gases and formed H_2O. However, case two selectivity of H_2 and CO were lower than those seen in case one for all reaction temperatures due to the increase in denominators as illustrated before. Figure 6.22 shows the variation of H_2 and CO selectivity with temperature for case two.

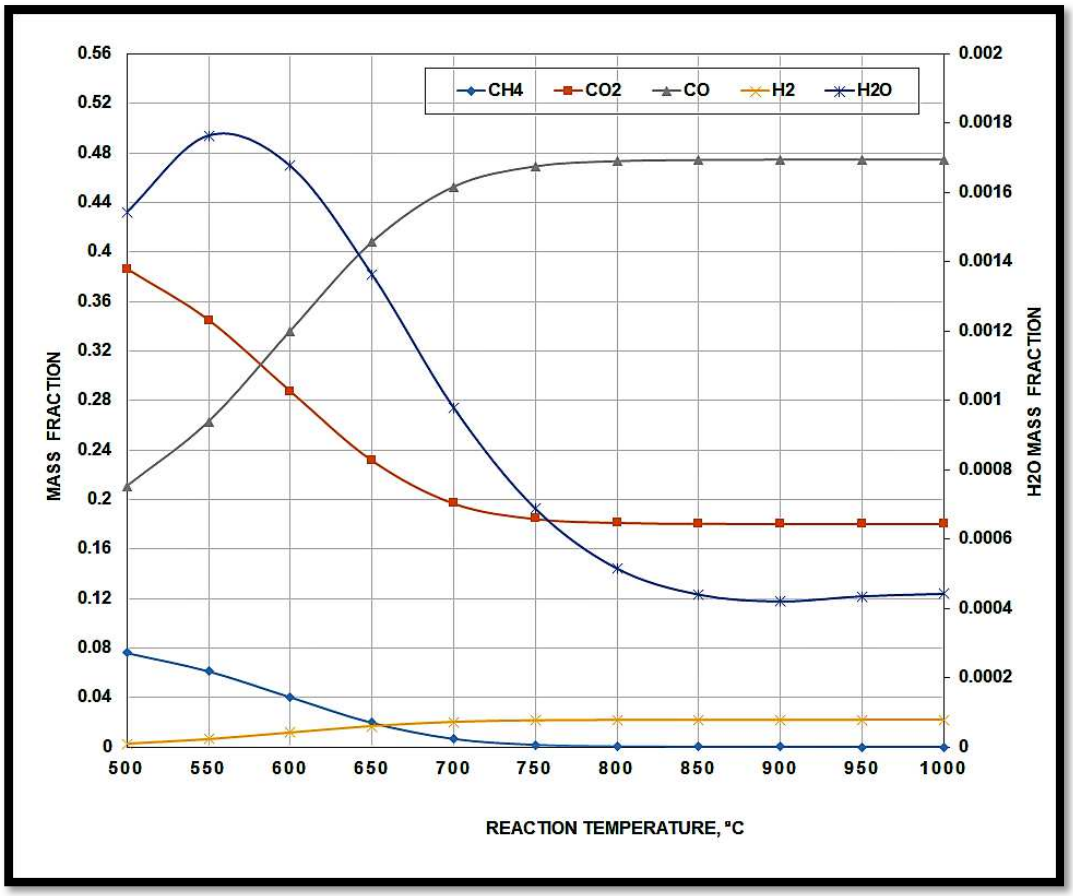

Figure 6.21. The effect of reactor temperature on the mass fraction of case two product gases.

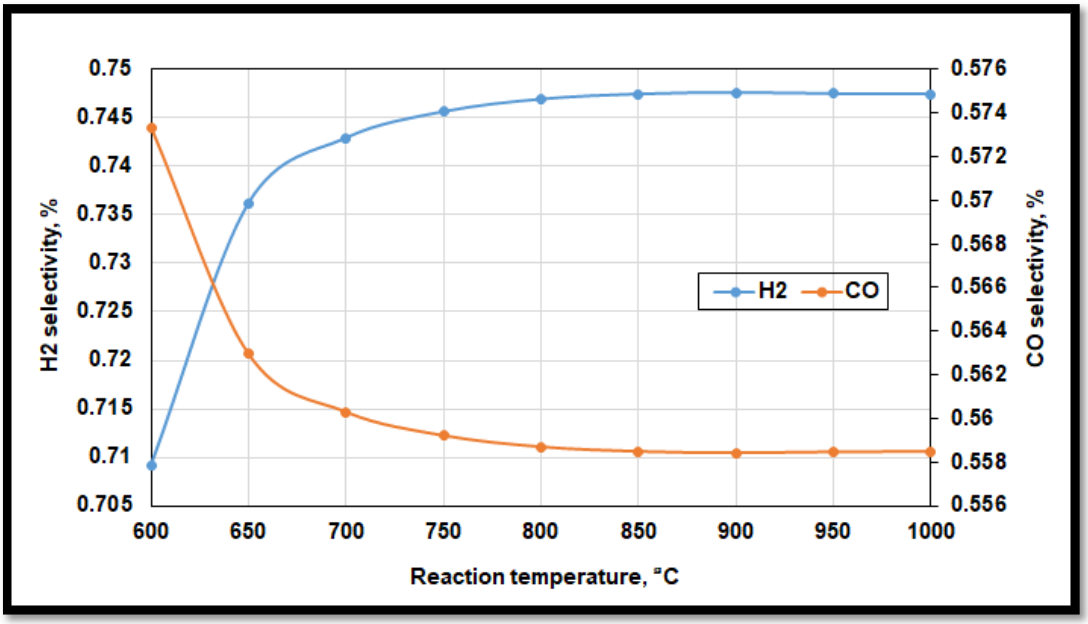

Figure 6.22. The effect of reactor temperature on the H_2 and CO selectivity of case two.

In figure 6.23, the effect of reaction temperature on the heat duty and resident time of the reaction for the medium feeding case is clarified. The simulation predicted lower heat duty at low temperatures, and higher than case one at high reaction temperatures.

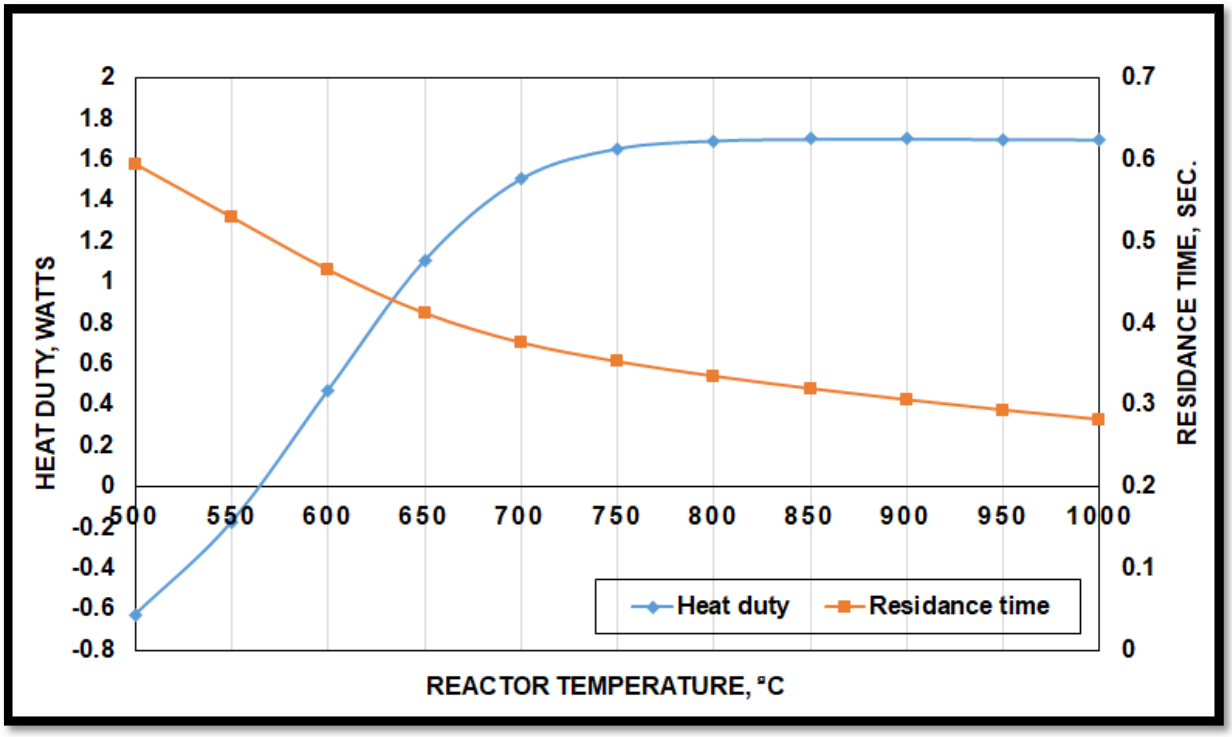

Figure 6.23. The variation of reaction heat duty and residence time with temperature for case two gas mixture.

6.6.2.2. The Effect of Catalyst Loading in Case Two

Catalyst loading has also an effect on the molar fraction of this case. In figures 6.24 and 6.25 the influence of different catalyst loading on the CH_4 – H_2 and CO_2 – CO is illustrated, respectively. The selectivity of H_2 has decreased with catalyst loading as the concentration of CH_4 increased and the concentration of H_2 decreased as shown in figure 6.24. This also explains the increase in CO selectivity as CO concentration increased and CO_2 decreases as shown in figure 6.25.

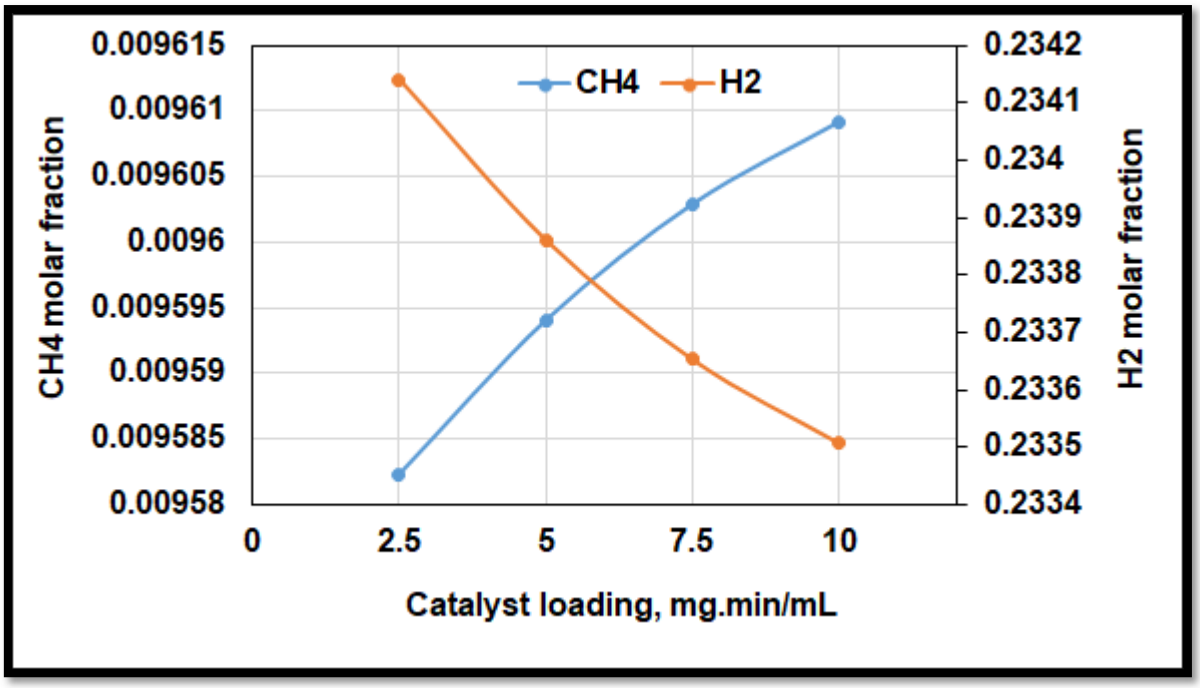

Figure 6.24. the effect of catalyst loading on CH_4 and H_2 concertation in case two.

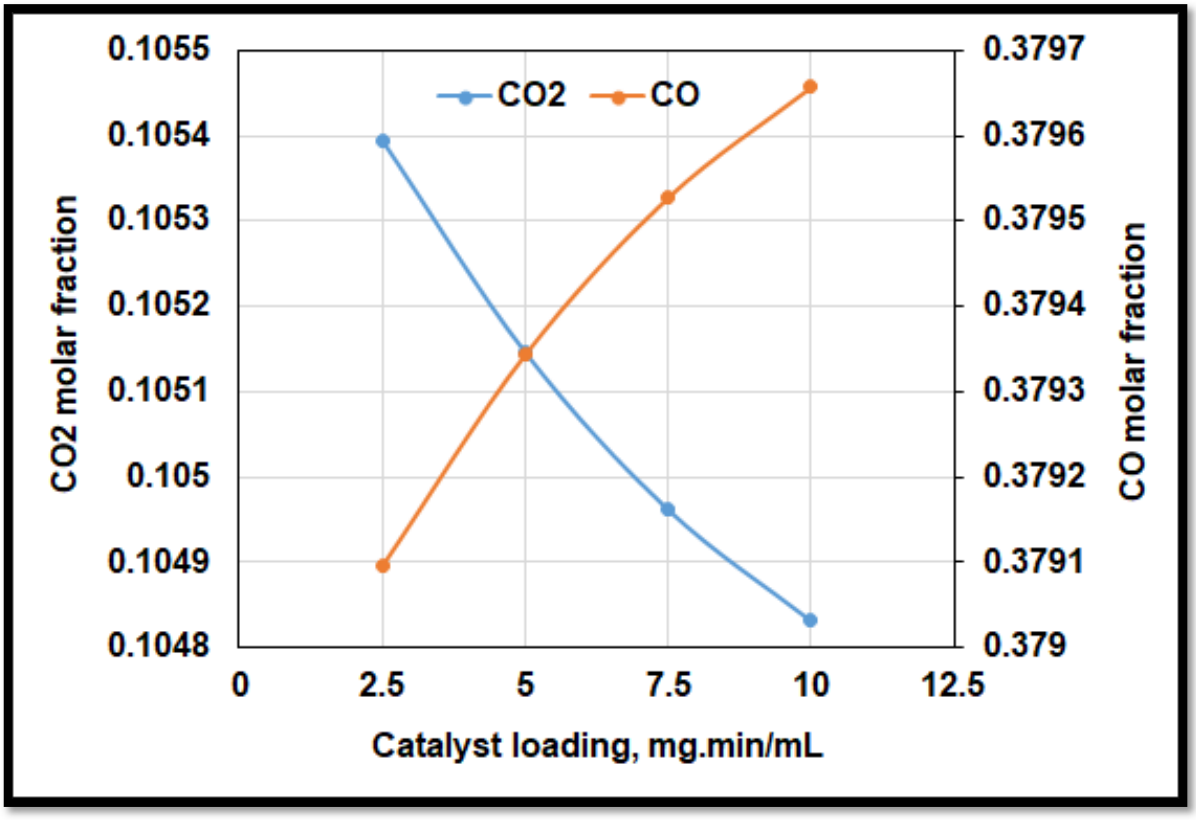

Figure 6.25. the effect of catalyst loading on CO_2 and CO concertation in case two.

The heat duty and residence time have a contradictory behaviour with catalyst loading as shown in figure 6.26. The rise in reaction heat duty with the increase of catalyst amount has been offset by a decrease in residence time.

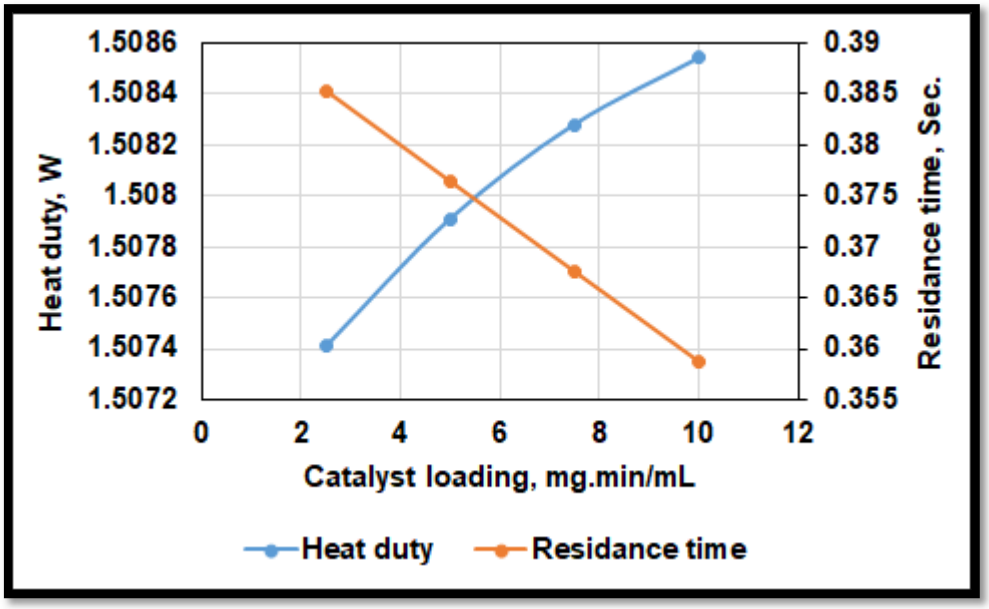

Figure 6.26. The effect of catalyst loading on heat duty and residence time of case two mixture.

6.6.3. Case Three Results

In the strong feeding case, the selectivity of H_2 and CO were lower than the previous two cases at the same reaction conditions. i.e. 100 mL/min flow rate at reaction temperature 700° C and 1 atm reaction pressure flows over 500 mg of activated catalyst. H_2 selectivity was 65.26% while the CO selectivity was 41.934% in this case.

6.6.3.1. The Effect of Reaction Temperature in Case Three

Reaction temperature has also a positive impact on the components transformations of case three mixture. Figure 6.27 shows the variation of the molar fraction change before and after the reactor for the case three gases. More gas conversion was been expected when the

reaction temperature has increased. On the other hand, the heat duty was also increased with the reaction temperature and residence time decreased as shown in figure 6.28.

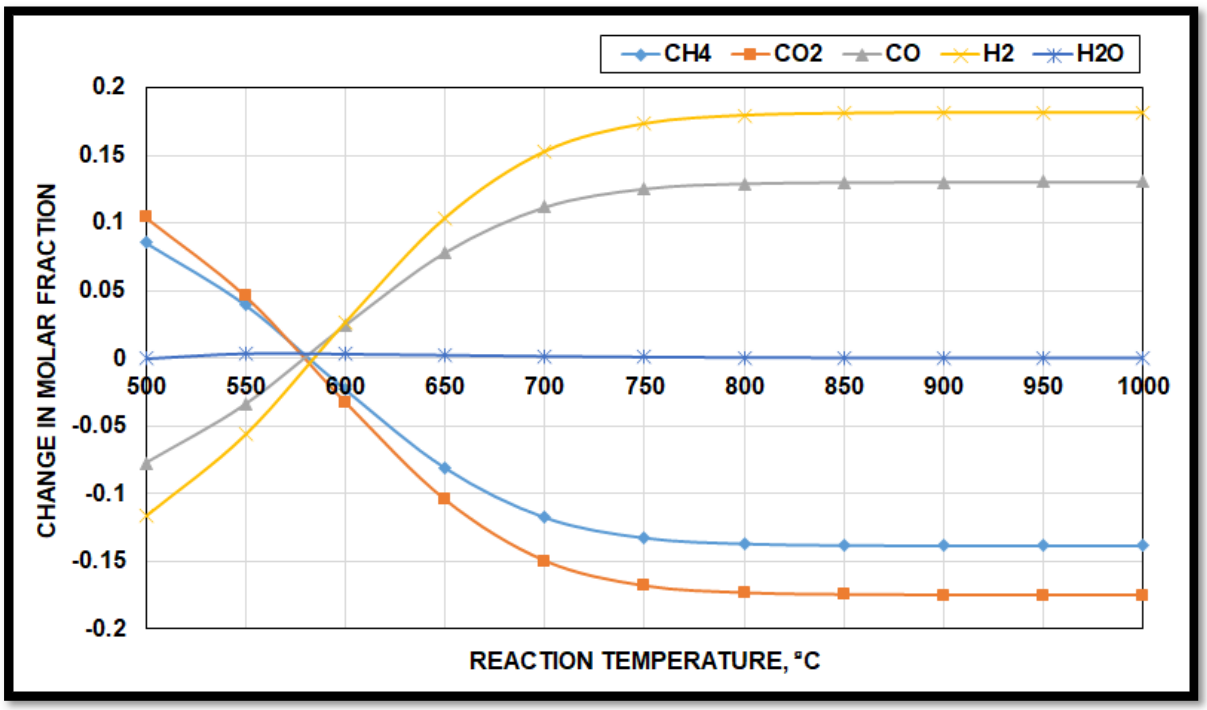

Figure 6.27. The effect of reaction temperature on the changing of case three gases before and after the reactor.

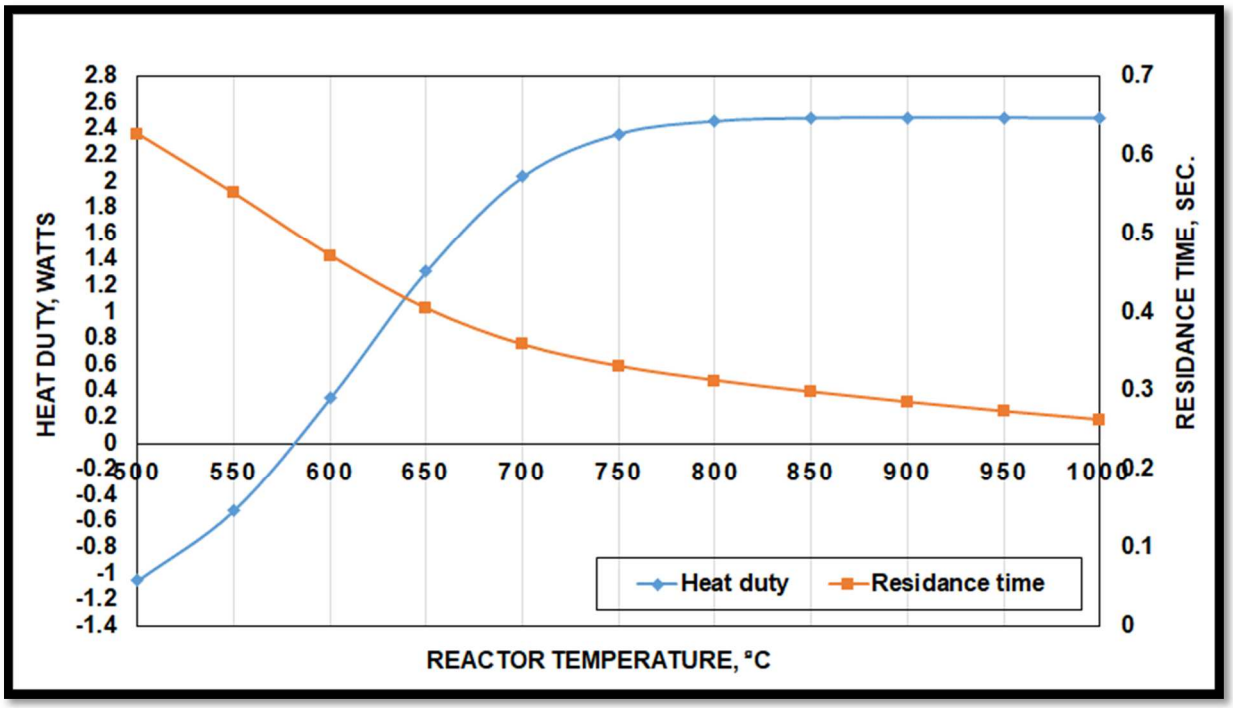

Figure 6.28. The variation of reaction heat duty and residence time with temperature for case three gas mixture.

6.6.3.2. The Effect of Catalyst Loading in Case Three

In case three, the catalyst loading has a very little effect on the conversion of gases. Figure 6.29 shows the variation of gases molar fraction with different catalyst loading. These comparatively small changings improved the CO selectivity and decreased the H_2 selectivity as shown in figure 6.30.

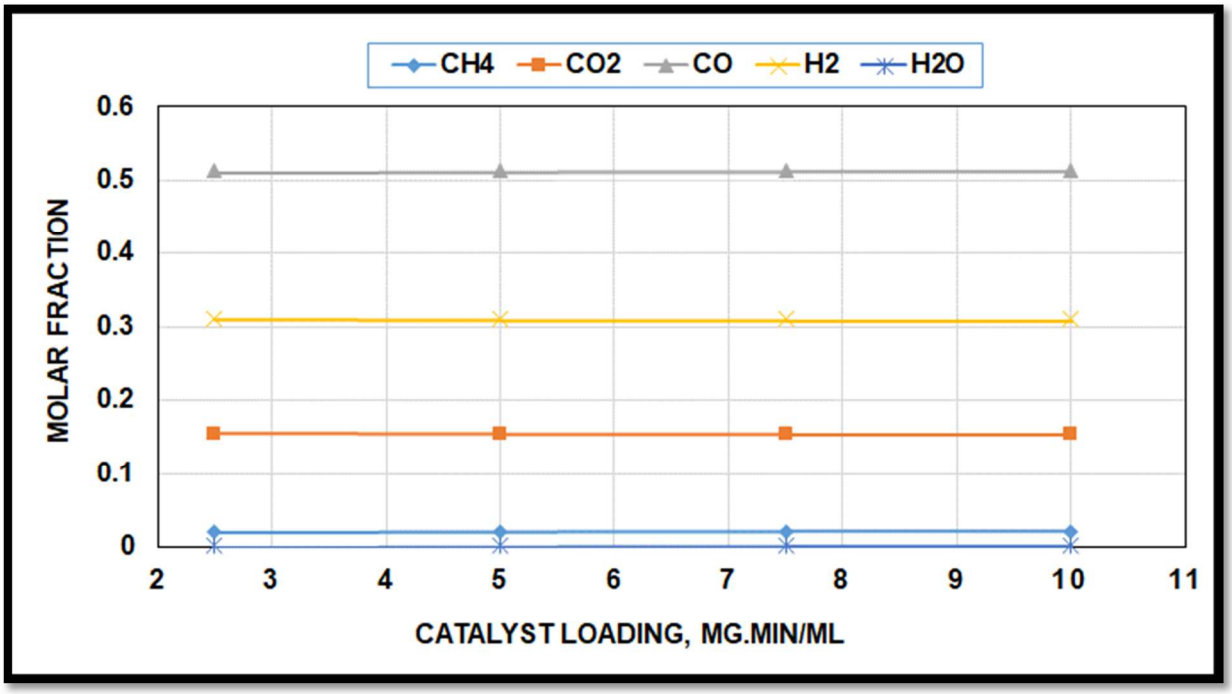

Figure 6.29. The effect of catalyst loading on the concentration of case three gases.

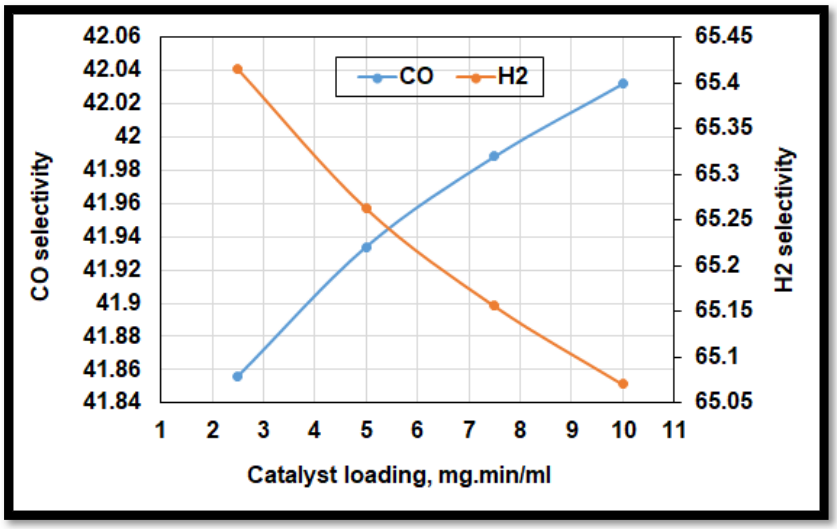

Figure 6.30. The effect of catalyst loading on the CO and H_2 selectivity in case three.

Moreover, as the heat duty increased slightly with catalyst loading the residence time decreased as shown in figure 6.31.

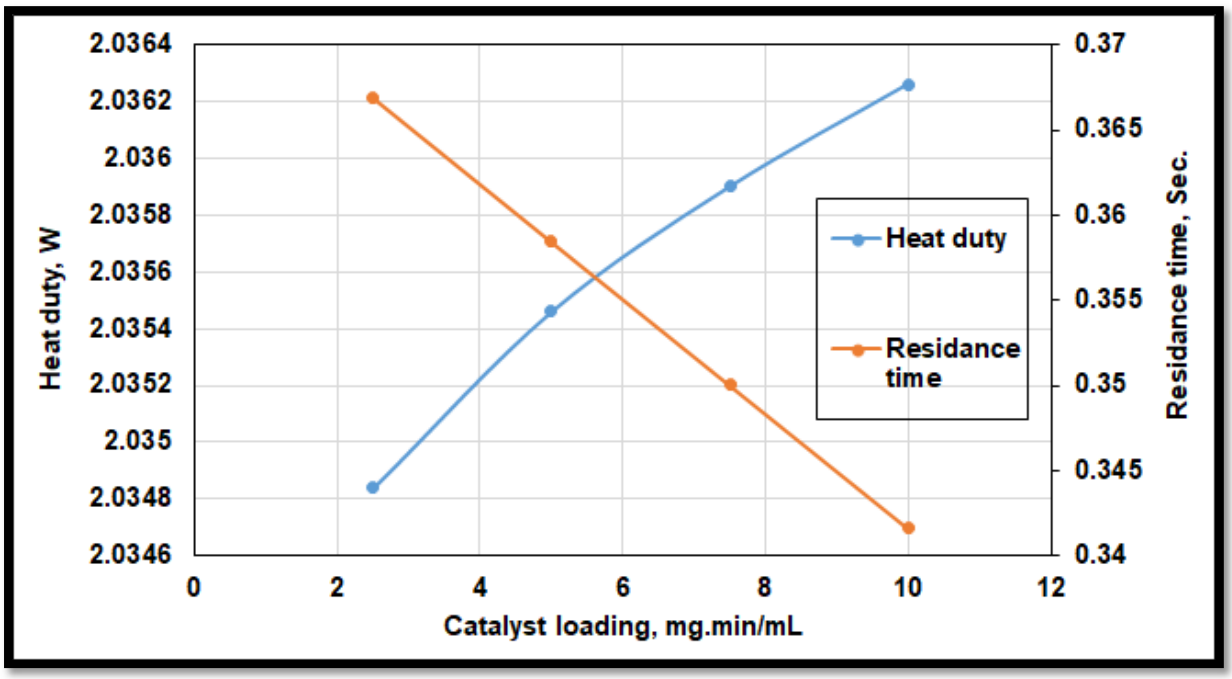

Figure 6.31. The effect of catalyst loading on the heat duty and residence time in case three.

6.6.4. Comparison Between Cases

Table 6-5 shows the selectivity of H_2 and CO for the three feeding cases at the same reaction conditions.

Table 6-5 Comparison between H_2 and CO selectivity for the three study cases.

Syngas	Selectivity (%)			Note
	Case one	Case two	Case three	
H_2	80.737	74.296	65.263	
CO	66.624	56.029	41.934	

To compare between the conversion rate of CH_4 and CO_2 and the H_2/CO molar ratio for the three cases, table 6-6 presents the value of these parameters for the same operational conditions. The values of these ratios are calculated using the following equations (Sun et al., 2011):

$$\mathrm{CH_4\ conversion} = \frac{\mathrm{CH_{4.in} - CH_{4.out}}}{\mathrm{CH_{4.in}}} \times 100\% \quad \text{..... 6-3}$$

$$\mathrm{CO_2\ conversion} = \frac{\mathrm{CO_{2.in} - CO_{2.out}}}{\mathrm{CO_{2.in}}} \times 100\% \quad \text{..... 6-4}$$

$$\mathrm{H_2/CO\ ratio} = \frac{\mathrm{H_{2.out}}}{\mathrm{CO_{out}}} \quad \text{..... 6–5}$$

The concentration of all components in all these equations are in mole fraction.

Table 6-6. The reactants conversion rates and H_2/CO ratio for the cases.

	Case one	Case two	Case three
CH_4 conversion (%)	93.506	89.869	84.797
CO_2 conversion (%)	49.266	49.376	49.257
H_2/CO ratio	0.624	0.616	0.605

The conversion of CH_4 and H_2/CO ratio were the highest in case one and the CO_2 conversion was slightly high in case two than the other cases. However, the strong feeding case was the lowest among the other cases under all conditions.

According to the above, the dilution gases have a significant effect in improving the selectivity of the syngas and enhance the conversion of the reactant gases. Moreover, the case three mixture consumed more heat than the other two cases at low residence time as listed in table 6-7 due to the large amount of reactive gases in it. Although the strong mixture has the highest production rate of the syngas (CO and H_2), this mixture has the lowest rate of produced syngas per watt of heat duty as shown in table 6-8.

Table 6-7. The heat duty and residence time for the three-case study.

	Unit	Case one	Case two	Case three
Heat duty	Watts	1.121	1.508	2.035
Residence time	Seconds	0.390	0.376	0.358

Table 6-8. The rate of produced syngas per process heat duty for the three cases.

Syngas	Net syngas production rate per heat duty (mL/min.W)		
	Case one	Case two	Case three
CO	8.024	6.973	5.501
H_2	9.021	8.386	7.531

In this context, the thermal energy required for the production of a one kmol of H_2 in the three cases are 41.4 kWh, 44.5 kWh and 49.6 kWh, respectively. Although, the simulation was done for a small flow rate (100mL/min), the thermal energy required for the production of H_2 was lower than the heat estimated by different references (De Falco et al., 2014).

6.6.4.1. The Effect of Reaction Temperature

The temperature of the reactor has a significant effect on the different reaction parameters such as CH_4 and CO_2 conversion rate and H_2/CO ratio. In figures 6.32 and 6.33, the conversion of CH_4 and CO_2 are shown. The conversion of CH_4 reached more than 99% for all cases at the reaction temperature 800 ^oC and more. The maximum CH_4 conversion rate was more than 99.99% recorded for case one at a reaction temperature of 1000 ^oC.

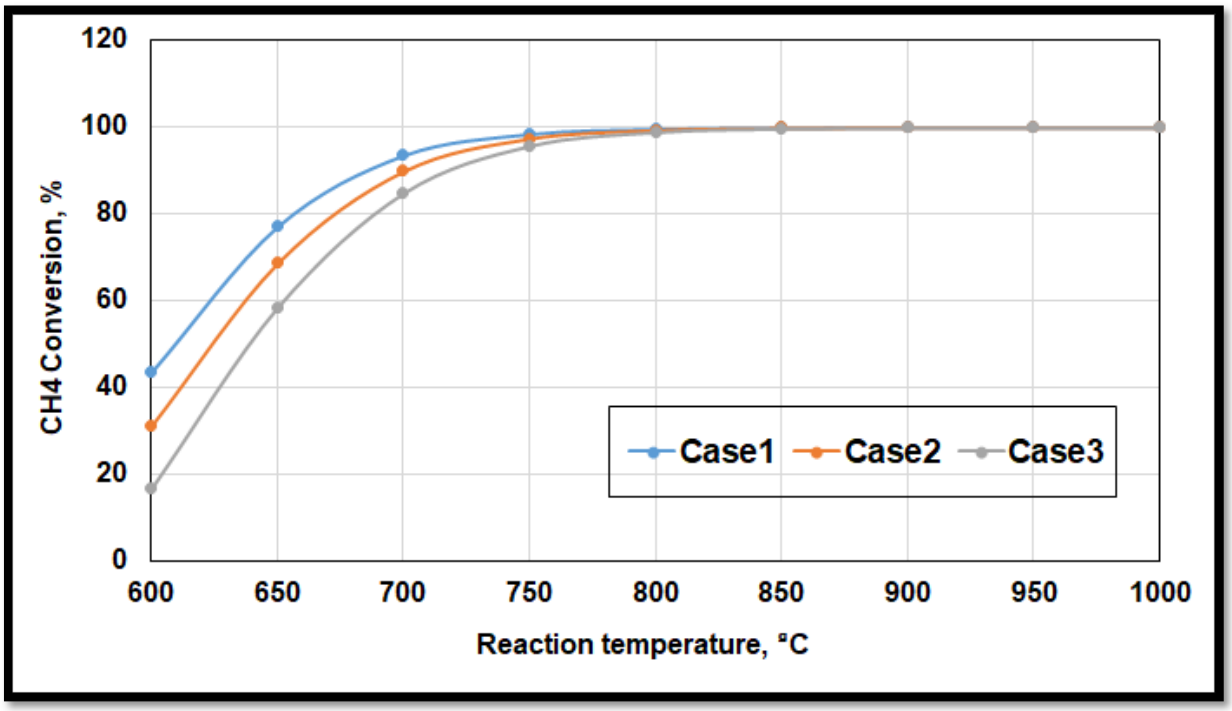

Figure 6.32. The effect of reaction temperature on the CH_4 conversion rate for the three cases.

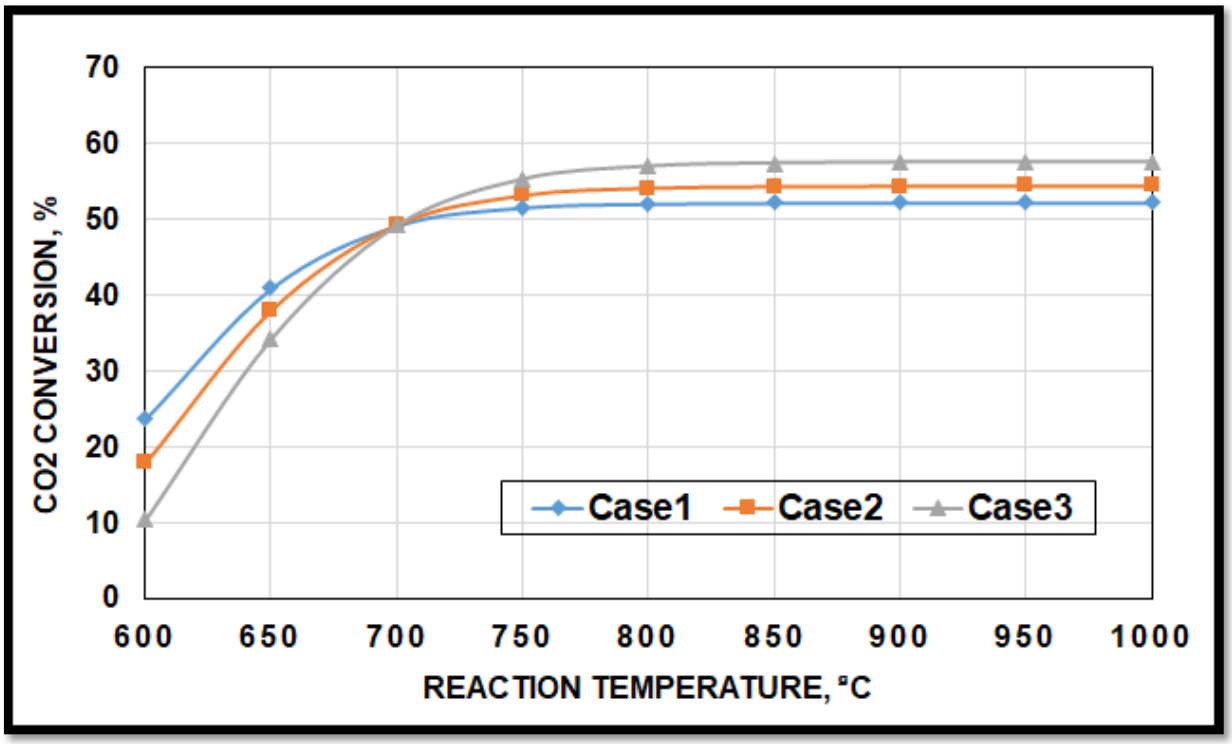

Figure 6.33. The effect of reaction temperature on the CO_2 conversion rate for the three cases.

On the other hand, the conversion of CO_2 reached its highest rates at temperatures above 750 ^oC with the preference to case three gas mixture. The maximum CO_2 conversion rate was 57.6% at a reaction temperature of 1000 ^oC in case three.

Regarding the CO and H_2 selectivity, the light gaseous mixture showed the best performance among the other cases at all reaction temperature as shown in figures 6.34 and 6.35. The maximum CO selectivity was 67.37% at a reaction temperature of 600 ^oC in case one and the maximum H_2 selectivity was 81.174% at 900 ^oC reaction temperature for case one too.

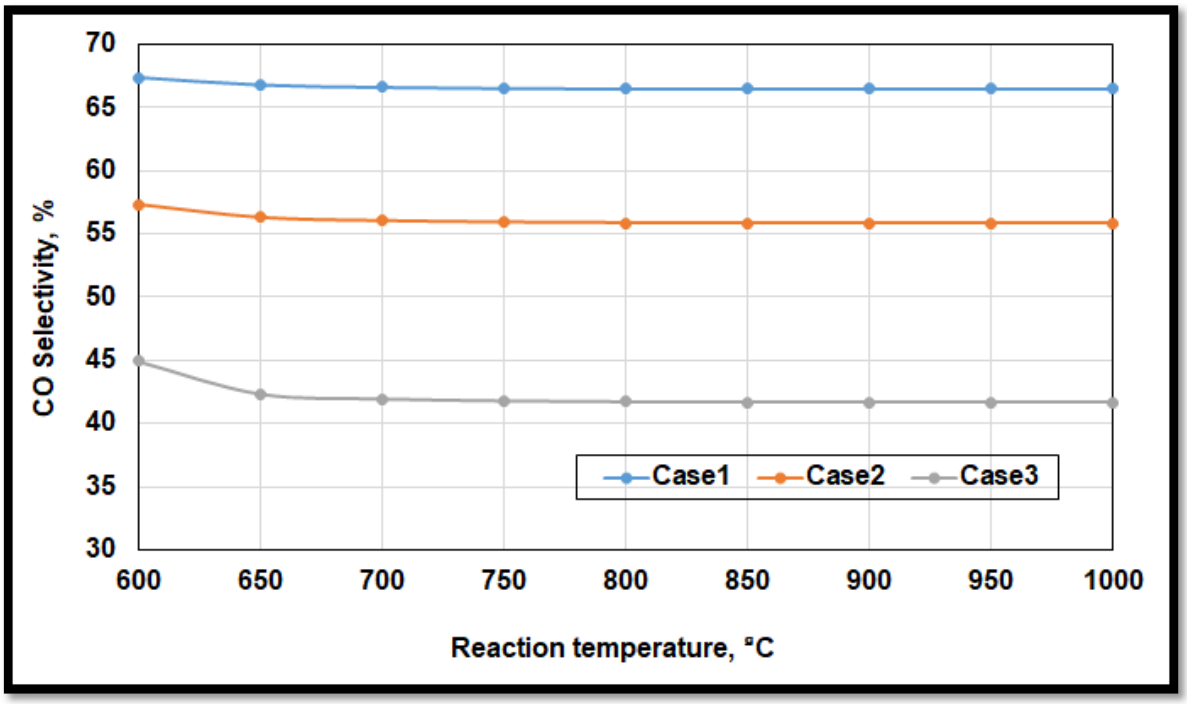

Figure 6.34. The effect of reaction temperature on the CO selectivity for different feeding cases.

In the same field, the H_2/CO ratio increased significantly after the reaction temperature exceeds the 600 ^oC for all cases and reached its highest values at 0.638 at temperatures more than 750^o C as shown in figure 6.36.

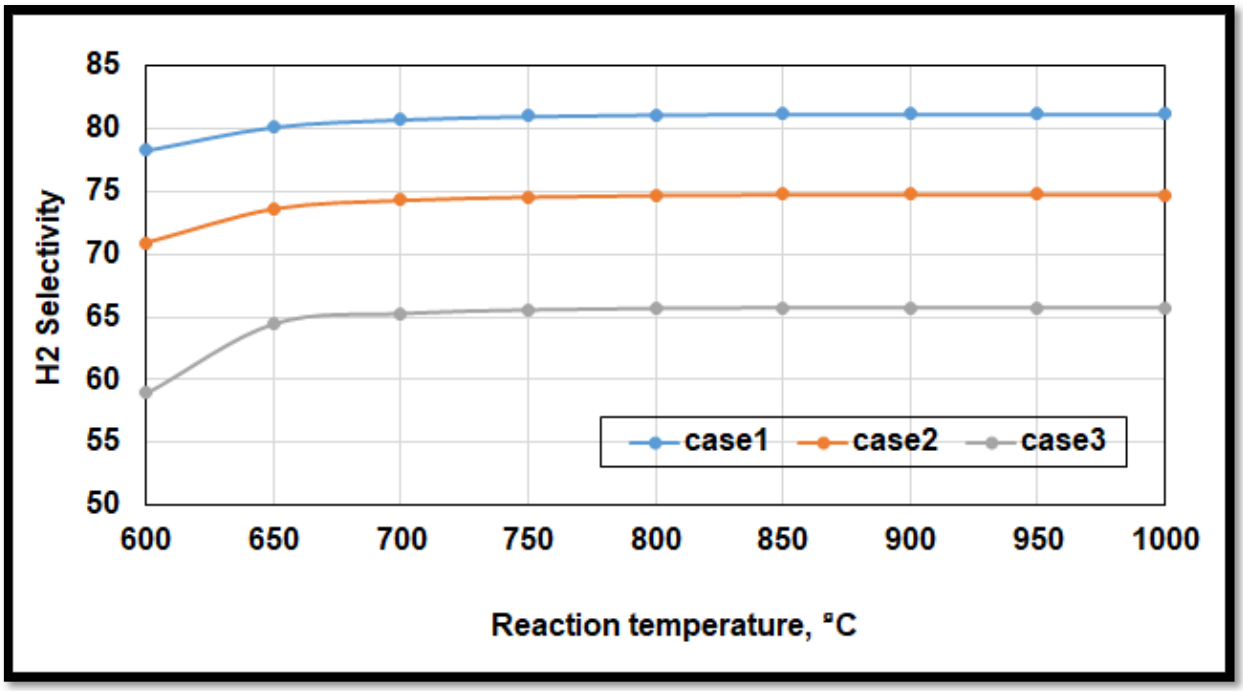

Figure 6.35. The effect of reaction temperature on the H_2 selectivity for different feeding cases.

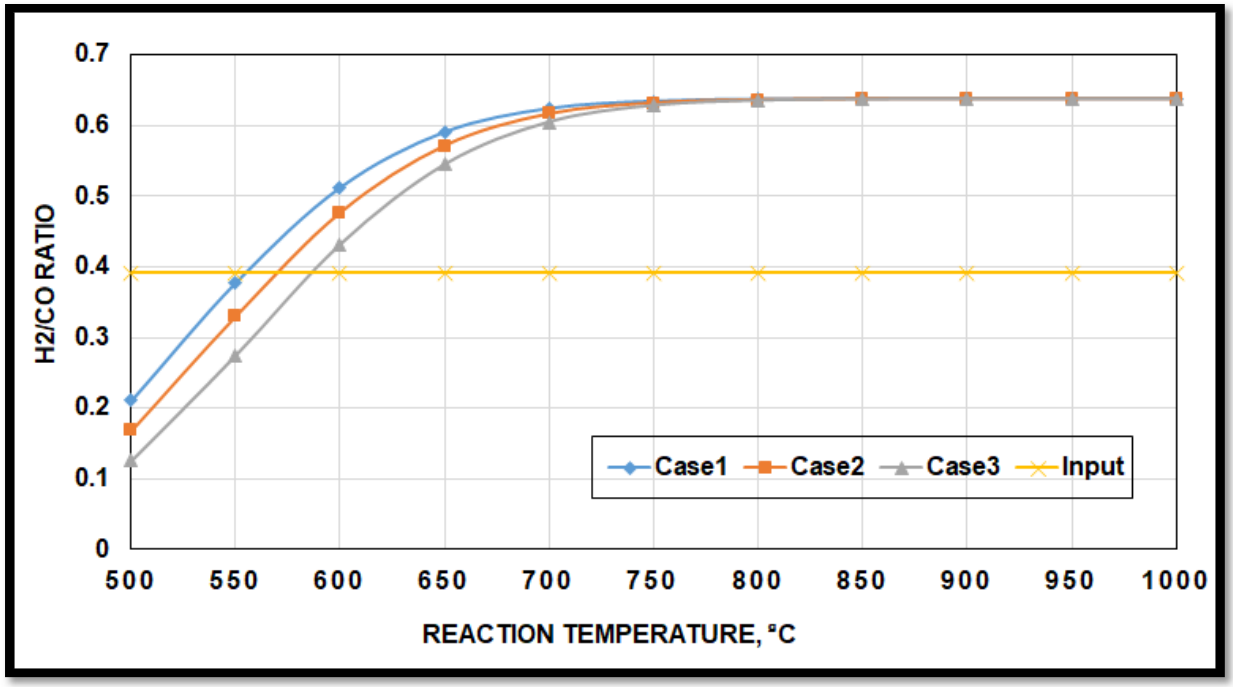

Figure 6.36. The effect of reaction temperature on the H_2/CO ratio for different feeding cases.

The heat duty for the three cases is shown in figure 6.37. The case three feeding mixture consumed higher heat than the other cases due to a large amount of the reactive gases as explained before.

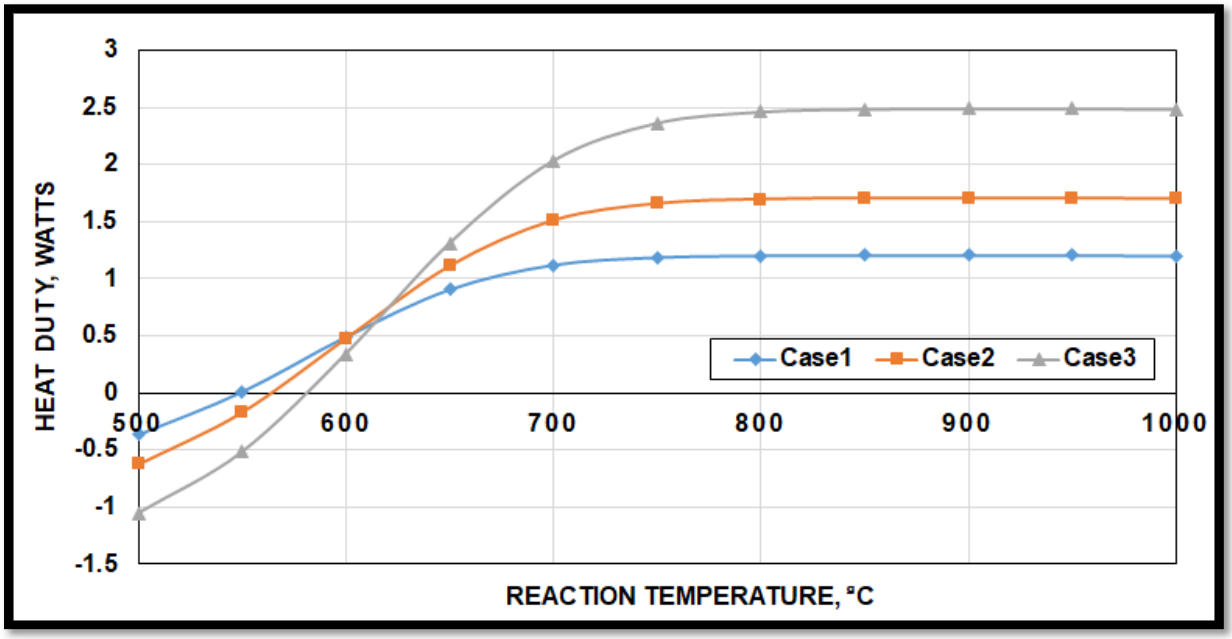

Figure 6.37. The effect of reaction temperature on the heat duty of the three feeding cases.

The production of hydrogen per thermal heat duty has increased with the increase of reaction temperature as shown in figure 6.38. The light feeding was estimated to produce the highest production of H_2 per total thermal duty at all reaction temperatures.

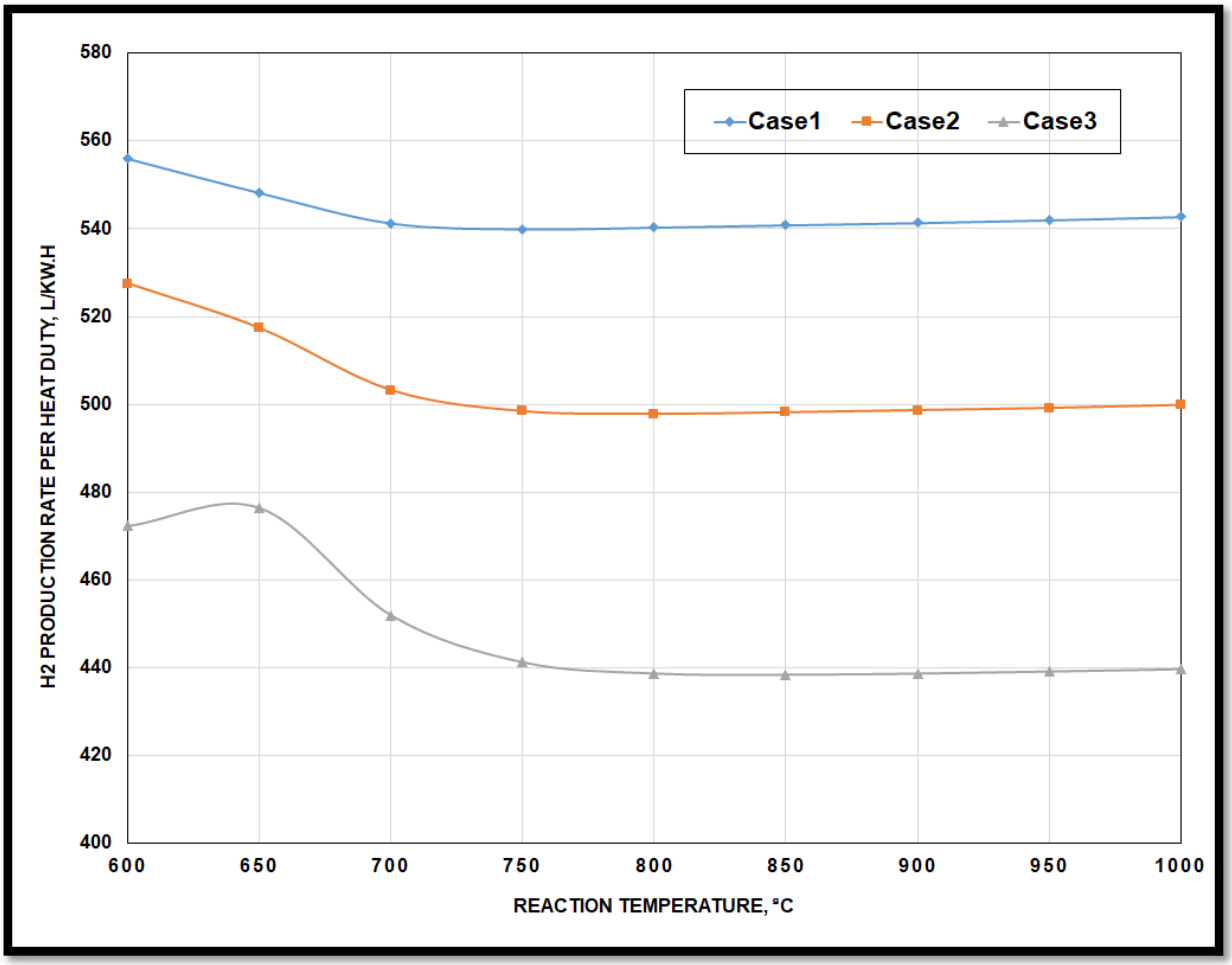

Figure 6.38. The effect of reaction temperature on the production rate of H_2 per each kWh of heat duty of the three feeding cases.

6.7. Conclusion

Production of high valuable gases using the new distributor in a BFBG has been demonstrated. Further improvements to the system were conceptualised via the use of a high temperature reformer in combination with different inert gases, catalyst and reaction temperatures. The improvement of the BFBG product gas has been simulated using Aspen Plus® software. The model has been validated with theoretical and experimental data from literature. Three different feeding conditions have been evaluated, i.e. light, medium and heavy feeding. The three cases were tested under the same conditions such as reaction temperature, pressure and catalyst loading.

At low reaction temperatures (500 and 550 ^{o}C), the system had a reverse effect for all cases. The concentration of CH_4 and CO_2 increased and H_2 and CO decreased due to the active reverse reactions at these low temperatures. However, the concentration of CH_4 and CO_2 started to decrease and H_2 and CO increased at the same time at 600 ^{o}C reaction temperature and above.

The conversion of CH_4 reached more than 99.99 % at temperature 1000 ^{o}C for case one and the conversion of CO_2 reached more than 57.6 % at 1000 ^{o}C temperature for case three. Meanwhile, the selectivity of H_2 reached more than 81 % at 900 ^{o}C reaction temperature for case one mixture and CO selectivity reached 67.37 % at 600 ^{o}C for the same case. The H_2/CO ratio for the products has also improved in this process. The ratio exceeded 0.637 in all cases at reaction temperatures greater than 800 ^{o}C.

The reaction temperature has also a significant effect on heat duty and residence time as the heat duty increased with temperature while residence time decreased. The maximum heat duty was 2.489 W at 900 ^{o}C for case three. On the other hand, the maximum H_2 production rate per thermal duty was recorded using case one mixture and reaction temperature of 1000 ^{o}C which is 542.7 Litter of H_2 per each kWh. Finally, the simulation showed little effect at various catalyst loading on the reaction parameters for all cases.

Chapter 7: Conclusion and Further Work

7.1. Introduction

This chapter is dedicated to highlight the results of all the previous works and how the implementation of all the new presented ideas can improve the delivery of usable gases from BFBG systems. The discussion is essentially focused on the use of a distributor that under the right conditions can generate complex hydrodynamics through the fluidized bed while ensuring that biomass has a better probability to being gasified into high hydrogen/carbon monoxide content product gases. The addition of a reformer, catalytic materials and inert atmospheres is also discussed in this development to complement the experimentally proved air distributor, thus ensuring that better syngas is obtained via concepts that can be easily applied to current system in order to make them more profitable.

7.2. Conclusions

1- Isothermal experiments of the BFBG have shown various BFBG performances for each of the four distributors analysed in this work, as illustrated in chapter 4. The experimental assessment is based on two main factors, pressure drop and bubble formation. Five positions along the inner wall were used to measure the pressure drop as cited in chapter four. The experimental results showed a different performance of the BFBG using the different distributors. For example, the small orifice distributors were better than the large orifice distributors in forming a uniform fluidised bed. From these, the triangular arrangement of orifices was better in producing bubbles and a uniform fluidised bed while showing a uniform pressure drop.

2- A large, complex multiphase simulation for the isothermal BFBG with the four distributors was carried out and explained in chapter 5. The influence of the gasifier

distributor design on the performance of the BFBG was studied in this simulation under isothermal conditions. The small holes distributors and the triangular holes arrangement distributors had better performance than the large holes distributors and square holes arrangement distributors which is the same finding in the experimental part. All designs showed formation of bubbles in different sizes and shapes.

Regarding the bed expansion, the simulation results showed a large bed expansion in the type D distributor (the small holes and triangular arrangement distributor) reaching more than 75 mm in compare with the other distributors. The bed expansion occurs due to the fluidisation of sand packed bed which indicates the effectivity of distributor to provide suitable air distribution. The comparison between pressure drop through the BFBG with the different distributors showed a uniform distribution of pressure drop for type D distributor and the variation of pressure for this distributor can be seen in heights more than the other distributor which indicates the wide of bed expansion.

The simulation results were validated with the experimental work and literature. The minimum percentage of differences between the average experimental results and the simulated ones was about 2% for type D distributor at the low superficial velocity and in the high pressure drop position (more than 500 pa) while the highest percentage of differences was about -90% for type A distributor at the high superficial velocity and in the low pressure drop position (less than 10 pa).

3- The use of the distributor was confirmed through a parallel Research Project. This process was simulated by using ASPEN PLUS®. The process showed very promising results at a reaction temperature of more than 600 °C. However, at a reaction temperature of 550 °C and below the reactions were reversed and the CH_4 and CO_2 concentrations have increased and the H_2 and CO concentrations have decreased.

This process accompanies with H_2O formation in different concentrations depending mainly on the reaction temperature.

Three different mixture were tested in this simulation, the light mixture (N_2-Ar-BFBG blend), the medium mixture (N_2-BFBG blend) and the strong mixture (BFBG blend only). The results showed a prevalence of the light mixture on the other mixtures in most of the produced gas properties. The strong mixture consumed more heat duty than the other mixtures.

The results depict a 99.99% conversion rate of the CH_4 in the product gas, which will be converted to syngas formed by Hydrogen and Carbon Monoxide. Furthermore, 57.6% of the CO_2 in the BFBG product gas can be converted to syngas. The maximum H_2 and CO selectivity for this process were estimated to be 81.2 % and 67.4 % respectively. The maximum H_2/CO ratio was about 0.64. In addition, the minimum thermal energy required to produce a one kmol of H_2 was 41.38 kWh for the light case mixture which is lower than the estimated by other refrence. There was a little effect of catalyst loading on the material conversion predicated by the simulation compares to the effect of reaction temperature.

7.3. Further Work

7.3.1. Experimental BFBG

In order to improve the experimental part of the bubbling fluidised bed gasifier there are many modifications that can be done to the system:

1- Measuring the local superficial velocity of the gas near the inner wall by using suitable velocity sensors which can add a new experimental factor. This is can be done synchronously with pressure drop measurement.

2- Using different particle sizes of sand (inert material) with or without a catalytic material and adding biomass material to the bed while testing the hydrodynamic behaviour of this regime. In this case, the relationship between these different particles can be spotted.

3- Testing different types of gas distributors such as the porous distributor and compare their performance with the perforated plate distributors.

7.3.2. Simulated BFBG

Regarding the OpenFOAM simulation of the BFBG many modifications can be added for future work:

1- Modify the OpenFOAM codes to simulate different particle sizes for different inert materials with or without a catalytic material and testing different biomass materials. This can provide a comprehensive visualisation for the system to go in deep this BFBG.

2- Including the effect of temperature and heat transfer in the simulation. However, this is will be very large and needs more computation time.

3- Including the reaction effect to simulate the overall gasification process. This is quite ambitious as this proposed simulation will produce very big data for a long computation time.

7.3.3. Post – Gasification Process Further Work

The improvement of BFBG product gas was assessed comprehensively by using ASPEN PLUS in chapter 6. This process aims to produce more syngas (H_2 and CO) from the BFBG product gas at the expense of the greenhouse components in the former. The simulation predicted good quantities of H_2 and CO that could be produced via this process.

However, the simulation results need at some point to be validated with some experimental work, thus they can be applied in industrial applications. Although not enough time was available to run these experiments, a comprehensive characterisation of all the needed parts was carried out under the hope to be able to perform these trials. In order to so, a Microwave system was conceptualised as the reforming device. Microwaves have the unique characteristic to deliver high energy pulses that if coupled with catalytic materials can generate high intensity energy regions, thus providing the required temperature for the reforming process to occur. Moreover, Cardiff University has a prestigious Microwave group who provided the initial insights of what can be the demonstration system for such a concept. As previously said, and unfortunately due to the lack of more time, experimental trials have been proposed using this device for future work.

The experimental system consists of the following parts:

1- A plug flow reactor (PFR): A 9mm ϕ x 100mm length quartz tube with 40mm reactive length as shown in figure 7.1.
2- Catalyst material: The catalyst material in this process is 10Ni/90%Al_2O_3 which has been activated in a hydrogen environment as shown in figure 7.2.
3- The heating system: A microwave cavity is used as the source of heating as shown in figure 7.3.
4- The BFBG product gas blend: This mixture consists of the following gases (CH_4 = 13.85%, H_2 = 15.7%, CO = 40.08% and CO_2 = 30.37%) in mole fraction. This gas mixture would be obtained from a 5-litters cylinder at 200 bar pressure as shown in figure 7.4.
5- Compact GC: The compact gas chromatograph will be used to analyse the composition of gases before and after the improvement process. Figure 7.5 shows the compact gas chromatograph.

Figure 7.1. The plug flow reactor (quartz tube).

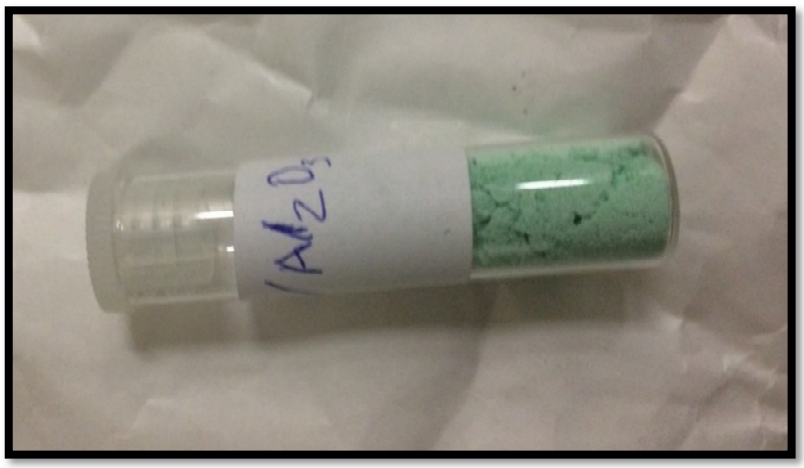

Figure 7.2. Activated catalyst.

Figure 7.3. The microwave cavity of the system.

Figure 7.4. BFBG product gas mixture.

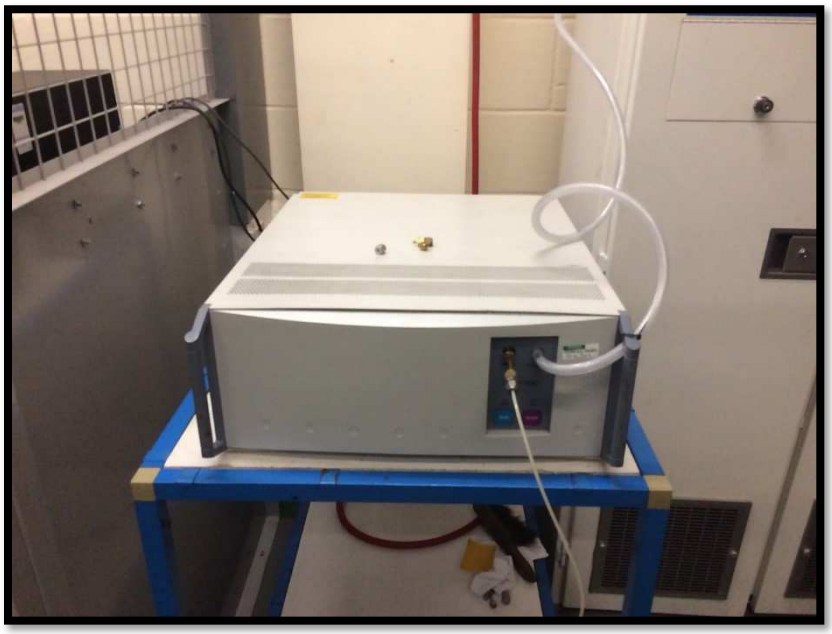

Figure 7.5. The compact gas chromatograph.

More work can be done with this system such as:

1- Using many types of catalytic material and testing their effects on the H_2 and CO selectivity. Although, the simulation showed a little effect of catalyst loading, using different catalyst types may have different results.

2- Using a conventional heating reformer and compare the results with the microwave system. This comparison can help to in choosing the system that can consume minimum heat duty with large H_2 selectivity.

References

ABATZOGLOU, N. & FAUTEUX-LEFEBVRE, C. 2016. Review of catalytic syngas production through steam or dry reforming and partial oxidation of studied liquid compounds. *Wiley Interdisciplinary Reviews: Energy and Environment,* 5**,** 169-187.

ABBAS, S., DUPONT, V. & MAHMUD, T. 2017. Kinetics study and modelling of steam methane reforming process over a NiO/Al2O3 catalyst in an adiabatic packed bed reactor. *International Journal of Hydrogen Energy,* 42**,** 2889-2903.

AGREEMENT, P. 2015. United nations framework convention on climate change. *Paris, France*.

AIGNER, M., GROSSO-GIORDANO, N. A., SCHÖTTLE, C., OKRUT, A., ZONES, S. & KATZ, A. 2017. Epoxidation of 1-octene under harsh tail-end conditions in a flow reactor II: impact of delaminated-zeolite catalyst surface area and structural integrity on catalytic performance. *Reaction Chemistry & Engineering,* 2**,** 852-861.

AKSOYLU, A. E., MADALENA, M., FREITAS, A., PEREIRA, M. F. R. & FIGUEIREDO, J. L. 2001. The effects of different activated carbon supports and support modifications on the properties of Pt/AC catalysts. *Carbon,* 39**,** 175-185.

AL-AKAISHI, A., VALERA-MEDINA, A., CHONG, C. & MARSH, R. 2017. CFD Analysis of the Fluidised Bed Hydrodynamic Behaviour inside an Isothermal Gasifier with different Perforated Plate Distributors. *Energy Procedia,* 142**,** 835-840.

AL-FARRAJI, A. 2017. *Chemical engineering and reactor design of a fluidised bed gasifier.* Ph.D. Dissertation, Cardiff University.

ALHUSSAN, K. A. 2013. Evolution In High Performance Computing And Its Effects On Extreme-Scale Simulations. *International Symposium On Computing In Atmospheric Sciences.* NCAR, Annecy, France: The National Center For Atmospheric Research.

AMASYALI, K. & EL-GOHARY, N. M. 2018. A review of data-driven building energy consumption prediction studies. *Renewable and Sustainable Energy Reviews,* 81**,** 1192-1205.

AMRANA, U. I., AHMADB, A. & OTHMAN, M. R. 2017. Kinetic based simulation of methane steam reforming and water gas shift for hydrogen production using Aspen Plus. *CHEMICAL ENGINEERING,* 56.

AMSDEN, A. A., O'ROURKE, P. & BUTLER, T. 1989. KIVA-II: A computer program for chemically reactive flows with sprays. Los Alamos National Lab., NM (USA).

ANDERSON, J. D. & WENDT, J. 1995. *Computational fluid dynamics*, Springer.

ANDERSON, T. B. & JACKSON, R. 1967. Fluid mechanical description of fluidized beds. Equations of motion. *Industrial & Engineering Chemistry Fundamentals,* 6**,** 527-539.

ANDERSSON, D. & KARLSSON, M. 2014. Investigation of the Effects of Introducing Hydrodynamic Parameters into a Kinetic Biomass Gasification Model for a Bubbling Fluidized Bed.

ANDREWS, M. & O'ROURKE, P. 1996. The multiphase particle-in-cell (MP-PIC) method for dense particulate flows. *International Journal of Multiphase Flow,* 22**,** 379-402.

ARCCA. [no date]. *ARCCA – Raven Supercomputing Cluster* [Online]. Available: https://www.cardiff.ac.uk/research-equipment/facilities/view/arcca-raven-supercomputing-cluster [Accessed 1 July 2016].

ARMSTRONG, L., GU, S. & LUO, K. 2010. Study of wall-to-bed heat transfer in a bubbling fluidised bed using the kinetic theory of granular flow. *International journal of heat and mass transfer,* 53**,** 4949-4959.

ARRHENIUS, S. 1889. Über die Reaktionsgeschwindigkeit bei der Inversion von Rohrzucker durch Säuren. *Zeitschrift für physikalische Chemie,* 4**,** 226-248.

AUZERAIS, F., JACKSON, R. & RUSSEL, W. 1988. The resolution of shocks and the effects of compressible sediments in transient settling. *Journal of Fluid Mechanics,* 195**,** 437-462.

BASU, P. 2006. *Combustion and gasification in fluidized beds*, CRC press.

BASU, P. 2015. *Circulating fluidized bed boilers Design, Operation and Maintenance*, Springer.

BASU, P., HORIO, M. & HASATANI, M. 1990. *Circulating Fluidized Bed Technology III,* Oxford, Pergamon.

BASU, P. & LARGE, J. F. 1988. *Circulating Fluidized Bed Technology II: Proceedings of the Second International Conference on Circulating Fluidized Beds, Compiègne, France, 14-18 March 1988,* Oxford, Pergamon.

BASU, P. & NAG, P. 1987. An investigation into heat transfer in circulating fluidized beds. *International journal of heat and mass transfer,* 30**,** 2399-2409.

BASU, P. & NAG, P. 1996. Heat transfer to walls of a circulating fluidized-bed furnace. *Chemical Engineering Science,* 51**,** 1-26.

BAWAH, A.-R., MALAIBARI, Z. O. & MURAZA, O. 2018. Syngas production from CO 2 reforming of methane over Ni supported on hierarchical silicalite-1 fabricated by microwave-assisted hydrothermal synthesis. *International Journal of Hydrogen Energy*.

BEHJAT, Y., SHAHHOSSEINI, S. & HASHEMABADI, S. H. 2008. CFD modeling of hydrodynamic and heat transfer in fluidized bed reactors. *International Communications in Heat and Mass Transfer,* 35**,** 357-368.

BELGIORNO, V., DE FEO, G., DELLA ROCCA, C. & NAPOLI, R. 2003. Energy from gasification of solid wastes. *Waste management,* 23**,** 1-15.

BENEROSO, D., BERMÚDEZ, J., ARENILLAS, A. & MENÉNDEZ, J. A. 2014. Integrated microwave drying, pyrolysis and gasification for valorisation of organic wastes to syngas. *Fuel,* 132**,** 20-26.

BENGUERBA, Y., DEHIMI, L., VIRGINIE, M., DUMAS, C. & ERNST, B. 2015. Modelling of methane dry reforming over Ni/Al 2 O 3 catalyst in a fixed-bed catalytic reactor. *Reaction Kinetics, Mechanisms and Catalysis,* 114**,** 109-119.

BERMÚDEZ, J., RUISÁNCHEZ, E., ARENILLAS, A., MORENO, A. & MENÉNDEZ, J. 2014. New concept for energy storage: microwave-induced carbon gasification with CO2. *Energy conversion and management,* 78**,** 559-564.

BODEN, T. A., MARLAND, G. & ANDRES, R. J. 2016. *Global, Regional, and National Fossil-Fuel CO2 Emissions* [Online]. Carbon Dioxide Information Analysis Center, Oak Ridge

National Laboratory, U.S. Department of Energy, Oak Ridge, Tenn., U.S.A. Available: http://doi.org/10.3334/CDIAC/00001_V2016 [Accessed 30 June 2016].

BODROV, I. & APEL'BAUM, L. 1967. Reaction kinetics of methane and carbon dioxide on a nickel surface. *Kinet. Catal,* 8**,** 379.

BRADFORD, M. C. & VANNICE, M. A. 1996. Catalytic reforming of methane with carbon dioxide over nickel catalysts II. Reaction kinetics. *Applied Catalysis A: General,* 142**,** 97-122.

BRADFORD, M. C. & VANNICE, M. A. 1998. CO2reforming of CH4over supported Pt catalysts. *Journal of Catalysis,* 173**,** 157-171.

BRAR, J., SINGH, K., WANG, J. & KUMAR, S. 2012. Cogasification of coal and biomass: a review. *International Journal of Forestry Research,* 2012.

BURTIN, P., BRUNELLE, J.-P., PIJOLAT, M. & SOUSTELLE, M. 1987. Influence of surface area and additives on the thermal stability of transition alumina catalyst supports. I: Kinetic data. *Applied Catalysis,* 34**,** 225-238.

CABEZAS-GOMEZ, L., DA SILVA, R. C., NAVARRO, H. A. & MILIOLI, F. E. 2008. Cluster identification and characterization in the riser of a circulating fluidized bed from numerical simulation results. *Applied Mathematical Modelling,* 32**,** 327-340.

CAMPBELL, C. S. & BRENNEN, C. E. 1985. Computer simulation of granular shear flows. *Journal of Fluid Mechanics,* 151**,** 167-188.

CAPECELATRO, J. & DESJARDINS, O. 2013. An Euler–Lagrange strategy for simulating particle-laden flows. *Journal of Computational Physics,* 238**,** 1-31.

CASCADE, O. 2005-2018. *SALOME 7.7.1* [Online]. Available: http://www.salome-platform.org/ [Accessed 1 July 2016].

CHEN, J. C. 2003. Surface Contact—Its Significance for Multiphase Heat Transfer: Diverse Examples. .*Journal of Heat Transfer,* 125**,** 549-566.

CHEN, J. C., GRACE, J. R. & GOLRIZ, M. R. 2005. Heat transfer in fluidized beds: design methods. *Powder Technology,* 150**,** 123-132.

CHEN, J. P. & KEAIRNS, D. 1975. Particle segregation in a fluidized bed. *The Canadian Journal of Chemical Engineering,* 53**,** 395-402.

CHEN, X. & WANG, J. 2014. A comparison of two-fluid model, dense discrete particle model and CFD-DEM method for modeling impinging gas–solid flows. *Powder Technology,* 254**,** 94-102.

CHEN, X. & WANG, J. 2017. Dynamic multiscale method for gas-solid flow via spatiotemporal coupling of two-fluid model and discrete particle model. *AIChE Journal,* 63**,** 3681-3691.

CHIBA, T., TERASHIMA, K. & KOBAYASHI, H. 1972. Behaviour of bubbles in gas—solids fluidized beds: initial formation of bubbles. *Chemical Engineering Science,* 27**,** 965-972.

CHO, R. 2011. *Is Biomass Really Renewable?* [Online]. Available: http://blogs.ei.columbia.edu/2011/08/18/is-biomass-really-renewable/ [Accessed 30 June 2016].

CHOUDHARY, V. R. & RAJPUT, A. M. 1996. Simultaneous Carbon Dioxide and Steam Reforming of Methane to Syngas over NiO− CaO Catalyst. *Industrial & engineering chemistry research,* 35**,** 3934-3939.

CIFERNO, J. P. & MARANO, J. J. 2002. Benchmarking biomass gasification technologies for fuels, chemicals and hydrogen production. *US Department of Energy. National Energy Technology Laboratory*.

CLEAN ENERGY CANADA 2016. A Year for the Record Books: Tracking the Energy Revolution—Global 2016 edition.

COLLINS JR, M. J. 2010. Future trends in microwave synthesis. *Future medicinal chemistry,* 2**,** 151-155.

COPPENS, M.-O. 2001. Method for operating a chemical and/or physical process by means of a hierarchical fluid injection system. Google Patents.

COUTO, N., ROUBOA, A., SILVA, V., MONTEIRO, E. & BOUZIANE, K. 2013. Influence of the biomass gasification processes on the final composition of syngas. *Energy Procedia,* 36**,** 596-606.

CRANFIELD, R. & GELDART, D. 1974. Large particle fluidisation. *Chemical Engineering Science,* 29**,** 935-947.

CUNDALL, P. A. & STRACK, O. D. 1979. A discrete numerical model for granular assemblies. *geotechnique,* 29**,** 47-65.

CZYLKOWSKI, D., HRYCAK, B., JASIŃSKI, M., DORS, M. & MIZERACZYK, J. 2016. Microwave plasma-based method of hydrogen production via combined steam reforming of methane. *Energy,* 113**,** 653-661.

DAWSON, K. 2016. *How does new nuclear generation help the energy trilemma?* [Online]. Available: https://pwc.blogs.com/energy_spotlight/2016/02/how-does-new-nuclear-generation-help-the-energy-trilemma.html [Accessed 22 December 2018].

DE FALCO, M., PIEMONTE, V., DI PAOLA, L. & BASILE, A. 2014. Methane membrane steam reforming: Heat duty assessment. *International journal of hydrogen energy,* 39**,** 4761-4770.

DESA, U. 2015. World Population Prospects, The 2015 Revision: Key Findings and Advance Tables. New York: United Nations: Working paper no. ESA/P/WP. 241. New York: United Nations Department of Economic and Social Affairs, Population Division.

DEUTSCHMANN, O., KNÖZINGER, H., KOCHLOEFL, K. & TUREK, T. 2011. Heterogeneous catalysis and solid catalysts, 2. development and types of solid catalysts. *Ullmann's Encyclopedia of Industrial Chemistry*.

DIGITRON 2017. Digital Pressure Meters (PM Series).

DING, J. & GIDASPOW, D. 1990. A bubbling fluidization model using kinetic theory of granular flow. *AIChE journal,* 36**,** 523-538.

DISKIN, A. M., CUNNINGHAM, R. H. & ORMEROD, R. M. 1998. The oxidative chemistry of methane over supported nickel catalysts. *Catalysis Today,* 46**,** 147-154.

E4TECH 2009. Review of Technologies for Gasification of Biomass and Wastes. NNFCC project 09/008.

EC, E. C. 2015. *Climate strategies & targets* [Online]. Available: https://ec.europa.eu/clima/policies/strategies_en [Accessed 22 December 2018].

ECE. 2016. *2030 Energy Strategy* [Online]. Available: https://ec.europa.eu/energy/node/163 [Accessed 30 June 2016].

ECOTRICITY. 2018. *The End of Fossil Fuels.* [Online]. Available: www.ecotricity.co.uk/our-green-energy/energy-independence/the-end-of-fossil-fuels [Accessed 15 August 2018].

EIA, U. S. 2013. International Energy Outlook 2013 With Projections to 2040. U.S. Energy Information Administration: Department of Energy: Washington, DC 20585.

EIA, U. S. 2016a. Annual Energy Outlook 2016 Early Release: Annotated Summary of Two Cases. U.S. Energy Information Administration: Department of Energy: Washington, DC 20585.

ERGUN, S. 1952. Fluid flow through packed columns. *Chem. Eng. Prog.,* 48**,** 89-94.

ERMAKOVA, M., ERMAKOV, D. Y. & KUVSHINOV, G. 2000. Effective catalysts for direct cracking of methane to produce hydrogen and filamentous carbon: Part I. Nickel catalysts. *Applied Catalysis A: General,* 201**,** 61-70.

ESI-OPENCFD. 2018. *OpenFOAM*® [Online]. Available: https://www.openfoam.com/about/ [Accessed 1 July 2016].

FAN, L. & ZHU, C. 1998. Principles of Gas-Solid Flows, Cambridge Series in Chemical Engineering. *Cambridge University Press, United Kingdom*.

FATTAHI, M., HOSSEINI, S. H. & AHMADI, G. 2016. CFD simulation of transient gas to particle heat transfer for fluidized and spouted regimes. *Applied Thermal Engineering,* 105**,** 385-396.

FERREIRA-APARICIO, P., GUERRERO-RUIZ, A. & RODRıGUEZ-RAMOS, I. 1998. Comparative study at low and medium reaction temperatures of syngas production by methane reforming with carbon dioxide over silica and alumina supported catalysts. *Applied Catalysis A: General,* 170**,** 177-187.

FERSCHNEIDER, G. & MEGE, P. 1996. Eulerian Simulation of Dense Phase Fluidized Beds. *Rev. Inst. Fr. Pét.,* 51**,** 301-307.

FOGLER, H. S. 2006. *Elements of chemical reaction engineering,* United States.

FOSCOLO, P., GIBILARO, L. & WALDRAM, S. 1983. A unified model for particulate expansion of fluidised beds and flow in fixed porous media. *Chemical engineering science,* 38**,** 1251-1260.

FOX, W., GREWAL, N. & MOEN, D. 1999. Wall-to-bed heat transfer in circulating fluidized beds. *International communications in heat and mass transfer,* 26**,** 499-508.

FRALEY, L., LIN, Y., HSIAO, K. & SOLBAKKEN, A. 1983. Heat transfer coefficient in circulating bed reactor. *ASME paper,* 83-HT-92, Seattle.

FRANKA, N. P., DRAKE, J. B. & HEINDEL, T. J. Minimum fluidization velocity and gas holdup in fluidized beds with side port air injection. ASME 2008 Fluids Engineering Division Summer Meeting collocated with the Heat Transfer, Energy Sustainability, and 3rd Energy Nanotechnology Conferences, 2008. American Society of Mechanical Engineers, 51-61.

GADALLA, A. M. & BOWER, B. 1988. The role of catalyst support on the activity of nickel for reforming methane with CO2. *Chemical Engineering Science,* 43**,** 3049-3062.

GANGURDE, L. S., STURM, G. S., VALERO-ROMERO, M., MALLADA, R., SANTAMARIA, J., STANKIEWICZ, A. I. & STEFANIDIS, G. D. 2018. Synthesis, characterization, and application of ruthenium-doped SrTiO3 perovskite catalysts for microwave-assisted methane dry reforming. *Chemical Engineering and Processing-Process Intensification,* 127**,** 178-190.

GAO, J., JIA, C., ZHANG, M., GU, F., XU, G. & SU, F. 2013. Effect of nickel nanoparticle size in Ni/α-Al 2 O 3 on CO methanation reaction for the production of synthetic natural gas. *Catalysis Science & Technology,* 3**,** 2009-2015.

GELDART, D. 1972. The effect of particle size and size distribution on the behaviour of gas-fluidised beds. *Powder Technology,* 6**,** 201-215.

GELDART, D. 1973. Types of gas fluidization. *Powder technology,* 7**,** 285-292.

GELDART, D. & BAEYENS, J. 1985. The design of distributors for gas-fluidized beds. *Powder Technology,* 42**,** 67-78.

GIDASPOW, D. 1986. Hydrodynamics of Fiuidizatlon and Heat Transfer: Supercomputer Modeling. *Applied Mechanics Reviews,* 39**,** 1-23.

GIDASPOW, D. 1994. *Multiphase flow and fluidization: continuum and kinetic theory descriptions*, Academic press.

GRACE, H. P. 1982. Dispersion phenomena in high viscosity immiscible fluid systems and application of static mixers as dispersion devices in such systems. *Chemical Engineering Communications,* 14**,** 225-277.

GREGOR, C., HERMANEK, M., JANCIK, D., PECHOUSEK, J., FILIP, J., HRBAC, J. & ZBORIL, R. 2010. The effect of surface area and crystal structure on the catalytic efficiency of iron (III) oxide nanoparticles in hydrogen peroxide decomposition. *European Journal of Inorganic Chemistry,* 2010**,** 2343-2351.

GUDE, V. G., PATIL, P., MARTINEZ-GUERRA, E., DENG, S. & NIRMALAKHANDAN, N. 2013. Microwave energy potential for biodiesel production. *Sustainable Chemical Processes,* 1**,** 5.

HAGEN, J. 2015. *Industrial catalysis: a practical approach*, John Wiley & Sons.

HALVORSEN, B. & ARVOH, B. 2009. Minimum fluidization velocity, bubble behaviour and pressure drop in fluidized beds with a range of particle sizes. *WIT Transactions on Engineering Sciences,* 63**,** 227-238.

HAMZEHLOUIA, S., JAFFER, S. A. & CHAOUKI, J. 2018. Microwave Heating-Assisted Catalytic Dry Reforming of Methane to Syngas. *Scientific reports,* 8**,** 8940.

HAO, Z., ZHU, Q., JIANG, Z., HOU, B. & LI, H. 2009. Characterization of aerogel Ni/Al2O3 catalysts and investigation on their stability for CH4-CO2 reforming in a fluidized bed. *Fuel processing technology,* 90**,** 113-121.

HARLOW, F. H. 1957. Hydrodynamic Problems Involving Large Fluid Distortions. *J. ACM,* 4**,** 137-142.

HARRIS, S. & CRIGHTON, D. 1994. Solitons, solitary waves, and voidage disturbances in gas-fluidized beds. *Journal of Fluid Mechanics,* 266**,** 243-276.

HELLAND, E., OCCELLI, R. & TADRIST, L. 2002. Computational study of fluctuating motions and cluster structures in gas–particle flows. *International Journal of Multiphase Flow,* 28**,** 199-223.

HO, G. S., FAIZAL, H. M. & ANI, F. N. 2017. Microwave induced plasma for solid fuels and waste processing: A review on affecting factors and performance criteria. *Waste Management*.

HOOMANS, B., KUIPERS, J., BRIELS, W. J. & VAN SWAAIJ, W. P. M. 1996. Discrete particle simulation of bubble and slug formation in a two-dimensional gas-fluidised bed: a hard-sphere approach. *Chemical Engineering Science,* 51**,** 99-118.

HOUGEN, O. A. & WATSON, K. M. 1943. Solid catalysts and reaction rates. *Ind. Eng. Chem,* 35**,** 529-541.

HRISTOV, J. 2002. MAGNETIC FIELD ASSISTED FLUIDIZATION–A UNIFIED APPROACH Part 1. Fundamentals and relevant hydrodynamics of gas-fluidized beds (batch solids mode). *Reviews in Chemical Engineering,* 18**,** 295-512.

HRISTOV, J. 2010. Magnetic field assisted fluidization–a unified approach. Part 8. Mass transfer: magnetically assisted bioprocesses. *Reviews in Chemical Engineering,* 26**,** 55-128.

IEA, I. E. A. 2018. World Energy Outlook 2018 (Executive Summary). International Energy Agency.

IPCC. 2013. *IPCC Factsheet: What is the IPCC?.* [Online]. Available: http://www.ipcc.ch/news_and_events/docs/factsheets/FS_what_ipcc.pdf [Accessed 15 June 2016].

ISMAIL, N. & ANI, F. 2014. Syngas Production from Microwave Gasification of Oil Palm Biochars. *Carbon (C),* 64**,** 79.40.

JAMRÓZ, P., KORDYLEWSKI, W. & WNUKOWSKI, M. 2018. Microwave plasma application in decomposition and steam reforming of model tar compounds. *Fuel Processing Technology,* 169**,** 1-14.

JAYARATHNA, C. K., HALVORSEN, B. M. & TOKHEIM, L.-A. 2014. Experimental and theoretical study of minimum fluidization velocity and void fraction of a limestone based CO2 sorbent. *Energy Procedia,* 63**,** 1432-1445.

JOKAR, S., RAHIMPOUR, M., SHARIATI, A., IULIANELLI, A., BAGNATO, G., VITA, A., DALENA, F. & BASILE, A. 2016. Pure Hydrogen Production in Membrane Reactor with Mixed Reforming Reaction by Utilizing Waste Gas: A Case Study. *Processes,* 4**,** 33.

JOKAR, S. M., PARVASI, P. & BASILE, A. 2018. The evaluation of methane mixed reforming reaction in an industrial membrane reformer for hydrogen production. *International Journal of Hydrogen Energy,* 43**,** 15321-15329.

KAART, S. 2002. *Controlling chaotic bubbles.* Doctor of Philosophy, Delft University of Technology.

KABALAN, B., WYLIE, S., MASON, A., AL-KHADDAR, R., AL-SHAMMA'A, A., LUPA, C., HERBERT, B. & MADDOCKS, E. Real-Time Optimisation of a Microwave Plasma Gasification System. Journal of Physics: Conference Series, 2011. IOP Publishing, 012027.

KARIM, W., SPREAFICO, C., KLEIBERT, A., GOBRECHT, J., VANDEVONDELE, J., EKINCI, Y. & VAN BOKHOVEN, J. A. 2017. Catalyst support effects on hydrogen spillover. *Nature,* 541**,** 68.

KARIMIPOUR, S. & PUGSLEY, T. 2011. A critical evaluation of literature correlations for predicting bubble size and velocity in gas–solid fluidized beds. *Powder Technology,* 205**,** 1-14.

KARPENKO, A., LEPPELT, R., PLZAK, V., CAI, J., CHUVILIN, A., SCHUMACHER, B., KAISER, U. & BEHM, R. 2007. Influence of the catalyst surface area on the activity and stability of Au/CeO 2 catalysts for the low-temperature water gas shift reaction. *Topics in Catalysis,* 44**,** 183-198.

KAWAGUCHI, T., SAKAMOTO, M., TANAKA, T. & TSUJI, Y. 2000. Quasi-three-dimensional numerical simulation of spouted beds in cylinder. *Powder Technology,* 109**,** 3-12.

KHAN, M. S., MITRA, S., GHATAGE, S., PENG, Z., DOROODCHI, E., MOGHTADERI, B., JOSHI, J. B. & EVANS, G. M. 2016. Pressure drop and voidage measurement in solid-liquid fluidized bed: Experimental, mathematical and computational study. *Chemeca 2016: Chemical Engineering-Regeneration, Recovery and Reinvention***,** 1019.

KIANG, K., LIU, K., NACK, H. & OXLEY, J. 1976. Heat transfer in fast fluidized beds. *In:* KEAIRNS, D. L. (ed.) *Fluidization Technology.* Washington, DC: Hemisphere,.

KIM, S. W., AHN, J. Y., KIM, S. D. & LEE, D. H. 2003. Heat transfer and bubble characteristics in a fluidized bed with immersed horizontal tube bundle. *International Journal of Heat and Mass Transfer,* 46**,** 399-409.

KINGSTON, H. M. & JASSIE, L. B. 1988. *Introduction to microwave sample preparation: theory and practice*, American Chemical Society.

KOBRO, H. & BRERETON, C. Control and fuel flexibility of circulating fluidised bed. Circulating Fluidized Bed Technology: Proceedings of the First International Conference, 1986. Elsevier, 263-272.

KUIPERS, J., TAMMES, H., PRINS, W. & VAN SWAAIJ, W. P. M. 1992a. Experimental and theoretical porosity profiles in a two-dimensional gas-fluidized bed with a central jet. *Powder technology,* 71**,** 87-99.

KUIPERS, J. A. M., PRINS, W. & VAN SWAAIJ, W. P. M. 1992b. Numerical calculation of wall-to-bed heat-transfer coefficients in gas-fluidized beds. *AIChE Journal,* 38**,** 1079-1091.

KUNII, D. & LEVENSPIEL, O. 1968. Bubbling bed model. Model for flow of gas through a fluidized bed. *Industrial & Engineering Chemistry Fundamentals,* 7**,** 446-452.

KUNII, D. & LEVENSPIEL, O. 1991a. *Fluidization engineering,* 80 Montvale Avenue, Stoneham, MA 02180, USA, Butterworth-Heinemann.

KUNII, D. & LEVENSPIEL, O. 1991b. Phase interchange coefficients in bubbling fluidized beds. *Journal of chemical engineering of Japan,* 24**,** 138-141.

KUSAKABE, K., SOTOWA, K.-I., EDA, T. & IWAMOTO, Y. 2004. Methane steam reforming over Ce–ZrO2-supported noble metal catalysts at low temperature. *Fuel Processing Technology,* 86**,** 319-326.

KWAUK, M. 1992. *Fluidization: idealized and bubbleless, with applications*, Ellis Horwood Ltd.

LAO, L., AGUIRRE, A., TRAN, A., WU, Z., DURAND, H. & CHRISTOFIDES, P. D. 2016. CFD modeling and control of a steam methane reforming reactor. *Chemical Engineering Science,* 148**,** 78-92.

LE QUÉRÉ, C., ANDREW, R. M., FRIEDLINGSTEIN, P., SITCH, S., HAUCK, J., PONGRATZ, J., PICKERS, P. A., KORSBAKKEN, J. I., PETERS, G. P., CANADELL, J. G., ARNETH, A., ARORA, V. K., BARBERO, L., BASTOS, A., BOPP, L., CHEVALLIER, F., CHINI, L. P., CIAIS, P., DONEY, S. C., GKRITZALIS, T., GOLL, D. S., HARRIS, I., HAVERD, V., HOFFMAN, F. M., HOPPEMA, M., HOUGHTON, R. A., HURTT, G., ILYINA, T., JAIN, A. K., JOHANNESSEN, T., JONES, C. D., KATO, E., KEELING, R.

F., GOLDEWIJK, K. K., LANDSCHÜTZER, P., LEFÈVRE, N., LIENERT, S., LIU, Z., LOMBARDOZZI, D., METZL, N., MUNRO, D. R., NABEL, J. E. M. S., NAKAOKA, S. I., NEILL, C., OLSEN, A., ONO, T., PATRA, P., PEREGON, A., PETERS, W., PEYLIN, P., PFEIL, B., PIERROT, D., POULTER, B., REHDER, G., RESPLANDY, L., ROBERTSON, E., ROCHER, M., RÖDENBECK, C., SCHUSTER, U., SCHWINGER, J., SÉFÉRIAN, R., SKJELVAN, I., STEINHOFF, T., SUTTON, A., TANS, P. P., TIAN, H., TILBROOK, B., TUBIELLO, F. N., VAN DER LAAN-LUIJKX, I. T., VAN DER WERF, G. R., VIOVY, N., WALKER, A. P., WILTSHIRE, A. J., WRIGHT, R., ZAEHLE, S. & ZHENG, B. 2018. Global Carbon Budget 2018. *Earth Syst. Sci. Data,* 10**,** 2141-2194.

LEOFANTI, G., PADOVAN, M., TOZZOLA, G. & VENTURELLI, B. 1998. Surface area and pore texture of catalysts. *Catalysis Today,* 41**,** 207-219.

LEVENSPIEL, O. 2002. G/S reactor models-packed beds, bubbling fluidized beds, turbulent fluidized beds and circulating (fast) fluidized beds. *Powder technology,* 1**,** 1-9.

LEVENSPIEL, O. 2004. *Modeling the Bubbling Fluidized Bed Reactor, BFB.* [Online]. Available: http://chemeng.mst.edu/facultystaffandfacilities/levenspiel/.

LEWIS, W., GILLILAND, E. & REED, W. A. 1949. Reaction of methane with copper oxide in a fluidized bed. *Industrial & Engineering Chemistry,* 41**,** 1227-1237.

LI, C., DAI, Z., LI, W., XU, J. & WANG, F. 2012. 3D numerical study of particle flow behavior in the impinging zone of an Opposed Multi-Burner gasifier. *Powder technology,* 225**,** 118-123.

LI, H. & MA, X. H. 3D Numerical Simulation of the Fluidized Bed's Cold Distributor. Applied Mechanics and Materials, 2011. Trans Tech Publ, 2112-2115.

LI, L., WANG, H., JIANG, X., SONG, Z., ZHAO, X. & MA, C. 2016. Microwave-enhanced methane combined reforming by CO2 and H2O into syngas production on biomass-derived char. *Fuel,* 185**,** 692-700.

LI, L., YANG, Z., CHEN, J., QIN, X., JIANG, X., WANG, F., SONG, Z. & MA, C. 2018. Performance of bio-char and energy analysis on CH 4 combined reforming by CO 2 and H 2 O into syngas production with assistance of microwave. *Fuel,* 215**,** 655-664.

LIM, M. S. & CHUN, Y. N. 2017. Biogas to Syngas by Microwave-Assisted Reforming in the Presence of Char. *Energy & Fuels,* 31**,** 13761-13768.

LINDLAR, H. & DUBUIS, R. 1966. Palladium catalyst for partial reduction of acetylenes. *Organic Syntheses*, 89-89.

LIU, Y., WANG, G., WANG, Q., WEI, X., SHAO, Q. & LIU, F. 2018. Comparison between isothermal and microwave gasification of lignite char for high syngas production. *Energy Sources, Part A: Recovery, Utilization, and Environmental Effects,* 40, 266-273.

LUN, C., SAVAGE, S. B., JEFFREY, D. & CHEPURNIY, N. 1984. Kinetic theories for granular flow: inelastic particles in Couette flow and slightly inelastic particles in a general flowfield. *Journal of fluid mechanics,* 140, 223-256.

LV, P., XIONG, Z., CHANG, J., WU, C., CHEN, Y. & ZHU, J. 2004. An experimental study on biomass air–steam gasification in a fluidized bed. *Bioresource technology,* 95, 95-101.

MA, Z. & ZAERA, F. 2014. Heterogeneous catalysis by metals. *Encyclopedia of Inorganic and Bioinorganic Chemistry*.

MACHIDA, M., EGUCHI, K. & ARAI, H. 1987. Effect of additives on the surface area of oxide supports for catalytic combustion. *Journal of catalysis,* 103, 385-393.

MARK, M. F. & MAIER, W. F. 1996. CO2-reforming of methane on supported Rh and Ir catalysts. *Journal of Catalysis,* 164, 122-130.

MASOUMIFARD, N., MOSTOUFI, N. & SOTUDEH-GHAREBAGH, R. 2010. Prediction of the maximum heat transfer coefficient between a horizontal tube and gas–solid fluidized beds. *Heat Transfer Engineering,* 31, 870-879.

MATTHEY, J. 2018. *Industrial Catalysis - Case study - steam reforming* [Online]. Available: http://resources.schoolscience.co.uk/johnsonmatthey/page17.htm [Accessed 22 December 2018].

MATTOS, L., RODINO, E., RESASCO, D., PASSOS, F. & NORONHA, F. 2003. Partial oxidation and CO2 reforming of methane on Pt/Al2O3, Pt/ZrO2, and Pt/Ce–ZrO2 catalysts. *Fuel Processing Technology,* 83, 147-161.

MAURER, S., GSCHWEND, D., WAGNER, E. C., SCHILDHAUER, T. J., VAN OMMEN, J. R., BIOLLAZ, S. M. & MUDDE, R. F. 2016. Correlating bubble size and velocity distribution in bubbling fluidized bed based on X-ray tomography. *Chemical Engineering Journal,* 298, 17-25.

MCKEEN, T. & PUGSLEY, T. 2003. Simulation and experimental validation of a freely bubbling bed of FCC catalyst. *Powder Technology,* 129**,** 139-152.

MCNAUGHT, A. D. & WILKINSON, A. 1997. *Compendium of chemical terminology,* Oxford (1997), Blackwell Science Oxford.

MICKLEY, H. S. & TRILLING, C. A. 1949. Heat transfer characteristics of fluidized beds. *Industrial & Engineering Chemistry,* 41**,** 1135-1147.

MULLER, P. 1994. Glossary of terms used in physical organic chemistry (IUPAC Recommendations 1994). *Pure and Applied Chemistry,* 66**,** 1077-1184.

NARVÁEZ, I., ORÍO, A., AZNAR, M. P. & CORELLA, J. 1996. Biomass Gasification with Air in an Atmospheric Bubbling Fluidized Bed. Effect of Six Operational Variables on the Quality of the Produced Raw Gas. *Industrial & Engineering Chemistry Research,* 35**,** 2110-2120.

NGOH, J. & LIM, E. W. C. 2016. Effects of particle size and bubbling behavior on heat transfer in gas fluidized beds. *Applied Thermal Engineering,* 105**,** 225-242.

NIH, W. R. 2018. ImageJ, image processing and analysis in Java. 1.52e ed.

O'CONNOR, K. & CRANDELL, J. 2012. Microwave Hydrogen Production from Methane. TECHNIKON LLC.

OGER, L. & SAVAGE, S. B. 2013. Airslide flows. Part 2—Flow modeling and comparison with experiments. *Chemical Engineering Science,* 91**,** 22-34.

OLOFSSON, I., NORDIN, A. & SÖDERLIND, U. 2005. *Initial review and evaluation of process technologies and systems suitable for cost-efficient medium-scale gasification for biomass to liquid fuels*, Umeå Universitet.

OSAKI, T., HORIUCHI, T., SUZUKI, K. & MORI, T. 1997. Catalyst performance of MoS2 and WS2 for the CO2-reforming of CH4 suppression of carbon deposition. *Applied Catalysis A: General,* 155**,** 229-238.

OSHIMA, K., SHINAGAWA, T., NOGAMI, Y., MANABE, R., OGO, S. & SEKINE, Y. 2014. Low temperature catalytic reverse water gas shift reaction assisted by an electric field. *Catalysis Today,* 232**,** 27-32.

ÖZKARA-AYDıNOĞLU, Ş. & AKSOYLU, A. E. 2013. A comparative study on the kinetics of carbon dioxide reforming of methane over Pt–Ni/Al2O3 catalyst: Effect of Pt/Ni Ratio. *Chemical engineering journal,* 215**,** 542-549.

PAGLIUSO, J. D., LOMBARDI, G. & GOLDSTEIN JR, L. 2000. Experiments on the local heat transfer characteristics of a circulating fluidized bed. *Experimental Thermal and Fluid Science,* 20**,** 170-179.

PAL, D. B. & PRASAD, R. 2014. *Study of water-gas shift reaction*, Lap lambert academic publishing.

PANNALA, S. 2010. *Computational Gas-Solids Flows and Reacting Systems: Theory, Methods and Practice: Theory, Methods and Practice*, IGI Global.

PANTOLEONTOS, G., KIKKINIDES, E. S. & GEORGIADIS, M. C. 2012. A heterogeneous dynamic model for the simulation and optimisation of the steam methane reforming reactor. *international journal of hydrogen energy,* 37**,** 16346-16358.

PAPADIKIS, K., GU, S. & BRIDGWATER, A. 2009. CFD modelling of the fast pyrolysis of biomass in fluidised bed reactors. Part B: Heat, momentum and mass transport in bubbling fluidised beds. *Chemical Engineering Science,* 64**,** 1036-1045.

PARK, N., PARK, M.-J., BAEK, S.-C., HA, K.-S., LEE, Y.-J., KWAK, G., PARK, H.-G. & JUN, K.-W. 2014. Modeling and optimization of the mixed reforming of methane: Maximizing CO2 utilization for non-equilibrated reaction. *Fuel,* 115**,** 357-365.

PARMAR, M. & HAYHURST, A. 2002. The heat transfer coefficient for a freely moving sphere in a bubbling fluidised bed. *Chemical Engineering Science,* 57**,** 3485-3494.

PATIL, D. H. & SHINDE, J. 2017. A Review Paper on Study of Bubbling Fluidized Bed Gasifier. *IJIRST –International Journal for Innovative Research in Science & Technology,* 4.

PHILIPPSEN, C. G., VILELA, A. C. F. & DALLA ZEN, L. 2015. Fluidized bed modeling applied to the analysis of processes: review and state of the art. *Journal of Materials Research and Technology,* 4**,** 208-216.

PHILLIPS, J. 2006. Different types of gasifiers and their integration with gas turbines. *Handbook of Gas Turbines By National Energy Technology Labratory.*

PHOTRON LIMITED 2006. FASTCAM-APX RS Hardware Manual.

PLUS, A. 2009. Aspen Technology. *Inc., version,* 11.

RADMANESH, R., CHAOUKI, J. & GUY, C. 2006. Biomass gasification in a bubbling fluidized bed reactor: experiments and modeling. *AIChE Journal,* 52**,** 4258-4272.

RICHARDSON, J. & PARIPATYADAR, S. 1990. Carbon dioxide reforming of methane with supported rhodium. *Applied Catalysis,* 61**,** 293-309.

ROBOCK, A. 1978. Internally and externally caused climate change. *Journal of the Atmospheric Sciences,* 35**,** 1111-1122.

ROSENSWEIG, R. 1995. Process concepts using field-stabilized two-phase fluidized flow. *Journal of electrostatics,* 34**,** 163-187.

ROTHENBERG, G. 2017. *Catalysis: concepts and green applications*, John Wiley & Sons.

RUIZ-OJEDA, L. M. & PEÑAS, F. J. 2013. Comparison study of conventional hot-water and microwave blanching on quality of green beans. *Innovative Food Science & Emerging Technologies,* 20**,** 191-197.

SALWE, A. M., PANDE, S. S. & KHAN, J. S. 2014. Effect of velocity and particle size on the coefficient of heat transfer in fluidized bed heat exchanger.

SANLISOY, A. & CARPINLIOGLU, M. O. 2018. Preliminary measurements on microwave plasma flame for gasification. *Energy, Ecology and Environment,* 3**,** 32-38.

SARAVANAKUMAR, A., HARIDASAN, T. & REED, T. B. 2010. Flaming pyrolysis model of the fixed bed cross draft long-stick wood gasifier. *Fuel Processing Technology,* 91**,** 669-675.

SHAO, Y., MENG, D., XU, C. C., PRETO, F. & ZHU, J. 2018. Ash Deposition in Air-Blown Gasification of Peat and Woody Biomass in a Fluidized-Bed Gasifier. *Energy & Fuels,* 32**,** 6788-6796.

SHEN, L. & ZHANG, M. 1998. Effect of particle size on solids mixing in bubbling fluidized beds. *Powder Technology,* 97**,** 170-177.

SHUKRIE, A., ANUAR, S. & OUMER, A. N. 2016. Air Distributor Designs for Fluidized Bed Combustors: A Review. *Engineering, Technology & Applied Science Research,* 6**,** 1029-1034.

SIARGO LTD. 2017. MEMS Mass Flow Meter MF5700 Series User Manual.

SIVAGAMI, K., RAVI KRISHNA, R. & SWAMINATHAN, T. 2016. Optimization studies on degradation of monocrotophos in an immobilized bead photo reactor using design of experiment. *Desalination and Water Treatment,* 57**,** 28822-28830.

SMIL, V. 2004. World history and energy. *Encyclopedia of energy,* 6**,** 549-561.

SNIDER, D. 2001. An incompressible three-dimensional multiphase particle-in-cell model for dense particle flows. *Journal of Computational Physics,* 170**,** 523-549.

SNIDER, D., OROURKE, P. & ANDREWS, M. 1997. An incompressible two-dimensional multiphase particle-in-cell model for dense particle flows. Los Alamos National Lab., NM (United States).

SORIA-VERDUGO, A., GARCIA-GUTIERREZ, L., GARCÍA-HERNANDO, N. & RUIZ-RIVAS, U. 2011. Buoyancy effects on objects moving in a bubbling fluidized bed. *Chemical engineering science,* 66**,** 2833-2841.

STURM, G. S., MUÑOZ, A. N., ARAVIND, P. & STEFANIDIS, G. D. 2016. Microwave-driven plasma gasification for biomass waste treatment at miniature scale. *IEEE Transactions on Plasma Science,* 44**,** 670-678.

SUN, G. & GRACE, J. R. 1990. The effect of particle size distribution on the performance of a catalytic fluidized bed reactor. *Chemical Engineering Science,* 45**,** 2187-2194.

SUN, G. & GRACE, J. R. 1992. Effect of particle size distribution in different fluidization regimes. *AIChE journal,* 38**,** 716-722.

SUN, J., WANG, Q., WANG, W. & WANG, K. 2018. Study on the synergism of steam reforming and photocatalysis for the degradation of Toluene as a tar model compound under microwave-metal discharges. *Energy,* 155**,** 815-823.

SUN, Y., RITCHIE, T., HLA, S., MCEVOY, S., STEIN, W. & EDWARDS, J. 2011. Thermodynamic analysis of mixed and dry reforming of methane for solar thermal applications. *Journal of Natural Gas Chemistry,* 20**,** 568-576.

SURMA, J. E. 1985. *The determination of bubble velocity in fluidized beds.* Montana State University-Bozeman, College of Engineering.

THAMMACHART, M., MEEYOO, V., RISKSOMBOON, T. & OSUWAN, S. 2001. Catalytic activity of CeO2–ZrO2 mixed oxide catalysts prepared via sol–gel technique: CO oxidation. *Catalysis Today,* 68**,** 53-61.

THAPA, R. K. & HALVORSEN, B. M. 2013. Study of flow behavior in bubbling fluidized bed biomass gasification reactor using CFD simulation.

THECCC. 2017. *Climate Change Legislation in the EU* [Online]. Available: https://www.theccc.org.uk/tackling-climate-change/the-legal-landscape/european-union-legislation/ [Accessed 30 June 2016].

TSUJI, Y., KAWAGUCHI, T. & TANAKA, T. 1993. Discrete particle simulation of two-dimensional fluidized bed. *Powder technology,* 77**,** 79-87.

TSUKADA, M. & HORIO, M. 1992. Maximum heat-transfer coefficient for an immersed body in a bubbling fluidized bed. *Industrial & engineering chemistry research,* 31**,** 1147-1156.

VALLANCE, C. 2018. *Reaction Kinetics* [Online]. Available: http://vallance.chem.ox.ac.uk/pdfs/KineticsLectureNotes.pdf [Accessed 30 May 2018].

VAN WILLIGEN, F. K., VAN OMMEN, J. R., VAN TURNHOUT, J. & VAN DEN BLEEK, C. 2003. Bubble size reduction in a fluidized bed by electric fields. *International Journal of Chemical Reactor Engineering,* 1.

WANG, B., YANG, Y., LI, L.-J. & CHEN, Y. 2009. Effect of different catalyst supports on the (n, m) selective growth of single-walled carbon nanotube from Co–Mo catalyst. *Journal of materials science,* 44**,** 3285-3295.

WANG, F.-J., CHEN, S., LEI, P.-K. & WU, C.-H. 2007. Effects of pressure drop and superficial velocity on the bubbling fluidized bed incinerator. *Journal of Environmental Science and Health, Part A,* 42**,** 2147-2158.

WANG, X., LI, N., ZHANG, Z., WANG, C., PFEFFERLE, L. D. & HALLER, G. L. 2012. High-yield hydrogen production from aqueous phase reforming over single-walled carbon nanotube supported catalysts. *ACS Catalysis,* 2**,** 1480-1486.

WANG, Y., CHEN, M., LIANG, T., YANG, Z., YANG, J. & LIU, S. 2016. Hydrogen generation from catalytic steam reforming of acetic acid by Ni/attapulgite catalysts. *Catalysts,* 6**,** 172.

WEN, C.-Y. & MILLER, E. 1961. Heat Transfer in Solids-Gas Transport Lines. *Industrial & Engineering Chemistry,* 53**,** 51-53.

WEN, C. & YU, Y. 1966. A generalized method for predicting the minimum fluidization velocity. *AIChE Journal,* 12**,** 610-612.

WNUKOWSKI, M. 2014. Decomposition of tars in microwave plasma–preliminary results. *Journal of Ecological Engineering,* 15.

WOOD, B. J., BASRI, Z. M. N. J. M., ALI, W. N. K. Z., WOOD, B., HASAN, Y., WOOD, B., JCX LIAU, S., WOOD, B., DP PHANG SEW PIGGOTT, C. & WOOD, R. 1986. Wood gas as engine fuel. Food and Agriculture Organization of the United Nations.

WU, W., JAYARATHNA, S. A. & HALVORSEN, B. M. 2008. Experimental study of effects of particle size distribution on bubble behavior for validation of CFD modeling of bubbling fluidized bed. *small,* 400**,** 600.

XIE, Q., BORGES, F. C., CHENG, Y., WAN, Y., LI, Y., LIN, X., LIU, Y., HUSSAIN, F., CHEN, P. & RUAN, R. 2014. Fast microwave-assisted catalytic gasification of biomass for syngas production and tar removal. *Bioresource technology,* 156**,** 291-296.

XU, J. & FROMENT, G. F. 1989. Methane steam reforming, methanation and water-gas shift: I. Intrinsic kinetics. *AIChE journal,* 35**,** 88-96.

XUE, J., CHEN, F., YANG, N. & GE, W. 2017. A study of the soft-sphere model in eulerian-lagrangian simulation of gas-liquid flow. *International Journal of Chemical Reactor Engineering,* 15.

YANG, L., PADDING, J., BUIST, K. & KUIPERS, J. 2017. Three-dimensional fluidized beds with rough spheres: Validation of a Two Fluid Model by Magnetic Particle Tracking and discrete particle simulations. *Chemical Engineering Science,* 174**,** 238-258.

YE, M., WANG, J., VAN DER HOEF, M. & KUIPERS, J. 2008. Two-fluid modeling of Geldart A particles in gas-fluidized beds. *Particuology,* 6**,** 540-548.

YOKOYAMA, S. & MATSUMURA, Y. 2008. *The Asian biomass handbook: a guide for biomass production and utilization*, The Japan Institute of Energy.

YOON, S. J. & LEE, J. G. 2012. Syngas production from coal through microwave plasma gasification: influence of oxygen, steam, and coal particle size. *Energy & Fuels,* 26**,** 524-529.

ZHANG, F., SONG, Z., ZHU, J., LIU, L., SUN, J., ZHAO, X., MAO, Y. & WANG, W. 2018. Process of CH 4-CO 2 reforming over Fe/SiC catalyst under microwave irradiation. *Science of The Total Environment,* 639**,** 1148-1155.

ZHANG, J., WANG, H. & DALAI, A. K. 2008. Kinetic studies of carbon dioxide reforming of methane over Ni− Co/Al− Mg− O bimetallic catalyst. *Industrial & Engineering Chemistry Research,* 48**,** 677-684.

ZHANG, K., KOGELSCHATZ, U. & ELIASSON, B. 2001. Conversion of greenhouse gases to synthesis gas and higher hydrocarbons. *Energy & Fuels,* 15**,** 395-402.

ZHANG, P., DUAN, J. H., CHEN, G. H. & WANG, W. W. 2015. Effect of bed characters on the direct synthesis of dimethyldichlorosilane in fluidized bed reactor. *Scientific reports,* 5**,** 8827.

ZHU, H., ZHOU, Z., YANG, R. & YU, A. 2008. Discrete particle simulation of particulate systems: a review of major applications and findings. *Chemical Engineering Science,* 63**,** 5728-5770.

ZIMMERMANN, S. & TAGHIPOUR, F. 2005. CFD modeling of the hydrodynamics and reaction kinetics of FCC fluidized-bed reactors. *Industrial & engineering chemistry research,* 44**,** 9818-9827.

ZOU, B., LI, H., XIA, Y. & MA, X. 1994. Cluster structure in a circulating fluidized bed. *Powder technology,* 78**,** 173-178.